Improving the Spectral Coverage and Resolution of the ISOLDE RILIS

Dissertation zur Erlangung des Grades

„Doktor der Naturwissenschaften“

am Fachbereich Physik, Mathematik und Informatik (FB 08)

der Johannes Gutenberg-Universität

in Mainz

Katerina Chrysalidis

geb. in Langen (Hessen)

Mainz, den 08.12.2019

Datum der mündlichen Prüfung: Mainz, den 29.11.2019

Abstract

This thesis concerns applications and developments of the Resonance Ionization Laser Ion Source (RILIS) at CERN-ISOLDE for ion beam production and laser spectroscopy. Laser developments, including the first operation of a grating-tuned Ti:sapphire combined with a thick etalon for linewidth reduction, the construction and characterization of a seeded Ti:sapphire ring cavity laser and the first demonstration of a Raman laser in the blue spectral range are presented. In-source laser spectroscopy on Dy isotopes has been performed, providing a valuable insight into the nuclear charge radii systematics near proton number $Z = 64$. This work also illustrates the resolution limit imposed by Doppler-broadening of the atomic spectral lines inside the ion source. Addressing this limitation, the Doppler-free 2-photon ionization technique has been developed, leading to its first successful "in-source" application. The future of this approach to significantly increase the spectral resolution of RILIS is discussed.

Contents

Contents

List of Tables

List of Figures

List of Figures

Introduction

"[..] For the first time in history a source of 'coherent' light has been attained.

This is another way of saying, that the long-sought 'laser' is no longer an elusive dream but, is indeed, an established fact. [...]

For the first time in scientific history we have achieved true amplification of light waves. We will have an important new scientific tool for investigating properties of matter and for performing basic experiments of physics. [...]"

Theodore H. Maiman in his speech at the press conference announcing the invention of the laser, New York, July 7 1960

1 Introduction

Theodore Maiman correctly predicted the impact that the invention of the laser would have on the world of science. Since its first demonstration in 1960 there were rapid developments, leading to the first tunable lasers only a few years later ([1, 2, 3, 4]). Before the development of tunable lasers, elements accessible to laser spectroscopy were mainly helium and neon, seeing as helium-neon lasers were providing laser light with the correct absorption wavelengths. The method of resonance laser ionization was introduced in the beginning of the 70s by V.N. Letokhov [5, 6], opening up a new field of fundamental physics experiments. Using resonance excitation of atoms or ions with laser light provided by tunable lasers, access to atomic properties of the elements and their isotopes can be gained and in addition deliver their nuclear ground state properties. The most recent review, published in 2016 by P. Campbell et al. [7], gives an overview over the laser spectroscopy techniques used for nuclear structure physics.

At CERN's Isotope Separator On-Line facility (ISOLDE, see section 3.1), laser spectroscopy is one of the most commonly used tools for nuclear structure studies. Several experiments use the technique to study isotopes with high resolution: COLLAPS, the oldest still existing laser spectroscopy experiment at ISOLDE [8], CRIS [9] and VITO [10]. A new set up, MIRACLS [11], is in the commissioning phase at the time of writing and will combine laser spectroscopy with a multi-reflection time of flight mass spectrometer (MR-ToF MS).

Another approach for laser spectroscopy is the so called "in-source laser spectroscopy" technique (see chapter 5). In contrast to the other techniques, it uses stepwise resonance laser ionization inside the ion source and is limited by the Doppler-broadening of the atomic lines inside the hot cavity environment. Originally, the Resonance Ionization Laser Ion Source (RILIS, see section 3.2) was proposed to serve the purpose of a spectroscopy experiment [12], providing the so-called 'spectroscopic' and 'ionizing' transitions. Over the years of RILIS operation this method has had a significant impact upon the field, especially in the mass range A>120 (see e.g. the latest publications [13, 14, 15, 16]). The main advantage of the in-source method is its unsurpassed sensitivity, as the initial ionization process used for radionuclide production is being studied. The spectroscopy

does not involve the losses associated with cooling, ion bunching or re-neutralization, which are necessary for other optical spectroscopy methods at ISOLDE. Detection of the ions created during a laser scan can be performed either via Faraday cups, decay spectroscopy setups (e.g. IDS [17]) or with the ISOLDE Penningtrap or MR-ToF MS (ISOLTRAP [18]).

The resolution limit of in-source laser spectroscopy is the Doppler-broadening of the atomic lines. The application of this method is therefore generally limited to the heavy-mass range for two main reasons: Doppler broadening is inversely proportional to the square root of the mass; and, as the mass increases, the field shifts and overall isotope shifts increase in magnitude with mass. Even so, hyperfine structures (HFS) are rarely fully resolved and the isotope shifts are only measurable for particularly sensitive transitions. Overall trends, crucial for determining e.g. the isotope shift and, in derivation, the changes in mean-squared charge radii, can be resolved. For more subtle parameters, like the hyperfine anomaly or magnetic and electric moments, an improved resolution, is often required.

The RILIS is the most selective of all ion sources used at ISOLDE. Resonance laser ionization can be applied for most elements, with only few exceptions (the non-metals). One limitation in the application of RILIS stems from the thick-target ISOL process, rather than the limitation of the laser system itself: the effusion/extraction of radiogenically produced isotopes which have too low a vapor pressure at the achievable operating temperature, the so-called "refractory" elements, is difficult or impossible. For the non-metals, the required laser wavelength and high ionization potential (IP) of the element limits the feasibility of RILIS ionization.

When looking at previous developments at the RILIS, the following topics were addressed:

- Implementation of solid state lasers: The original RILIS laser system consisted of copper vapor (CV) laser pumped dye lasers. After replacing the pump lasers by diode pumped solid state (DPSS) lasers [19], the addition of tunable solid state Ti:sapphire lasers removed the need of (rather inconvenient) dyes in the infrared spectral range and made set up in parallel to operation feasible. This work was

described in the thesis of S. Rothe [20].

- Enhancement of the operational capabilities: The operational capabilities of the RILIS were improved mainly by opting for motorized and automated solutions for wavelength, timing and beam pointing stabilization. Additionally, the data acquisition and list of observable parameters was improved. Crucially, an automated machine protection system was implemented to take immediate action, and alert a laser operator in the event of a malfunction such as a leak of laser dye. This way, no need for an on-shift RILIS operator exists, making it possible to operate the RILIS for longer periods of time and more frequently than before. This work was performed by R. Rossel for his theses [21, 22].

- Increase of the selectivity: The ratio of surface ionized isobaric contamination to laser ionized species, can be improved in different ways. One of them is by use of the Laser Ion Source and Trap (LIST), which has been successfully applied in in-source laser experiments ([23, 24, 25]). The LIST is equipped with a repeller, which can suppress surface ions. The laser ionization no longer takes place inside the hot cavity, which is why ion confinement is realized with an RF-field inside the LIST volume. The development on the LIST work was done in the scope of the theses by D. Fink [26] and S. Richter [27]. The work is continued at the University of Mainz by R. Heinke (thesis: to be submitted in 2019).

  Other paths for decreasing the isobaric contamination have been investigated as well. One of those relies on the ion source material itself for a decrease of surface ion creation, making use of materials with low work functions [28]. Another approach for isobars which effuse faster than the element of interest is to gate on the laser pulse and limit the extraction of ion beam to these time intervals [29].

- Increase of the versatility: For elements which cannot be surface ionized, either the RILIS or electron impact ionization can be used. At ISOLDE, electron impact ionization is realized with the Versatile Arc Discharge Ion Source (VADIS). Due

to the design properties of liquid targets at ISOLDE, only the VADIS is (so far) compatible with them. For recently performed in-source laser spectroscopy experiments on Hg, the combination of the two ionization mechanisms was investigated in the thesis work by T. Day Goodacre [30]. The VAD(L)IS mode ("L" for laser) was successfully characterized, optimized [31] and used on-line [15, 13]. For increased extraction efficiency of the laser ions inside the VADIS volume, in depth investigations, encompassing plasma simulations, were launched. By making the extraction voltage variable, the VADIS can now be better adjusted for laser ionization [32]. This work was performed by Y. Martinez in the scope of her thesis [33].

All of these topics tackled different problems and the developments have played a significant role in the success of much of the physics program at ISOLDE. After the successful developments in the past years, many of them are being continued, e.g. the LIST and VAD(L)IS developments. Two more key factors have so far not been addressed though: on the one hand, the spectral coverage and on the other hand the spectral resolution of the RILIS laser system. The spectral coverage is limited by the fact that, during on-line operation, UV pumped dyes are avoided due to the high operational costs and inconvenience. The spectral resolution is limited by the Doppler-broadening inside the hot cavity ion source. Both of these topics have been addressed in the scope of the thesis presented here.

This thesis has been split into sections, following the natural developments of the RILIS laser system and its applications: First, in chapter 3 the spectral coverage of the RILIS laser system will be addressed, showing the development of a Raman laser for RILIS applications. Additionally, examples of laser ionization scheme development, aiming at increasing the versatility, stability and number of accessible elements of the setup will be presented in chapter 4. Afterwards, the spectral resolution and current limits of the RILIS laser system will be addressed. The example of "conventional" in-source laser spectroscopy of dysprosium, discussed in chapter 5 shows what can be achieved without reducing the Doppler-broadening and use of what was, so far, the "narrow linewidth"

$(0.8-1.0\,\mathrm{GHz})$ operation. After this example, the first steps towards Doppler-free 2-photon spectroscopy will be introduced to the reader in chapter 6. The work presented here encompasses the first positive results regarding the implementation of this new technique and will discuss which further developments are required for future routine applications.

Theoretical Background

In this chapter section 2.1 to section 2.3 were copied directly from the Master's thesis of K. Chrysalidis, published on the CERN document server under record no. 2227955 (Master thesis K. Chrysalidis). Since the compilation is already publicly available, for this thesis it was avoided to repeat work already done by the author.

The theoretical background for tunable lasers (section 2.4) and Raman lasers (section 2.5) have been added, since they will be referred to later on in section 3.3.

2.1 Atomic Structure

2.1.1 Hydrogen Atom

In order to calculate the discrete energy levels of the hydrogen atom it is necessary to solve the time independent Schrödinger equation

$$H \left| \Psi \right\rangle = E \left| \Psi \right\rangle \tag{2.1}$$

for a single electron in the Coulomb-potential of the proton. The Schrödinger equation yields

$$-\frac{\hbar^2}{2m_e}\Delta_e\psi - \frac{\hbar^2}{2m_p}\Delta_p\psi - \frac{Ze^2}{4\pi\epsilon_0 r}\psi = E\psi(\boldsymbol{r}_e, \boldsymbol{r}_p) \tag{2.2}$$

with: m_e, m_p mass of the electron/proton, charge $q = Ze$, $\boldsymbol{r}_{e,p}$ radius vector of electron/proton, $\Delta_{e,p}$ Laplace operator with respect to $\boldsymbol{r}_{e,p}$. One can choose polar coordinates (r, θ, ϕ) to solve this radially symmetric problem. The use of the reduced mass μ sets the center of gravity to the point of origin of the system and the Hamilton operator becomes:

$$H = -\frac{\hbar^2}{2\mu}\Delta + V_C(r) \quad \text{where} \quad \mu = \frac{m_e m_p}{m_e + m_p} \quad \text{and} \quad V_C(r) = -\frac{e^2}{4\pi\epsilon_0 r} \tag{2.3}$$

Introducing the Laplace operator in the polar coordinates one obtains the Schrödinger equation in the following form:

$$\begin{aligned}
\left\{\frac{1}{r^2}\left[\frac{\partial}{\partial r}\left(r^2\frac{\partial}{\partial r}\right) + \frac{1}{\sin\theta}\frac{\partial}{\partial\theta}\left(\sin\theta\frac{\partial}{\partial\theta}\right) + \frac{1}{\sin^2\theta}\frac{\partial^2}{\partial\phi^2}\right]\right\}\Psi(r,\theta,\phi) \\
= -\frac{2\mu}{\hbar^2}\left\{E - V_C(r)\right\}\Psi(r,\theta,\phi)
\end{aligned} \tag{2.4}$$

As the potential is spherically symmetric, the wavefunction can be separated into a radial part R_{ln} and an angular part Y_{lm}:

$$\Psi_{nlm}(r,\theta,\phi) = R_{ln}(r)Y_{lm}(\theta,\phi) \tag{2.5}$$

$n \in \mathbb{N}$ is the principal quantum number, l is the orbital angular momentum ($0 < l < n-1$) and m is the magnetic quantum number ($-l < m < l$). l and m can take on a number of different values for a definite n but still lead to the same energy (see Equation 2.7), corresponding to a n^2 degeneracy of the energy levels. The spherical harmonics $Y_{lm}(r)$

can be solved with the help of the associated Legendre polynomials. Substituting $R_{ln}(r)$ with $u_{nl}(r)/r$ one gains the expression

$$\frac{\mathrm{d}^2 u_n(r)}{\mathrm{d}r^2} + \frac{2\mu}{\hbar^2} \left[E_n + \frac{e^2}{4\pi\epsilon_0 r} - \frac{\hbar^2 l(l+1)}{2\mu r^2} \right] u_n(r) = 0 \tag{2.6}$$

This gives the energy eigenvalues for $u_n(r)$

$$E_n = -\frac{\mu e^2}{2\hbar^2 (4\pi\epsilon_0)^2 n^2} = -\frac{\mu e^2}{8\epsilon_0^2 h^2} = -R_\mu \frac{1}{n^2} \tag{2.7}$$

where R_μ is the (mass reduced) Rydberg constant. If one defines the ground state of an atom as its point of zero energy, then the ionization potential can be defined as the convergence of the states of the principal quantum number for $n \to \infty$, so that

$$E_{IP} = E_n + \frac{R_\mu}{n^2}. \tag{2.8}$$

2.1.2 Fine Structure Splitting

The fine structure describes the removal of the energy level degeneracy for same n. Due to relativistic effects and the coupling of electron spin and orbital momentum a splitting in the energy levels is observed, so that discrete levels can be spectroscopically resolved. The correction terms can be obtained using perturbation theory, leading to additional terms in the Hamiltonian:

$$H = H_0 + H_{rel} + H_{ls} + H_D \tag{2.9}$$

H_{rel} takes into account the relativistic treatment of the electron inside the proton's Coulomb potential. With $E = \sqrt{p_e^2 c^2 + m_e^2 c^4}$ (p_e: electron momentum, c: speed of light), the electron gains in mass and therefore in kinetic energy.

H_D is called the Darwin-term. It only affects the s-orbit and changes the effective potential at the nucleus. It takes into account quantum fluctuations, which make it impossible to determine the electron position more precisely than $\lambda_{compton} = \hbar/(m_e c)$.

H_{ls} corrects for the spin-orbit coupling. It takes into account the magnetic moments of the electron due to the coupling of the spin s with the orbital angular momentum l. The magnetic spin moment of the electron has two discrete spatial orientations. This causes an additional energy, where spin and orbital angular momentum are coupled, giving the total angular momentum $\boldsymbol{j} = \boldsymbol{l} + \boldsymbol{s}$ (with $|l - s| \leq j \leq l + s$):

$$\Delta E \approx \frac{\mu_0 Z e^2}{4\pi m_e^2 r^3}(\boldsymbol{l} \cdot \boldsymbol{s}) \propto \frac{\hbar^2}{2}\left[j(j+1) - l(l+1) - s(s+1)\right] \tag{2.10}$$

With some further calculations which take into account the time-averaged value of r related to the probability of finding the electron at the location r and including the hydrogen wave functions, one finally obtains the total energy

$$E_{nj} = E_n\left[1 + \frac{Z^2\alpha^2}{n}\left(\frac{1}{j+1/2} - \frac{3}{4n}\right)\right] \tag{2.11}$$

with Sommerfeld's fine structure constant $\alpha = \frac{e^2}{4\pi\epsilon_0 \hbar c} \approx \frac{1}{137}$.

2.1.3 Hyperfine Structure and Isotope Shift

The hyperfine structure takes into account the specific nucleus and its resulting interaction with the electrons. The nucleus with spin $\boldsymbol{I}$ has a nuclear magnetic moment μ_K, which interacts with the magnetic field $\boldsymbol{B}_j$ which is produced by the electrons at the nucleus . This leads to a splitting of the energy levels into $(2F+1)$ hyperfine components. $\boldsymbol{F}$ is the total angular momentum which is the sum of the total angular momentum $\boldsymbol{j}$ and the nuclear spin I. The selection rule is $|I - J| \leq F \geq I + J$ where a transition is only possible if ΔF is ± 1 or 0. The magnitude of the hyperfine structure splitting is strongly dependent on the atomic configurations and is typically several orders-of-magnitude smaller than the fine structure splitting, as demonstrated by Table 2.1.
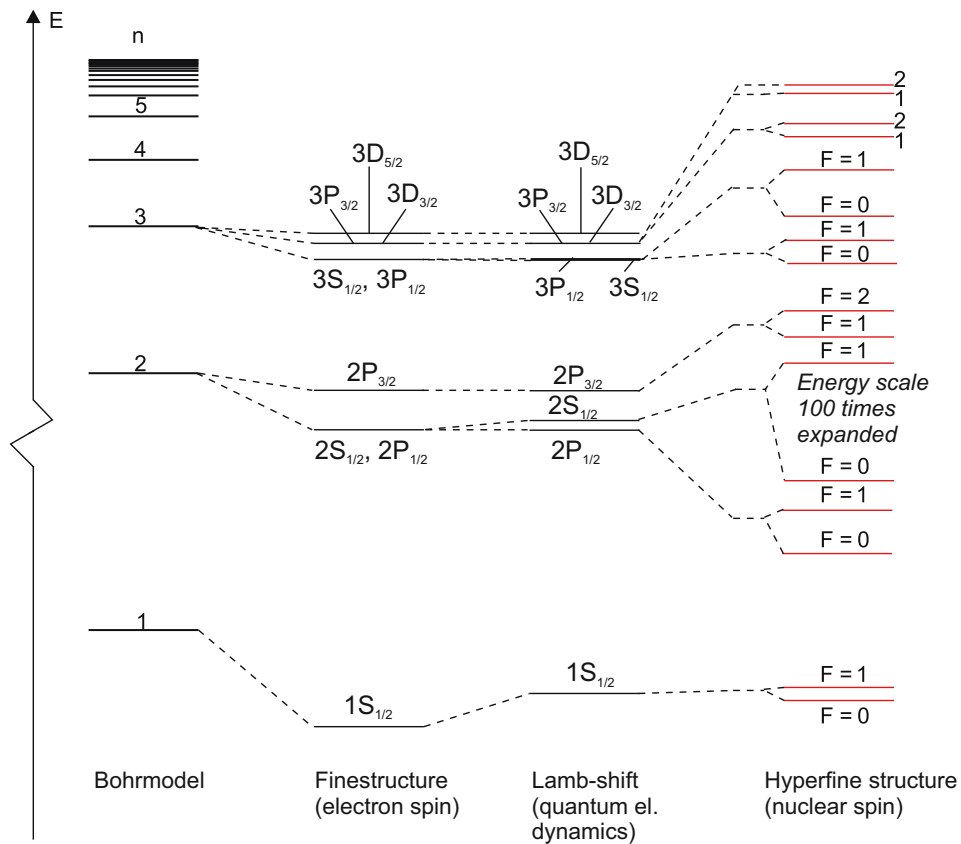
Figure 2.1: *The level scheme of the H atom is schematically shown with all interaction effects. The fine, hyperfine structure and the Lamb-shift are not drawn to scale as the splittings and shifts would be too small to depict [34].*

	cm^{-1}	eV	GHz
Fine structure	$1-1000$	$10^{-4} - 10^{-1}$	$10-10000$
Hyperfine structure	$10^{-3} - 1$	$10^{-7} - 10^{-4}$	$0.01-10$

Table 2.1: *Scale of the fine and the hyperfine structure*

Figure 2.1 shows the level scheme of the hydrogen atom in order to give a better understanding of the complete atomic structure in general. The structure gets more complicated for heavier atoms. When considering those atoms the ground state proper-

ties of the nucleus change between two isotopes of the same element. Aside of variations in spin and moments, this is due to mass and volume effects, that influence the energy difference of the atomic levels by changing the reduced mass of the nucleus-electron system and the size or shape of the nucleus.

2.1.4 Atoms With More Than One Electron

If an atom has more than one electron mutual electrostatic and magnetic interactions between the electrons arise. Additionally there is a new symmetry, which arises from two electrons being exchanged but indistinguishable. The simplest of such systems is the helium atom, in which two electrons interact. Many of the principles that can be deducted from this system also apply to more complex systems. One of these is the Pauli-principle, which states that the total wavefunction of a system with more than one electron is always antisymmetric with regard to the exchange of two electrons. Each state can only be described with a complete set of quantum numbers (n, l, m_l, m_s) and can only be occupied by one single electron. The orbital angular momenta and spins of the N electrons can couple to a total angular momentum $\vec{J}$. For most atoms LS-coupling occurs, where the orbital angular momenta $\vec{l_i}$ and the spins $\vec{s_i}$ of the single electrons couple to a total orbital angular momentum $\vec{L} = \sum_{i=1}^{N} \vec{l_i}$ and a total spin $\vec{S} = \sum_{i=1}^{N} \vec{s_i}$, so that $\vec{J} = \vec{L} + \vec{S}$.

Alternatively the so called jj-coupling is observed in some atomic systems, where the orbital angular momentum $\vec{l_i}$ and spin $\vec{s_i}$ of one single electron couple to the total angular momentum $\vec{j_i}$ of that electron. These then couple to the total angular momentum $\vec{J} = \sum_{i=1}^{N} \vec{j_i}$ of the atom. This form of coupling predominantly appears in heavy atoms and for higher excited states, as the coupling between different electrons gets suppressed.

2.1.5 Rydberg Atoms

This section is summarizing the more extensive chapter on Rydberg atoms and Rydberg spectroscopy by V.S. Letokhov [35] (p. 65 ff).

Highly excited atoms often have one electron moving in an enlarged orbit far away from the nucleus and from the other electrons' orbits. Most atomic characteristics exhibit a strong and increasing dependency on the principal quantum number n. Their atomic collision cross section for example grows with n^4, their radiative lifetime with n^3 while the binding energy is reduced with $1/n^2$ and the finestructure splitting with $1/n^3$. These Rydberg atoms can reach very large diameters in the range of µm. Due to the reduction in electron binding energy and the increase in collision cross section it becomes quite easy to ionize the atom, either via collisional processes, via application of external electrical fields or just by black body radiation. This makes a spectroscopic study of these states rather easy through their identification via registration of the resulting positive ion or free electron. If ionization is achieved through the use of external electrical fields, the linear Stark coefficient, which can lead to a split in the energy spectrum, scales with a factor of n^2 and may have to be taken into account in the analysis in the Rydberg spectrum.

In a Rydberg atom the outer electron experiences the nucleus with the charge Z screened by $Z-1$ other electrons. This scenario is analogous to that of the hydrogen atom, where only a charge of $+e$ is present. A distinction between the Rydberg atom and the hydrogen atom is made by introducing the effective principal quantum number n^*. n^* comprises the quantum defect $\delta(n)$ and the energy can therefore be written as follows:

$$E_n = E_{IP} - \frac{R_\mu}{(n^*)^2} = E_{IP} - \frac{R_\mu}{(n - \delta(n))^2} \tag{2.12}$$

2.2 Light-Atom Interaction

In order to build the foundation for the following section about resonance ionization spectroscopy, this section will give an overview of how atoms interact with photons.

2.2.1 Atomic Transitions

The most fundamental theorem of physics, namely the conservation of energy, implies that the total energy of a system (here: atom-photon) must remain constant. The state of an atom can change either via emission or absorption of a photon. Due to the conservation of energy this process can be easily described. In a two-level system with the states $|1\rangle$ and $|2\rangle$ with the according energies $E_1 < E_2$, this leads to the following three possibilities:

- **Absorption:** A photon with energy $h\nu$ is being absorbed by the atom, so that the electron goes from $|1\rangle$ into $|2\rangle$, where $E_2 = E_1 + h\nu$.

- **Spontaneous emission:** An atom spontaneously goes from $|2\rangle$ into $|1\rangle$ whereby it emits a photon of energy $E_2 - E_1$. The emission can occur in any direction.

- **Stimulated emission:** An external light field stimulates the emission of a photon, so that $|2\rangle \rightarrow |1\rangle$. The photon from the external field and the photon resulting from the emission have the same energy of $h\nu = E_2 - E_1$ and additionally the same direction of propagation.

The probability for the above mentioned processes are given by the Einstein coefficients A_{21} for the spontaneous and B_{21} for the stimulated emission. A_{21} does not depend on the radiation field w_ν, whereas B_{21} does. The absorption must be equal to the total emission while under stationary conditions the number densities $N_{1,2}$ are time independent and therefore

$$B_{12}w_\nu N_1 = (B_{21}w_\nu + A_{21})N_2. \tag{2.13}$$

Assuming a thermal equilibrium the ratio of N_2/N_1 follows the Boltzmann distribution

$$\frac{N_2}{N_1} = \frac{g_2}{g_1}e^{(E_1-E_2)/kT} = \frac{g_2}{g_1}e^{(-h\nu)/kT} \tag{2.14}$$

where $g_{1,2}$ is the statistical weight of a state with energy E and total angular momentum

quantum number J. Using Planck's formula of the spectral energy density of the thermal radiation field

$$w_\nu = \frac{8\pi h\nu^3}{c^3} \frac{1}{\mathsf{e}^{(h\nu)/kT} - 1} \tag{2.15}$$

and inserting Equation 2.14 into 2.13 leads to

$$B_{21} = \frac{g_1}{g_2} B_{12}$$
$$\text{and} \quad A_{21} = \frac{8\pi h\nu^3}{c^3} B_{21} \tag{2.16}$$

For a transition $E_2 \to E_1$ the wave functions $\psi_{1,2}$ of both states have to be taken into account. Therefore the transition dipole moment M_{21} is introduced and defined by

$$\boldsymbol{M}_{21} = e \int \psi_2^* \boldsymbol{r} \psi_1 \mathrm{d}\tau. \tag{2.17}$$

The M_{21} are also known as Matrix elements. If some of them are zero, the corresponding transitions cannot occur, they are forbidden. This helps to define selection rules for allowed transitions. In general the following apply:

$$\Delta J = 0, \pm 1 \qquad J = 0 \to J = 0 \text{ is forbidden}$$
$$\Delta m_J = 0, \pm 1 \qquad m_J = 0 \to m_J = 0 \text{ is forbidden if } \Delta J = 0 \tag{2.18}$$

For the LS coupling $\Delta S = 0$, $\Delta L = 0, \pm 1$ and $\Delta l = \pm 1$ (for the transition electron) apply. The jj coupling obeys to $\Delta j = 0, \pm 1$ for one of the electrons and $\Delta j = 0$ for all the other electrons.

The parity π of the atomic system is preserved. This means that as one photon (negative parity) is absorbed, the parity of the final state needs to change in regard to the initial state, so $\pi_i = -\pi_f$.

2.2.2 Line Shape and Width

There are four main effects that affect the line shape and width[1]:

- **Natural linewidth**: It is called the natural linewidth, because it is not induced by any external effects and solely dependent on the lifetimes of the atomic states. It can be derived from Heisenberg's uncertainty principle for the energy, $\Delta E = h/(2\pi\tau)$, provided that the decay of the state follows a simple exponential. The corresponding broadening of the transition frequency is given by the spread of the transition frequency, so that

$$\Delta\nu = \frac{1}{2\pi}\left(\frac{1}{\tau_1} + \frac{1}{\tau_2}\right). \tag{2.19}$$

  The lineshape has a Lorentzian profile and is centered around the frequency $\nu_0 = (E_2 - E_1)/h$:

$$g(\nu) = \frac{\Delta\nu/2\pi}{(\nu - \nu_0)^2 + (\Delta\nu/2)^2} \tag{2.20}$$

- **Collision broadening:** Inelastic collisions result in transitions between atomic energy levels. Collision broadening is assumed to be negligible in the laser ion source at ISOLDE due to the insufficient vapor density. In gas cell laser ion sources it is often dominant though [38]. The energy shift is expanded simply by adding a term f_{col} which is the collision rate:

$$\Delta\nu = \frac{1}{2\pi}\left(\frac{1}{\tau_1} + \frac{1}{\tau_2} + 2f_{col}\right) \tag{2.21}$$

- **Saturation broadening:** Once the saturation limit of populating a state is reached a homogeneous broadening takes place, building up a flat top profile on the line shape. A detailed formalism which takes into account the energy density matrices of the different states is given in [39]. A slightly more simplified explanation is given in [37], where the saturation broadening is specifically derived for a two level

---

[1]This section is mainly based on [36] and [37].

system. A more "hands-on" explanation is given in [40]:

$$I'(\nu) = \frac{S \cdot I(\nu)}{1 + S \cdot I(\nu)} \tag{2.22}$$

$I(\nu)$ is the spectral distribution without saturation broadening. S denotes the saturation parameter and is given with $S(\nu) = P(\nu)/\bar{R}$, with the pump rate $P(\nu)$ and the mean relaxation rate of the energetically higher state $\bar{R}$. The spectral resolution is therefore reduced if the laser power exceeds the saturation power for the transition. For determining the region in which saturation starts, the formula

$$W(P) = W_0 + m \cdot P + A\frac{P/P_0}{1 + P/P_0} \tag{2.23}$$

can be applied for fitting. W_0 denotes the background (surface ionization, non-resonant ionization) and m the growth of the ionization volume because of the Gaussian mode profile of the laser. P_0 gives the saturation power, at which half of the maximal transition rate A via resonant ionization is reached.

The three above mentioned effects are called homogeneous broadening effects. The following one is called *inhomogeneous*, as different atoms posses differing line shape functions or center frequencies.

- **Doppler broadening:** An atom which is moving with a certain velocity $\boldsymbol{v}$ along a certain direction exhibits a spectrum that is shifted by $\pm(\boldsymbol{v}/c)\nu_0$ in regard to the central frequency ν_0 due to the Doppler effect. The sign depends on the viewing point of the observer (+ towards, - away from observer). In a thermal equilibrium atoms follow a Boltzmann distribution, so that the number of absorbed or emitted atoms in a frequency interval $[\nu, \nu + \delta\nu]$ is

$$n(\nu)\mathrm{d}\nu = \frac{c_0 N}{\nu_0\sqrt{2\pi k_B T/m_0}}\mathrm{e}^{-[c_0(\nu-\nu_0)/(\nu_0\sqrt{2k_B T/m_0})]} \tag{2.24}$$

The intensity distribution follows a Gaussian profile with a FWHM of:

$$\Delta\nu_D = \frac{2\nu_0}{c_0}\sqrt{\frac{2k_B T \ln 2}{m_0}} \tag{2.25}$$

Taking into account the fact that the distribution of the emitted and absorbed atoms follows a Lorentzian line shape due to their finite lifetime a convolution of a Gaussian and Lorentzian line shape has to be made, which gives a Voigt (intensity) profile

$$I(\nu) = \frac{\Delta\nu I_0 N c_0}{2\pi^{3/2}\nu_0\sqrt{2k_B T/m_0}}\int_0^\infty \frac{e^{-[c_0^2(\nu-\nu')^2/(\nu'^2 2k_B T/m_0)]}}{((\nu-\nu')^2 + (\Delta\nu/2)^2)} \tag{2.26}$$

with $\nu' = \nu_0(1 + v_Z/c_0)$ where v_Z is the velocity along the axis of observation.

2.3 Stepwise Photo-Ionization

In 1971 R. V. Ambartsumian, V. P. Kalinin and V. S. Letokhov published an article on the *two-step selective photo-ionization of rubidium atoms by laser radiation* ([5]). It was one of the first experiments using the resonance ionization technique. With two or more lasers one successively excites dipole transitions in an atom so that finally the total applied energy is higher than the ionization potential. This method exploits the uniqueness of the ionization scheme required for a chosen element due to its atomic structure 'fingerprint', resulting in an element selective (and some cases isomer or isotope selective) ionization process.

There are different processes that may contribute to the ionization of a (highly excited) atom.

2.3.1 Surface Ionization

One mechanism, which can lead to unwanted isobaric contamination at ISOL facilities, is surface ionization. Based on the work by J. Eggert [41] M.N. Saha derived the ionization state of an element in a gas after evaporation from a surface with a certain temperature

[42]. This formula is e.g. used in astrophysics to classify the spectra of stars. Applying it inside a cavity with a surface which has a work function W the Saha-Langmuir equation results [43] [2]:

$$\frac{n_+}{n_0} = \frac{g_+}{g_0} \exp\left(\frac{W - E_{IP}}{k_B T}\right) \tag{2.27}$$

It describes the "degree of ionization", namely the ratio from surface ions n_+ to neutral atoms n_0. $g_{+,0}$ are statistical weights for the ionic and atomic states. The equation shows that the surface ionization depends on the work function W and the ionization potential E_{IP}. If the ionization potential is low the surface ionization is high, therefore alkalies and also lanthanides are easily surface ionized.

The Saha-Langmuir equation can only be used as an estimation of the ionization probability in a single atom/surface interaction. The actual surface ionization efficiency does also depend on the ion survival after the wall collision and the average number of atom-wall collisions per atom, so that experimental data is needed for better assessment.

2.3.2 Laser-Light Induced Ionization

The three possibilities for laser-light induced ionization are the following (schematically depicted in Figure 2.2):

- **Resonant ionization via autoionizing states:** An AIS is an electron configuration with a total excitation energy that exceeds the ionization energy of the atom. Ionization occurs as a prompt non-radiative decay of this state. The typically short lifetime of an AIS is responsible for its characteristically broad linewidth. The cross section for this process can be up to three orders of magnitude higher than for non-resonant ionization, therefore needing less laser power to achieve saturation. Usually autoionizing states show a very typical line shape, namely the one described by U. Fano in [45]. The cross section results from the coupling of a discrete state

---

[2]as mentioned in the paper by M. Dresser there is a paper by I. Langmuir & K. Kingdon [44] that is often cited for the Saha-Langmuir equation but does not truly give it in the form in which it is generally known today
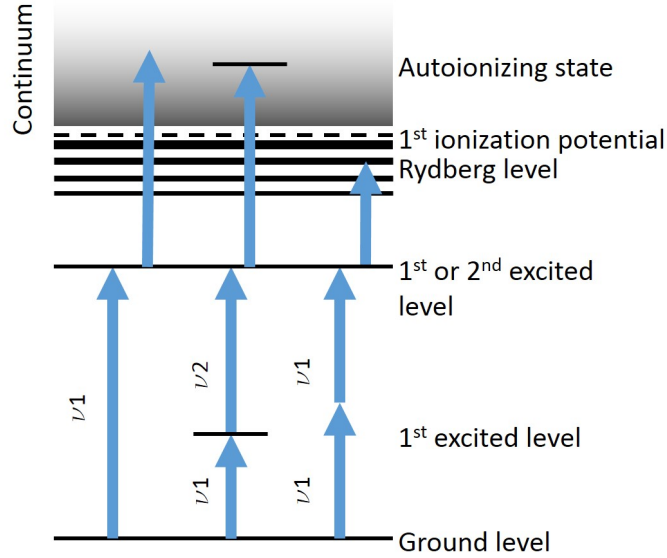
Figure 2.2: *In this sketch the different possibilities of laser ionization are shown. Depending on the ionization scheme two or three lasers are needed for the ionization process.*

with the underlying continuum and the cross section can be described with

$$\sigma(q, \epsilon) = \frac{(q + \epsilon)^2}{1 + \epsilon^2} \quad \text{with} \quad \epsilon = \frac{E - E_R}{\Gamma/2}. \tag{2.28}$$

The parameter q is the so called skewness of the line and can have either a positive or negative sign. For $q < 0$ the abscissa in Figure 2.3 has to be reversed. The reduced energy ϵ gives the energy difference to the position of the resonance in units of the half width $\Gamma/2$.

- **Non-resonant ionization:** For non-resonant ionization the last step is provided by a laser operating at a wavelength that corresponds to a photon energy that exceeds the difference between the IP and the upper state energy of the excitation scheme. Usually high power frequency doubled Nd:YAG ($532\,\text{nm}$) lasers with Gaussian beam profile are used. The fluence condition

$$\sigma_{ni} \Phi_i \tau_l > 1 \tag{2.29}$$
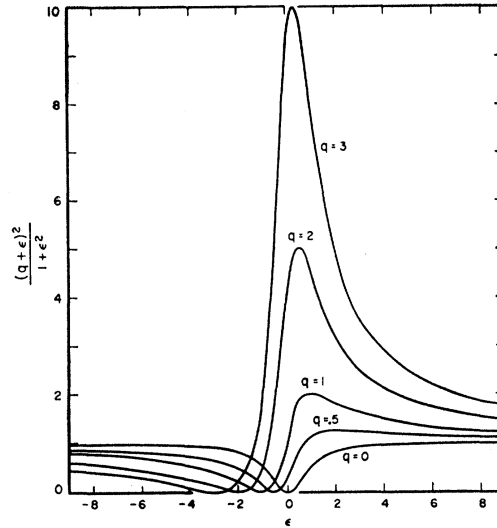
Figure 2.3: *Typical Fano lineshapes for different values of* q *[45]*

must be met [46]. As the cross section σ_{ni} is usually low for this process ($10^{-19} - 10^{-17}\,\mathrm{cm}^2$) the photon flux Φ_i must be high. With utilization of pulsed lasers with pulse length τ_l in the nanosecond range an average power of the order of around $100\,\mathrm{W}$ at $10\,\mathrm{kHz}$ repetition rate would have to be met. This is not achieved in the current RILIS setup (see [47]), so that those transitions are normally not saturated and the ion current dependency on power is linear.

- **Ionization via Rydberg states:** The concept of Rydberg atoms has been discussed in detail in subsection 2.1.5. As stated there the binding energy reduces with $1/n^2$ so that once the electron is in the excited Rydberg state it becomes easy to ionize either by applying an electric field, collision with other atoms/ions or just simply via the absorption of black body radiation inside the hot cavity.

2.3.3 Applications of Resonance Photo-Ionization

One of the experimental applications for the photo-ionization is resonance ionization mass spectrometry (RIMS). Mass selectivity can be achieved using a mass filter dispersive element, realized e.g. by a sector field magnet, a quadrupole mass filter or a time of flight apparatus. The RIMS technique is for example used for the ultra trace analysis of

rare isotopes in environmental samples. This is done in the working group LARISSA in Mainz. The preparation of clean samples for the ECHo project is another recent usage [48]. There is no scanning of the mass, but a chemically produced sample with long lived isotopes which can be purified using resonance ionization in combination with a mass separator.

The combination of using a mass separator with a resonance ionization laser ion source is also used at ISOLDE. At ISOLDE it is possible to extract samples of short lived isotopes as extraction of isotopes occurs immediately after production, with a target/ion-source and ion beam delivery system combined in a single machine (see [49]). Using the aforementioned combination of separator for mass selectivity and laser ionization another application, the resonance ionization spectroscopy (RIS) is possible. For RIS the wavelength of the lasers is scanned in order to determine nuclear or atomic properties of different elements or across an isotope chain for a single element. Nowadays, thanks to the development of very narrow linewidth lasers and geometries that make Doppler free ionization possible, a sub-Doppler resolution can be achieved in experiments where RIS is applied. With the special case of in-source spectroscopy where the ionization is happening directly in the ion source, isotope shifts can be measured with enough precision to give insight into the variation of the nuclear structure with varying number of neutrons (see e.g. [50, 15]). A more detailed discussion, including a recent result of in-source spectroscopy performed at ISOLDE ([51]) is discussed in chapter 5.

2.4 Laser Principle and Tunable Lasers

The following section will summarize the basic principles of lasers in general and in more detail relevant aspects on tunable lasers. All techniques for lasers that are currently in use at the ISOLDE laser ion source (see chapter 3) will be laid out. Even though subsection 3.3.2 will go into detail on developments that have been realized in regard with the Ti:sapphire lasers during the scope of this thesis, the underlying principles are based on the theory presented here.

2.4.1 Light Amplification by Stimulated Emission of Radiation - **LASER**

The word "laser" already encompasses the principle, on which the coherent radiation which it emits, is based. The initial photons are amplified, by increasing the population of the upper state of the laser transition $|2\rangle$ until it is bigger than the lower state $|1\rangle$. This process is called "population inversion". The most simple system with only two levels, is not compatible for a laser. In atomic transition absorption and emission are competing processes, automatically leading to a population ratio of $1/2$. Therefore, all laser media feature a higher level-set.

The first laser medium in use, i.e. ruby, provides a three-level system: by an excitation process, such as optical excitation, electric discharge or current flow, the system is driven from the ground state $|1\rangle$ into the upper state $|2\rangle$. State $|2\rangle$ decays to $|3\rangle$ and then back to $|1\rangle$. For population inversion of level $|3\rangle$ vs. $|1\rangle$, the lifetime of $|2\rangle$ must be considerably shorter than the one of $|3\rangle$. Overall, the process in a three-level system is not very efficient and requires high gain in order to achieve sufficient population inversion.

Most modern lasers are based on four-level systems: excitation from $|1\rangle$ into $|2\rangle$ is followed by a rapid decay into $|3\rangle$. The laser transition leads from $|3\rangle$ to $|4\rangle$ and from there another fast transition leads back to the ground state $|1\rangle$. Both the three- and the four-level systems are schematically depicted in Figure 2.4.
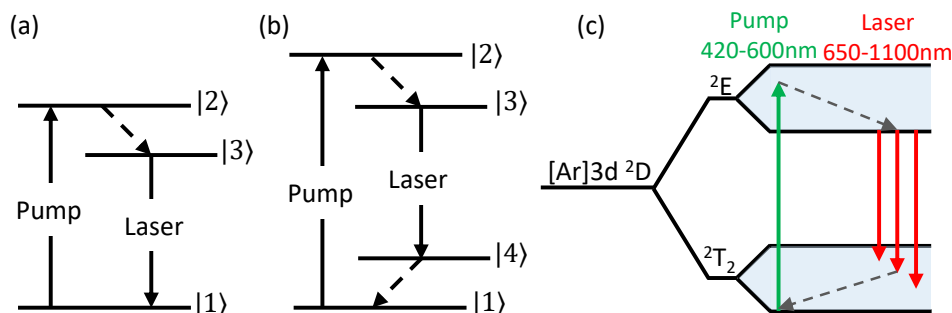

Figure 2.4: *Level laser scheme for (a) three- and (b) four-level laser system. (c) shows the laser level scheme for a Ti:sapphire laser. The dashed lines show fast decays.*

The two most common (quasi)four-level laser media are Nd:YAG (neodymium doped

yttrium aluminum garnet), emitting light at 1064 nm and Ti:sapphire (titanium doped sapphire, Ti^{3+}:Al_2O_3). While Nd:YAG lasers emit light on a single line only, Ti:sapphire lasers have a broad emittance curve from 650-1100 nm. The Ti^{3+} ground state $[Ar]3d^2D$ is split into two vibrational bands, $^2T_2$ and ^2E, stemming from the coupling to the field and vibration of the sapphire crystal lattice. The population is pumped from the $^2T_2$ ground state into the ^2E band, where fast, non-radiative decay happens within the band. The laser transition leads from there into the broad $^2T_2$ band, giving rise to the broad emittance curve of the Ti:sapphire laser medium and then back to the ground state, as shown in Figure 2.4(c). At room temperature the lifetime of the lasing transition is 3.2 μs. The pump transition from $^2T_2 \rightarrow {}^2E$ covers 420-600 nm and can be excited using efficiently strong laser radiation within this spectral range. The most common pump lasers are therefore frequency doubled Nd:YAG at 532 nm or Nd:YLF at 527 nm.

For all lasers, efficient light amplification is ensured by placing the gain medium inside an optical resonator, also called cavity. The most simple cavity consists of only two mirrors, of which one is partially reflective, allowing laser light to exit the cavity. For gain media with broad emission curves, the desired wavelength has to be chosen by so-called frequency selective elements.

2.4.2 Laser Frequency Selection

Multiple different possibilities exist to effectively select and amplify the desired frequency of a laser. The most simple approach is a frequency selective coating on the cavity mirrors, allowing only a specific wavelength range to be reflected. The free spectral range (FSR) of the "bare" cavity is a result of the resonance condition of a standing wave:

$$L = m\frac{\lambda}{2}, \quad m = 1, 2, 3, ... \tag{2.30}$$

This leads to the spectral range (frequency)

$$\Delta\nu_{\mathsf{FSR}} = \frac{c}{2L}, \quad \text{with the speed of light} \quad c = \lambda\nu \tag{2.31}$$

Multiple other frequency selective processes exist and will be described in the following paragraphs.

Diffraction Grating

The first frequency selective method applied for tunable lasers used a diffraction grating inside the cavity [4]. Often the gratings are installed in "Littrow" configuration, where the first order of the chosen wavelength is reflected back into the cavity. Constructive interference on the grooves of the grating surface is reached when the optical path difference δs of the individually reflected components equals $m\lambda$, where $m \in \mathbb{N}$ is the so-called diffraction order. The interference maxima of the order m are related to the incident angle α by

$$m\lambda = 2g\sin(\alpha), \tag{2.32}$$

where g is the lattice constant, given in mm/grooves. The resolving power, or linewidth of the laser, depends on the number of grooves n_{grooves} which are illuminated and the relation is given by

$$\frac{\lambda}{\Delta\lambda} = mn_{\text{grooves}}. \tag{2.33}$$

Therefore, one possible option of decreasing the linewidth of a grating laser, lies in expanding the beam, e.g. with a prism beam expander inside the cavity. This method leads to higher losses inside the cavity though and therefore reduces the output laser power.

Lyot Filter

The Lyot or birefringent filter is based on the polarization-dependent phase-shift inside birefringent material [52, 53, 54]. Depending on the polarization and propagation direction of the light, it experiences different refractive indices n_o and n_e inside the lattice structure of e.g. a birefringent crystal. This leads to an elliptical polarization of the

transmitted beam with a phase shift of

$$\delta(\lambda) = \frac{2\pi}{\lambda}(n_o - n_e)L \tag{2.34}$$

where L is the length of the crystal. Due to the polarization-dependent amplification inside the gain medium and multiple Brewster surfaces inside the cavity (e.g. the Ti:sapphire crystal itself), a strong loss of the s-polarized component is achieved. Only light which is p-polarized light is sufficiently amplified. Assuming parallel polarization of the incident and the transmitted p-polarized component, the transmission function is given by

$$I(\lambda) = I_0 \cos^2\left(\frac{(n_o - n_e)\pi L}{\lambda}\right) \tag{2.35}$$

By tuning the angle of the filter in respect to the incident light beam, the refractive index n_e is changed and therefore the resulting frequency with p-polarization. Usually a Lyot filter consists of more than one plate, three in the case of the Mainz Z-cavity (see subsection 3.3.2), with integer thickness ratio of e.g. $1 : 4 : 16$. The FSR of a Lyot filter is given by

$$FSR_{\text{Lyot}} = \frac{c}{L(n_o - n_e)}. \tag{2.36}$$

Fabry-Pérot Interferometer (Etalon)

A Fabry-Pérot interferometer (FPI), more commonly referred to as an etalon when used inside a laser resonator, consists of some (semi) transparent plates with two reflective surfaces, reflectivity R, spaced by a distance d. In itself, it is a cavity, with an FSR as described in Equation 2.31. Usually substrates are used, so that the medium specific refractive index n_{medium} has to also be taken into account. The beam passing through the etalon is split up by multiple reflections inside it, with an angle β relative to the planar surface, leading to a phase shift of

$$\delta(\beta) = \frac{2\pi}{\lambda}2n_{\text{medium}}d\cos(\beta) \tag{2.37}$$

between the transmitted components. The transmission function, given by an Airy function, is

$$I(\beta) = I_0 \frac{(1-R)^2}{(1-R)^2 + 4R\sin^2(\beta/2)}. \tag{2.38}$$

By defining $q = 4R/(1-R)^2$, another characteristic property of the etalon, called the finesse $\mathcal{F}$ can be given as

$$\mathcal{F} \sim \frac{\pi\sqrt{q}}{2}. \tag{2.39}$$

It is the ratio between the FWHM of the transmission peaks and the FSR. If the damping is low and the reflectivity is high, the values for $\mathcal{F}$ become large. By variation of the etalon thickness, the FSR can become broader (smaller d) or narrower (bigger d). In the Mainz Z-resonator design this is mainly responsible for the linewidth of the laser. By combining one thin and one thick etalon in the same cavity, narrow linewidths can be achieved, whilst the tuning range remains variable.

2.5 Stimulated Raman Scattering

Stimulated Raman scattering (SRS) is a technique based on the Raman effect/scattering. During the Raman scattering process, photons are inelastically scattered by molecules in contrast to the elastic scattering process, called Rayleigh scattering. The photons excite the molecules to higher energies and are emitted in the de-excitation process. They posses lower energy (or higher wavelength) than the incident photons, as some energy is converted to either vibrational (crystal/lattice structure) or rotational (in gas) energy inside the molecules. The emitted light is called "Stokes line". Multiple Stokes lines can be observed, as the photons with lower energy can be re-absorbed, loose energy and be re-emitted at higher wavelength, as shown schematically in Figure 2.5. The Raman effect was predicted in 1923 [55] and first observed in 1928 [56, 57], long before the invention of the laser. It was and is still commonly used for Raman spectroscopy for material analysis, e.g. in chemistry.

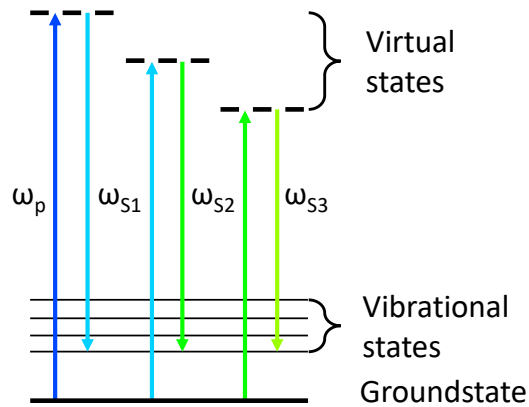Figure 2.5: *Schematic process of stimulated Raman scattering. The initial pump wavelength ω_p is converted to the first Stokes order ω_{S1}. It can be re-absorbed to generate higher Stokes orders.*

Since the strong light fields of lasers became available, Raman spectroscopy has become simpler though. It is thanks to its continued applications in spectroscopy, that the stimulated amplification of light inside a non-linear medium was first observed. In the following text, only solid state media will be considered, as they are the common choice for exploiting the SRS for laser applications.

If an initial pump beam creates the Stokes line, stimulated scattering can occur, similar to the stimulated emission of light within a laser. The processes, even though showing some similarities overall, are quite different in their nature. SRS is a non-linear effect of the third order, mainly depending on the vibrational structure of the lattice. The phase matching relation between the pump and the Stokes waves is automatically satisfied, as the coherent lattice vibration can only be driven by the pump and Stokes waves in proper phase to the Stokes growth. This enables very simple applications, e.g. Raman amplifiers, which are optical fibers based on materials in which the initial light can be converted and then continuously amplified. Another application are laser type cavities, in which the Stokes light is reflected back into the Raman medium for stimulated amplification.

Even though first Raman lasers were developed using gases [58] as the active media, solid state Raman lasers are much more common. This can be mainly attributed to the compactness and high gain of the solid state media. Of high interest in sold state applications are either optical fibers, such as glass or silica [59], or crystals. Liquid media are possible to use, though not common, and e.g. liquid nitrogen has been shown to work as a Raman laser [60].

Among the crystalline Raman media, the most important ones are diamond, $LiIO_3$ and tungstate crystals, like KGW [61]. Depending on the crystal, the Raman shift, gain (cm/GW) and thermal conductivity (directly related to the thermal stability) vary greatly. As shown in Table 2.2, diamond offers the biggest shift, gain and best thermal stability.

Table 2.2: *Raman shifts and gain coefficients for different Raman crystals. The data in this table has been copied from [62] but was originally put together with data from [63, 64].*

Crystal	Raman Shift $[cm^{-1}]$	Gain Coeff. at 1064 nm [cm/GW]	Gain Coeff. at 532 nm [cm/GW]	Damage Threshold $[GW/cm^2]$	Thermal Conductivity $[Wm^{-1}K^{-1}]$
Diamond	1332.5	15-20	50	-	>1800
KGW	768	4.4	11.8	10	2.6 [100]
	901	3.5			3.8 [010]
$Ba(NO_3)_2$	1047	11	47	0.4	1.17
$BaWO_4$	926	8.5	40	-	3

Most commonly, Raman lasers or amplifiers are driven by Nd:YAG or Nd:YLF lasers in their fundamental or higher harmonic wavelength. Some small output wavelength tunability can be achieved by varying the temperature and therefore vibrational states of the Raman crystal. Cavities can also be build in such a way, that the second or third Stokes order is amplified, so that more than one line becomes accessible. Since the Raman shift is fixed, the size of the wavelength shift depends on the pump wavelength. This is shown by a simple calculation

$$\Delta\lambda = \frac{1}{\lambda^{-1} - \nu_{shift} \cdot 10^{-7}} - \lambda \qquad (2.40)$$

and the results for diamond and KGW ([010] and [100] orientation), with wavelength characteristic shifts are plotted in Figure 2.6.
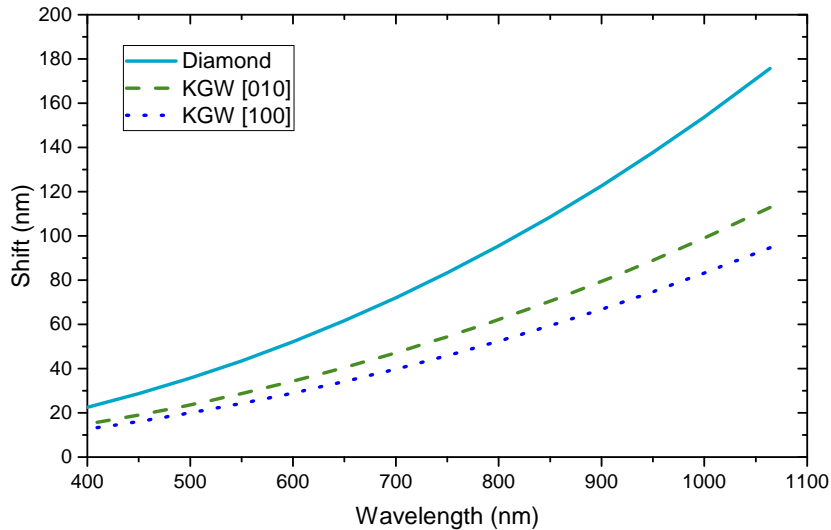
Figure 2.6: *Typical wavelength shifts for diamond and KGW in the two possible polarization configurations over the spectral range covered by intra-cavity doubled Ti:sapphire up to fundamental Nd:YAG.*

The data summarized in Table 2.2 and Figure 2.6 shows, that even though the wavelength shift is bigger for large wavelengths, due to the lower gain it might be more efficient to shift the higher harmonics of e.g. the Ti:sapphire directly. As will be discussed in subsection 3.3.5, the second harmonic of a Ti:sapphire laser can be used directly for Raman conversion, due to the high gain in this wavelength region and the Gaussian beam quality, achievable with intra cavity frequency doubling.

Experimental Setup

The Resonance Ionization Laser Ion source (RILIS) at CERN's Isotope Separator On-Line Facility (ISOLDE) is one of the oldest laser ion sources of its type world-wide. The first demonstration as an efficient and element-selective ion source took place in 1992 [65]. Since then it has been constantly improved and new laser developments have greatly enhanced its operational capacities, making it the most commonly used ion source at ISOLDE for over 10 years.

The versatile laser system, unique at an on-line facility, is based on operation of both dye and solid-state lasers. A wavelength range of 210-950 nm can be spanned this way, reducing set up time and allowing for the most convenient and efficient energies to be used for the resonance ionization steps.

The recent capabilities and developments of the ISOLDE RILIS have been published in 2017 in an overview article *Ion beam production and study of radioactive isotopes with the laser ion source at ISOLDE* in J. Phys. G (44) by V. Fedosseev, K. Chrysalidis, T.

Day Goodacre, B. Marsh, S. Rothe, C. Seiffert and K. Wendt.Since **Publication 1** gives a detailed description not only of the RILIS method itself, but of recent developments as well, the following sections will briefly summarize the most important aspects of the laser system. It will outline progress that was made for improving the operation of the Mainz Ti:sapphire lasers in subsection 3.3.2. New developments, aiming at increasing the tunable wavelength range of the Ti:sapphire lasers to avoid UV pumped dyes will be presented in subsection 3.3.5. This state-of-the-art technique has been investigated since October 2018, the results of which are presented in **Publication 2**.

3.1 ISOLDE

This section 3.1 has been copied directly from section 2.1 of the Master's thesis of K. Chrysalidis, published on the CERN document server under record no. 2227955 (Master thesis K. Chrysalidis). Figure 3.1 has been updated to the newest available format [66]. The most recent publications about ISOLDE can be found in J. Phys. G (44) by M. Borge et. al [67] and R. Catherall et. al [49].

The radioactive beam facility ISOLDE[1] at CERN, Geneva (Switzerland) is situated at the PS Booster (PSB). The PSB has a diameter of 50 m. Protons with an initial energy of 50 MeV are accelerated to energies of 1.0 or 1.4 GeV. They are released in pulses of 2.4 µs length with a repetition rate of 1.2 s and an intensity of up to 3×10^{13} protons/pulse.

Exotic radioisotopes are produced at ISOLDE either by fission, fragmentation or spallation processes in a thick target which is irradiated by the proton beam. The production rate is proportional to the beam flux of the proton beam and also to the number of atoms in the target that are being hit by it. The ISOLDE target unit consists mainly of the target container, filled with the target material which depends on the desired production of elements and their isotopes. Connected to this is a transfer line and the ion source. If needed a mass marker with either a non calibrated sample (for example

---

[1]**I**sotope **S**eparator **O**n-**L**ine **DE**vice
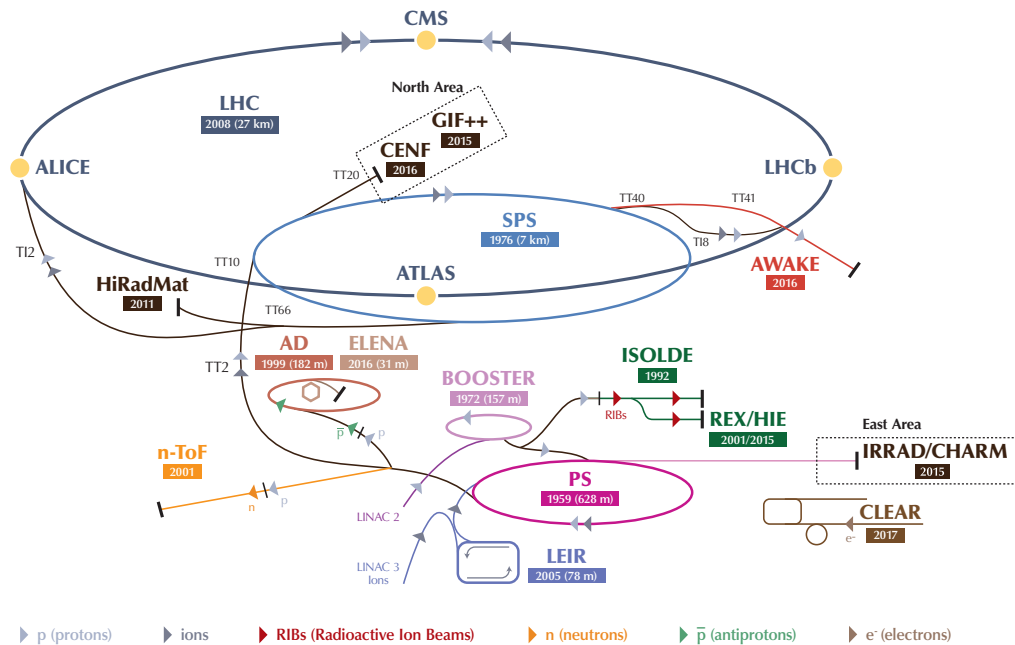
Figure 3.1: *Overview of the accelerator complex at CERN [66]. ISOLDE (green) is situated at the Booster (pink).*

for beam tuning) or a calibrated sample of a well-defined amount of stable isotopes can be attached to the back of the transfer line. All elements are resistively heated in order to release atoms in vapor form. Once the atoms have been ionized in the ion source (either by surface, laser or plasma ionization), the ions are extracted with an extraction electrode and guided through mass separator systems after which the ion beam is further directed to one of the many experimental setups in the ISOLDE hall.
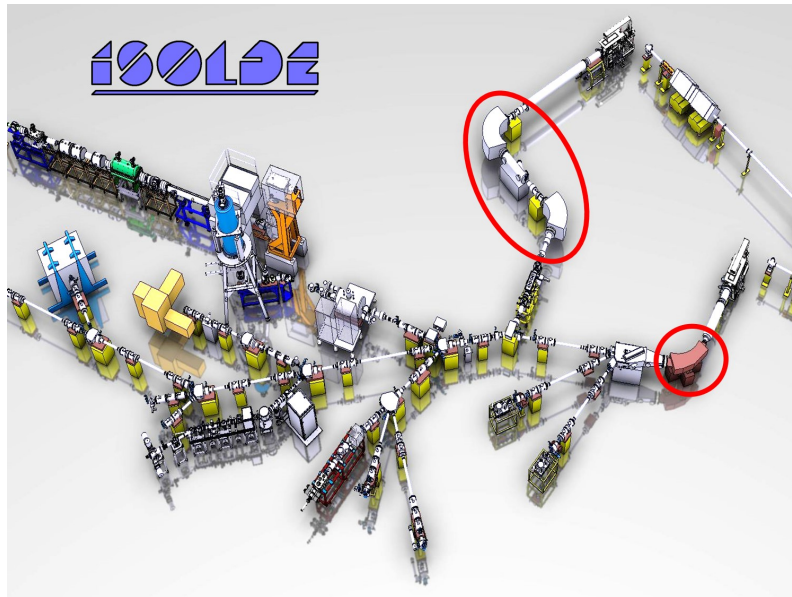
Figure 3.2: *The general layout of the ISOLDE separators (circled in red) and the beam lines leading to various fixed experiments. Towards the left the beam lines go further into the HIE-ISOLDE setup, where post acceleration of the beam takes place in order to get higher beam quality. The drawing has been downloaded from the ISOLDE web page and slightly modified.*

ISOLDE can offer several different beams at the same time. This is made possible by two separator setups which both have their own target. One of the separators is called GPS (**G**eneral **P**urpose **S**eparator) and involves only one magnet with a bending angle of 70°. An electrostatic switchyard is situated behind the separator magnet, allowing for the simultaneous extraction of three mass separated beams. The other, so called, HRS (**H**igh **R**esolution **S**eparator) consists of a 90° bending magnet and a 60° magnet. It offers a mass resolution of more than 5000.

There are "stationary" and "traveling" installations, meaning that some experiments have fixed beam lines and positions in the hall while others are only attached to a beamline for the period of the experiment and have to be taken away afterwards. There are installations for nuclear and laser spectroscopy, mass measurements, solid-state and surface studies. There are also some biophysics experiments where sample collections for further e.g. medical applications are taken. An overview of the ISOLDE separators

and some of the fixed installations can be seen in Figure 3.2.

3.2 <u>Publication 1</u> - Ion beam production and study of radioactive isotopes with the laser ion source at ISOLDE

The RILIS laser system has been introduced in detail in section 3.3 and the process of resonance ionization has been outlined in section 2.3. The following publication is a summary of developments at the RILIS up to January 2017 and gives an overview of the RILIS technique and its most recent applications.

Contribution: As member of the RILIS team since late 2015 I have contributed to many of the aspects presented in the paper: I have contributed to the improvement of the laser system, conducted ionization scheme development (published separately e.g. in [68, 69, 70, 71]), taken part in laser ion source developments and participated in experimental campaigns of in-source laser spectroscopy and electron affinity measurements ([72]). In addition I contributed to the preparation of the manuscript by providing figures and giving feedback.

Ion beam production and study of radioactive isotopes with the laser ion source at ISOLDE[*]

Valentin Fedosseev[1], Katerina Chrysalidis[1,2], Thomas Day Goodacre[1,3], Bruce Marsh[1], Sebastian Rothe[1] [iD], Christoph Seiffert[1] and Klaus Wendt[2]

[1] CERN, Geneva, Switzerland
[2] Institut für Physik, Johannes Gutenberg-Universität, Mainz, Germany
[3] School of Physics and Astronomy, The University of Manchester, Manchester, United Kingdom

E-mail: Valentin.Fedoseev@cern.ch

CrossMark

Abstract

At ISOLDE the majority of radioactive ion beams are produced using the resonance ionization laser ion source (RILIS). This ion source is based on resonant excitation of atomic transitions by wavelength tunable laser radiation. Since its installation at the ISOLDE facility in 1994, the RILIS laser setup has been developed into a versatile remotely operated laser system comprising state-of–the-art solid state and dye lasers capable of generating multiple high quality laser beams at any wavelength in the range of 210–950 nm. A continuous programme of atomic ionization scheme development at CERN and at other laboratories has gradually increased the number of RILIS-ionized elements. At present, isotopes of 40 different elements have been selectively laser-ionized by the ISOLDE RILIS. Studies related to the optimization of the laser–atom interaction environment have yielded new laser ion source types: the laser ion source and trap and the versatile arc discharge and laser ion source. Depending on the specific experimental requirements for beam purity or versatility to switch between different ionization mechanisms, these may offer a favourable alternative to the standard hot metal cavity configuration. In addition to its main purpose of ion beam production, the RILIS is used for laser spectroscopy of radioisotopes. In an ongoing experimental campaign the isotope shifts and hyperfine structure of long isotopic chains have been measured by the extremely sensitive in-source laser spectroscopy method. The studies performed in the lead region were focused on nuclear deformation and

---

[*] This article belongs to the Focus on Exotic Beams at ISOLDE: A Laboratory Portrait special issue.

shape coexistence effects around the closed proton shell $Z = 82$. The paper describes the functional principles of the RILIS, the current status of the laser system and demonstrated capabilities for the production of different ion beams including the high-resolution studies of short-lived isotopes and other applications of RILIS lasers for ISOLDE experiments.

1. Introduction

The physical composition and intensity of ion beams, produced at radioactive ion beam facilities such as ISOLDE depends strongly on the type of ion source used to ionize the isotope of interest. At ISOLDE thick targets typically containing high-Z materials are used. Nuclear reactions induced by 1.4 GeV protons delivered from CERN Proton Synchrotron Booster accelerator yield a great variety of radionuclides. Often the isotope of interest is produced along with an overwhelming quantity of isobars which, if ionized, contaminate the ion beam transmitted through the ISOLDE mass separators. Therefore, a means of element selection in the extraction and ionization of radionuclides is often necessary if an isotope-pure ion beam is required.

At ISOLDE, the requirements for both selective and efficient ionization are largely fulfilled by the resonance ionization laser ion source (RILIS).

This ion source is based on the method of step-wise resonant excitation of atomic transitions by wavelength tuneable laser radiation: the laser wavelengths are precisely tuned so that the photon energies match successive electron transition energies of an ionization scheme as shown in figure 1. The valence electron is promoted to a high-lying energy level and then removed from the atom by a subsequent resonant step (via an autoionizing state), by non-resonant photoionization (to the continuum), or by collisional or field ionization (via a Rydberg level). Since each atomic element possesses a unique electronic energy level structure, the laser radiation interacts only with the chosen atomic species. The physics of the laser resonance photoionization process is described in the textbooks by Letokhov [1] and by Hurst and Payne [2]. In section 2.1 we will present only the basic considerations of laser–atom interaction relevant for efficient ionization.

An isobar-selective laser ion source based on laser resonant atomic photoionization was first proposed for on-line radioactive ion beam production at the 'On-line in 1985 and beyond—a workshop on the ISOLDE programme' event [3]. The technique was demonstrated at the Leningrad Nuclear Physics Institute (LNPI, now PNPI) in 1988 [4] and at ISOLDE in 1990 [5–7]. Based on these developments and the first application of the laser ion source in a physics experiment on radioactive ^{152}Ho at LNPI [8], the installation of a permanent laser ion source at the PS-BOOSTER ISOLDE facility was proposed to the ISOLDE Committee in 1993 [9].

Following this proposal, within a short period of time the laser ion source laboratory was established in the ISOLDE experimental hall. It was equipped with copper vapour lasers (CVL) and dye lasers, which, together with the necessary optical and mechanical components, were supplied by the Institute of Spectroscopy of the Russian Academy of Sciences (Troitsk, Moscow region) as a contribution to the ISOLDE programme. The first physics experiment to use the laser ion source was the study of neutron-rich silver isotopes [10] in 1994, during which the half-lives of $^{125\text{-}127}$Ag were determined. This success triggered
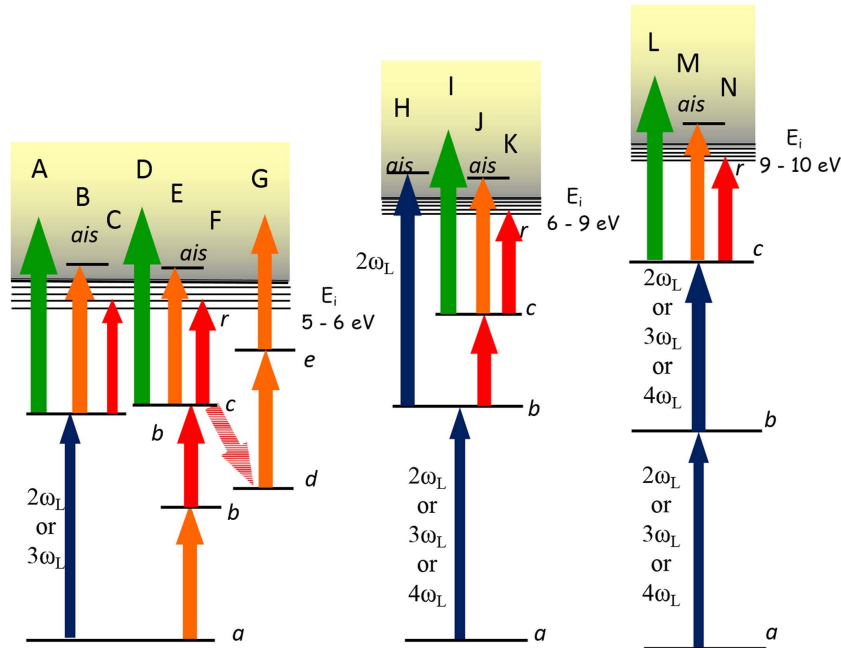
Figure 1. Resonance ionization pathways used by the ISOLDE RILIS. The laser configurations and number of transitions required are somewhat governed by the value of ionization potential E_i. The blue lines indicate transitions which require the generation of higher harmonics of laser radiation: frequency doubling ($2\omega_L$), tripling ($3\omega_L$) or quadrupling ($4\omega_L$).

several requests for other applications of the laser ion source by ISOLDE users. Laser ionized beams of Mn [11], Ni [12], Be, Zn, Cu and Cd [13] were produced at ISOLDE in the few subsequent years.

Using the CVL pumped dye laser system, isotopes of 26 different elements had been selectively laser-ionized at ISOLDE by the year 2007 [14]. Later on, the RILIS capabilities were significantly extended through several upgrades of the laser system, namely, a replacement of CVLs by Nd:YAG lasers [15], the installation of new commercial dye lasers and the addition of a complementary Nd:YAG-pumped Ti:Sapphire laser system [16, 17]. Today, the RILIS installation is a versatile, remotely-operated, dual laser system comprising state-of–the-art solid state and dye lasers capable of generating multiple high-quality laser beams at any wavelength in the range of 210–950 nm [18]. The current list of ion beams available for production at ISOLDE using the RILIS includes 40 elements (see section 4.1 for details). In section 2 we describe the basic principles of the RILIS method including the ionization process in a hot tubular metal cavity and the laser system itself. Newly developed approaches, such as the laser ion source and trap (LIST) [19] and the versatile arc discharge and laser ion source (VADLIS) [20] are described in section 3. Section 4 is devoted to RILIS applications which, in addition to the standard mode of RILIS operation for efficient and selective ionization of a requested element, includes the operation of the RILIS lasers in a high-resolution mode for laser probing of different isotopes and nuclear isomers of the chosen element. This highly sensitive laser spectroscopy method for the study of unstable isotopes

was pioneered at LNPI [21]. At ISOLDE it was further developed as the 'in-source resonance ionization spectroscopy (RIS)' method [22] and applied in a number of experiments for the study of nuclides far from stability. Examples of this application are presented in section 4.3. The concluding section contains a review of current work on RILIS development and outlook to future extension of RILIS capabilities and applications at ISOLDE.

2. RILIS method

2.1. Laser resonance ionization of atoms

A free atom can be excited and ionized with a high probability through a resonant interaction with the radiation from a series of pulsed lasers tuned to match the energy of consecutive transitions between atomic states. Figure 1 illustrates the typical schemes of resonance excitation and ionization used by the RILIS.

Each atomic transition between bound states *a* and *b* (for schemes depicted in figure 1 this could be applied also for transitions b-c, c-r and d-e), can be characterized by an absorption cross section

$$\sigma_{ab} = \frac{g_a}{g_b} \frac{\lambda_{ab}^2}{4\pi^2} \frac{A_{ba}}{\Delta\nu_t^{ab}}, \tag{1}$$

where g_a and g_b are the degeneracy of the levels *a* and *b* respectively, λ_{ab} is the wavelength of the illuminating laser, A_{ba} is the Einstein coefficient and $\Delta\nu_t^{ab}$ is the spectral width of the transition between states *a* and *b* in the laser atom interaction region. The kinetics of multi-step excitation and ionization can be modelled by simple rate equations. By solving the equation system for atomic levels interacting with laser light and integrating the ion production over the pulse duration one can obtain the ionization efficiency η_{lp} resulting from a single act of excitation and ionization by synchronized laser pulses of given duration t_{Lk} and energy density $\mathcal{E}_k$ (here index *k* refers to a step number in the excitation process). The dependence of the η_{lp} versus laser energy density reveals that an efficiency saturation is possible. The use of short laser pulses for resonant excitation minimizes the losses due to the spontaneous decay of excited atomic states. If $t_{L1} < \tau_b$ (τ_b is the decay time of the excited state *b*) the laser pulse energy density required for saturation of the resonant transition between bound states is linked to its cross section as

$$\mathcal{E}_{ab}^{\text{sat}} = \frac{h\nu_{ab}}{2\sigma_{ab}} \frac{\Delta\nu_L^{ab}}{\Delta\nu_t^{ab}}, \tag{2}$$

where *h* is the Planck constant, ν_{ab} is the frequency of the laser light and $\Delta\nu_L^{ab}$ is the spectral line width of the laser driving the transition. A complete spectral coverage of the available atoms is required in order to maximize the efficiency of a resonant excitation, i.e.

$$\Delta\nu_L^{ab} \geqslant \Delta\nu_t^{ab}. \tag{3}$$

The absorption cross sections of allowed electric dipole transitions between bound atomic states typically have values in the range of $\sim 10^{-10}$–10^{-15} cm^2. Saturation can therefore be achieved using a nanosecond-scale laser pulse length with an energy density in the range of $\sim 10^{-6}$–10^{-3} J cm^{-2}.

Transitions to the ionization continuum are much weaker, with absorption cross sections in the range of $\sigma_i \leqslant 10^{-17}$ cm^2. Correspondingly, a higher energy density is required to saturate such an ionizing transition, which for laser pulse at the light frequency ν_i is defined as

$$\mathcal{E}_i^{\text{sat}} = \frac{h\nu_i}{\sigma_i}. \tag{4}$$

The ionization efficiency of schemes using transitions to the continuum (paths A, D, I, L on figure 1) is usually limited by the laser pulse energy available for the last step. Using schemes with transitions to autoionizing or highly excited Rydberg states is advantageous since the cross sections are typically 2–3 orders of magnitude larger than those of non-resonant transitions to the continuum.

Autoionizing states ('ais' in figure 1) are the bound atomic states lying above the ionization threshold which exist in multi-electron atoms due to an excitation of two or more electrons. Each of these electrons undergo a transition between discrete quantum states so that the total excitation energy of the atomic system exceeds the ionization limit. This energy can then be quickly redistributed between the excited electrons in a non-radiative process which results in to the emission of a free electron and leaves the atom in an ionic state. Schemes with 'ais' excitation are indicated in figure 1 by letters B, E, H, J, M.

Not all atoms possess autoionizing states conveniently accessible by the RILIS laser tuning range. However, practically any atom can be excited to levels with high principal quantum numbers n lying in the vicinity of the ionization threshold, the so called Rydberg levels. Since the energy required for ionization of Rydberg atoms is very small (order of meV), ionization of atoms excited to such states can be efficiently driven by an interaction with an external electric field, black-body radiation or collisions with other particles. Ionization schemes involving Rydberg states are presented in figure 1 by the letters C, F, K, N. In practice, the use of such schemes at the RILIS is not routinely practiced due to the limited power output of an additional laser beam at the required wavelength. Furthermore, the lack of precise control of the ionization mechanism of Rydberg atoms adds an element of uncertainty regarding the reproducibility of the performance of such ionization schemes.

Nevertheless, in certain cases where the alternative approach of using a high power 532 nm laser beam for non-resonant ionization results in an unacceptable increase in background due to enhanced ionization of molecular beam contaminants, the use of a Rydberg or autoionizing state can achieve a higher degree of ion beam purity without significantly compromising ionization efficiency.

2.2. Ionization in a hot cavity

The ISOLDE RILIS lasers operate at a pulse repetition rate of $f = 10\,\text{kHz}$ and perform ionization of atoms inside a hot cavity: a refractory metal tube, with an internal diameter $d = 3\,\text{mm}$ and length $L = 34\,\text{mm}$ that is typically heated to $\sim$2000 °C. The heating method is resistive, resulting in a longitudinal electrical potential. This potential accelerates ions created inside the hot cavity towards the extraction aperture. The cavity is connected to the target container where the radio-isotopes are produced. The laser beams are directed along the axis of the cavity from the ion extraction site as depicted in figure 2.

The hot cavity concept was developed to enable efficient ionization of a continuous supply of atoms moving in a vacuum through the path of pulsed laser beams. The geometry of the cavity provides confinement of atoms within the laser beam during the time interval between consecutive laser pulses while the hot environment prevents adsorption of non-volatile species on the internal cavity walls. In addition, ions created in the hot cavity are confined due to the negative plasma sheath potential caused by a thermal electron emission of the cavity walls [23]. The nature of ion confinement and extraction in the hot cavity is identical to that of thermal ion sources that have been developed and used at isotope separators many years [24–28].
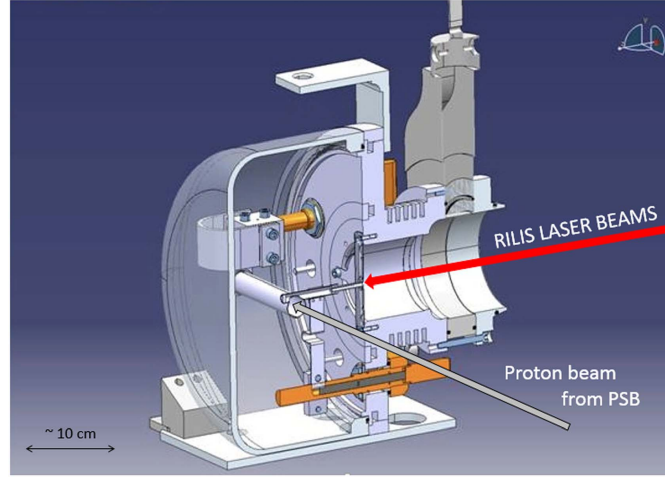
Figure 2. Target and hot cavity ion source assembly.

Atoms with a relatively low ionization potential $E_i \leqslant 6$ eV can be surface ionized quite efficiently in the hot cavity. Fundamentally this process is independent of the element-selective resonance laser ionization process but it is the principal source of isobaric impurity of RILIS ion beams. It is possible to optimize the design and operating conditions of the RILIS hot cavity to minimize the contribution of thermal ionization while preserving its ion confinement properties. In particular, the surface ionization degree α_s strongly depends on the wall temperature T as derived from the Saha–Langmuir equation

$$\alpha_s = \frac{n_{is}}{n_{0s}} = \frac{g_i}{g_0} \exp\left(\frac{\phi - E_i}{kT}\right), \tag{5}$$

where n_{is} and n_{0s} are concentrations of ion and neutrals near the surface, g_i and g_0 are the statistical weights of the ionic and atomic ground states, ϕ is the work function of the electron emitting surface. The surface ionization efficiency β_s is defined then as

$$\beta_s = \frac{n_{is}}{n_{is} + n_{0s}} = \frac{\alpha_s}{1 + \alpha_s}. \tag{6}$$

In a hot cavity with small exit aperture atoms collide with the surface many times which, under the assumption of a non-zero probability of ion survival and extraction from the cavity volume, will result in a higher ionization efficiency than defined by (5) and (6). The expression for the resulting cavity ionization efficiency η_s has been proposed in [28] taking into account the mean number of collisions of atoms with the walls κ and the probability γ of an ionized particle to leave the cavity as ion:

$$\eta_s = \frac{\beta_s \gamma \kappa}{1 - \beta_s(1 - \gamma \kappa)}. \tag{7}$$

The survival of ions inside the cavity is supported by the negative plasma sheath potential Φ_p which has been derived in [23] from the Boltzmann relation for charge densities at the wall and inside the cavity volume in the form

$$\Phi_p = \frac{kT}{2e} \ln\left(\frac{n_{is}}{n_{es}}\right), \tag{8}$$

where e is the electron charge and n_{es} is the concentration of electrons near the surface which is governed by Richardson's law

$$n_{es} = 2\left(\frac{2\pi mkT}{h^2}\right)^{3/2} \exp(-\phi/kT). \qquad (9)$$

Obviously, the contribution of surface ionization could be reduced by decreasing the temperature. In addition, using low work function materials for cavity walls is helpful both for decreasing surface ionization and for increasing the depth of plasma potential due to a more intense emission of electrons at a given temperature. The effect of work function on the laser/ surface ionization ratio has been demonstrated experimentally in [7, 29]. It is also known that the RILIS selectivity can be improved by operating the cavity at a reduced temperature. However, at too low ion source temperature the reduced plasma potential results in an increased probability of recombination of laser ions at the walls, thereby decreasing the laser ion source efficiency. One must also consider the temperature-dependence of wall sticking times, which can impair the ion source efficiency of non-volatile species with short half-lives, but which will not be apparent when optimizing the ion source for a stable isotope.

For efficient laser ionization in a hot tubular cavity the diameters of laser beams are to be adapted to the ion source internal diameter as to completely fill the internal volume of the source. In this case the laser ionization efficiency can be estimated as

$$\eta_{las} = \frac{\gamma\eta_{1l}f}{\gamma\eta_{1l}f + (2/3)(d/L^2)\bar{v}}, \qquad (10)$$

where $\bar{v}$ is the mean thermal velocity of atoms. This expression is obtained assuming a linear decrease of the atom number density along the tube with $L \gg d$ [30].

The ion extraction probability γ depends on the strength of electrical field created by resistive heating of the cavity and the value of plasma sheath potential (8). It is important to note that macroscopic presence of positively-ionized impurities can significantly influence the plasma sheath [23]. Species with a low ionization potential are therefore especially harmful as their ion density near the surface can exceed the electron density, thereby changing the sign of Φ_p to positive. In this case the ion confinement mechanism does not work anymore. On several occasions a drastic reduction of laser ion yield has been observed following an uncontrollable release from mass markers charged with high-capacity alkali dispensers.

2.3. RILIS laser system

One of the valuable operational advantages of using the laser ionization for production of radioactive ion beams is the possibility to situate the lasers and most of the associated laser beam control equipment outside of the radioactive target and separator areas. This facilitates any work on setup and maintenance of the technically complex laser systems since the access to the laser installation is not affected by the protons-on-target operation. At ISOLDE the RILIS laser cabin is located inside the experimental hall on a platform above the ion beam lines and the entrance door to the high resolution separator (HRS) area as depicted in figure 3.

This location enables laser beam transport to the front-ends of either of the ISOLDE separators (see figure 3). The required combinations of laser beams are generated inside the laser laboratory (RILIS cabin in figure 4) and directed to one of the two exit ports. Further on, the laser beams are transported within metal tubes and steered towards the mass separator using 40×40 mm fused-silica right-angle prisms. The final prism of each laser path is installed opposite to the window of the mass separator vacuum chamber, intercepting the line-of-sight to the ion source extraction aperture. The lengths of the optical paths from the laser cabin to an ion source position are 18 m and 23 m for GPS and HRS respectively.

An additional optical beam path from the RILIS cabin has been established to enable laser-access to the ISOLDE RF cooler and buncher, ISCOOL, which is installed downstream of the HRS. A laser beam from RILIS can be injected into the ISCOOL through a window in
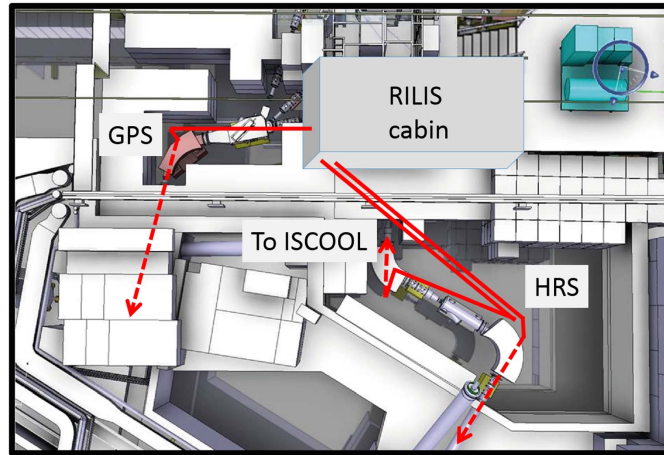
Figure 3. Schematic view of RILIS laser cabin location in ISOLDE experimental hall. Laser beam transport optics are installed in the areas of the general purpose separator (GPS) and the HRS to direct the laser radiation to the respective ion source or to the linear gas-filled Paul trap ISCOOL.
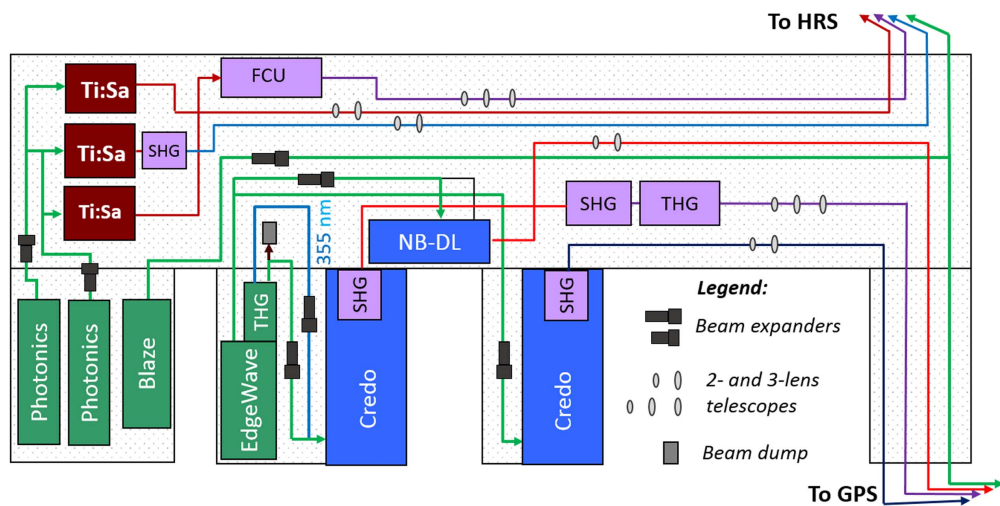
Figure 4. Layout of the RILIS laser installation. Three Ti:sapphire lasers (Ti:Sa) are pumped by two Photonics Nd:YAG lasers; two Credo and one narrow-band (NB-DL) dye lasers are pumped by the EdgeWave Nd:YAG laser; the beam from the Blaze Nd:YVO$_4$ laser is directed to the ion source of either GPS or HRS separator. Frequency conversion (up to 4ω) is performed using modules for second harmonic generation (SHG), third harmonic generation (THG) and a frequency conversion unit (FCU). Mirrors and other optical elements for splitting and transporting laser beams are not shown for simplicity.

the 60° magnet. Laser–ion interactions inside ISCOOL have so far been exploited for optical pumping of manganese ions to a metastable state of the ion for a laser spectroscopy study at the COLLAPS experiment [31]. Further applications of this laser access point, such as laser-induced molecular breakup, are foreseen.

During on-line ISOLDE operation the mass separator areas are not accessible because of a high ambient radiation dose rate. However, all required manipulations with lasers beams, including the setup and maintenance of the laser installation can be safely performed inside the laser cabin, which is shielded from the adjacent mass separator areas by ⩾80 cm thick concrete walls.

The principal components of RILIS installed in the laser cabin are following:

- Laser installation with optics for distribution and shaping of laser beams (see figure 4).
- Instruments for measuring the properties of laser radiation, in particular average power, wavelength, linewidth, pulse duration, beam profile.
- Opto-mechanical systems for launching and precise alignment of laser beams into the ion source cavities of either GPS or HRS front-ends as well as to the linear gas-filled RFQ trap for ion beam cooling and bunching ISCOOL installed at the exit of HRS.
- Opto-mechanical system and instrumentation for observation of reference laser beams, which are representative in size, shape and relative positions of the overlapping laser beams at the ion source location.
- FPGA-based RILIS machine protection system (RMPS) to detect potentially hazardous operational faults in the laser system [32]. This reacts automatically to prevent such equipment damage by taking the appropriate laser equipment control function and alerting the laser operator.
- Atomic beam unit [33] for reference measurements of ion signals and development of ionization schemes.

The layout of RILIS laser installation is depicted in figure 4. The laser setup includes wavelength-tuneable lasers based on two different types of the gain medium: liquid solutions of organic dyes and solid state titanium-doped sapphire crystals (Ti:Sa, chemical formula $Ti^{+3}:Al_2O_3$).

A selection of ∼15 laser dyes are available for operation of the dye lasers with 355 or 532 nm pumping. Each kind of dye molecule has a specific range of absorption and emission. Liquid solution of a laser dye typically enables a 20–50 nm wide laser tuning range. For dye laser pumping a green beam at 532 nm, or a UV beam at 355 nm is available: the frequency-doubled and tripled output of the 10 kHz Nd:YAG INNOSLAB laser (EdgeWave GmbH, model CX16III-OE). The overall tuning ranges possible from the selection of laser dyes using green or UV pumping are 540–860 nm and 390–580 nm respectively. The residual beam at the fundamental wavelength 1064 nm currently is not used and dumped externally. A RILIS upgrade in 2010 included the replacement of the home-made dye lasers with commercial dye lasers supplied by Sirah Lasertechnik GmbH (model Credo Dye) and the narrow-band dye laser supplied by DMK Laser Microsystems Co. Ltd (Russia). The latter contains a Fabry–Perot etalon inside the resonator, which reduces the laser line width to 0.8 GHz. By removing the etalon the laser can be switched to a broad line width mode of operation.

The suite of Ti:Sa lasers was installed at RILIS as a complementary system to the dye lasers [16, 17]. These lasers offer a broad tuning range of 680–950 nm in the infrared part of optical spectrum extendable to 210–475 nm by harmonic generation. Pumping of the Ti:Sa lasers is performed by the green 532 nm beams of two intra-cavity frequency-doubled Nd:YAG lasers (Photonics Industries International Inc., model DM-60-532). A narrow linewidth operating mode of the Ti:Sa laser has been developed [34, 35] to satisfy the requirements of the in-source RIS and nuclear isomer selectivity.

Figure 5 presents the approximate wavelength tuning curves of RILIS lasers. The output power at fundamental wavelength emitted by dye lasers in the visible range is in general higher than that of the Ti:Sa lasers in IR because the dye lasers are equipped with
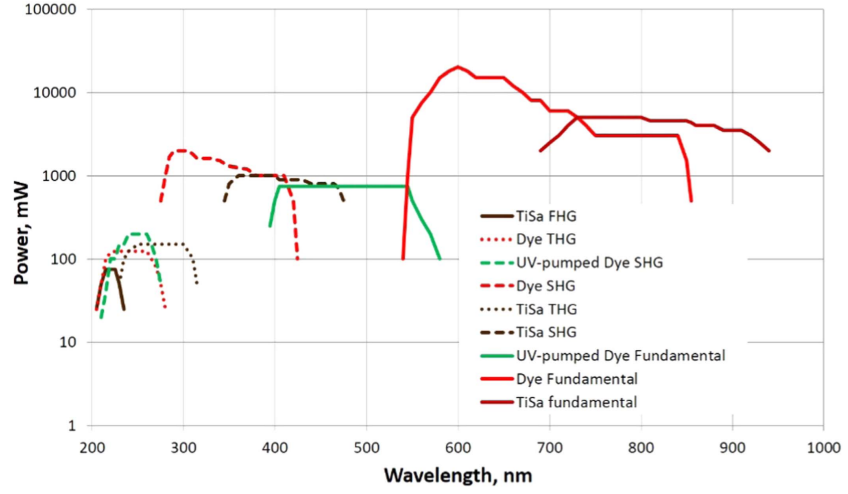
Figure 5. Wavelength tuning curves of the RILIS dye and Ti:Sa lasers including frequency multiplication by second harmonics generation (SHG), third harmonics generation (THG) and fourth harmonics generation (FHG).

amplification stages which can accept a higher pumping power (up to a total of 60 W per laser). For Ti:Sa lasers the pumping power is limited to approximately 20 W by the damage threshold of Ti:Sa crystal, the cavity optics and by thermally-induced laser output instabilities.

The most recent addition to the system of RILIS lasers is the frequency-doubled Nd:YVO$_4$ Blaze 532-40-HE laser (built by Lumera Laser GmbH and supplied via Coherent Inc.), which emits a high quality TEM$_{00}$ beam at 532 nm. As it was demonstrated in [36], this laser beam has an excellent focusing capability thus enabling a twofold increase of ionization efficiency for schemes with non-resonant transitions at the last step. The Blaze laser can also be used for pumping the dye lasers.

All pump lasers and the Blaze laser are operated synchronously at the pulse repetition rate of 10 kHz.

Multiple synchronized 10 kHz triggering signals, each with appropriate logic, widths and adjustable delays are provided by a Quantum Composers 9538 8-channel digital delay pulse generator.

The key parameters of RILIS lasers are summarized in table 1.

The transverse dimensions of each pumping beam are modified using spherical lens beam expanders adjusted so as to match the requirements of the Ti:Sa and dye lasers. Expanders with a fixed 3× expansion factor have been chosen for the Photonics beams used to pump Ti:Sa lasers. Variable 2×–8× beam expanders with anti-reflection coating for 532 and 355 nm are installed in the beams of EdgeWave and Blaze lasers.

The focusing of the RILIS beams into the ion source cavity is achieved using telescopes installed in the laser cabin at appropriate distances from each corresponding laser. For the focusing of a real laser beam over a long distance L the telescope has to be configured to ensure a sufficiently large beam diameter D on its exit lens which can be defined from the relation between the beam radius at waist w_0, laser light wavelength λ and beam quality factor M^2:

$$2w_0 = M^2 \frac{4\lambda}{\pi} \frac{L}{D}. \tag{11}$$

Since the RILIS lasers do not produce ideal Gaussian beams, M^2 may be large, therefore a beam expansion to a diameter of 10–20 mm at the launch point in the laser laboratory is

Table 1. Key parameters of RILIS lasers.

| Laser source	Wavelength, nm	Max. power, W	Pulse duration (FWHM), ns	Line width, GHz
Nd:YAG *EdgeWave CX16III-OE*, beam A	532	80	8	
Nd:YAG *EdgeWave CX16III-OE*, beam B	532	40	9	
Nd:YAG *EdgeWave CX16III-OE*, beam C	355	20	11	
Nd:YAG *Photonics DM-60-532* (2 units)	532	60	130–170	
Nd:YVO$_4$ *Coherent Blaze 532-4-HE*	532	40	17	
Dye laser *SIRAH Credo* (2 units)	390–860	20	7	12
Narrow-band dye laser *DMK Microsystems*	390–860	10	10	0.8 or 15
Ti:Sa laser (3 units, narrow-band option)	680–950	6	30–50	0.8 or 5
Second harmonic of dye lasers	215–425	2	6	
Second harmonic of Ti:Sa lasers	340–475	1	~30	
Third harmonics of dye lasers	210–270	0.2	5	
Third harmonics of Ti:Sa lasers	235–315	0.15	~30	
Fourth harmonics of Ti:Sa lasers	210–235	0.15	~30	
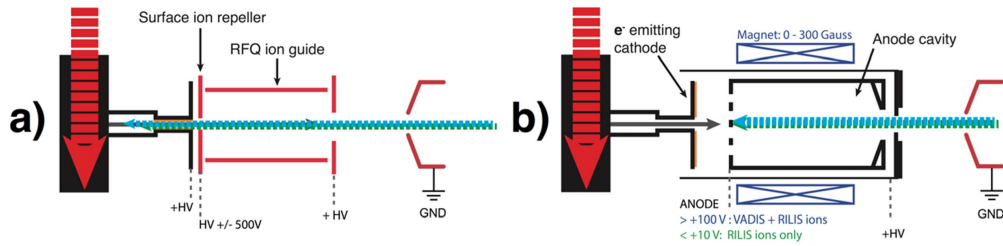
Figure 6. Alternatives to the hot-cavity laser ion source at ISOLDE. (a) The LIST for high selectivity through active surface ion suppression, (b) the VADLIS, the most versatile ion source option at ISOLDE.

typically required to achieve a laser beam waist similar in size to the 3 mm diameter aperture of the ion source cavity. For round beams the telescopes are composed of two spherical lenses, while for elliptical beams, which are usually produced in the process of harmonic generation, telescopes including cylindrical and spherical lenses are used to optimize the aspect ratio.

Up to four laser beams can be simultaneously launched to the GPS or HRS area using a set of closely mounted dielectric mirrors located next to the laser beam exit ports of the RILIS room. The beams pass through a fused silica wedged plate installed at the half-way point of the optical path to the ion source. This generates two spatially separated $\approx 4\%$ reflections which are directed back to the reference beam observation system situated in the laser room. For other RILIS applications, discussed in section 4.4, it is also possible to transmit a laser beam to the ISCOOL ion beam cooler-buncher or to the GLM beam line inside the ISOLDE hall. An optical fibre link also exists for beam transport to and from the laser laboratory of the collinear resonance ionization spectroscopy (CRIS) experiment. A detailed description of most aspects of the RILIS laser installation can be found in [18].

3. New concepts of laser ion sources at ISOLDE

3.1. Ion source for highest selectivity: LIST

The LIST was developed as a means of applying the RILIS technique whilst achieving orders-of-magnitude suppression of thermal ions from the ISOLDE target, transfer line and hot-cavity assembly. As can be seen in figure 6, the LIST consists of three main components:

- *Ion repeller*. Situated immediately downstream of the hot cavity exit, the repeller, operating in the range of $+/-500$ V, enables switching between 'ion guide' ($-$ve polarity) and 'LIST mode' ($+$ve polarity) to either extract or repel ions emerging from the hot-cavity.
- *RFQ ion guide*. The RFQ ion guide (1 MHz, 500 V p-p) positioned immediately after the repeller and on-axis with the hot cavity, provides transverse confinement of ions drifting along the length of the LIST.
- *LIST end plate*. This aperture, which is the end plate of the LIST structure, opposite to the repeller, is required to screen the LIST volume from the electrical potential of the grounded extraction electrode. This ensures that laser-ions created inside the LIST do not suffer from an energy spread that would be incompatible with the subsequent isotope-selective mass separation of the ion beam.

Table 2. A compilation of surface-ion suppression factors measured during off-line and on-line operation of the ISOLDE LIST.

Isotope	Ion current or count rate		Unit	Suppression factor
	Ion guide mode	LIST mode		
^{23}Na$^{\mathrm{offline}}$	75	0.4	pA	200
^{48}Ti$^{\mathrm{offline}}$	145	Bg	pA	$>10^3$
^{174}Yb$^{\mathrm{offline}}$	3	Bg	pA	$>10^2$
^{26}Na	75 000	Bg	β/μC	$>10^5$
^{30}Na	1400	Bg	β/μC	$>10^4$
^{46}K	13 000	Bg	β/μC	$>10^5$
^{205}Fr	610 000	25	α/supercycle	2500
^{212}Fr	80	2	pA	70
^{220}Fr	15 000	Bg	α/supercycle	$>10^3$

The letter T ('trap') of the LIST acronym is somewhat misleading since the LIST offers only two-dimensional (transverse) confinement of ions and therefore acts as an ion guide, rather than as an ion trap. At the ISAC-TRIUMF facility, this distinction has been acknowledged by the use of the IG-LIS (ion guide laser ion source) acronym [37], although this name has the potential to be confused with that of the IGLIS (in gas laser ionization and spectroscopy) method used at gas-catcher ISOL facilities.

The LIST name is in fact inherited from the initial concept of the LIST as a miniature gas-filled Paul trap, proposed by Blaum *et al* in 2003 [38]. To meet the durability, efficiency and reliability demands of the on-line ISOLDE target assembly, this initial LIST concept was greatly simplified towards its current form. This work was conducted by a CERN/Mainz collaboration led by the LARISSA group of Wendt and was the subject of several PhD theses [39–41]. Some key functionality (ion beam cooling and bunching) first proposed by Blaum has therefore been lost whilst the primary function of achieving orders-of-magnitude selectivity improvements has been demonstrated under normal on-line operating conditions with a UCx target [42]. So far the LIST has been successfully used for the production of pure Mg [19] and Po [42, 43] beams. Table 2 is a summary of the LIST suppression factors that have been measured during off-line and on-line operation at ISOLDE. In many cases the LIST-mode surface ion rate was below the detection limit of the device used for determining the ion rate. In these cases, it is only possible to state a lower limit of the suppression factor. For the most recent LIST device, which was built with the minimum acceptable distance of the LIST repeller from the hot cavity exit of 1 mm, the estimated RILIS efficiency loss factor was 20. This was determined by comparing the LIST mode and ion guide mode RILIS ion rates.

3.2. Hybrid plasma-laser ion source: VADLIS

The VADLIS [20] has become an established ion source option at ISOLDE in recent years. Currently this approach makes use of a standard ISOLDE FEBIAD (the VADIS) ion source [44] as a laser–atom interaction volume, as seen in figure 6(b). When operating at low anode voltage (<10 V), and with optimized cathode and magnetic field settings, the FEBIAD cavity becomes an effective environment for selective laser resonance ionization. In the numerous off-line and on-line tests, under standard operating conditions, a RILIS-mode efficiency typically equal to or greater than the FEBIAD-mode efficiency for the element of interest has been obtained.

To date, the VADLIS has been applied at ISOLDE for resonance ionization of Ga, Mo, Ba, Hg, Mg and Cd. For the latter three, this involved on-line operation for the production of radioisotopes.

The examples of Hg, Mg, Ba and Mo highlight several of the unique capabilities of the VADLIS ion source:

Hg—The highest intensity neutron-deficient mercury beams at ISOLDE have been produced using lead targets. The molten lead bath target is attached to the ion source via a spiral, temperature-controlled chimney (lead vapour condenser), which is currently only compatible with FEBIAD-type ion sources. The VADLIS is therefore currently the only option for achieving selective resonance laser ionization of isotopes from molten targets. In 2015, a campaign to study both neutron deficient and neutron rich mercury isotopes by in-source RIS was, in fact, the first on-line application of the VADLIS for a physics experiment [45].

Mg—During 2016, an ISOLTRAP experiment aimed to study ^{21}Ne and ^{23}Mg isotopes in the same experiment using a SiC target coupled to a VD5 VADIS [46]. On account of their atomic structure and high ionization potential, noble gases ions cannot be created by the surface or RILIS ion sources, hence the FEBIAD-type source is required for this experiment. Under normal operation, the isobaric background generated at mass 23, (predominantly ^{23}Na), proved overwhelming for the successful ^{23}Mg. The use of the VADLIS method enables quick switching to the RILIS-mode of VADLIS operation, significantly enhancing the ^{23}Mg beam intensity whilst providing a moderate suppression of ^{23}Na and orders-of-magnitude suppression of all other background isobars.

Ba—On account of the relatively low ionization potential of barium (5.21 eV), barium beams can be efficiently produced at ISOLDE using a surface ion source operating at high temperature (>2000 °C). Under these conditions the beam purity for radiogenic Ba$^+$ is typically poor due to the readily surface-ionized contaminants: mainly caesium and indium isobars. Fluorination of the target material can address this, resulting in the creation of BaF$_2$, which is extracted as BaF$^+$ from a FEBIAD source. This has proven effective for the purification of neutron-deficient barium beams produced from lanthanum targets since BaF$^+$ ions occupy a mass region devoid of isobaric contamination. For neutron-rich Ba beams however, a UCx target is required. In this case the abundantly produced europium and samarium isotopes appear as isobaric contaminants in the extracted BaF$^+$ beams. As an alternative approach, an optimal laser ionization scheme for atomic barium has been developed and tested in combination with both the hot-cavity and the VADLIS ion sources. Since the anode grid of the VADIS cavity is positively charged, surface ions created in the hot cathode region are actively repelled. Furthermore, unlike the situation for the hot cavity RILIS, RILIS-mode VADLIS laser ion survival is not reliant on electron emission from the cavity walls. Neglecting condensation/wall sticking considerations, optimal RILIS efficiency can therefore be achieved at a lower temperature, further reducing the surface-ionized proportion of the extracted ion beam. The VADLIS therefore offers the possibility to increase the selectivity of the laser ion source. A comprehensive Ba$^+$ ion yield assessment is required to fully validate this approach however, in offline tests a Ba$^+$ laser to surface ion ratio of 8 has been achieved in the VADLIS (compared to 1 for hot-cavity RILIS) under typical operating conditions. A further increase in selectivity could be realised through the use of an anode cavity made from a low-work function material.

Mo—A resonance ionization scheme for the refractory metal molybdenum was developed in an off-line test at ISOLDE by RIS using the RILIS in 2016. On account of the low vapour pressure at the typical ion source operating temperature, speculative ionization scheme development for elements such a Mo is challenging in the absence of any means of assessing

the presence of a sufficient supply of the atoms of interest. By offering the possibility of easy switching between RILIS and VADIS ionization modes the VADLIS removes this degree of uncertainty: a VADIS-mode Mo ion current was first established, demonstrating the availability of a suitable quantity of Mo atoms. Then, after switching to RILIS-mode, the spectroscopic search for Mo ionization schemes could begin with a pre-established knowledge of the availability of the sample as well as a reference value for the expected ion rate.

4. RILIS applications

4.1. Ion beam production

The principal application of RILIS is the production of ion beams of elements required for ISOLDE experiments. As the isotopic selectivity provided by the mass-separation in most cases is sufficient for the purpose of an experiment, laser ionization is required to be only an element-selective process. Moreover, when the hyperfine splitting of the ground atomic state exceeds the spectral width of applied laser light, a significant fraction of atoms may not interact with the laser radiation, thus reducing the ionization efficiency. Therefore, whenever possible the spectral bandwidth of laser radiation should be sufficiently broad in order to cover the hyperfine structure. In addition, using such broad-band laser radiation facilitates studies of long isotopic chains by reducing the sensitivity of ionization process to the isotope shift of resonant atomic transitions.

Effective ion beam production requires stable laser performance during round-the-clock operation. Until 2014 this was ensured by continuous supervision of the RILIS installation by laser experts working in shifts. In order to facilitate both laser operation and performance monitoring, a comprehensive LabVIEW-based system of remote control and equipment monitoring of RILIS has been developed [32, 34, 47, 48]. It is known as REACT: the RILIS equipment acquisition and control tool. Due to this development complemented by the implementation of the machine protection system RMPS, autonomous functioning of RILIS during normal operation became safe and reliable. Thus, the goal of a transition from the shift-based to the on-call-based operation has been achieved.

In general, the purity requirements for specific isotopic beams specify directions of laser ionization scheme development, while wavelength and power capabilities of the RILIS laser system define the range of elements accessible for efficient laser ionization. Most of the elements in the Periodic table could potentially be resonantly excited and ionized using the RILIS lasers system. However, the range of ion beams at ISOLDE is defined by the production and release properties of ISOLDE targets. In particular, radioactive isotopes of refractory metals are not released as free atoms at the target temperature $\leqslant 2200\,^{\circ}$C. Therefore, the RILIS is applied mainly to the more volatile elements with resonant transition wavelengths above 210 nm.

The list of elements ionized with RILIS at ISOLDE is presented in table 3. It includes information about the applied ionization schemes with an indication to the specific type of excitation pathway illustrated in figure 1. Whenever available, the data on ionization efficiency are included. These are absolute efficiency measurements made using calibrated samples and/or relative values of laser ion current observed in comparison with a surface ion current under typical operational parameters of the hot cavity ion source. The last column of table 3 gives references to first publications on the specific scheme development or application. Some additional details (lasers used, dyes) can be found in [18].

Table 3. RILIS ionization schemes applied at ISOLDE.

Element	Type of scheme[a]	λ₁ (vac) nm	λ₂ (vac) nm	λ₃ (vac) nm	Efficiency Abs. %	Laser/surf.	Isotopes A	Reference
Li	D	670.96	610.53	532		0.6	6–11	[49]
Be	H	234.93	297.41	—	>7		7, 9–12, 14	[13]
Mg	I	285.30	552.99	510.69 & 578.37	10		21–35	[50]
				532				[15]
Al	A	308.30 & 309.37	510.69 & 578.37	—	>20	100	26–36	[51]
			532					[18]
Ca	J	422.79	585.91	655.18		300	40–54	[40, 52]
Sc	I	327.46	720.03	510.69	15	400	Stable	[53]
Cr	J	357.97	698.03	579.31	~20	2200	48–63	[49, 54]
Mn	J	279.91	628.44	510.69	19		48–69	[11]
				647.52				[15]
Fe	L	372.10	321.26	532	>4	10⁵	54–62	[55]
Co	I	304.49	544.61	510.69 & 578.37	>6		Stable	[51]
Ni	J	305.17	611.28	748.42	6.6	8000	56–70	[12]
Cu[e]	I	327.49	793.53	510.69	>7		57–78	[13]
	H		287.98	—	5			[56]
Zn	I	213.92	636.41	510.69			58–82	[13]
				532				[15]
Ga	A	287.51	510.69 & 578.37	—	21	20–30	61–86	[57]
		287.51 & 294.50	532	—		>100		[14]
Ge	I	275.54	569.35	532	>2		Stable	[49, 58]
Y	I	408.49	582.07	582.07		16	Stable	[51]
		414.40	662.55	510.69		88		[53]
Mo	M	379.93	415.91	635.16			Stable[b]	[55]
Ag[e]	I	328.16	546.7	510.69 & 578.37	14		101–130	[10, 59]
				532				[17]
Cd	L	328.16	421.21	532				[18, 47]
	I	228.87	644.02	510.69	10		98–133	[13]
				532				[17]

16

Table 3. (Continued.)

Element	Type of scheme[a]	λ₁ (vac) nm	λ₂ (vac) nm	λ₃ (vac) nm	Efficiency Abs. %	Efficiency Laser/surf.	Isotopes A	Reference
In[e]	A	304.02	510.69 & 578.37	—		7	100–135	[60, 61]
		304.02 & 325.70	532					[18]
Sn	I	303.50	607.08	607.08	0.2			[6]
	J	301.00	811.40	823.68	9		105–138	[30, 62]
		286.30						[18, 63]
Sb	I	217.65	560.36	510.69	2.7		128–139	[53]
				532				[18]
Te	J	214.35	573.52	901.51	>18		Stable	[58]
Ba	B	350.21	653.71			1	Stable	[49]
	A		532	—				[20]
Ba+	L	455.53	223.35	532	1.2[c]		Stable	[49]
Pr	I	461.90	900.00	532			Stable	[17, 47]
Nd	D	588.95	597.10	597.10		15	138–140 and stable	[15, 64]
Sm	E	600.58	675.34	676.37		6	140–143 and stable	[17, 65]
Tb	E	579.72	551.80	618.43		>1.8	149, 159	[51, 66]
Dy	D	626.08	607.66	510.69	20	50	149–164	[53]
				532				[17]
Ho	I	418.80	776.22	532		12	163, 165	
	I	405.50	623.43	532	>20	60		[18]
	J			838.36		45		
Tm	E	589.73	571.40	575.67	>2		Stable[d]	[6, 67]
Yb	E	555.80	581.23	581.23	15	20	155–178	[4, 6]
	A	267.28	532	—				[18, 47]
Au[e]	M	267.67	306.63	674.08	>3		176–198, 201, 202	[68]
Hg[e]	L	253.73	313.28	532	6		177–208	[18, 45, 49, 69]
Tl[e]	A	276.87	510.69 & 578.37	—	27	100	179–205	[51]
			532					[15]
Pb[e]	I	283.39	600.35	510.69 & 578.37	3		182–215	[70]
			601.33	532				[17]

Table 3. (Continued.)

Element	Type of scheme[a]	λ_1 (vac) nm	λ_2 (vac) nm	λ_3 (vac) nm	Efficiency		Isotopes A	Reference
					Abs. %	Laser/ surf.		
Bi[e]	I	306.86	555.36	510.69 & 578.37	6		187–218	[51]
				532				[18]
Po[e]	I	245.08	539.03	510.69			192–211, 216–219	[71]
			843.62					
	K	255.88	843.62	532				[15]
	K	255.88	843.62	593.94				[40]
At[e]	I	216.29	795.45	532			194–211, 217–219	[72]
			915.46	532				[47]
	K		795.45	617.55				
Ra	E	714.32	784.03	557.65		3	214, 222–234	[45, 55]
	G			615.28				

[a] According to notations of figure 1.
[b] Ionized in VADIS cavity.
[c] Efficiency of conversion of singly charged Ba^+ ions to the doubly charges ions Ba^{++}.
[d] Beams produced at the old SC-ISOLDE-3 facility.
[e] Elements for which isomer selective ionization has been applied.

4.2. Separation of nuclear isomers

In addition to element selectivity, the RILIS offers a unique opportunity to select or enhance the fraction of a certain nuclear isomer in the produced ion beam. This is based on a sensitivity of the hyperfine structure of atomic transitions used for resonance ionization to the nuclear spins and nuclear moments. If the isomeric difference in the hyperfine structure exceeds the experimentally observed width of excitation resonance then the laser can be tuned to the specific wavelength which provides a preferential ionization of the desired nuclear state. This capability of resonance photoionization process has been demonstrated in [65] and actually applied at ISOLDE in some of the early examples of RILIS use, namely for the production of isomeric silver [59] and copper [56] beams.

Although nuclear isomerism is a rather general phenomenon, the hyperfine structure differences are not always sufficiently large as to be resolved by the RILIS lasers in the hot-cavity laser ion source conditions, where the spectral width of excitation resonances is defined by the Doppler broadening of atomic absorption lines. Therefore, the isomer selective ionization has been applied for a limited range of RILIS beams. Elements for which isomer-selective ionization has been achieved are indicated by the superscript letter (e) in table 1.

4.3. In-source RIS

As indicated in table 1, the RILIS dye and Ti:Sa lasers can be operated in a reduced line width mode. With sufficiently high resolution the ionization efficiency becomes sensitive to the isotope shift or hyperfine structure splitting. Combining this enhanced resolution with a wavelength-stabilized laser scan procedure therefore enables a spectroscopic study of these features. The laser spectra can then be analysed to extract nuclear ground state or isomer properties (charge radii and moments) and these can be charted along the isotope chain of the element of interest. Since the laser scan directly influences the ion production rate, this approach, known as in-source RIS, is the most sensitive laser spectroscopy method at ISOLDE.

The resolution of in-source RIS is limited by the Doppler broadening, $\Delta\nu_D$ of atomic transitions inside the high temperature ionization environment, given by the following

$$\Delta\nu_D = 7.16 \times 10^{-7}\nu_0(T/A)^{1/2}, \tag{12}$$

where ν_0 is the frequency of the atomic transition and A is the atomic mass number. For the heavier elements, however, the Doppler broadening approaches the line width of RILIS narrow-band lasers and, crucially, the field shift dominates the overall isotope shift and becomes comparable with the Doppler width of atomic transitions, as is illustrated in figure 7.

Thus, for elements with high Z the Doppler-limited resolution of in-source RIS enables the extraction of valuable nuclear structure information, particularly if the spectroscopic transition involves an s-electron, which experiences a greater sensitivity to nuclear changes due to its maximal wave-function overlap with the nucleus. The accuracy of spectral measurements below 100 MHz is achievable [74].

Data acquisition links with a variety of ion detection systems available at ISOLDE have been established [22, 48] to ensure laser-scan compatibility across the range of radioisotope decay modes and the abundancy distribution along an isotope chain: $(\alpha/\beta/\gamma)$ detection with the Leuven Windmill system [75]; direct ion counting with the ISOLTRAP multi-reflection time-of-flight mass separator [76]; and ion beam current measurements using the ISOLDE Faraday cups. Collectively these detection methods enable the determination of ion production rates from the nA range to as few as 0.01 ions per second [77].
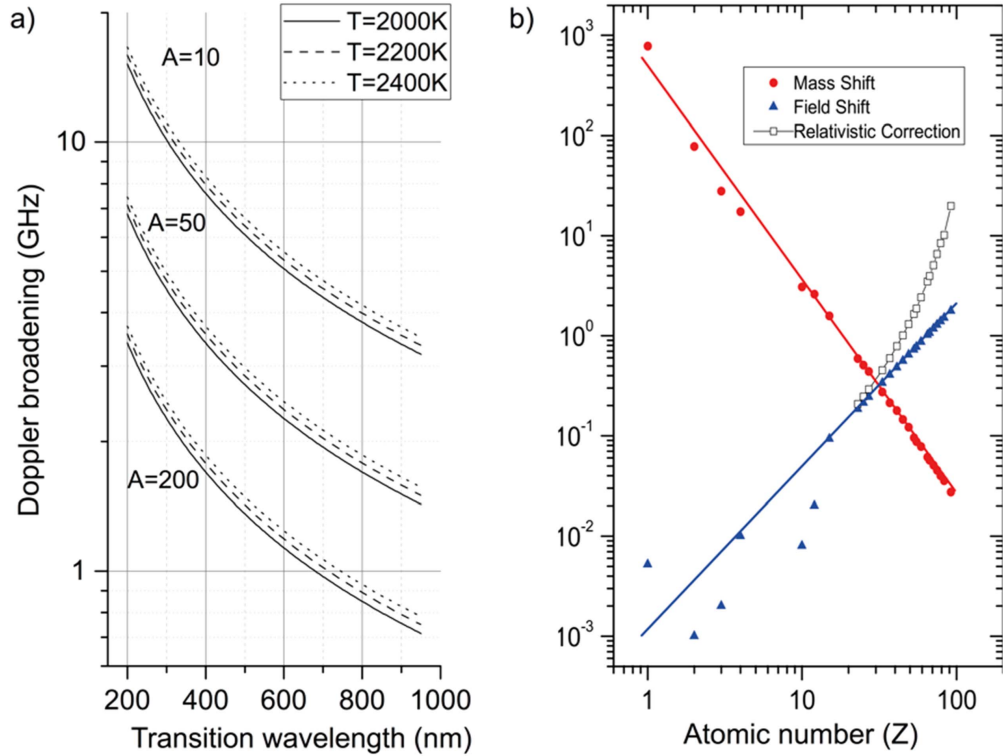
Figure 7. (a) The mass, wavelength and temperature dependence on the Doppler broadening. (b) The relative contribution of the mass shift and field shift to the total isotope shift as a function of the atomic number Z (Reproduced from [73]. 2013 The Royal Swedish Academy of Sciences. All rights reserved).

The RIS application of the RILIS is the most demanding in terms of the monitoring, control and stability requirements of the laser system. Optimizing the spectral resolution requires below-saturation laser power level for the spectroscopic transition. This means that factors such as laser beam positioning, power and pulse timing stability become critical to the acquisition of laser scans without experimentally-induced distortions. Continuous and comprehensive recording of the experimental conditions, as well as active stabilization of laser power, beam position and pulse timing synchronization has been developed to accommodate this requirement [48]. These advanced features of the RILIS installation are gradually being adopted to the benefit of increased reliability and autonomy for normal RILIS operation.

Following the series of experiments on the study of nuclear spins and electromagnetic moments of Cu isotopes [56, 78–80] the in-source RIS collaboration has performed extensive laser and nuclear-spectroscopic studies of isotopes in the lead region, namely the Tl [81], Pb [70, 82–84], Hg [45], Bi [85], Po [43, 77, 86, 87], At and Au chains [22, 88]. Our recent activity in this field has revisited the neutron-deficient Au and Hg isotopes, which were first studied at ISOLDE approximately four decades ago: the very first optical spectroscopy experiments performed at an ISOL facility [89–92]. This early work was instrumental in the discovery of the shape co-existence phenomenon and revealed two of the most striking examples of sudden nuclear shape changes in the known nuclear chart: the dramatic odd–even shape staggering of the neutron-deficient Hg isotopes, and the abrupt and pronounced shape change of the Au nuclei isotopes. The in-source spectroscopy method has brought the most

exotic isotopes available at ISOLDE within reach. By observing the return to a quasi-spherical nuclear shape as we move from the neutron mid-shell towards the proton dripline we have finally determined the end-point of these renowned features of the nuclear chart.

4.4. Other applications of the RILIS laser installation

In addition to ion beam production, the RILIS laser system offers the opportunity to exploit various laser–ion and laser–molecule interactions for the purposes of ion beam preparation and investigation. To maximize the scope for RILIS applications other than ion beam production, laser beam transport has been established to several locations in the ISOLDE hall: the ISCOOL ion beam cooler-buncher, the GANDALPH experiment, and the CRIS experimental beamline. The following is summary of the already realised and possible future applications of this additional functionality of the RILIS laser system.

ISCOOL: Laser access to the trapping region of the ISCOOL was initially established for the purposes of optical pumping of manganese ions. This technique, which was pioneered at the JYFL IGISOL facility [93], enables the preparation of the ions in a favourable state for subsequent study by collinear laser spectroscopy. The Mn ions are illuminated with laser radiation tuned to resonance with the 230.50 nm transition from the $^7S_3$ ionic ground state to the $^5P_3$ excited state at $43\,370.51\,\mathrm{cm}^{-1}$. The subsequent radiative decay has a non-negligible probability of populating the $^5S_2$ metastable state at $9472.97\,\mathrm{cm}^{-1}$. Since the residency time of the ion cloud in the laser interaction region is long compared to the RILIS laser duty cycle, multiple laser–ion interactions are inevitable and the result is that the ion ensemble is 'pumped' into the metastable state. In this particular case, this was favourable since it enabled the subsequent collinear fluorescence laser spectroscopy to be performed [31] using a more convenient 295 nm transition from the metastable state to the $^5P_3$ state. Another possible foreseen application of this optical pumping method may be the ability to influence the probability of a subsequent charge exchange process prior to the study of a neutral atom beam by laser spectroscopy. Finally, laser beam access to ISCOOL will make possible any future investigation of laser-induced dissociation of molecular ions inside the trapping region. This may be of interest for cases where the formation of a volatile molecule is the only means of releasing the element of interest from the ISOLDE target.

GANDALPH: The GANDALPH setup is a transportable experimental beamline, initially designed to study the electron affinities of the radioactive elements astatine and polonium [94, 95]. The experiment applies the technique of laser photodetachment spectroscopy where a frequency tunable laser beam is overlapped collinearly with a beam of negative ions of the isotope to study. The neutralized fraction of the beam is detected as a function of photon energy; the electron affinity can be derived from the threshold energy of neutralization. GANDALPH was first connected to the GLM beamline and transport of one laser beam from RILIS was established. The first successful electron affinity measurement of a radioactive isotope was performed on ^{128}I. Further details on GANDALPH and the first results can be found in a dedicated article in this issue [96].

CRIS: The initial commissioning and first results obtained by the CRIS experiment relied on the frequency-doubled output from a RILIS narrow-band Ti:Sa laser, which was transmitted to the CRIS beam line via an optical fibre [97]. Scanning control of the RILIS laser was made possible by a remote interface to the shared variables of the REACT system. An additional future application of this infrastructure may be the transmission of a single mode CW laser beam from CRIS to the RILIS laboratory for pulsed amplification using the RILIS lasers. This would result in a laser with a Fourier limited line width suitable for a proposed campaign of sub-Doppler in-source spectroscopy studies [98].

5. Conclusions and outlook

Ion production by resonance laser ionization has emerged as an essential capability of modern ISOL facilities. As a result of the increased demand for laser ionized beams, the ISOLDE RILIS has undergone constant development since 1994. The modern RILIS system is now the most capable and heavily used system of its kind worldwide. The ongoing RILIS development is focused on three main areas:

Laser technologies—for improved reliability, stability, efficiency and spectral resolution (when required).

Ionization schemes—to increase efficiency and number of accessible elements.

Ion sources—for increased selectivity and/or efficiency.

The latter of these is particularly challenging due to the resources required to construct and test new innovations. For example, the LIST concept, proposed in 2003, required more than 10 years of modification and characterization until it finally became operational at ISOLDE in 2014. On the other hand, improving the ion beam intensity from an ISOL facility through ion source development is typically more cost effective than achieving the same gain through an increase in target size or driver beam intensity. Furthermore, ion source selectivity improvements not only improve experimental conditions, they also reduce the build-up of an unwanted radioactive inventory downstream of target assembly.

As was discussed in section 2.2, the high-temperature resistively heated surface ion source cavity offers the combination of simplicity and robustness, along with atom confinement and high ion survival probability which is crucial for efficient laser ion source operation with pulsed lasers. Such features are unmatched in alternative laser ion source options however the problem of thermally ionized isobaric contamination can be overwhelming for many ion beams of interest. Tackling this issue is a main focus of ongoing laser ion source R&D. The LIST has proven effective but comes at the cost of an often-unacceptable efficiency reduction. An alternative approach is to enhance and exploit the pulsed nature of the laser-ion creation. The extracted laser-ion bunch characteristics have been studied at length and the inverse proportionality of the bunch length to the longitudinal cavity voltage is documented [99]. Mishin, one of the pioneers of the laser ion source, proposed a further enhancement of this effect by allowing the laser-ions to emerge from the hot cavity inside a field-free drift-region of equal length to the cavity [100]. An ion generated at the rear of the cavity has a longer distance to travel to reach the end of the drift region than an ion generated at the cavity exit but it experiences the full cavity longitudinal voltage drop and therefore travels faster and eventually catches up with the slower ion. The result is that the ion bunch reaches a time focus at the extraction position. The ion bunch compression is limited only by the cavity voltage and turn-around time of ions with a thermal velocity component directed towards the target during the ionization. Initial studies and simulations suggest that a selectivity improvement of at least two orders of magnitude may be achievable, with little reduction in overall RILIS efficiency. The many potential pre-requisites of this project are currently under various stages of ongoing development: high resistance cavity; 10 kHz pulsed heating with duty cycle/voltage modulation; use of the LIST as a drift region; and sub microsecond fast beam gating.

Naturally, for the development of new ion beams at ISOL facilities, the target and ion source development are often intertwined. This is the case for an ongoing project aimed at the extraction of refractory transition metals from ISOLDE through the formation of weakly-bound volatile molecules. An investigation of the suitability of the RILIS lasers for molecular break-up and subsequent resonance ionization of the refractory metal atom is foreseen [101] as part of a feasibility study conducted at ISOLDE.

Finally, RIS or radioactive isotopes, the flagship of RILIS operation, is reaching an applicability limit since the prolific measurement campaign has now addressed almost all of the feasible measurement cases in the heavy-isotope region. A further-reaching exploitation of this method, for both isomer selective ionization and for nuclear structure studies, will require a means of overcoming the Doppler-broadening limitation. This can be realised through the development of a laser ion source environment with counter-propagating laser beams (achievable through the insertion of a mirror inside the ion source or transfer line). In this case, if an ionization scheme which requires a 2-photon transition is used, and this transition is accessed by a narrow linewidth (Fourier limited) injection-seeded pulsed laser, Doppler-free two-photon spectroscopy becomes possible: the Doppler shift of each atom, as seen by the incoming laser beam, is exactly compensated for by the opposite Doppler shift seen by the reflected laser beam. The first application of this method at ISOLDE for the study of silicon isotopes has already been proposed [98].

In conclusion, the RILIS has a long and successful history as an essential component of the ISOLDE ion beam production process. The subsequent adoption of the RILIS method as a key consideration for ISOL facilities worldwide is testament to this. Nevertheless, despite its over two decades of operation at ISOLDE, significant scope still remains to further develop RILIS methods for new and particularly challenging ISOLDE beams.

Acknowledgments

ORCID

Sebastian Rothe ⓘ https://orcid.org/0000-0001-5727-7754

References

[1] Letokhov V S 1987 *Laser Photoionization Spectroscopy* (Orlando, FL: Academic)
[2] Hurst G S and Payne M G 1988 *Principles and Applications of Resonance Ionization Spectroscopy* (Bristol: Hilger)
[3] Letokhov V S and Mishin V I 1984 Laser photoionization pulsed source of radioactive atoms *On-Line in 1985 and Beyond—A Workshop on the ISOLDE Programme—Abstracts (Zinal, Switzerland, 18–24 June 1984)* p D7 (http://cds.cern.ch/record/152322)
[4] Alkhazov G D, Letokhov V S, Mishin V I, Panteleyev V N, Romanov V I, Sekatsky S K and Fedoseyev V N 1989 Highly effective Z-selective photoionization of atoms in a hot metallic cavity followed by electrostatic confinement of the ions *Pis'ma Zh. Techn. Fiz.* **15** 63–6
[5] Fedoseev V N, Kudryavtsev Y A, Letokhov V S, Mishin V I, Ravn H, Sundell S, Kluge H J and Scheerer F 1991 A laser ion source for on-line separation *Resonance Ionization Spectroscopy 1990—Proc. 5th Int. Symp. on RIS and its Applications (Varese, Italy, 16–21 September 1990)* ed J E Parks and N Omenetto (Bristol: IOP) pp 129–32

[6] Scheerer F, Fedoseyev V N, Kluge H-J, Mishin V I, Letokhov V S, Ravn H L, Shirakabe Y, Sundell S and Tengblad O 1992 A chemically selective laser ion source for on-line mass separation *Rev. Sci. Instrum.* **63** 2831–3

[7] Mishin V I, Fedoseyev V N, Kluge H J, Letokhov V S, Ravn H L, Scheerer F, Shirakabe Y, Sundell S and Tengblad O 1993 Chemically selective laser ion-source for the CERN-ISOLDE on-line mass separator facility *Nucl. Instrum. Methods Phys. Res.* B **73** 550–60

[8] Alkhazov G D, Batist L K, Bykov A A, Vitman V D, Letokhov V S, Mishin V I, Panteleyev V N, Sekatsky S K and Fedoseyev V N 1991 Application of a high efficiency selective laser ion source at the IRIS facility *Nucl. Instrum. Methods Phys. Res.* A **306** 400–2

[9] Barker J 1993 Request for implementation and further development of the ISOLDE laser ion-source *Proposal to ISOLDE Committee* CERN-ISC-93-10; ISC-P-47 CERN. Geneva. ISOLDE Experiments Committee (http://cds.cern.ch/record/297272)

[10] Fedoseyev V N *et al* 1995 Study of short-lived silver isotopes with a laser ion source *Z. Phys.* A **353** 9–10

[11] Fedoseyev V N *et al* 1997 Chemically selective laser ion source of manganese *Nucl. Instrum. Methods Phys. Res.* B **126** 88–91

[12] Jokinen A *et al* 1997 Selective laser ionization of radioactive Ni-isotopes *Nucl. Instrum. Methods Phys. Res.* B **126** 95–9

[13] Lettry J *et al* 1998 Recent development of the ISOLDE laser ion source *Rev. Sci. Instrum.* **69** 761–3

[14] Fedosseev V N *et al* 2008 ISOLDE RILIS: new beams, new facilities *Nucl. Instrum. Methods Phys. Res.* B **266** 4378–82

[15] Marsh B A *et al* 2010 The ISOLDE RILIS pump laser upgrade and the LARIS laboratory *Hyperfine Interact.* **196** 129–41

[16] Rothe S, Marsh B A, Mattolat C, Fedosseev V N and Wendt K 2011 A complementary laser system for ISOLDE RILIS *Proc. Int. Nuclear Physics Conf. 2010 (Vancouver, Canada, 2010)*
Rothe S, Marsh B A, Mattolat C, Fedosseev V N and Wendt K 2011 *J. Phys.: Conf. Ser.* **312** 052020

[17] Fedosseev V N *et al* 2012 Upgrade of the resonance ionization laser ion source at ISOLDE on-line isotope separation facility: new lasers and new ion beams *Rev. Sci. Instrum.* **83** 02A903

[18] Rothe S, Day Goodacre T, Fedorov D V, Fedosseev V N, Marsh B A, Molkanov P L, Rossel R E, Seliverstov M D, Veinhard M and Wendt K D A 2016 Laser ion beam production at CERN-ISOLDE: new features—more possibilities *Nucl. Instrum. Methods Phys. Res.* B **376** 91–6

[19] Fink D A *et al* 2015 On-line implementation and first operation of the laser ion source and trap at ISOLDE/CERN *Nucl. Instrum. Methods Phys. Res.* B **344** 83–95

[20] Day Goodacre T *et al* 2016 Blurring the boundaries between ion sources: the application of the RILIS inside a FEBIAD type ion source at ISOLDE *Nucl. Instrum. Methods Phys. Res.* B **376** 39–45

[21] Alkhazov G D *et al* 1992 A new highly efficient method of atomic spectroscopy for nuclides far from stability *Nucl. Instrum. Methods Phys. Res.* B **69** 517–20

[22] Marsh B A *et al* 2013 New developments of the in-source spectroscopy method at RILIS/ISOLDE *Nucl. Instrum. Methods Phys. Res.* B **317** 550–6

[23] Huyse M 1983 Ionization in a hot cavity *Nucl. Instrum. Methods* **215** 1–5

[24] Beyer G J, Herrmann E, Piotrowski A, Raiko V J and Tyrroff H 1971 A new method for rare-earth isotope separation *Nucl. Instrum. Methods* **96** 437–9

[25] Johnson P G, Bolson A and Henderson C M 1973 A high temperature ion source for isotope separators *Nucl. Instrum. Methods* **106** 83–7

[26] Latuszynski A and Raiko V I 1975 Studies of the ion source with surface-volume ionization *Nucl. Instrum. Methods* **125** 61–6

[27] Kirchner R 1981 Progress in ion source development for on-line separators *Nucl. Instrum. Methods* **186** 275–93

[28] Kirchner R 1990 On the thermoionization in hot cavities *Nucl. Instrum. Methods Phys. Res.* A **292** 203–8

[29] Schwellnus F *et al* 2009 Study of low work function materials for hot cavity resonance ionization laser ion sources *Nucl. Instrum. Methods Phys. Res.* B **267** 1856–61

[30] Fedoseyev V N, Huber G, Köster U, Lettry J, Mishin V I, Ravn H L and Sebastian V (ISOLDE Collaboration) 2000 The ISOLDE laser ion source for exotic nuclei *Hyperfine Interact.* **127** 409–16

[31] Babcock C *et al* 2016 Quadrupole moments of odd-A $^{53-63}$Mn: onset of collectivity towards $N = 40$ *Phys. Lett.* B **760** 387–92

[32] Rossel R E 2015 A distributed monitoring and control system for the laser ion source RILIS at CERN-ISOLDE *Master's Thesis* Hochschule RheinMain University of Applied Sciences Wiesbaden Rüsselsheim (https://cds.cern.ch/record/2093538)

[33] Chrysalidis K 2016 Resonance ionization spectroscopy of europium: the first application of the PISA at ISOLDE-RILIS *Master's Thesis* Johannes Gutenberg-Universität Mainz (http://cds.cern.ch/record/2227955)

[34] Rossel R E 2011 Programming of the wavelength stabilization for a titanium:sapphire laser using LabVIEW and implementation into the CERN ISOLDE RILIS measurement system *Bachelor's Thesis* Hochschule RheinMain University of Applied Sciences Wiesbaden Rüsselsheim (https://cds.cern.ch/record/1523721)

[35] Rothe S, Fedosseev V N, Kron T, Marsh B A, Rossel R E and Wendt K D A 2013 Narrow linewidth operation of the RILIS titanium: sapphire laser at ISOLDE/CERN *Nucl. Instrum. Methods Phys. Res.* B **317** 561–4

[36] Marsh B, Fedosseev V, Fink D, Day Goodacre T, Rothe S, Seliverstov M, Imai N, Sjodin M and Rossel R 2013 Suitability test of a high beam quality Nd: YVO$_4$ industrial laser for the ISOLDE RILIS installation *Technical Report* CERN-ATS-Note-2013-007 TECH CERN. Geneva. ATS Department (https://doi.org/10.17181/CERN.F65D.P3NR)

[37] Raeder S, Heggen H, Lassen J, Ames F, Bishop D, Bricault P, Kunz P, Mjøs A and Teigelhöfer A 2014 An ion guide laser ion source for isobar-suppressed rare isotope beams *Rev. Sci. Instrum.* **85** 033309

[38] Blaum K, Geppert C, Kluge H-J, Mukherjee M, Schwarz S and Wendt K 2003 A novel scheme for a highly selective laser ion source *Nucl. Instrum. Methods Phys. Res.* B **204** 331–5

[39] Schwellnus F 2010 Entwicklung von Ionenquellen zur Optimierung von Selektivität und Effizienz bei der resonanten Laserionisation *PhD Thesis* Johannes Gutenberg-Universität Mainz

[40] Fink D A 2014 Improving the selectivity of the ISOLDE resonance ionization laser ion source and in-source laser spectroscopy of polonium *PhD Thesis* Ruprecht-Karls-Universität Heidelberg (https://cds.cern.ch/record/1697785)

[41] Richter S 2015 Implementierung der Laserionenquellenfalle LIST bei ISOLDE und Validierung der Spezifikationen Effizienz und Selektivität *PhD Thesis* Johannes Gutenberg-Universität Mainz

[42] Fink D A *et al* 2013 First application of the laser ion source and trap (LIST) for on-line experiments at ISOLDE *Nucl. Instrum. Methods Phys. Res.* B **317** 417–21

[43] Fink D A *et al* 2015 In-source laser spectroscopy with the laser ion source and trap: first direct study of the ground-state properties of ^{217,219}Po *Phys. Rev.* X **5** 011018

[44] Penescu L, Catherall R, Lettry J and Stora T 2010 Development of high efficiency versatile arc discharge ion source at CERN ISOLDE *Rev. Sci. Instrum.* **81** 02A906

[45] Day Goodacre T 2017 Developments of the ISOLDE-RILIS for radioactive ion beam production and the results of their application in the study of exotic mercury isotopes *PhD Thesis* The University of Manchester (https://cds.cern.ch/record/2254839)

[46] Breitenfeldt M 2013 Q-values of mirror transitions for fundamental interaction studies *Tech. Proposal to the ISOLDE and Neutron Time-of-Flight Committee* CERN-INTC-2013-003; INTC-P-369 CERN. Geneva. ATS Department

[47] Rothe S 2012 An all-solid state laser system for the laser ion source RILIS and in-source laser spectroscopy of astatine at ISOLDE, CERN *PhD Thesis* Johannes Gutenberg-Universität Mainz (doi:10.17181/CERN.0HNZ.7Z6X) (http://cds.cern.ch/record/1519189)

[48] Rossel R E, Fedosseev V N, Marsh B A, Richter D, Rothe S and Wendt K D A 2013 Data acquisition, remote control and equipment monitoring for ISOLDE RILIS *Nucl. Instrum. Methods Phys. Res.* B **317** 557–60

[49] Day Goodacre T *et al* 2014 Developments for the ISOLDE resonance ionization laser ion source RILIS *ISOLDE Workshop and Users Meeting 2014 '50th Anniversary Edition' (CERN, Switzerland, 15–17 December 2014)* pp 4–5 Book of abstracts (http://indico.cern.ch/event/334117/book-of-abstracts.pdf)

[50] Fedoseyev V N 1999 The use of lasers for the selective ionization of radionuclei for RIB generation *AIP Conf. Proc.* **475** 296

[51] Köster U, Fedoseyev V N and Mishin V I 2003 Resonant laser ionization of radioactive atoms *Spectrochim. Acta* B **58** 1047–68

[52] Marsh B A, Fedosseev V N, Fink D A, Day Goodacre T, Rossel R E, Rothe S, Fedorov D V, Imai N, Seliverstov D M and Molkanov P 2014 RILIS applications at CERN/ISOLDE *Hyperfine Interact.* **227** 101–11

[53] Fedosseev V N, Marsh B A, Fedorov D V, Köster U and Tengborn E 2005 Ionization scheme development at the ISOLDE RILIS *Hyperfine Interact.* **162** 15–27

[54] Day Goodacre T, Chrysalidis K, Fedorov D V, Fedosseev V N, Marsh B A, Molkanov P L, Rossel R E, Rothe S and Seiffert C 2017 The identification of autoionizing states of atomic chromium for the resonance ionization laser ion source (RILIS) of the ISOLDE radioactive ion beam facility *Spectrochim. Acta* B **129** 58–63

[55] Day Goodacre T *et al* 2016 The ISOLDE RILIS in 2016, achievements, developments and future plans *ISOLDE Workshop and Users Meeting 2016 (CERN, Switzerland, 07–09 December 2016)* p 19 Book of abstracts (http://indico.cern.ch/event/561089/book-of-abstracts.pdf)

[56] Köster U *et al* 2000 Isomer separation of ^{70g}Cu and ^{70m}Cu with a resonance ionization laser ion source *Nucl. Instrum. Methods Phys. Res.* B **160** 528–35

[57] Zherikhin A N, Letokhov V S, Mishin V I, Muchnik M E and Fedoseyev V N 1983 Production of photoionic gallium beams through stepwise ionization of atoms by laser radiation *Appl. Phys.* B **30** 47–52

[58] Day Goodacre T, Fedorov D, Fedosseev V N, Forster L, Marsh B A, Rossel R E, Rothe S and Veinhard M 2016 Laser resonance ionization scheme development for tellurium and germanium at the dual Ti:Sa-dye ISOLDE RILIS *Nucl. Instrum. Methods Phys. Res.* A **830** 510–4

[59] Jading Y *et al* 1997 Production of radioactive Ag ion beams with a chemically selective laser ion source *Nucl. Instrum. Methods Phys. Res.* B **126** 76–80

[60] Muchnik M L, Orlov Y V, Parshin G D, Chernyak E Y, Letokhov V S and Mishin V I 1983 Generation of an indium ion beam by selective multistage laser photoionization of atoms *Sov. J. Quantum Electron.* **13** 1515–7

[61] Dillmann I *et al* 2002 Selective laser ionisation of $N \geqslant 82$ indium isotopes: the new r-process nuclide ^{135}In *Eur. Phys. J.* A **13** 281–4

[62] Scheerer F, Albus F, Ames F, Kluge H-J and Trautmann N 1992 An efficient excitation scheme for resonance ionization of tin in a laser ion source *Spectrochim. Acta* B **47** 793–7

[63] Liu Y *et al* 2006 Laser ion source tests at the HRIBF on stable Sn, Ge and Ni isotopes *Nucl. Instrum. Methods Phys. Res.* B **243** 442–52

[64] Zuzikov A D, Mishin V I and Fedoseev V N 1988 Laser resonance photoionization spectroscopy of excited and autoionization atomic states of rare-earth elements: III. Neodimium *Opt. Spectrosc.* **64** 287–8

[65] Mishin V I *et al* 1987 Resonance photoionization spectroscopy and laser separation of ^{141}Sm and ^{164}Tm nuclear isomers *Opt. Commun.* **61** 383–6

[66] Fedoseev V N, Mishin V I, Vedeneev D S and Zuzikov A D 1991 Laser resonant photoionization spectroscopy of highly excited and autoionization states of terbium atoms *J. Phys. B: At. Mol. Opt. Phys.* **24** 1575–83

[67] Mishin V I, Sekatski S K, Fedoseev V N, Buyanov N B, Letokhov V S, Alkhazov G D, Barzakh A E, Denisov V P, Ivanov V S and Chubukov I Y 1987 Ultrasensitive resonance laser photoionization spectroscopy of the radioisotope chain $^{157-172}$Tm produced by a proton accelerator *Sov. Phys.—JETP* **66** 235–42

[68] Marsh B A, Fedosseev V N and Kosuri P 2006 Development of a RILIS ionization scheme for gold at ISOLDE, CERN *Hyperfine Interact.* **171** 109–16

[69] Day Goodacre T *et al* 2017 RILIS-ionized mercury and tellurium beams at ISOLDE CERN *Hyperfine Interact.* **238** 41

[70] Andreyev A N *et al* 2002 Nuclear spins, magnetic moments and α-decay spectroscopy of long-lived isomeric states in ^{185}Pb *Eur. Phys. J.* A **14** 63–75

[71] Cocolios T E *et al* 2008 Resonant laser ionization of polonium at RILIS-ISOLDE for the study of ground- and isomer-state properties *Nucl. Instrum. Methods Phys. Res.* B **266** 4403–6

[72] Rothe S *et al* 2013 Measurement of the first ionization potential of astatine by laser ionization spectroscopy *Nat. Commun.* **4** 1835

[73] Blaum K, Dilling J and Nörtershäuser W 2013 Precision atomic physics techniques for nuclear physics with radioactive beams *Phys. Scr.* T **152** 014017

[74] Fedosseev V N, Fedorov D V, Horn R, Huber G, Köster G, Lassen J, Mishin V I, Seliverstov M D, Weissman L and Wendt K 2003 Atomic spectroscopy studies of short-lived isotopes and nuclear isomer separation with the ISOLDE RILIS *Nucl. Instrum. Methods Phys. Res.* B **204** 353–8

[75] Andreyev A N *et al* 2010 New type of asymmetric fission in proton-rich nuclei *Phys. Rev. Lett.* **105** 252502

[76] Wolf R *et al* 2012 On-line separation of short-lived nuclei by a multi-reflection time-of-flight device *Nucl. Instrum. Methods Phys. Res.* A **686** 82–90

[77] Seliverstov M D *et al* 2013 Charge radii of odd-A $^{191–211}$Po isotopes *Phys. Lett.* B **719** 362–6

[78] Weissman L *et al* 2002 Magnetic moments of ^{68}Cu^{g,m} and ^{70}Cu^{g,m1,m2} nuclei measured by in-source laser spectroscopy *Phys. Rev.* C **65** 024315

[79] Stone N J, Köster U, Rikovska Stone J, Fedorov D V, Fedoseyev V N, Flanagan K T, Haas M and Lakshmi S 2008 The magnetic dipole moments of ^{58}Cu and ^{59}Cu by in-source laser spectroscopy *Phys. Rev.* C **77** 067302

[80] Flanagan K T *et al* 2009 Nuclear spins and magnetic moments of ^{71,73,75}Cu: inversion of $\pi 2p_{3/2}$ and $\pi 1f_{5/2}$ Levels in ^{75}Cu *Phys. Rev. Lett.* **103** 142501

[81] Barzakh A E *et al* 2017 Changes in mean-squared charge radii and magnetic moments of $^{179–184}$Tl measured by in-source laser spectroscopy *Phys. Rev.* C **95** 014324

[82] De Witte H *et al* 2007 Nuclear charge radii of neutron-deficient lead isotopes beyond $N = 104$ midshell investigated by in-source laser spectroscopy *Phys. Rev. Lett.* **98** 112502

[83] Seliverstov M D *et al* 2009 Charge radii and magnetic moments of odd-A $^{183-189}$Pb isotopes *Eur. Phys. J.* A **41** 315–21

[84] Sauvage J *et al* 2009 Nuclear structure of ^{189}Tl states studied via $\beta+/$EC decay and laser spectroscopy of $^{189m+g}$Pb *Eur. Phys. J.* A **39** 33–48

[85] Barzakh A *et al* (On behalf of Leuven-Gatchina-ISOLDE-Mainz-Manchester-York and Windmill-ISOLTRAP-RILIS collaboration) 2016 Shape staggering, shape coexistence and beta-delayed fission in bismuth isotopes studied by in-source laser spectroscopy (IS608) *ISOLDE Workshop and Users Meeting 2016 (CERN, Switzerland, 07–09 December 2016)* p 2 Book of abstracts (http://indico.cern.ch/event/561089/book-of-abstracts.pdf)

[86] Cocolios T E *et al* 2011 Early onset of ground state deformation in neutron deficient polonium isotopes *Phys. Rev. Lett.* **106** 052503

[87] Seliverstov M D *et al* 2014 Electromagnetic moments of odd-A $^{193–203,211}$Po isotopes *Phys. Rev.* C **89** 034323

[88] Andreyev A N *et al* (Windmill Collaboration) 2014 *β-Delayed Fission and In-Source Laser Spectroscopy in the Lead Region Report* CERN-INTC-2014-013; INTC-SR-029 CERN. Geneva. ISOLDE and Neutron Time-of-Flight Experiments Committee

[89] Bonn J, Huber G, Kluge H-J, Kugler L and Otten E W 1972 Sudden change in the nuclear charge distribution of very light mercury isotopes *Phys. Lett.* B **38** 308–11

[90] Kühl T, Dabkiewicz P, Fischer H, Kluge H-J, Kremmling H and Otten E-W 1977 Nuclear shape staggering in very neutron-deficient Hg isotopes detected by laser spectroscopy *Phys. Rev. Lett.* **39** 180–3

[91] Ulm G *et al* 1986 Isotope shift of ^{182}Hg and an update of nuclear moments and charge radii in the isotope range ^{182}Hg–^{206}Hg *Z. Phys.* A **325** 247–59

[92] Wallmeroth K *et al* 1987 Sudden change in the nuclear distribution of very light gold isotopes *Phys. Rev. Lett.* **58** 1516–9

[93] Cheal B *et al* 2009 Laser spectroscopy of niobium fission fragments: first use of optical pumping in an ion beam cooler buncher *Phys. Rev. Lett.* **102** 222501

[94] Rothe S 2013 Preparation of negative ion beams for the determination of the electron affinity of polonium and astatine by laser photodetachment *Letter of Intent* CERN-INTC-2013-037; INTC-I-148 CERN, Geneva, ISOLDE and Neutron Time-of-Flight Experiments Committee (https://doi.org/10.17181/CERN.YJ9E.K5F5)

[95] Rothe S 2016 Determination of the electron affinity of astatine and polonium by laser photodetachment *Proposal* CERN-INTC-2016-017; INTC-P-462 CERN, Geneva, ISOLDE and Neutron Time-of-Flight Experiments Committee (https://doi.org/10.17181/CERN.OZFJ.5MKK)

[96] Rothe S *et al* 2017 Laser photodetachment of radioactive ^{128}I^{-} *J. Phys. G: Nucl. Part. Phys.* submitted

[97] Flanagan K T *et al* 2013 Collinear resonance ionization spectroscopy of neutron-deficient francium isotopes *Phys. Rev. Lett.* **111** 212501

[98] Garcia Ruiz R F 2017 Exploring the feasibility of production and laser spectroscopy experiments of exotic silicon isotopes *Letter of Intent* CERN-INTC-2017-026; INTC-I-176 CERN. Geneva. ISOLDE and Neutron Time-of-Flight Experiments Committee

[99] Lettry J, Catherall R, Köster U, Georg U, Jonsson O, Marzari S and Fedosseev V 2003 Alkali suppression within laser ion-source cavities and time structure of the laser ionized ion-bunches *Nucl. Instrum. Methods Phys. Res.* B **204** 363–7

[100] Mishin V I, Malinovsky A L and Mishin D V 2009 Resonant ionization laser ion source (RILIS) with improved selectivity achieved by ion pulse compression using in-source time-of-flight technique *AIP Conf. Proc.* **1104** 207

[101] Seiffert C and Ballof J 2017 Extraction of refractory elements by laser induced breakup and ionisation of Molybdenum Carbonyls *Letter of Intent* CERN-INTC-2017-031; INTC-I-178 CERN, Geneva, ISOLDE and neutron Time-of-Flight Experiments Committee (https://cds.cern.ch/record/2241995)

3.3 Laser system

The laser system of the Resonance Ionization Laser Ion Source at ISOLDE, described in detail in **Publication 1**, is the most versatile of all laser ion sources in respect to wavelength range coverage, achievable output power and operation conditions. It is comprised of a set of tunable solid-state Ti:sapphire and dye lasers. All of these tunable lasers are pumped by fixed-frequency DPSS (Diode Pumped Solid State) lasers at 532 nm with repetition rates of 10 kHz and varying pulse lengths. A 40 W, fixed frequency laser at 532 nm for non-resonant ionization into the continuum is also available, ensuring efficient ionization wherever resonant ionization steps are unknown, unavailable or inefficient. The overall wavelength spectrum which can be covered by the combined laser system is schematically presented in Figure 3.3. A brief introduction into the tunable lasers is given below.
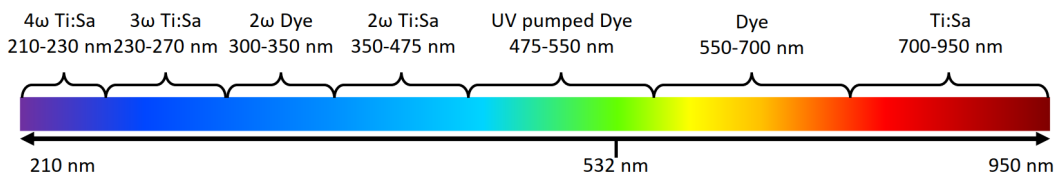

4ω Ti:Sa	3ω Ti:Sa	2ω Dye	2ω Ti:Sa	UV pumped Dye	Dye	Ti:Sa
210-230 nm	230-270 nm	300-350 nm	350-475 nm	475-550 nm	550-700 nm	700-950 nm

Figure 3.3: *Spectral coverage provided by the RILIS laser system.*

3.3.1 Dye Lasers

The oldest widely tunable light sources are dye lasers [4]. Based on fluorescing molecular complexes in solvents such as ethanol, a broad spectral range from the blue to deep infra red (IR) can be covered. Before the development of solid-state lasers, the pump sources were gas lasers, such as excimer or copper-vapor (CV) lasers. They offer light in the UV to green wavelength range. Depending on the specific dye, lasing efficiencies of up to 40 % can be achieved. The first stage consists of the resonator, in which lasing is achieved and the wavelength is selected via a grating. The light can be subsequently amplified further in non-wavelength selective amplification stages seeded by the initially produced laser light. Due to the high gain of the laser medium, even for single-pass amplification high output powers can be achieved. Through frequency conversion into

higher harmonics, UV light can be generated.

The dye lasers used at the ISOLDE-RILIS are commercial Sirah Credo dye lasers with a typical linewidth of 15 GHz. They have one oscillator and one amplifier dye cell and are pumped by a 5 ns long pulse at 10 kHz repetition rate by an IS-Series Edgewave laser. The Nd:YAG pump laser is standardly used with its output at 532 nm, generated by internal frequency doubling. For some wavelengths, UV pumping is required, for which a third harmonic generation unit can be installed and an output at 355 nm can be generated for pumping the dye lasers.

During standard operation, the dye lasers are used with 532 nm pumping, covering a wavelength range from 550-700 nm and the corresponding frequency doubled range of 275-350 nm. Dyes for these ranges show high efficiencies. They also offer comparatively long life times, meaning that the time between required dye changes can be as long as 4-5 days (for continuous operation). For on-line operation, during which long-term, low maintenance and stable power output is required, this is less optimal than running with solid-state lasers. Nevertheless, the ease of setup, high power output and their wavelength capabilities render the dye lasers a useful and irreplaceable component of the RILIS installation.

UV pumping at 355 nm is not used frequently. If possible, schemes comprising wavelengths in the range of 470-550 nm are avoided. This range, limited by the frequency doubled Ti:sapphire and the fundamental dye laser (pumped at 532 nm), can only be covered by frequency mixing, with a sophisticated set up and often yielding low efficiencies (see e.g. [73]) or dyes absorbing the UV light. UV induced degradation of the dye is the main reason for efficiency loss, sometimes within only a few hours of operation. For on-line operation these dyes are therefore avoided, as round-the-clock interventions would be required. As will be shown in subsection 3.3.5, Raman shifting the frequency doubled Ti:sapphire wavelength range would allow parts of this spectral range to be covered.
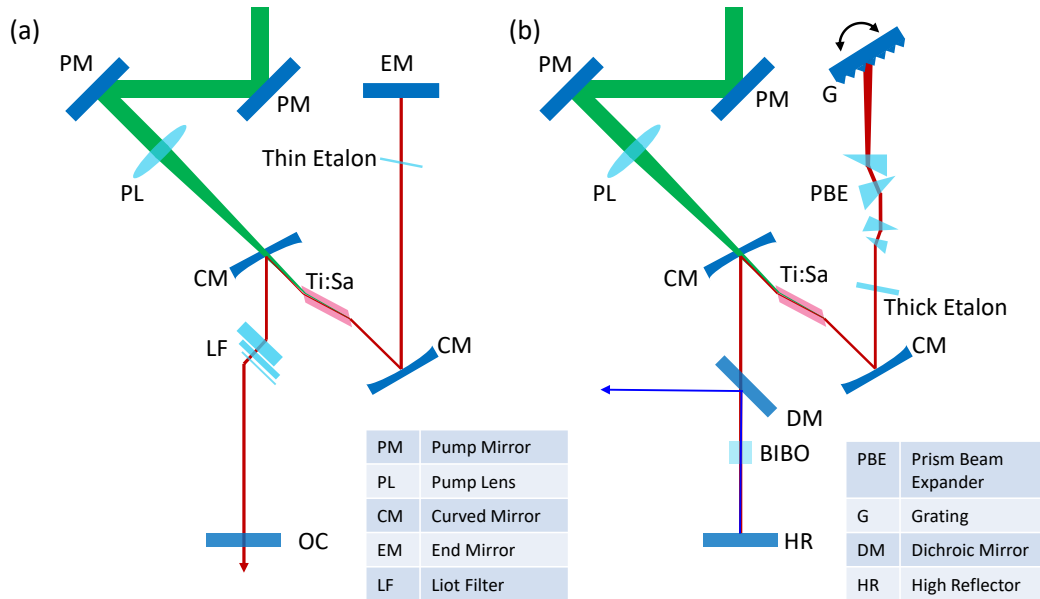
Figure 3.4: *(a) Z-cavity Ti:sapphire laser used at the ISOLDE RILIS. (b) Grating Ti:sapphire layout as used for Dy in-source spectroscopy. The laser was intra-cavity frequency-doubled and the linewidth narrowed by introducing a thick etalon.*

3.3.2 Ti:sapphire Laser

The Ti:sapphire lasers (see Figure 3.4) used at RILIS are based on the **Z-cavity** design from Mainz (see e.g. [20]). They have been continuously improved ever since they were first developed. When pumped with green (532 nm) light, the titanium doped sapphire crystals ($Ti^{3+}:Al_2O_3$) emit light in a wavelength range of 670-1070 nm. The peak of the emittance curve lies around 800 nm and typically lasing in the Z-resonators is achieved in the range of 700-950 nm. Wavelength-specific coatings on the cavity mirrors together with frequency selective elements such as a birefringent (Lyot) filter and etalon are used for tuning of the lasers. The linewidth of the output light is $\approx$ 5 GHz (for a 0.3 mm thick etalon), measured with a LM-007 *(CLUSTER LTD Moscow)* wavelength meter. The pumping is provided by frequency doubled Nd:YAG lasers at 10 kHz repetition rate. Different pump lasers are in use in the various laboratories utilizing these Ti:sapphire lasers. At RILIS, Photonics Industries DM-60 pump lasers with a pulse length of 200 ns and a non-Gaussian beam shape have been used since

the first installation of the Ti:sapphire lasers. Recently, they are being replaced by new pump lasers, the Innolas Nanio, with pulse lengths of $30-40$ ns. The Gaussian beam profile of these pump lasers lowers the lasing threshold from ≈ 6 W required with the PX to now ≈ 4.5 W, as shown in Figure 3.5. Some drawbacks have been observed in the wavelength tunability and are under investigation. Additionally, the shorter pulse length leads to higher peak intensities of the laser pulse. This has been found to cause problems in non optimal air quality laboratory environments, increasing the risk of burning the Ti:sapphire crystal surface and in some cases even the interior structure of the crystals.
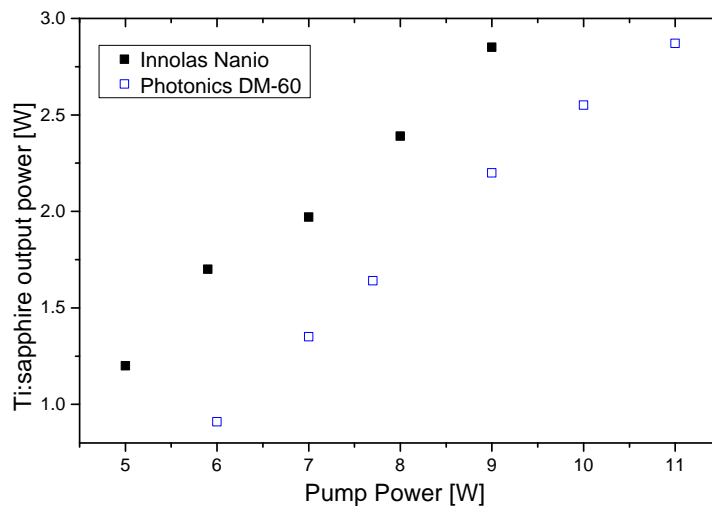

Figure 3.5: *Pump power versus generated Ti:sapphire laser power output for the Innolas Nanio and the Photonics DM-60 pump lasers. Both data sets were taken with a bare Z-cavity (no frequency selective elements) with a broadband mirrorset (0000).*

Another Ti:sapphire laser type is using a **continuously tunable grating cavity** as shown in Figure 3.4. A prism beam expander is installed in front of the grating. The bandwidth of the grating laser is dependent on the expansion factor, with lower expansion leading to higher bandwidth. The expander used in the RILIS grating laser leads to a bandwidth of ~ 5 GHz (measured with the LM-007), similar to the Z-cavity. It is a laser which is suited well for ionization scheme development when continuous tunability over a large spectral range is required.

For both cavity designs, intra cavity frequency doubling has become the new standard
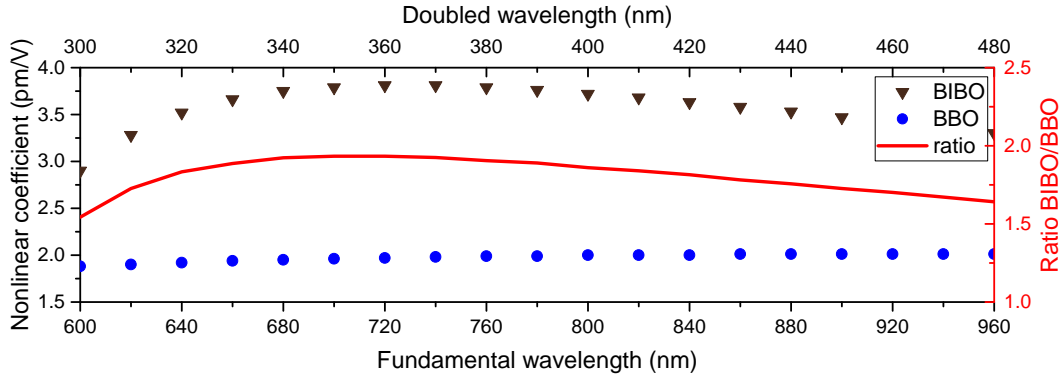

Figure 3.6: *Comparison of the nonlinear coefficient, directly proportional to the conversion efficiencies, for BiBo and BBo crystals. It is evident that wherever possible, BiBO should be used for higher power output.*

for generating the blue spectral range at the ISOLDE-RILIS. Prior to the efforts of the work presented in this thesis, attempts had been made to deliver stable power output, but were not successful. The reason was the use of bismuth borate (BiB_3O_6) crystals for SHG which require stable temperature conditions and careful tuning when used inside the resonator. The nonlinear coefficient of BiBO is at least 1.5 times bigger than the one for BBO. The same holds true for the conversion efficiency which scales linearly (see Figure 3.6). The main disadvantage is therefore the reduced temperature tolerance, described in detail e.g. in [74]. Nevertheless, since the beam shape of the blue light is Gaussian, the efforts were repeated during the work for the thesis presented here. In order to ensure stable power output, the laboratory temperature has to be stable during operation, so turning on/off any additional nearby pump lasers can lead to drifts which need correcting for. When setting up the IC doubling with BiBO, the crystal must be left to reach a stable temperature, since there is some self-absorption of the generated blue light, increasing the internal temperature. Once this is the case, the phase-matching angle requires retuning. After repeating this process a few times, the power output is usually stable. Active heating or cooling of the crystal would greatly simplify this procedure and would in addition make tuning the phase-matching angle unnecessary, since the temperature could be adjusted to match the wavelength (at 800 nm $0.15°$ per

10 degrees Kelvin).

3.3.3 Narrow Linewidth Intra-Cavity Frequency-Doubled Grating Ti:sapphire Laser

For in-source laser spectroscopy, which will be explained in more detail in chapter 5, or for isomer selectivity (used e.g. for indium decay spectroscopy [75]), the linewidth of the Ti:sapphire laser in the Z-cavity configuration is reduced by insertion of a 6 mm thick etalon, usually an uncoated YAG substrate [76]. The linewidth is thus narrowed down to about 800 MHz. The mode of the thick etalon is 0.3 cm^{-1} wide, and the spacing between the modes is 0.4 cm^{-1} . By scanning the thin and the thick etalon in a synchronous way, a continuous tuning range of up to 1.5 cm^{-1} can be achieved.

For in-source laser spectroscopy of dysprosium (see section 5.5) performed in the scope of this thesis, the grating Ti:sapphire laser configuration was used for the first time with an additional thick etalon (see Figure 3.4). The setup enabled quick switching between narrower linewidth (for spectroscopy) and broader linewidth (for optimal ion beam production) operation, simply by inserting or removing the thick etalon. After insertion of the thick etalon, first a scan of the grating was performed. The resulting data containing the position of the grating versus the output wavelength was fitted with a linear curve. Afterwards, a position closely matching the required transition wavelength was chosen. The thick etalon was then scanned, and set to operate in the branch next to the flashpoint (normal incidence orientation) of the etalon for optimal power output whilst ensuring maximum stability. Using the control software developed for the dual etalon Z-cavity (see [76, 20]), the grating position was re-adjusted whilst scanning the thick etalon, leading to a tuning range of > 2 cm^{-1} . The main drawback during the use of the grating Ti:sapphire laser, was the large hysteresis of the rotation stage which the grating was mounted on. Depending on the scan direction, there was a horizontal offset between the linear curves for the grating calibration. This lead to loss of stabilization, when changing the wavelength scan direction.

For future spectroscopy investigations into a prism beam expander with a higher expan-

sion factor may be preferable. This would enhance the tunability, at the cost of power output. This is usually acceptable as the spectroscopic transition often has a high transition strength and deliberate attenuation of the laser power is performed in any case to avoid saturation broadening.

3.3.4 Construction and Characterization of a Seeded Ti:sapphire Ring Cavity Laser

For the purpose of Doppler-free in-source 2-photon spectroscopy, outlined in chapter 6, narrow linewidths ($<$100 MHz) and high output power are required. For this purpose, a new laser was built and commissioned in the scope of this thesis: A ring cavity, seeded by a continuous wave (CW) laser, was constructed on a breadboard using the layout depicted in Figure 3.7. The design is a standard bow-tie cavity and was optimized for compactness, since the RILIS laser laboratory is restricted with respect to available space. The cavity design and operational parameters are based on previous designs from Mainz/Jyväskylä [77, 78].

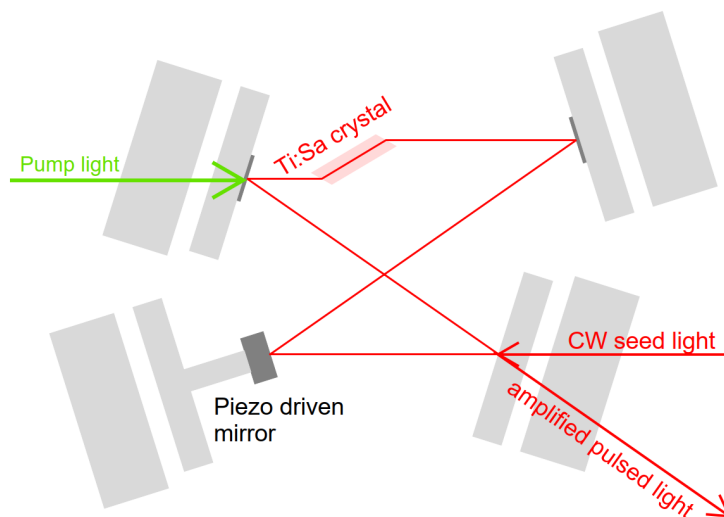The compact design lead to a decrease of the resonator length. Since there are no

Figure 3.7: *Schematic layout of the miniaturized ring cavity. The correctly scaled pdf can be used as template for building the cavity up on a breadboard.*

frequency selective elements, the laser linewidth is directly coupled to the resonator length. By measuring the pulse length of the cavity output the time-bandwidth product TBP of linewidth $\Delta\nu$ and pulse width τ_P, $TBP = \Delta\nu \times \tau_P$, can be used for calculating the linewidth. Assuming a Gaussian or a sech^2 time profile, the TBP is 0.44 or 0.315, respectively. The pulse length (FWHM) measured for the compact ring resonator was $\tau_P =$18 ns. Depending on the time profile, this leads to a linewidth of 24.4 or 17.5 MHz. Since it was not possible to deconvolute the lineshape of the laser pulse, the average between a Gaussian and sech^2 TBP was taken and leads to an estimated linewidth of 21 MHz.

For stabilization of the cavity a *TEM Messtechnik LaseLock* was used, as it has been shown to be suitable for locking the laser resonator. Additional, passive damping in the form of Sorbothane isolators was required between the breadboard and the laser table to achieve reliable locking conditions, even under high noise levels introduced e.g. by the dye laser circulators.

The seed efficiency with a broadband mirrorset (0000) was determined by using a low-power seed (2 mW) from a widely tunable CW seed laser (*M-Squared Laser Systems SolsTiS*). The lower and upper seed limits were set by the locking of the CW laser and not the ring cavity. Results for the total output power and seed efficiency for a pump power of 11.5 W are shown in Figure 3.8. The efficiency was calculated the same way as described in the thesis by V. Sonnenschein [79]:

$$\text{Seed efficiency} = \frac{P_{locked}}{P_{free}} - 1. \tag{3.1}$$

P_{locked} was the power with the LaseLock stabilizing the cavity, resulting in light circulating uni-directionally inside the cavity. P_{free} was the power output without locking the cavity, measured in the same output direction as the locked laser light. Comparison to results obtained in [79] shows a much flatter efficiency profile and a significant improvement in efficiency at the edges of the tuning range. A second cavity, identical to the one presented here has been installed at the CRIS laser laboratory in ISOLDE, due to the usefulness and simplicity of the set up.
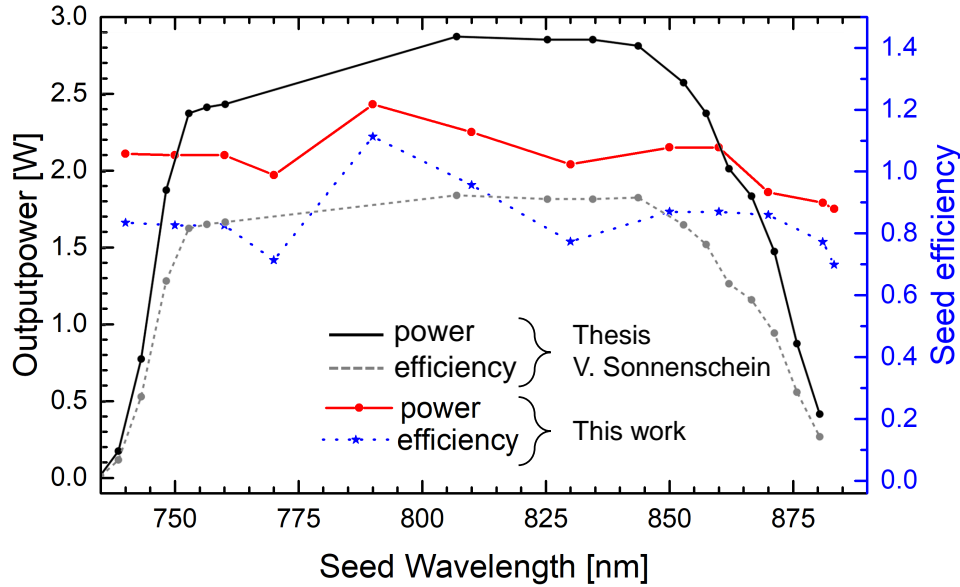
Figure 3.8: *Comparison of power output and seed efficiency of the ring cavity from this work (red and blue lines) and the data from [79]. For this thesis a pump power of 11.5 W and a seed power of 2 mW were used. For the data from [79] a seed power of 15 mW was used but no information on pump power is given.*

3.3.5 Raman Lasers - Expanding the Ti:sapphire Laser Spectral Range

As mentioned in subsection 3.3.1, the spectral gap between 470 nm and 550 nm is currently one of the drawbacks of the RILIS laser system. Raman lasers have become increasingly common in recent years and Raman crystals for stimulated Raman scattering are commercially available. During the work of this thesis, a novel approach at bridging the spectral gap, so far only accessible by UV pumped dyes, was taken. A diamond crystal was used for shifting the blue light generated by IC doubling of a Ti:sapphire laser. Even though the system development is not yet finished, promising initial results were obtained and show the wavelength tunability alongside the linewidth dependencies on the pump laser, summarized in **Publication 2**. The approach taken in this work utilizes blue pump light. As was shown in section 2.5, the wavelength shift in the blue is smaller than in the red or infrared. Nevertheless, it was chosen for simplicity,

offering the advantage of higher gain and the additional convenience of direct conversion to visible wavelengths.

In later iterations of the cavity design, it should be considered to utilize the Raman crystal in an intra-cavity fashion, doubling it directly with a non-linear crystal matched to the Raman and not the Ti:sapphire light. Since the power density in the closed Ti:sapphire resonator is several times higher than the power of the IC doubled blue light, single or double pass through the diamond should generate enough power to efficiently frequency double the Raman shifted light. This way, using diamond at e.g. 900 nm, the first Stokes would be at 1120 nm. Phasematching the angle of BIBO ($172°$), this would lead to light at 560 nm. The resulting light would be shifted 80 nm further, compared to the first Stokes of Raman shifted IC doubled light. This is schematically shown in Figure 3.9.
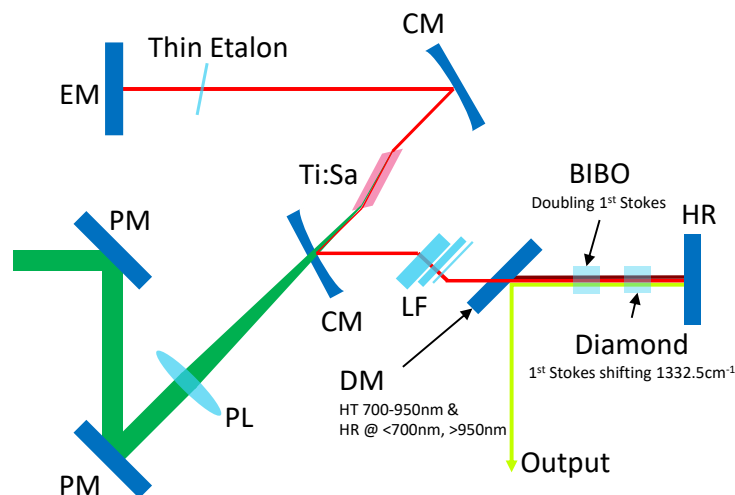

Figure 3.9: *Proposed possible configuration of intra-cavity shifting the Ti:sapphire fundamental light with a Raman medium. The resulting 1st Stokes can be subsequently frequency doubled with e.g. a BiBO crystal.*

The task of building and commissioning of such a system lies outside of the aim of the work presented here. Nevertheless, the groundwork has been laid out for a new solid-state laser system, further improving the versatility and operational capacities of the ISOLDE-RILIS.

3.4 <u>Publication 2</u> - Continuously tunable diamond Raman laser for resonance laser ionization

The following publication is a feasibility study and presents the first results obtained for a novel Raman laser for RILIS. Since the linewidth behavior of the Stokes compared to the pump laser is not well established, the focus of the work was on developing a set up in which the pump linewidth is matched by the Stokes output. The publication will be of high interest not only for the Raman laser community, but will have a great impact on the wavelength generation capacities for all solid-state laser ion sources around the world. It was accepted for publication in Optics Letters and published as editor's pick.

Contribution: I pursued the idea of shifting the Ti:sapphire spectral range, after reading about Raman lasers, seeing the possible advantages for RILIS applications. I designed and built the cavity presented in the publications, performed the measurements, analyzed the data and finally prepared the manuscript.

Optics Letters

Continuously tunable diamond Raman laser for resonance laser ionization

Katerina Chrysalidis,[1,2,*] Valentin N. Fedosseev,[1] Bruce A. Marsh,[1] Richard P. Mildren,[3] David J. Spence,[3] Klaus D. A. Wendt,[2] Shane G. Wilkins,[1] and Eduardo Granados[1]

[1]CERN, 1217 Geneva, Switzerland
[2]Institut für Physik, Johannes Gutenberg-Universität, 55099 Mainz, Germany
[3]MQ Photonics Research Centre, Macquarie University, NSW 2109, Australia
*Corresponding author: katerina.chrysalidis@cern.ch

We demonstrate a highly efficient, tunable, ~5 GHz linewidth diamond Raman laser operating at 479 nm. The diamond laser was pumped by a wavelength-tunable intra-cavity frequency-doubled titanium sapphire (Ti:Sapphire) laser operating at around 450 nm, at a repetition rate of 10 kHz with a pulse duration of 50 ns. The Raman resonator produced a continuously tunable output with high stability, high conversion efficiency (28%), and beam quality ($M^2 < 1.2$). We also demonstrate that the linewidth and tunability of the pump laser is directly transferred to the Stokes output. Our results show that diamond Raman lasers offer great potential for spectroscopic applications, such as resonance laser ionization, in an all-solid-state platform.   © 2019 Optical Society of America

https://doi.org/10.1364/OL.44.003924

At the CERN-ISOLDE Radioactive Ion Beam (RIB) Facility, a large variety of (radioactive) isotopes are produced with the isotope separator on-line (ISOL) technique in order to study their fundamental nuclear and atomic properties [1]. The ISOLDE Resonance Ionization Laser Ion Source (RILIS) is the most selective of the ion sources. It is based on stepwise resonance excitation and ionization of atoms, making use of element-specific energy level configurations [2]. For efficient ionization, the linewidths are matched to the Doppler-broadening of the atomic lines (including fine and hyperfine structure splittings), usually lying in the range of 5–15 GHz (see [2]). Additionally, in order to account for the various atomic configurations, a broad spectral coverage across the UV to IR range is required. Laser systems operating at a repetition rate of 10 kHz are used to ensure that each atom is subject to ionization before exiting the hot cavity [3]. The required laser power depends on the chosen atomic transition and can range from mW to W.

Currently, the strategy used at the ISOLDE RILIS that meets all the aforementioned specifications comprises the use of a dual-laser system with nanosecond titanium sapphire (Ti:Sapphire) and dye lasers. The spectral range is increased by frequency-mixing stages capable of generating virtually any

wavelength between 210–950 nm (see [2,4]). Even though this solution meets all the specifications, it can require high operational costs. Especially, UV-pumped dyes require frequent changes (up to once every 10 h) for maintaining adequate power output. This is detrimental for the operation of the experimental facility over many days or weeks. Therefore, a strong interest exists in finding a simple and compact all-solid-state laser alternative that can provide a widely tunable output across the spectrum at the required repetition rate.

A potential solution relies on the use of stimulated Raman scattering (SRS) in combination with tunable Ti:Sapphire lasers to access the spectrum traditionally occupied by UV-pumped dye lasers (in particular, the 475–540 nm band). During the last five decades, SRS, resulting from a photon–phonon inelastic interaction in Raman-active media [5], has established itself as a versatile method to generate wavelengths that are otherwise difficult to produce. When compared to optical parametric oscillators (OPOs) and other nonlinear (often tedious and inefficient) conversion techniques like frequency mixing (see e.g., [6]), Raman lasers are simple to construct, do not require management of phase matching, and can be operated at any chosen repetition rate [7].

A large number of Raman-active materials have been investigated to date, showing stark differences in terms of wavelength shift, transparency, phonon-dephasing time, or Raman gain, to name a few [8,9]. Traditionally, the attention has been focused on the enhancement of the conversion efficiency and wavelength coverage. Three main factors led to the choice of diamond in the work presented here: the large wavelength shift of 1332.5 cm^{-1}, which converts the 450 nm pump laser directly to 479 nm in a single Stokes shift; its high Raman gain at visible wavelengths (50 cm/GW at 532 nm [10]); and ultrabroad transparency from the mid-IR [11] down to deep UV wavelengths [12]. With the advent of the continuous-wave (CW) narrow-linewidth single-longitudinal-mode (SLM) diamond Raman laser, detailed experimental studies regarding the emission linewidth of Raman converters have been published [13–15]. However, studies regarding the linewidth characteristics of highly efficient nanosecond broadband diamond Raman lasers, which are suitable candidates for resonance laser ionization experiments, remain scarce in the literature.

The aim of the present study is to demonstrate that the output of broadly tunable solid-state lasers can be efficiently Raman shifted to new wavelengths maintaining the pump laser linewidth. In our experiments, we employed a widely tunable, frequency-doubled Ti:Sapphire laser at 450 nm for generating the first Stokes order inside a diamond at around 479 nm. We demonstrate a continuously tunable output with a conversion efficiency of >28% while maintaining a constant linewidth of ~5 GHz in the 475–500 nm spectral range.

Figure 1 shows a schematic diagram of the experimental setup. The pump light at 450 nm was provided by an intracavity frequency-doubled Ti:Sapphire laser (Z-cavity layout; for more details see [16]). It was pumped by the second harmonic of a Q-switched Nd:YAG laser (Innolas Nanio 532-20-V) producing up to 18 W of 532 nm light at 10 kHz repetition rate, of which 8 W were used. The resulting pulse length of the Ti:Sapphire is 50 ns long, with a smooth temporal profile of Gaussian shape. The second harmonic of the Ti:Sapphire laser was efficiently produced by intracavity frequency-doubling, and exhibited a TEM_{00} Gaussian mode with an $M^2 < 1.3$. The efficiency of second-harmonic generation was optimized by placing the crystal in one of the arms of the Ti:Sapphire resonator with a relatively small beam diameter. Frequency selection and tunability is obtained by using a birefringent filter and a thin (0.3 mm) Fabry–Perot etalon while frequency conversion is achieved within a 6 mm thick bismuth borate (BiB_3O_6) crystal.

With this configuration, the system was capable of producing approximately 1.2 W of average power at 450 nm. This output was focused into the diamond crystal by a 100 mm focal length lens, producing a waist of 57 ± 5 μm in diameter. The linewidth (FWHM) of the 450 nm light was measured with a high-precision laser radiation spectrum analyzer and wavelength meter LM-007 *(CLUSTER LTD Moscow)* as 6.5 ± 0.9 GHz. This linewidth is about a factor of $\sqrt{2}$ wider than the fundamental linewidth of the Ti:Sapphire laser.

A synthetic diamond crystal (low-birefringence, low-nitrogen, chemical vapor deposition (CVD)-grown single crystal, Element Six Ltd.) with dimensions of 8 mm (length) × 2 mm (width) × 2 mm (height), plane-cut for beam propagation along the ⟨110⟩ axis, was selected as the Raman laser medium. In order to access the highest Raman gain coefficient, the fundamental and Stokes beams were copolarized along the ⟨111⟩ axis [17] by means of a $\lambda/2$-plate placed before the cavity (see Fig. 1). In order to avoid any potential etalon effects introduced by the uncoated Raman medium [18], the diamond was placed at an angle of 10° with respect to the resonator mode. Incidence at Brewster's angle was
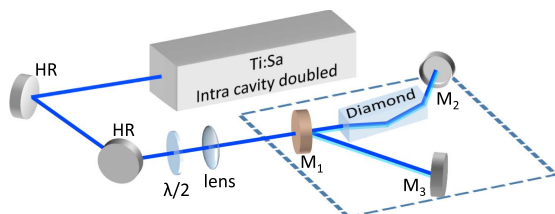
also tested; however, this arrangement produced an ellipticity that significantly decreased the available pump intensity, therefore increasing the lasing threshold.

The diamond laser resonator was designed specifically for the pump pulse energy available (~65 μJ). It is a stable cavity composed of three curved mirrors (M_1, M_2, and M_3). The reported output power is the sum of the leakages through the mirrors and all four reflections off of the diamond crystal, thereby representing the single-beam power that could be obtained using low-transmission mirrors, antireflection coating on the diamond surfaces, and a single output coupler. The total output coupling was estimated to be approximately 63%. Mirror M_1 is a dichroic curved mirror with a radius of curvature (ROC) of 500 mm, a transmission of 60% at 450 nm, and >90% reflectivity at 479 nm. Mirrors M_2 and M_3 are broadband high-reflecting mirrors (>99%) with ROCs of 24 mm and 150 mm, respectively.

The external resonator employed in the present study differs substantially from the previously reported extracavity nanosecond diamond Raman lasers [17,19,20], where the pulse energy allowed for the use of larger resonator waist sizes for efficient laser operation. In our particular case, the pulse energy is comparatively low, while the pump pulse duration is several times longer. These facts enable the use of a stable cavity with a small waist and compact overall size.

The distances between the three curved mirrors was systematically adjusted in order to maximize the Stokes output power, obtaining a well-matched cavity waist of ~60 μm in diameter ($1/e^2$). The optimal distance between M_1 and M_2 was found to be approximately 48 mm (not including the refractive index of the diamond crystal), whereas the distance between M_1 and M_3 was set to 125 mm. The total round trip time of the cavity was estimated to be 1.28 ns, which is substantially less than the pump pulse duration of 50 ns, enabling efficient Raman conversion. Consequently, the measured slope efficiency for the first Stokes was 79%, reaching a maximum conversion efficiency of 28%, as shown in Fig. 2. The lasing threshold was 40 μJ, and the maximum output power achieved (183 mW)

Fig. 1. Schematic layout of the Raman laser setup. An intracavity frequency-doubled Ti:Sapphire laser at 450 nm was used for pumping a diamond crystal. The cavity (dotted box) consists of three curved mirrors. The surface reflections of the diamond itself were used for coupling out the Raman converted laser light.
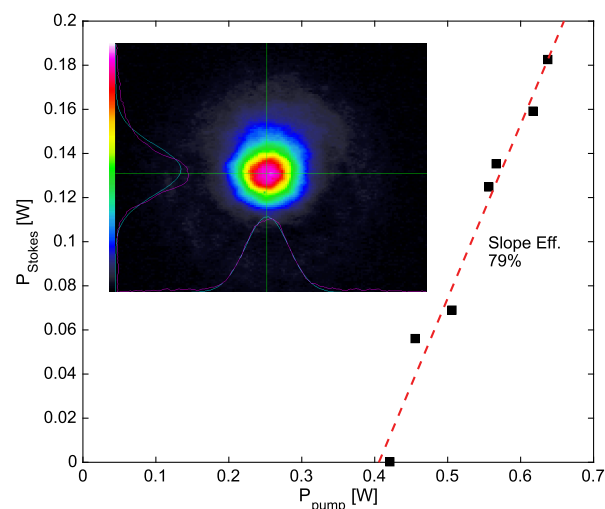

Fig. 2. Slope efficiency of the Raman laser presented here is 79% for the first Stokes order. The inset shows the near-field image of the first Stokes output.

was limited only by the pump laser power. The output beam quality was measured using a beam profiler (*Coherent Inc. LaserCam-HR II*; see the inset of Fig. 2) to be $M^2 < 1.2$, marginally smaller than the one measured for the Ti:Sapphire pump laser.

The coupling between pump and Stokes by SRS is a complex process, depending strongly on the spatial, spectral, and temporal arrangement of the fields involved. In general, the bandwidth of the laser fields relates to the time scale of amplitude and phase fluctuations. In our particular case, where the time scale of the fluctuations is much slower than the dephasing time ($T_2 = 5.7a\epsilon 7$ ps for diamond [21]), the material excitation is considered to be in "steady state" [22]. This is also obvious when comparing the pump laser linewidth ($\Delta\omega_P = 6.5$ GHz) to the diamond spontaneous Raman scattering linewidth ($\Delta\omega_R \approx 45 – 57$ GHz [21]).

While the spontaneous Stokes noise fields may have a larger bandwidth than the pump laser, the Stokes output linewidth is driven to match the pump laser linewidth in the high-gain limit [22]. In this case, all the power in the emission linewidth of the pump laser is effective for amplifying the Stokes field. For resonance ionization applications, it is therefore preferred to operate with a relatively small spot (large gain and high output coupling) in order to converge rapidly to a linewidth similar to that of the pump laser.

The spectral characteristics of the Raman laser emission were studied using a LM-007 and a *HighFinesse/Ångstrom WS/6* wavelength meter with an absolute accuracy of 100 MHz and 600 MHz, respectively. The principal component of the LM-007 wavelength meter is a block of four thermostabilized neon-filled Fizeau interferometers that have different bases (3 μm, 50 μm, 1.5 mm, and 40 mm). In this work, the laser line profiles, a convolution of the first Stokes linewidth and instrumental width was measured using interferometer 3, which has an instrumental width of ~5.3 GHz and a resolution of <1 GHz. Multiple output spectra were measured and averaged for different pump power conditions between 0.4–0.65 W (corresponding to 56–183 mW output power), and the results are shown in Fig. 3. As can be seen, the output had a smooth Lorentzian line shape and a linewidth of around 5 ± 1 GHz, independent of the pump power used.

The results are consistent with the expected output linewidth when approaching the high Raman gain limit regime. The output Stokes linewidth is slightly narrower than the pump laser linewidth for all measured powers, and a factor of 10 times smaller than the spontaneous Stokes noise field. In addition, the measured Stokes linewidth is down to 4 GHz for low pump power conditions and slightly increasing up to 5.8 GHz at maximum pump power. For the case of relatively narrow pump linewidth ($\Delta\omega_P \ll \Delta\omega_R$), the initially broad Stokes noise spectrum with $\Delta\omega_S \approx 57.5 \pm 6$ GHz is gain-narrowed by the factor $[\ln 2/(g_0 I_P z)]^{1/2}$, where g_0 is the gain coefficient, I_P is the averaged pump intensity, and z is propagation distance [23]. Assuming $g_0 = 50$ cm/GW, an average pump intensity of $I_P = 25$ MW/cm^2, the amplified Stokes noise linewidth after a few passes through the diamond is already smaller than the pump laser linewidth (the cavity photon lifetime is ~1.2 ns at 479 nm). The gain at threshold, however, is already high enough to make the Stokes spectrum closely duplicate the one of the pump, with a degree of similarity expected to get closer as the gain increases towards full output power.
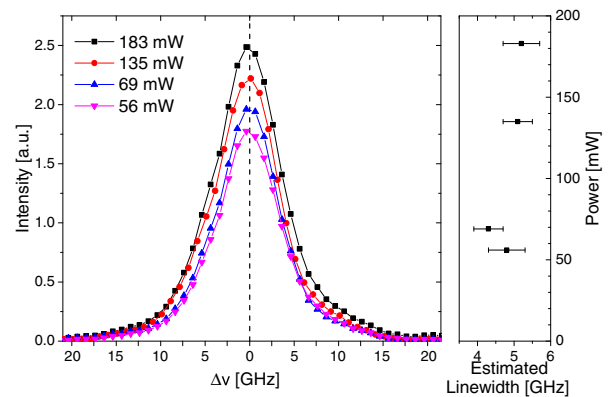

Fig. 3. On the left, the central peaks of the LM-007 wavelength meter, Fizeau interferometer #3 (base 1.5 mm), recorded at different output powers are shown. The intensity has been scaled relative to the pump power. On the right, the results of the linewidth measurements from fitting the spectra taken with the LM-007 are shown for the different pump powers. More details can be found in the text.

The output wavelength was continuously tuned by adjusting the pump laser center wavelength using a thin etalon. Even though the tunable range of the pump laser covers the 350–475 nm range, the results shown represent only a small tuning range that covers 450.28–450.33 nm (corresponding to a shifted output between 479.02–479.08 nm) in order to study in detail the output Stokes linewidth variation when tuning through the Stokes cavity free spectral range (FSR) and the full linewidth of the pump laser. Stokes spectra were measured continuously while the pump laser was tuned in power and center wavelength simultaneously.

Figure 4 shows the 1st Stokes wavenumber and measured linewidth (at FWHM) for a range of pump wavelengths at different pump powers. These scans were performed in a random manner, without adjustments of the Raman cavity, in order to test the versatility and stability of the technique. Consequently, the data are scattered unevenly across the plot. Continuous output tunability was achieved due to the small frequency spacing of the fundamental cavity modes (FSR ≈ 815 MHz). This is apparent in Fig. 4 as a linewidth variation of ~1 GHz in the Stokes output during tuning.

It is important to note that the effect of the cavity FSR can become detrimental when shorter resonators are employed. In general, the resonator length is designed for efficient Raman conversion. For nanosecond pump pulses, the resonator is usually as short as possible in order to maximize the number of passes through the gain media. Since the Raman effect is free of spatial hole burning [24], for cavities with a FSR approaching the pump linewidth, the output Stokes is usually composed of an ensemble of well-spaced longitudinal modes, which is not effective for resonance ionization applications.

The results demonstrate that a synthetic low-birefringence diamond is suitable for realizing highly efficient, linewidth invariant, Raman shifters across the visible spectrum. The linewidth behavior is dictated by the specific properties of the pump source and the characteristics of the gain medium and resonator design. Here, we propose a Raman laser system designed for spectroscopic applications that require large
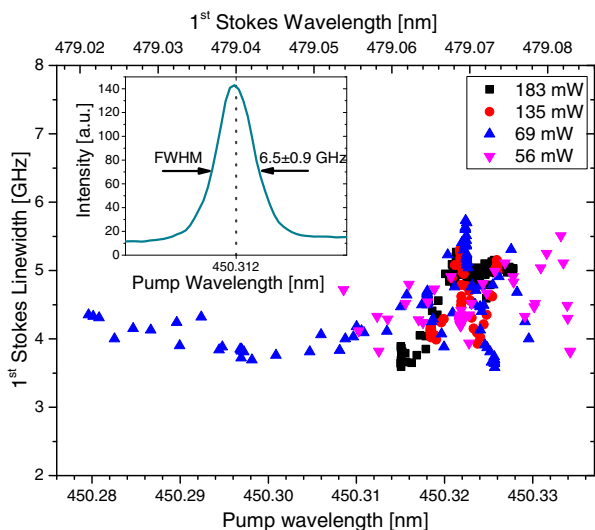
Fig. 4. Linewidth measurement of the 1st Stokes order using a *HighFinesse/Ångstrom WS/6*, taken at different output powers, while adjusting the pump wavelength. The inset shows the pump linewidth measured with the LM-007 wavelength meter at a fixed wavelength.

tunability and a specific linewidth in the low GHz range. Furthermore, the presented work shows that the capabilities of solid-state laser systems, as used, e.g., at the ISOLDE RILIS, can be easily expanded by diamond Raman lasers. The spectral coverage can be significantly improved, without drawbacks concerning the reliability or performance of the installation. The reduction in operational requirements opens up new possibilities for using ionization schemes containing wavelengths between 475–540 nm. This is of special importance for facilities that are not equipped with a dual Ti:Sapphire/dye laser systems (e.g., [25–27]).

Further optimizations of the Raman laser cavity design are foreseen, aiming for an easy-to-use, wavelength-independent add-on for the Ti:Sapphire lasers. Steps towards this have been taken, simplifying the current cavity layout significantly. It is expected that for the end of the CERN long shutdown 2 (LS2), such a system will be available for standard use at the RILIS laboratory.

REFERENCES

1. R. Catherall, W. Andreazza, M. Breitenfeldt, A. Dorsival, G. J. Focker, T. P. Gharsa, T. J. Giles, J. L. Grenard, F. Locci, P. Martins, S. Marzari, J. Schipper, A. Shornikov, and T. Stora, J. Phys. G **44**, 094002 (2017).
2. V. Fedosseev, K. Chrysalidis, T. Day Goodacre, B. Marsh, S. Rothe, C. Seiffert, and K. Wendt, J. Phys. G **44**, 084006 (2017).
3. V. Mishin, V. Fedosseev, H.-J. Kluge, V. Letokhov, H. Ravn, F. Scheerer, Y. Shirakabe, S. Sundell, and O. Tengblad, Nucl. Instrum. Methods Phys. Res. Sect. B **73**, 550 (1993).
4. S. Rothe, T. Day Goodacre, D. Fedorov, V. Fedosseev, B. Marsh, P. Molkanov, R. Rossel, M. Seliverstov, M. Veinhard, and K. Wendt, Nucl. Instrum. Methods Phys. Res. Sect. B **376**, 91 (2016).
5. R. Loudon, Adv. Phys. **13**, 423 (1964).
6. P. Naubereit, J. Marín-Sáez, F. Schneider, A. Hakimi, M. Franzmann, T. Kron, S. Richter, and K. Wendt, Phys. Rev. A **93**, 052518 (2016).
7. H. Pask, Prog. Quantum Electron. **27**, 3 (2003).
8. T. T. Basiev, A. A. Sobol, P. G. Zverev, V. V. Osiko, and R. C. Powell, Appl. Opt. **38**, 594 (1999).
9. J. A. Piper and H. M. Pask, IEEE J. Sel. Top. Quantum Electron. **13**, 692 (2007).
10. D. J. Spence, E. Granados, and R. P. Mildren, Opt. Lett. **35**, 556 (2010).
11. A. Sabella, J. A. Piper, and R. P. Mildren, Opt. Lett. **39**, 4037 (2014).
12. E. Granados, D. J. Spence, and R. P. Mildren, Opt. Express **19**, 10857 (2011).
13. O. Lux, S. Sarang, O. Kitzler, D. J. Spence, and R. P. Mildren, Optica **3**, 876 (2016).
14. X. Yang, O. Kitzler, D. J. Spence, R. J. Williams, Z. Bai, S. Sarang, L. Zhang, Y. Feng, and R. P. Mildren, Opt. Lett. **44**, 839 (2019).
15. D. J. Spence, O. Kitzler, J. Lin, H. M. Pask, S. C. Webster, N. Hempler, G. P. A. Malcolm, and R. P. Mildren, in *European Conference on Lasers and Electro-Optics and European Quantum Electronics Conference (CLEO/Europe-EQEC)* (Optical Society of America, 2017), paper CA_11_2.
16. S. Rothe, B. Marsh, C. Mattolat, V. Fedosseev, and K. Wendt, J. Phys. Conf. Ser. **312**, 052020 (2011).
17. A. Sabella, J. A. Piper, and R. P. Mildren, Opt. Lett. **35**, 3874 (2010).
18. G. Hernandez, *Cambridge Studies in Modern Optics 3: Fabry–Perot Interferometers* (Cambridge University, 1986).
19. R. P. Mildren, J. E. Butler, and J. R. Rabeau, Opt. Express **16**, 18950 (2008).
20. R. P. Mildren and A. Sabella, Opt. Lett. **34**, 2811 (2009).
21. K. Lee, B. J. Sussman, J. Nunn, V. Lorenz, K. Reim, D. Jaksch, I. Walmsley, P. Spizzirri, and S. Prawer, Diaond. Relat. Mater. **19**, 1289 (2010).
22. D. J. Spence, Prog. Quantum Electron. **51**, 1 (2017).
23. M. G. Raymer, J. Mostowski, and J. L. Carlsten, Phys. Rev. A **19**, 2304 (1979).
24. O. Lux, S. Sarang, R. J. Williams, A. McKay, and R. P. Mildren, Opt. Express **24**, 27812 (2016).
25. J. Lassen, P. Bricault, M. Dombsky, F. Izdebski, J. P. Lavoie, M. Gillner, T. Gottwald, F. Hellbusch, A. Teigelhoefer, A. Voss, K. D. A. Wendt, F. D. McDaniel, and B. L. Doyle, AIP Conf. Proc. **1099**, 769 (2009).
26. N. Lecesne, R. Alvès-Condé, , E. Coterreau, F. De Oliveira, M. Dubois, J. L. Flambard, H. Franberg, T. Gottwald, P. Jardin, J. Lassen, F. Le Blanc, R. Leroy, C. Mattolat, A. Olivier, J. Y. Pacquet, A. Pichard, S. Rothe, M. G. Saint-Laurent, and K. Wendt, Rev. Sci. Instrum. **81**, 02A910 (2010).
27. T. Sonoda, M. Wada, H. Tomita, C. Sakamoto, T. Takatsuka, T. Noto, H. Iimura, Y. Matsuo, T. Kubo, T. Shinozuka, T. Wakui, H. Mita, S. Naimi, T. Furukawa, Y. Itou, P. Schury, H. Miyatake, S. Jeong, H. Ishiyama, Y. Watanabe, and Y. Hirayama, Hyperfine Interact. **216**, 103 (2013).

Resonance Laser Ionization Scheme Development

A major foundation for successful application of RILIS is the identification of laser ionization schemes for efficient ionization. The following chapter will briefly summarize the method in section 4.1. Afterwards, scheme development conducted during the time of this work will be presented. In **Publication 3** the efforts towards production of selenium ion beams at ISOLDE are summarized, where the two possible approaches of either ionization of atomic or of molecular selenium have been investigated. A few additional ionization schemes, developed during this work but not yet published otherwise, will be discussed in section 4.2 to section 4.5. Unless indicated otherwise, the figures of the ionization schemes were extracted from the RILIS database, which automatically generates figures of the schemes when data on the energy levels is supplied. The schemes were additionally adjusted to show information, which is not automatically displayed when

extracting the figures.

4.1 Method

An ideal laser ionization scheme has to fulfill the following criteria in order of importance:

- High achievable ionization efficiency,

- Selectivity,

- Ease of laser set up,

- Low maintenance.

In most cases the RILIS is used since it provides high (often $>10\,\%$) ionization efficiencies. It is selective by default, but in cases where non-resonant ionization into the continuum is used, the high power non resonant step can cause background through additional surface ionization. Therefore, if a higher selectivity can be achieved by use of a transition to an autoionizing state, this is always the preferred option as long the efficiency is comparable. In the case of the ISOLDE RILIS, many laser configurations are possible due to the versatility of the installation. Low maintenance is required due to the fact that the RILIS at times needs to provide ionization continuously for more than one week. Therefore, as discussed in subsection 3.3.1, some dyes are not considered for standard operation of the ion source. In general, dye lasers require higher maintenance, so that even though they are simpler to set up, Ti:sapphire lasers are often the preferred choice. In conclusion it can be stated, that the aim of an ionization scheme is to fulfill all four criteria as best as possible, whilst allowing for maximum integrated yield and beam time for the users of the ISOLDE facility.

The basis of scheme development is a careful analysis of data from literature, best summarized in databases like NIST [80], Kuruzc [81] or Grotrian [82]. For most known elements, extensive atomic spectroscopy has been carried out, yielding at least one or often more possible first-step transitions. According to the strength of the transition, some can be discarded, since they would require high laser powers to saturate. Taking

into account the selection rules for atomic transitions (see subsection 2.2.1), often a second step (if needed) can be found in literature. From the level reached with the first step, a scan for autoionizing transitions can be conducted. Depending on the atomic structure of the element, there can be a large number (see e.g. [68]) of states, while for other elements only a few states are present. Depending on the autoionizing transition, sometimes the path via non-resonant ionization can yield a higher ionization efficiency. It has the drawback of background enhancement, since the additional thermal load leads to an increase of surface ionized species. In some cases, where atomic transitions are not well documented or no spectroscopy has been carried out, a first step together with a powerful non-resonant step is used and a third laser is scanned in order to find a suitable second-step transition. For all of these spectroscopic endeavors, it is crucial to surpass the total energy required for ionization. The ionization via Rydberg states, as discussed in section 2.3, is possible but usually not efficient enough for RILIS applications.

4.2 <u>Publication 3</u> - Developments towards the delivery of selenium ion beams at ISOLDE

As will be discussed in the following publication, selenium is not yet readily available at ISOLDE. In the past, molecular beams were extracted for post-accelerated beam experiments. This can help to decrease the background, if a molecular mass is chosen for which contaminating species possess a different A/q. The laser ionization scheme development was carried out for providing an alternative to the molecular ion beam extraction. The work was performed in close collaboration with the ISOLDE target team, since the beam formation and extraction were not well characterized. Even though the final results are not conclusive, it is clear that the publication will be beneficial for future developments. It demonstrates that production and extraction of some elements from thick targets can be very complex.

Contribution: I led the laser ionization scheme developments, by studying the relevant literature, set up the required lasers, performed the experiment and analyzed the resulting

data (new states and ionization scheme efficiency). I planned and executed the laser set up for the measurements performed on-line at ISOLDE and was present for the yield measurements for all three different target units used. I led the preparation of the manuscript, with contributions from J. Ballof, who is the second author of this paper. He led the molecular (ion) beam developments and prepared the discussion of this technique (sections 3&4 of the manuscript).

Regular Article – Experimental Physics

Developments towards the delivery of selenium ion beams at ISOLDE

K. Chrysalidis[1,2,a], J. Ballof[1,3,b], Ch.E. Düllmann[3,4,5], V.N. Fedosseev[1], C. Granados[1], B.A. Marsh[1],
Y. Martinez Palenzuela[1,6], J.P. Ramos[1], S. Rothe[1], T. Stora[1], and K. Wendt[2]

1 CERN, 1211 Geneva, Switzerland
2 Institut für Physik, Johannes Gutenberg-Universität, 55099 Mainz, Germany
3 Institiut für Kernchemie, Johannes Gutenberg-Universität, 55099 Mainz, Germany
4 Helmholtz-Institut Mainz, 55099 Mainz, Germany
5 GSI Helmholtzzentrum für Schwerionenforschung, 64291, Darmstadt, Germany
6 KU Leuven, Instituut voor Kern- en Stralingsfysica, 3001 Leuven, Belgium

Abstract. The production of selenium ion beams has been investigated at the CERN-ISOLDE facility via
two different ionization methods. Whilst molecular selenium (SeCO) beams were produced at ISOLDE
since the early 1990s, recent attempts at reliably reproducing these results have so far been unsuccessful.
Here we report on tests of a step-wise resonance laser ionization scheme for atomic selenium using the
ISOLDE Resonance Ionization Laser Ion Source (RILIS). For stable selenium an ionization efficiency of
1% was achieved. During the first on-line radioisotope production tests, a yield of $\approx 2.4 \times 10^4$ ions/μC
was measured for ^{71}Se$^+$, using a ZrO$_2$ target with an electron impact ion source. In parallel, an approach
for extraction of molecular carbonyl selenide (SeCO) beams was tested. The same ion source and target
material were used and a maximum yield of $\approx 3.6 \times 10^5$ ions/μC of ^{71}SeCO$^+$ was measured.

1 Introduction

CERN-ISOLDE is an isotope separation on-line facility [1, 2], where isotopes can be produced, then ionized and extracted within one apparatus, often in a selective (isotope purity) and efficient (up to several percent overall efficiency) process. This method provides the means to supply ion beams of exotic isotopes, far from stability, with half-lives as low as several ms [3]. For this purpose, protons, provided by the CERN Proton Synchrotron Booster (PSB) with an energy of 1.4 GeV, impinge on a thick target. Reaction products created by spallation, fragmentation or fission are then evaporated from the target material and ionized. The target and ion source assembly is situated on a 20–60 kV high voltage platform and is resistively heated causing the reaction products to diffuse through the target material and effuse into the ion source. Once the atoms or molecules have been ionized, they are extracted by the grounded extraction electrode situated downstream of the ion source. The temperature of ion source and target container are controlled by two separate electrical circuits, allowing to independently adjust the temperatures within a wide range.

Three main methods are used at ISOLDE to produce ion beams: thermal ionization on a hot metal surface, electron impact ionization in a FEBIAD-type (Forced Electron Beam Induced Arc Discharge) ion source or VADIS (Versatile Arc Discharge Ion Source) [4], and laser resonance ionization. The laser-atom interaction can take place in different environments: a hot cavity surface ion source [5], a radio-frequency ion guide LIST (Laser Ion Source and Trap) [6] or a VADIS operated at reduced anode voltage [7,8].

Several attempts have been made to produce selenium beams at ISOLDE in the past, namely for Coulomb excitation studies using post-accelerated ^{70}Se [9]. Such an experiment requires a beam purity in the order of 90%. Due to the abundance of isobaric contaminants expected at the desired atomic masses, un-selective FEBIAD ionization of elemental selenium is not expected to yield the required purity for the proposed Coulomb-excitation experiment using HIE-ISOLDE [10,11]. Even the element selective RILIS process might not yield the required purity, since selenium ($Z = 34$) is located half-way between the

surface ionizable elements gallium ($Z = 31$) and rubidium ($Z = 37$). Isobars of one of these elements tend to be produced at comparable or higher yields for most Se isotopes. Thus all neutron-rich Se isotopes ($A > 80$) produced from GeV proton-induced fission of any type of U or Th target will likely suffer from isobaric Rb, while spallation-produced neutron-deficient Se isotopes up to about ^{73}Se will suffer from isobaric Ga. In some cases the isobars are stable (^{67,69}Ga and ^{85,87}Rb), allowing decay spectroscopy studies. However, these isobars will still affect any type of experiment that is disturbed by stable contaminants, due to ion load limitations (such as ion beam bunching and charge breeding before post-acceleration). However, for the molecular beam ^{x}SeCO$^+$, fewer contaminant isobars are expected, which are mainly ^{27}Al^{x+1}Br$^+$ [12] and $^{x-4}$Ge^{32}S$^+$.

In a past experiment, contamination from isobaric ^{72}Ga$^+$ was avoided by extracting selenium in the form of a SeCO$^+$ beam, through the use of a FEBIAD-type ion source. The SeCO$^+$ was subsequently broken up inside the Electron Beam Ion Source (EBIS) of the REX-ISOLDE and the resulting Se^{n++}-ions were post-accelerated. The disadvantage of this approach is that a significant amount of the ions of interest are lost, due to the distribution among different molecular fractions [13]. Furthermore, many low-energy experiments at ISOLDE, which are situated upstream of the EBIS, are not readily able to make use of molecular beams (solid state physics implantations, collinear laser spectroscopy, etc.). These experiments would profit from the production of elemental Se$^+$ beams. The Resonance Ionization Laser Ion Source (RILIS) [14], which is the most commonly used ion source at ISOLDE, can provide this alternative and generate an element-selective way of ionizing selenium.

2 Laser ionization of selenium atoms

2.1 Atomic structre of selenium

Selenium belongs to the chalcogens (oxygen group) along with oxygen (O), sulfur (S), tellurium (Te) and polonium (Po). Chalcogens have six valence electrons and relatively high ionization energies, which decrease with increasing atomic number. They are therefore not efficiently surface ionized in the typical Ta, W or Re surface ion source at maximum temperatures of around 1800–2500 °C. At ISOLDE, laser ionization schemes for Te and Po have been developed and applied in past experiments [15,16].

The information on the atomic level structure of Se atom available in [17] is mostly based on the spectral data obtained in [18,19]. The electronic configuration of the Se atomic ground state is $[\mathrm{Ar}]4s^24p^4\,^3\mathrm{P}$ with $J = 2$. The state $[\mathrm{Ar}]4s^24p^4\,^3\mathrm{P}$ forms a triplet as shown in fig. 1. An estimation of thermal population of these states can be derived from Boltzmann distribution calculations. At $T = 2000$ °C (used for the measurements, see sect. 4), 83% of the $^3\mathrm{P}_2$ state is populated, whilst the $^3\mathrm{P}_1$ and $^3\mathrm{P}_0$ states are populated with 14% and 3% respectively. The lowest-lying energy level accessible via a single-photon transition is the
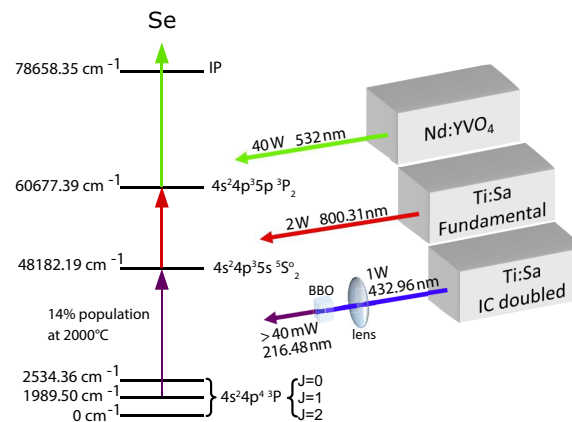

Fig. 1. Ionization scheme for atomic selenium alongside the RILIS lasers which provided the excitation steps with their respective powers. The first step is provided by intra-cavity (IC) frequency doubling a Ti:Sapphire laser and subsequent frequency doubling of this blue output in a single pass through a BBO crystal to generate UV light at 216.5 nm. The Ti:Sapphire lasers are pumped by frequency doubled Nd:YAG lasers at 532 nm. Typical pulse lengths are ≈ 50 ns. The Nd:YVO$_4$ is a BLAZE laser from *Coherent*. The population for the metastable level used for the chosen first step excitation is given. Level configurations and energies are from [17], vacuum wavelengths are given.

$4s^24p^35s\,^5\mathrm{S}_2^o$ state at an energy of 48182.19 cm^{-1}. Excitation to this state can be achieved either from the ground state $^3\mathrm{P}_2$ (207.55 nm$_{\mathrm{vac}}$) or from the first metastable state $^3\mathrm{P}_1$ (216.48 nm$_{\mathrm{vac}}$). The transition from the ground state is the preferred option for optimal ionization efficiency due to the thermal population distribution.

2.2 RILIS laser set up and ionization scheme development

The current status of the ISOLDE RILIS is described in detail in reference [14]. Typically 2-3 tunable, pulsed (10 kHz repetition rate) laser beams are temporally and spatially overlapped inside the ion source cavity and tuned to an element-specific multi-step resonance ionization scheme. The optimal ionization scheme is typically determined for each element by a dedicated resonance ionization spectroscopy study. An ideal ionization scheme is one that combines maximum efficiency with a convenient (reliable, easy to set up and maintain) laser configuration.

For generating the first excitation step, an attempt was made to produce 207.55 nm$_{\mathrm{vac}}$ light by 4th harmonic generation using a Ti:sapphire laser with an intra-cavity second harmonic generation (SHG) and focusing its ≈ 1 W blue output with a 150 mm focal length lens, into a $6 \times 5 \times 4$ mm BBO crystal (type 1 SHG - angle 79.7°, supplied by CRYSTECH INC). Although up to 50 mW at 207.55 nm$_{\mathrm{vac}}$ was achieved, destructive absorption of

Table 1. Second step transitions investigated during the ionization scheme development for selenium, with the first step set to $216.48\,\mathrm{nm_{vac}}$. The relative ion beam intensities achieved using these second steps, compared to the most efficient ionization scheme using the $4p^35p\,{}^3\mathrm{P}_2$ state are given. The expected laser power transmission to the ion source is $\approx 70\%$ for the non-resonant step at $532\,\mathrm{nm}$. The 5 new transitions that were found are marked in bold.

2nd step ΔE [cm^{-1}]	E_{total} [cm^{-1}]	3rd step	rel. int.
12495.20	60677.39	532 nm	1
24901.15	73082.34	scan for AI	
24912.21	73094.40		5×10^{-3}
24870.10	73052.29	532 nm	7×10^{-3}
24860.73	73042.92		3×10^{-2}
24435.99	72618.18		1×10^{-5}
17376.5(2)	**65558.7(2)**		
17380.4(2)	**65562.6(2)**		
17422.0(2)	**65604.2(2)**	532 nm	1×10^{-5}
17744.5(2)	**65926.7(2)**		
17795.5(2)	**65977.7(2)**		

this wavelength in the BBO crystal occurred within minutes. The severe loss of 4th harmonic generation efficiency therefore renders this approach impractical.

Therefore, the metastable state with the estimated population of 14% was used for the measurements described in this work (see fig. 1). The clear disadvantage is an expected loss in efficiency of a factor ≈ 6, due to the lower thermal population at $2000\,^\circ\mathrm{C}$ compared to the ground state. The required wavelength of $216.48\,\mathrm{nm_{vac}}$ was generated by 4th harmonic generation of a Ti:sapphire laser operating at $865.92\,\mathrm{nm_{vac}}$. The same method described above, this time with a BBO crystal at 69.7°, was used.

For the initial verification of the laser beam position and overlap, transitions known from the literature [18] were tested as second steps. An additional laser, operating at $532\,\mathrm{nm}$ with a power of $40\,\mathrm{W}$ ($10\,\mathrm{kHz}$ repetition rate and $17\,\mathrm{ns}$ pulse length), was used for non-resonant ionization into the continuum. The power of this laser was stable for all measurements listed in table 1 and the position inside the ion source remained fixed through the use of an active beam stabilization system. The first of the second-step transition tested leads to the $4s^24p^35p\,{}^3\mathrm{P}_2$ level at a total energy of $60677.388\,\mathrm{cm}^{-1}$, corresponding to a required transition wavelength of $\approx 800.31\,\mathrm{nm_{vac}}$. The alternative transition to the $4s^24p^35p\,{}^3\mathrm{P}_1$ state was not tested due to the lower J quantum number of this state. The lower occupancy of this level ($2J+1$) is expected to result in a reduced maximum ionization efficiency [20]. Several other transitions that can be found in literature were tested and are listed in table 1. The relative intensities compared to the ionization pathway via the $4s^24p^35p\,{}^3\mathrm{P}_2$ level were of the order of 1×10^{-5}–3×10^{-2}. No further investigations into these states were performed since, based on previous experience, it is not reasonable to expect that a transition

to an autoionizing state from these levels would yield more than a factor 3–5 enhancement in ionization efficiency [21].

Therefore, a search for new second-step transitions was performed by scanning the second step laser wavelength in the range of 720–920 nm and 558–592 nm. These scans were carried out using respectively a grating-based Ti:sapphire laser and a Rhodamine 6G dye laser available at the RILIS laser laboratory. In the range covered by the Ti:sapphire laser, no second-step transitions were found. The wavelength scan of the dye revealed five resonances, which could not be attributed as transitions from the $4s^24p^35s\ {}^5\mathrm{S}_2^o$ state to any of the higher levels tabulated in [17]. Since each of those resonances was observable only under presence of the laser beam at $216.48\,\mathrm{nm_{vac}}$, it is reasonable to conclude that new excited levels, linked by the optical transitions with the $4s^24p^35s\ {}^5\mathrm{S}_2^o$ state, were found. The transitions and respective levels are listed in table 1. It is worth to mention that the table of lines observed in the arc spectrum of selenium (see [18]) contains four lines with frequencies very close to the newly found transitions ($17376.46\,\mathrm{cm}^{-1}$, $17380.37\,\mathrm{cm}^{-1}$, $17421.99\,\mathrm{cm}^{-1}$ and $17795.41\,\mathrm{cm}^{-1}$). However, the authors of [18] did not designate these transitions to the level used in our work. Neither of the transitions resulted in a sufficiently intense ion rate to be considered as a part of a favorable ionization scheme.

2.3 Laser ionization efficiency measurement

The RILIS efficiency is measured as the percentage of a calibrated-mass sample that is extracted and detected as an ion beam during optimal RILIS conditions. A sample with a calibrated amount of selenium (natural abundance) atoms (in standard solution of 5% HNO_3 on Ta foil) was inserted into one of the resistively heated capillary ovens, referred to as "mass markers" [22]. This was attached to the transfer line of the empty target container, as is schematically depicted in fig. 2. The sample was gradually evaporated over > 5 hours and the ion current was measured using a Faraday cup during this time. Integrating this measurement over the evaporation time reveals the total number of ions that reach the detection point (after extraction and mass separation).

The efficiency was determined to be $\approx 0.6\%$. Due to instabilities in the UV generation for the first step excitation, the power of this step was deliberately limited to $40\,\mathrm{mW}$ by moving the 4th harmonic generation crystal away from the focus of the intra-cavity generated blue light. Absorption-induced damage to the crystal is then reduced, resulting in a more stable operation. When reducing the power of the first step from $\approx 80\,\mathrm{mW}$ (on the laser table) to $40\,\mathrm{mW}$, a drop in ion current of factor 2 was observed. If the UV light is kept at $80\,\mathrm{mW}$, a correction with a factor of 2 can be applied to the calculated result from the data. Previously the RILIS at ISOLDE (or TRIUMF respectively) has been operated over extensive periods with UV light of comparable wavelengths, $e.g.$ for ionization of Zn ($65\,\mathrm{mW}$ on the table at $213.9\,\mathrm{nm}$) or Sb ($40\,\mathrm{mW}$ on the table at $217.6\,\mathrm{nm}$) respectively (see
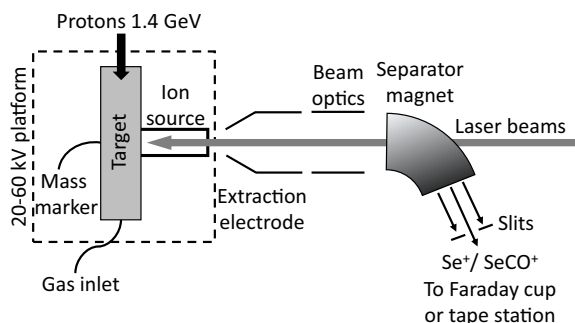
Fig. 2. Schematic view of the experimental set up (not to scale) of the target and ion source. Laser beams were directed into the ion source through a window in the mass separator vacuum chamber. The gas inlet for the production of molecular Se beams was attached to the side of the target container and the mass marker to the back of the transfer line. More details are given in the text.

also [23], table 4). Thus, stable operation with at least 65 mW of UV light can be guaranteed, leading to the efficiency value of 1%.

No uncertainty is quoted for the efficiency measurement since only a single measurement was performed. Nevertheless, this type of ISOL efficiency measurement is known to be susceptible to fluctuations due to several contributing factors such as an accumulation of the sample in cold spots of the target/ion source assembly, losses of a portion of the sample in preparation and initial target heating. The value should therefore be considered as a lower limit. Should reliable production of $207.5\,\mathrm{nm_{vac}}$ for a first step transition from the ground state become feasible, a laser ionization efficiency of about 10% can be expected, due to the higher thermal population of this state.

3 Production of molecular selenium

Molecular selenium beams were first reported in 1992 by Hagebø *et al.* [24] who operated a ZrO_2 fiber target equipped with a FEBIAD source under an additional oxygen partial pressure of $7 \times 10^{-4}\,\mathrm{mbar}$. The selenium was extracted as carbonyl selenide (SeCO) and allowed spectroscopic studies on the isotopes [67,68]Se. However, the exact mechanism of molecular formation remained unclear. Parts of the ion source assembly were proposed as source of carbon which was likely emitted by the graphite grid of a FEBIAD MK5 ion source [25]. Also the source of oxygen remained unclear since the absence of SeCO beams was not confirmed prior to oxygen injection, and after discontinuing the oxygen injection, the SeCO beams did not deplete. A partial pressure of free oxygen is expected from the hot oxide target material itself. Despite this intrinsic presence of oxygen, the influence of additional oxygen supply was tested in 2016 at ISOLDE. Air, containing ca. 21% oxygen, was injected through a calibrated leak of $3.7 \times 10^{-5}\,\mathrm{mbar\,L\,s^{-1}}$ into a zirconia fiber target, as shown schematically in fig. 2. After injection, the radioactive ion

yields of $^{67}Ge^{32}S^+$ and $^{71}SeCO^+$ decreased by factors of ten and two, respectively. A more recent suggestion is that SeCO formation is fostered by injection of carbon dioxide gas, which decomposes to carbon monoxide and oxygen at typical operation temperatures of the target and ion source. This in turn, would open up the classic synthetic route for carbonyl selenide (SeCO) [26].

The production mechanism of the compound inside the target unit was investigated, since issues regarding the stability of ion beam extraction had been observed. A steep decrease in the yields of carbonyl selenide was found, the most likely cause being a depletion of the carbon or oxygen source. To investigate the formation mechanism, tests at the ISOLDE off-line mass separator [27] were performed using target unit #605 which was equipped with a VADIS ion source [4], ZrO_2 fibers inside the tantalum target container and an oven supplying selenium. The setup allowed to study the influence of operation parameters on SeCO formation, which could be determined as the ratio between the extracted beams of $^{nat}Se^+$ and $^{nat}SeCO^+$. Target container and ion source cathode temperatures have been deduced from a calibration curve obtained by variation of the applied heating current, while monitoring the temperature with a pyrometer. The temperature of the ion source was measured at the cathode of the ion source assembly. Whilst varying the ion source cathode temperature in the range from 1960 to 2100 °C did not significantly affect the SeCO formation, a substantial influence of the target container temperature on the SeCO formation was observed. At low temperatures, the extraction is shifted towards the atomic selenium. The target unit was additionally equipped with a calibrated leak to introduce 99% isotopically enriched $^{13}CO_2$ into the ion source. The rate of the leak was initially chosen to be $2.5 \times 10^{-5}\,\mathrm{mbar\,L\,s^{-1}}$ and was later increased to $1.0 \times 10^{-4}\,\mathrm{mbar\,L\,s^{-1}}$ and $1.2 \times 10^{-3}\,\mathrm{mbar\,L\,s^{-1}}$. The corresponding ^{13}CO partial pressures of 4.0×10^{-5}, 1.6×10^{-4} and $1.9 \times 10^{-3}\,\mathrm{mbar}$, are expected to form in the ion source, based on the conductance estimation in the molecular flow regime and assuming, that CO_2 quantitatively breaks up to CO, in agreement with the Boudouard equilibrium.

The presence of ^{13}C inside the ion source could be verified in the extracted beams. For the largest leak rate, 177 nA of $^{12}CO^+$ and 2330 nA of $^{13}CO^+$ were measured, while the current on the mass of $^{13}CO^+$ was below 3 nA before injection of $^{13}CO_2$. Despite the expectations, the extracted $^{nat}SeCO$ beams are dominated by the ^{12}C isotope, and $^{nat}Se^{13}CO$ could not be unambiguously identified in the mass spectrum. Thus, the results indicate that the injected carbon dioxide does not serve as primary carbon source for carbonyl selenide formation. Furthermore, the formation of SeCO is significantly affected by the target temperature, as discussed in more detail in sect. 4.

An elementary analysis by electron-dispersive X-ray spectroscopy (EDS) did not show carbon above the detection limit of typically 0.1% in the zirconia target material itself. While the result shows, that no important carbon fraction is present in the material, a contribution of carbon *e.g.* originating from the decomposition of minor

amounts of zirconium carbide at elevated temperatures cannot be excluded. Another source of carbon are the structural parts of the target assembly, which is obvious from intense CO^+ beam typically extracted from freshly assembled target units without charge in the target container.

So far, injection of tetrafluoromethane (CF_4) was found to regenerate radioactive SeCO beams after depletion of the sideband, albeit at a lower yield. Further investigations are ongoing.

4 On-line yield measurements with ZrO_2 as target material

Two different target units (#605 and #612) with Yttria-stabilized zirconia fibers as target material were used for carbonyl selenide ion beam production. The target material was supplied by Zircar Zirconia Inc., PO BOX 287 87 Meadow Road, NY 10921 Florida, type ZYBF-5, lot #30D-96. Both target units were equipped with FEBIAD-type ion sources. Due to the decreasing production of SeCO during operation of the first target unit #605, it was investigated if the carbon inventory of the original FEBIAD MK5 source [25] can be exploited to foster SeCO formation. The earlier FEBIAD sources contained graphite parts (accelerating grid, outer ring of outlet plate), which were found responsible for a substantial carbon monoxide beam at elevated temperatures. These parts have been replaced by molybdenum within the development of the VADIS ion source [27]. Therefore for target unit #612 the molybdenum grid of the VADIS source was replaced by a graphite grid. Other than this part, the ion sources were identical. To minimize the reduction of the carbon inventory during offline conditioning, the heating time of the target before online operation was minimized for unit #612. This resulted in an initial CO^+ current of 540 nA for target unit #612, which was ca. five times the value of target unit #605, measured under comparable conditions.

Due to this additional supply of carbon, an enhancement of molecular formation of SeCO was therefore expected for the second target, unfortunately, this was not the case. Additionally, a comparison between a VADIS-ionized molecular beam of $SeCO^+$ and a resonantly laser ionized atomic beam in VADLIS mode (running with an anode voltage < 10 V) [7] was made with target #605. For the VADLIS measurements laser powers were optimized for efficiency, meaning that the first step was operated at 80 mW.

Yields of radioactive species for both target units were measured using gamma-ray spectroscopy with the ISOLDE tapestation [28], located at the central beamline, which is equipped with a plastic scintillator and a high purity germanium detector. The obtained yields strongly depend on the history of target heating and temperatures during the measurement. The yields for the different ionization mechanisms are given in fig. 3, alongside the temperature dependence and time evolution in fig. 4. Due to
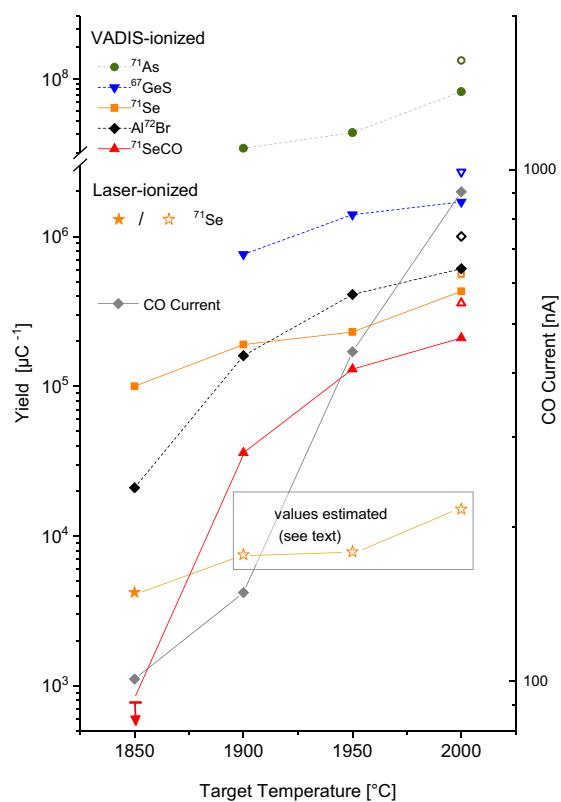

Fig. 3. Radioactive ion beam yields obtained from target #605 [ZrO] at the beginning of the run in dependence of the target container temperature. Open symbols represent measurements at an ion source cathode temperature of 2100 °C, otherwise the ion source cathode temperature was 2050 °C. The yield of laser-ionized $^{71}Se^+$ was only measured at a target temperature of 1850 °C, laser-ionized yields at higher temperatures were estimated by eq. (1). See text for details.

limited availability of beam time, the yield of laser ionized selenium could only be measured at the target temperature of 1850 °C. Contrarily, significant yields of molecular species were only present at higher target temperatures. It is well established that the fraction of radioactive species released from the target material before their decay typically increases with target temperature (see *e.g.* [29]). For prospective users of laser-ionized selenium beams, it is of interest to estimate the yield at higher temperatures. Thus, an estimation of expected laser-ionized selenium yields is required, which also allows a comparison of electron-impact and laser ionization yields. Within the given order of intensity (< 1 pA), the radioactive beam intensity scales linearly with the amount of neutrals introduced into the ion source. The latter equally holds for laser and electron impact ionization. Measurements with the FEBIAD source allow an estimation of the increase in atomic selenium injected into the ion source. In the FEBIAD source two major ionization channels
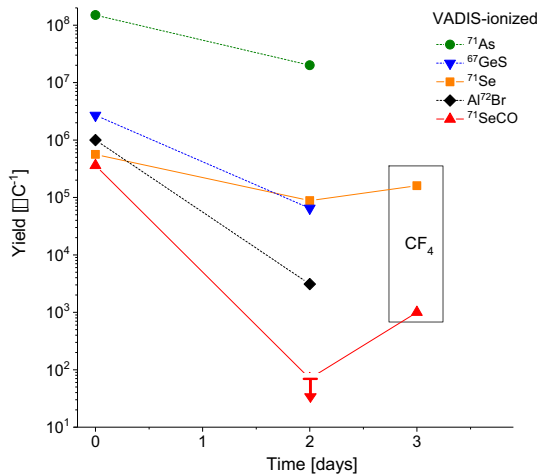
Fig. 4. Evolution of yields: After two days, the yield of $^{71}SeCO^+$ decreased below the detection limit of $\approx 200\,\text{ions}/\mu C$. Injection of CF_4 (after 3 days) could partially recover the beam. The connecting lines between the data points were inserted to guide the eye.

are expected to contribute to the extracted atomic Se^+ beams. Besides ionization of atomic selenium, an additional contribution is given due to dissociative ionization of selenium containing molecules. A search for selenium containing molecules other than SeCO including ^{71}SeO, ^{71}SeC, ^{71}SeF, $^{71}SeF_2$, $^{71}SeF_3$, $^{71}SeBr$, $^{71}SeCl$ and $^{71}SeAl$ remained unsuccessful. The dimer Se_2 as well as SSe have not been measured, however, the compounds are not predicted to be stable by the software package HSC above $1500\,^\circ C$ [30]. Thus, we assume that besides ionization of atomic selenium, only dissociative ionization of carbonyl selenide significantly contributes to the extracted Se^+ beams. The dissociative ionization can be expressed as $SeCO + e^- \rightarrow Se^+ + CO + 2e^-$. To the best of our knowledge, partial ionization cross sections of SeCO have not yet been reported. Within the offline studies prior to online operation of target units #605 and #612, the ratio of stable $^{nat}SeCO^+$ to $^{nat}Se^+$ beams was measured. The highest ratio found was, $^{nat}SeCO^+$ having twice the intensity of $^{nat}Se^+$ at an Anode voltage of $170\,V$. The ratio of injected neutral Se and SeCO is not known. However, from this measurement, it can be concluded, that no more than one third of the SeCO is extracted as atomic selenium ion beam. The value is in agreement with a fragmentation pattern published by Marquart *et al.* [31], which was measured at an electron energy of $70\,eV$. The neutral flow of atomic selenium $n_{Se}(T)$ at temperature T, can be conservatively estimated from the beam currents I of Se^+ and $SeCO^+$ as

$$n_{Se}(T_2) = \frac{I_{Se}(T_2) - 1/3 I_{Se}(T_2)}{I_{Se}(T_1) - 1/3 I_{Se}(T_1)} n_{Se}(T_1). \qquad (1)$$

Yields of laser-ionized selenium scaled using eq. (1) are included in fig. 3.

Additionally the observed contaminants for different masses of the atomic and molecular beams are given in the same fashion. A significantly higher yield (factor 35) was achieved when using electron impact ($SeCO^+$) compared to laser (Se^+) ionization. The drawback of this method, as can be concluded from the overview given in fig. 3, is the high amount of contamination after installation of the target, which was at least one order of magnitude higher than that of the species of interest. A potential contamination of sulfur is also indicated by a peak pattern in the stable beam mass spectrum in the range from 60 to $62\,amu$. This is the dominant beam of a freshly prepared unit, and matches the pattern of carbonyl sulfide (SCO). However, after two days the intensity of the $AlBr^+$ and GeS^+ contaminants reduced by factors of 300 and 40, respectively, whilst atomic Se^+ is only reduced by a factor of 3.5 (cf. fig. 4). The reduction of yields with operation time of the target is a common behavior of thick target units, and often attributed to a degradation of the target material during operation at elevated temperatures [32]. The precise origin of the decreasing yields in the given target and ion source setup along within the discrepancy in the values has not been studied. A depletion of a molecular sideband can be caused by a lack of one species necessary to form the sideband. For example, outgassing of aluminum prevents formation of $AlBr^+$. Assuming continuous release of atomic selenium from the target material, the depletion of the SeCO sideband might be caused by depletion of the precursor compounds. Additionally, competitive reactions, like formation of carbonyl sulfide instead of carbonyl selenide, might contribute to a depletion of the sideband. Nevertheless, if control over molecular formation of SeCO can be achieved, the extraction of molecular selenium might provide a relatively pure beam. The yield evolution of target unit #605 is shown in fig. 4. Two days after installation of the target unit #605, ^{71}Se yields above the detection limit of $200\,\text{ions}/\mu C$ could not be measured anymore on the mass of $^{71}SeCO$. However, two hours after injection of CF_4 at a flow rate of $2.3 \times 10^{-5}\,\text{mbar}\,L\,s^{-1}$ the yield of $^{71}SeCO^+$ was found to have recovered to $1.0 \times 10^3/\mu C$. Eight hours after the beginning of CF_4 injection, a yield of $1.6 \times 10^3/\mu C$ was found. Thus, the vanishing of the $^{71}SeCO^+$ sideband is not related to sintering of the target material, which is in many other cases a common mechanism for material degradation.

5 On-line yield measurements with Ta foils as target material

Attempts were also made to extract selenium from a previously irradiated tantalum foil target (#565), which had no mass markers attached to it. It was equipped with a Ta surface ion source operated at $2150\,^\circ C$ with the target temperature set to $2100\,^\circ C$. Calculations with ABRABLA [33] suggest that the production rate for ^{70}Se is a factor of ≈ 80 less than for ZrO_2. Although, as no SeO formation is expected, the increased proportion of atomic
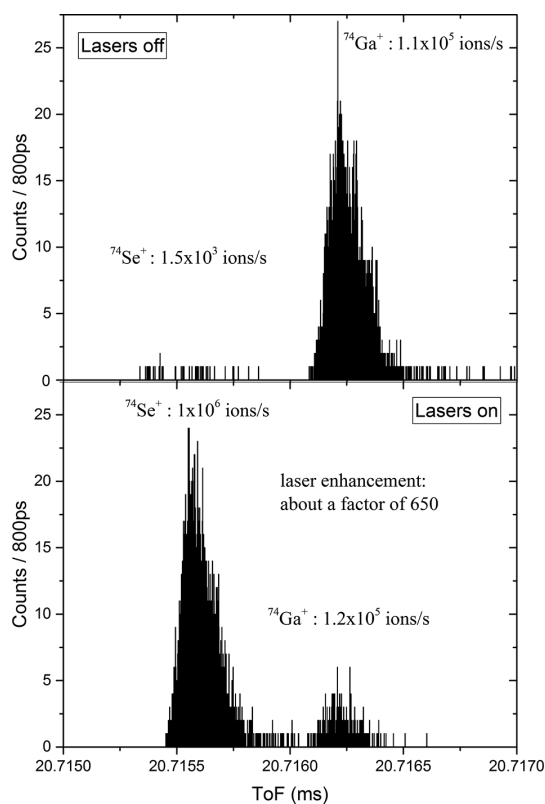
Fig. 5. $A = 74$ ion beam measured with the ISOLTRAP MR-ToF MS without and with laser ionization using a Ta foil target (#565). The measurements were 30 and 3 ms long respectively. The enhanced laser-ionized fraction of the beam (above the surface-ionized Se$^+$ and isobars) is clearly visible. The graphs were provided by F. Wienholtz.

selenium available for laser ionization combined with the standard surface ion source could lead to similar yields. With the lasers set to the according transitions (powers before launch: 1st step 80 mW, 2nd step 2 W, 3rd step 40 W), no signal above the Faraday cup detection limit was observed for any of the stable selenium isotopes. The only signal seen was with use of the multi-reflection time-of-flight mass spectrometer (MR-ToF MS) [34], which is capable of single ion counting. With this, stable ^{74}Se$^+$ (radiogenic, produced in the target material) was observed, but attempts at detecting radioactive species failed. Due to the very limited amount of time for this measurement, which prohibited further optimization attempts, no conclusion about the reason for the low yield can be drawn. The high sensitivity of the MR-ToF MS allowed the measurement of both laser- and surface-ionized selenium. The enhancement factor for laser over surface ionization was 650, and is clearly visible in fig. 5. Also visible is the isobaric contamination composed of ^{74}Ga$^+$, which was less intense than the laser-ionized selenium.

6 Conclusion

A RILIS ionization scheme for selenium has been tested off-line and on-line at ISOLDE, yielding an efficiency of $> 1\%$ in a hot-cavity ion source. This value is expected to reach up to 10% if a reliable means of accessing the ground state atomic population is achieved. Laser-ionized radiogenic selenium production was investigated for ZrO$_2$ and Ta foil targets during on-line tests at ISOLDE. In the case of the ZrO$_2$ targets the RILIS-mode of the VADLIS was compared with standard electron impact ionization of either elemental or molecular (SeCO) selenium. The ^{71}Se$^+$ ion beam produced by electron impact ionization was dominated by a 10× more intense background of electron-impact ionized ^{71}As$^+$. Whilst in RILIS mode the production of ^{71}Se$^+$ was free of radioactive isobaric contamination (no detection of ^{71}As$^+$), a loss of factor ≈ 35 in the ion rate was observed compared to electron impact ionization. Taking into account non-optimal conditions of laser ionization (low population of starting level) and assuming overcoming the technical difficulty of producing stable emission of laser light at 207.5 nm, the expected yield of laser-ionized selenium could reach the same order of magnitude as was obtained using the electron impact ionization.

For the Ta-foil target, RILIS ions were observed but the extracted ion rates were negligible, remaining below the Faraday cup detection limit. The molecular SeCO beams, extracted from the ZrO$_2$ targets, could neither provide the required yields and purity. Additionally the observed drop of molecular formation during the period of the measurements showed that further investigations into the production of these beams need to be made.

7 Outlook

For a better understanding of the molecular formation, the underlying chemical processes will be investigated by thermodynamic simulations and in a dedicated experimental setup. Moreover, target materials which favor atomic Se production should be tested in combination with the standard hot-cavity RILIS configuration. Should additional time for laser ionization scheme development become available, further investigations for identifying transitions to autoionizing states can be made to improve the laser ionization scheme efficiency. Scanning the range of either the frequency-doubled dye or Ti:sapphire lasers would provide access to an unexplored energy range of the continuum.

Data Availability Statement This manuscript has no associated data or the data will not be deposited. [Authors' comment: All data can be made available by the authors upon reasonable request.]

Publisher's Note The EPJ Publishers remain neutral with regard to jurisdictional claims in published maps and institutional affiliations.

References

1. M.J.G. Borge, B. Jonson, J. Phys. G **44**, 044011 (2017).
2. R. Catherall *et al.*, J. Phys. G **44**, 094002 (2017).
3. U. Köster *et al.*, in *Exotic Nuclei and Atomic Masses (ENAM 98)* (ASCE, 1998) pp. 989–994.
4. L. Penescu *et al.*, Rev. Sci. Instrum. **81**, 02A906 (2010).
5. V.I. Mishin *et al.*, Nucl. Instrum. Methods B **73**, 550 (1993).
6. D.A. Fink *et al.*, Nucl. Instrum. Methods B **344**, 83 (2015).
7. T. Day Goodacre *et al.*, Nucl. Instrum. Methods B **376**, 39 (2016).
8. Y. Martinez Palenzuela *et al.*, Nucl. Instrum. Methods B **431**, 59 (2018).
9. A. M. Hurst *et al.*, Phys. Rev. Lett. **98**, 072501 (2007).
10. D. Doherty, J. Ljungvall, Technical report CERN-INTC-2014-057. INTC-P-423 (2014).
11. N. Orce *et al.*, Technical Report CERN-INTC-2012-067. INTC-P-368 (2012).
12. U. Köster *et al.*, Nucl. Instrum. Methods B **204**, 303 (2003).
13. F. Wenander, JINST **5**, C10004 (2010).
14. V.N. Fedosseev *et al.*, J. Phys. G **44**, 084006 (2017).
15. T. Day Goodacre *et al.*, Nucl. Instrum. Methods A **830**, 510 (2016).
16. T.E. Cocolios *et al.*, Nucl. Instrum. Methods B **266**, 4403 (2008).
17. NIST database, extracted January (2017).
18. J.E. Ruedy, R.C. Gibbs, Phys. Rev. **46**, 880 (1934).
19. C. Morillon, J. Vergès, Phys. Scr. **10**, 227 (1974).
20. V.N. Fedosseev *et al.*, Opt. Spectrosc. **57**, 552 (1984).
21. T. Day Goodacre *et al.*, Nucl. Instrum. Methods A **830**, 510 (2016).
22. H.L. Ravn, S. Sundell, L. Westgaard, Nucl. Instrum. Methods **123**, 131 (1975).
23. B. Marsh, *Contribution to the CAS-CERN Accelerator School: Ion Sources, Senec, Slovakia, 29 May - 8 June 2012*, https://cds.cern.ch/record/1445287 (CERN, 2013).
24. E. Hagebø *et al.*, Nucl. Instrum. Methods B **70**, 165 (1992).
25. S. Sundell, H. Ravn, Nucl. Instrum. Methods B **70**, 160 (1992).
26. T.G. Pearson, P.L. Robinson, J. Chem. Soc. (Resumed), pp. 652–660 (1932).
27. L. Penescu, *Techniques to produce and accelerate radioactive ion beams*, PhD Thesis, Bucharest, Polytechnic Inst (2009).
28. M. Turrión *et al.*, Nucl. Instrum. Methods B **266**, 4674 (2008).
29. R Kirchner, Nucl. Instrum. Methods B **70**, 186 (1992).
30. A. Roine, HSC Chemistry 7.1. http://www.hsc-chemistry.net (2010) (online; accessed 19 July 2015).
31. J.R. Marquart, R.L. Belford, H.A. Fraenkel, Int. J. Chem. Kinet. **9**, 671 (1977).
32. J.P. Ramos, Nucl. Instrum. Methods B, https://doi.org/10.1016/j.nimb.2019.05.045.
33. A. Kelic *et al.*, arXiv:0906.4193 (2009).
34. R.N. Wolf *et al.*, Nucl. Instrum. Methods A **686**, 82 (2012).

4.3 Titanium

Titanium, a transition metal, has so far not been extensively studied at thick target ISOL facilities. This can be attributed to the fact, that it belongs to the so-called refractory metals. They can either form molecules with the target material, binding them to it, or their volatility is low and much higher temperatures than achievable in the target heating would be required for release. Recently though, $^{51-55}$Ti has been successfully measured at TRIUMF's Ion Trap for Atomic and Nuclear science (TITAN) [83]. TRIUMF has a thick target as well, the main difference to ISOLDE lying in the proton driver beam, which in TRIUMF's case has 500 MeV energy with 250-300 μA beam current. At ISOLDE, radiogenically produced titanium has so far not been extracted, but since laser ionization is possible, the RILIS was set up to investigate the feasibility. Stable titanium is abundantly present in the target/ion source assembly due to minuscule traces left by machining tools. Therefore no additional sample was required for beam tuning and scheme development.

In [84], a scheme for titanium with one blue first step (394.98 nm$_{vac}$), a red second step (703.78 nm$_{vac}$) and non-resonant ionization with 532 nm laser light was investigated. At the time of the studies at ISOLDE, the second step used in [84] was not compatible with the laser set up. Therefore, an alternative step was used. The first step leads from the $3d^24s^2$ a^{3}F$_2$ ground state to the $3d^34p$ y^{3}D$_1^o$ state at 25317.81 cm^{-1}. From there, the second-step transition led to the $3d^4$ ^{3}D$_2$ state at an energy of 38476.084 cm^{-1}. The ionization is achieved through non-resonant radiation at 532 nm. The ionization potential lies at 55072.3 cm^{-1}, requiring light with a wavelength of 602 nm or less for ionization.

Titanium possesses two thermally populated states at $3d^24s^2$ a^{3}F with $J = 3$ (E$_1$ =170.13 cm^{-1}) and $J = 4$ (E$_2$ =386.87 cm^{-1}) respectively. By using the Boltzmann equation, it is possible to calculate the percentage of atoms P_a populating each of the three states:
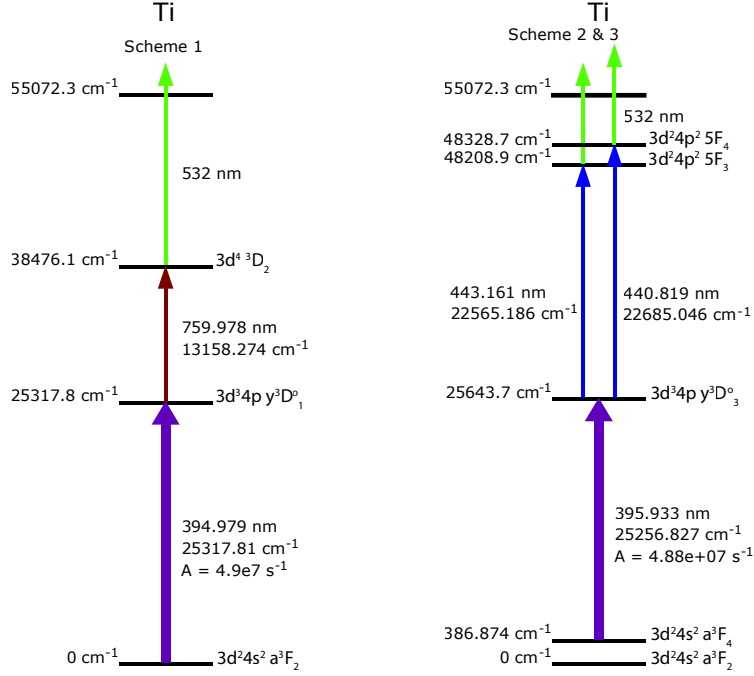
$$P_a = (\phi/\Phi) \times 100 \tag{4.1}$$

Figure 4.1: *Laser ionization schemes for titanium starting from the ground state (left) and second excited state (right). The thermal population of the states according to the Boltzmann distribution is 27 % and 38 %, respectively.*

with

$$\phi = g_a \exp(E_a/kT) \tag{4.2}$$

and

$$\Phi = \sum_i g_i \exp(E_i/kT) \tag{4.3}$$

g represents the degeneracy of the state, subscript a a specific atomic state with energy E, k is the Boltzmann constant, T and subscript i represents the group of atomic states with a significant thermal population. When assuming a temperature of 2200 K, corresponding to an ion source temperature typically used at ISOLDE, the population of the ground state is calculated to be 27 %, the first thermally populated state has 34 % and the next state has 38 %. This implies that a transition not starting from the ground state should access a higher number of atoms in the ion source. For this reason, a comparison of a scheme using the second excited state at 386.87 cm^{-1} was carried

out.

Since the state used in scheme 1 (see Figure 4.1) is not accessible from the thermally populated state (forbidden transition due to $\Delta J = -2$ or -3), an alternative second step was identified, leading to either $3d^2 4p^2\ {}^5F$ with $J =$3 or 4 at 48208.887 cm^{-1} or 48328.747 cm^{-1}, respectively. According to the available data from NIST on the line intensities, the second-step transition in scheme 3 should have higher intensity than the one in scheme 1. Both second step transitions with $\Delta J =$0 and $+1$ were tested, with the expectation of higher ion current for $\Delta J = +1$ [85]. The results of the scheme comparison is presented in Table 4.1. In all cases, the powerful green laser for non-resonant ionization was not blocked while determining the effect of the first two steps. It was simply advanced in time by 100 ns, so that the induced thermal load and therefore background conditions remained the same.

Table 4.1: *Ion currents measured for the different laser ionization schemes tested for titanium. The background was measured with only the green laser going into the ion source.*

	Step 1	Step 2	Green	Ion current [pA]
Scheme 1	X	X	X	2200
	X	X	100 ns early	55
	X		100 ns early	1.7
		X	100 ns early	1.7
Background			X	1.7
Scheme 2 (ΔJ= 0)	X	X	X	60
	X	X	100 ns early	3.5
	X		100 ns early	1.7
		X	100 ns early	1.7
Scheme 3 (ΔJ= +1)	X	X	X	320
	X	X	100 ns early	23

Both schemes tested from the second excited state at 386.87 cm^{-1} were less efficient than the scheme using the ground state transition, tested under the same conditions, even though they have similar transition strength, as indicated in Figure 4.1. Addi-

tionally, the second steps could not be compared between the blue-red-green and the blue-blue-green schemes. Even though the relative intensities given in NIST differ, attributing a higher intensity to the transitions from the excited states, the conditions under which the data were taken cannot be compared directly to literature. This should be kept in mind for future work, since the case of titanium showed that the relative line intensities from the database cannot necessarily be trusted tp predict the performance of a scheme within the hot-cavity environment.

4.4 Molybdenum

Similarly to titanium, molybdenum is a transition metal with a low volatility at ISOLDE target temperatures and to date there has been no successful extraction of radiologically produced molybdenum from an ISOLDE target. There are on-going investigations into extracting a molecular form, in which the Mo atoms can be bound without reacting with the target material, as has been successfully demonstrated for boron [86]. Depending on if the ion beam will be used in the low- or in the high-energy physics part of ISOLDE, different possibilities of continuing the use of the molecules once they effuse into the ion source exist: breakup of the molecule and ionization of the free molybdenum atom or, alternatively, ionization and extraction of the molecule with subsequent breakup inside the Electron Bombardment Ion Source (EBIS or "charge breeder") [87]. The first approach is needed when delivering beam to the low-energy experimental set ups, since the EBIS is only connected to the post-acceleration part of the ISOLDE beam-line.

For breakup of the molecules inside the ion source, most commonly a plasma ion source is used, since the electron energy is high enough to induce it. Another possibility, still under investigation, is laser induced break-up, utilizing a short-pulse, high peak power laser. If this method can be shown to be successful, subsequent stepwise resonant ionization could be used to selectively ionize the molybdenum atom. The laser timing of the pulses can be tuned in such a way, that the resonant ionization would begin just after the break-up. At this time, no outcome of the laser induced molecular break-up can

be reported. Nevertheless, laser ionization scheme development on stable molybdenum was already performed in a preparatory manner.

The ionization scheme development was performed using an ISOLDE target/ion source assembly, with a VADIS plasma ion source [88]. The advantage of this plasma ion source is that the anode grid material is made from molybdenum, supplying enough atoms for laser spectroscopy. Thus, no additional sample was required and it was possible to perform the development work with an existing target unit.
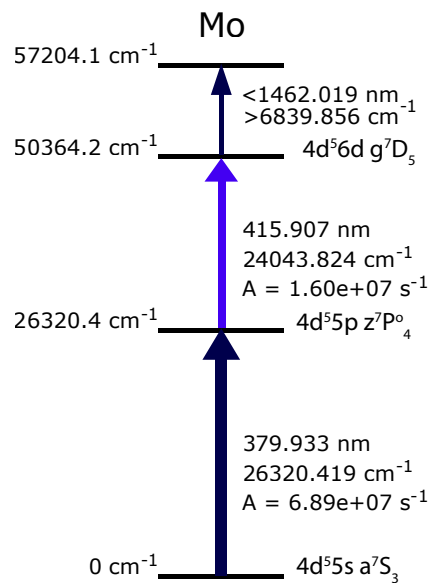

Figure 4.2: *Resonance ionization scheme for molybdenum. The first two resonant steps chosen from literature data [81] for laser ionization of molybdenum.*

Literature gives several first-step transition possibilities with transition strength in the order of $> 10^7\,\mathrm{s}^{-1}$. In order to simplify the laser set up and to avoid dye lasers for increased reliability, all transitions requiring frequency doubled dye or frequency tripled Ti:sapphire light were excluded. Taking into account the increased transition probability for a $\Delta J = +1$ transition, one first step was singled out for the scheme development tests. From there, the second step transition was chosen. Out of the seven possible transitions listed in literature [81], only one fulfilled the requirements in terms of transition strength ($> 10^7\,\mathrm{s}^{-1}$) and achievable wavelength (UV pumped dyes were excluded, for reasons discussed already in chapter 3). With these first two blue steps, generated

by frequency doubled Ti:sapphire lasers as shown in Figure 4.2, a search for autoionizing states was conducted.

The ionization potential of molybdenum lies at an energy of $57204.1\,\mathrm{cm^{-1}}$. The first two steps already bring the energy to $50364.2\,\mathrm{cm^{-1}}$, so that all fundamental wavelengths generated by RILIS lasers (dye and Ti:sapphire) can be used in the search for autoionizing states. So far, the wavelength regions, covered by the most frequently used dyes, DCM (610-650 nm), Rhodamine B (590-614 nm) and Rhodamine 6G (558-574 nm), have been investigated. Overall, in this spectral region a total number of 15 autoionizing transitions were found and are all listed in Table 4.2. No relative intensities are given for the

Table 4.2: *Autoionizing states from the 2nd excited state at $50364.2\,\mathrm{cm^{-1}}$ found in the scans with DCM, Rhodamine B and Rhodamine 6G dye .*

ΔE [cm^{-1}]	Wavelength [nm$_{air}$]	E_{total} [cm^{-1}]
15741.08(1)	635.280	66105.28
15744.07(1)	635.160	66108.27
15753.91(2)	634.763	66118.11
15761.52(2)	634.456	66125.72
15781.39(1)	633.658	66145.59
15812.06(2)	632.429	66176.26
15815.09(2)	632.307	66179.29
15821.23(1)	632.062	66185.43
16624.39(1)	601.526	66988.59
16626.59(1)	601.446	66990.79
16628.23(1)	601.387	66992.43
17514.06(1)	570.970	67878.26
17456.26(1)	572.860	67820.46
17457.20(2)	572.830	67821.40
17458.35(1)	572.792	67822.55

AI, since there was no sufficient amount of time for investigating the saturation of each one of the states. As long as saturation is not reached, the ion current is increasing linearly with power. Therefore no assumption can be made about the realistic relative intensities of the AIS without a saturation investigation for each.

With the power available at the time of the scans, the highest ion current was reached with the AI transition leading to a total energy of $66108.3\,\mathrm{cm^{-1}}$. The saturation mea-

surement, shown in Figure 4.3 clearly indicates that even with a power of 3.3 W (before launch into ion source), no saturation was achieved. Nevertheless, the ionization efficiency was compared to non-resonant ionization with a green laser with a total power of ~35 W (before launch into ion source). The enhancement of the non-resonant step over the signal with only the first two resonant steps was a factor of 10, whilst the AI transition gives an enhancement of factor 64. This means that during an experiment, the power loss of the dye laser would have to be at least a factor of 6 for the AI transitions to decrease to the level of non-resonant ionization.
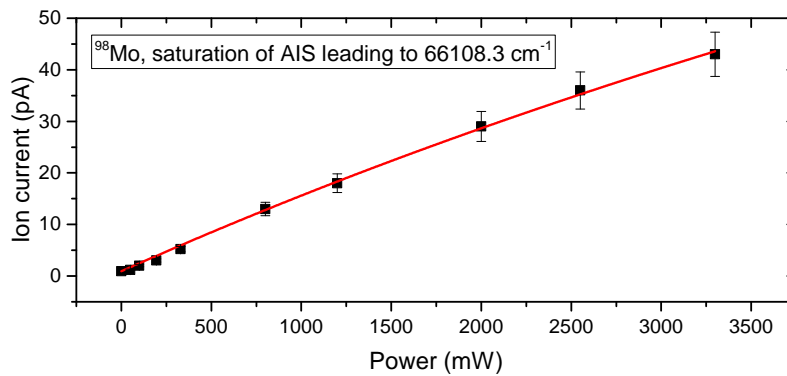

Figure 4.3: *Saturation measurement for the AIS leading from $50364.2 \rightarrow 66108.3\,cm^{-1}$. According to the fit (see Equation 2.23), saturation would set in at ~16 W.*

4.5 Samarium

Samarium, a lanthanide with an IP of 5.64 eV, has been routinely provided as an ion beam to the ISOLDE user community since the installation of RILIS. The ionization scheme applied until 2017 utilizes three dye lasers [89]. The second and third step have similar wavelengths, $\omega_{2,air} = 675.337$ nm and $\omega_{3,air} = 676.375$ nm. Due to this, stabilizing the laser beams in the reference area is difficult, since the separation of the laser beams with the grating is minuscule in the distance from the grating to the position sensitive detector (PSD). Additionally, with the pump power available from the Edgewave laser, only two dye lasers can be pumped. The Blaze laser, usually used for non-resoannt ionization, has to be utilized as a second pump and therefore its beam path has to be

altered accordingly. Overall, this complicates the laser set up.

 In order to find a simpler scheme, literature (NIST database) was consulted, taking into account the thermal population (see Table 4.3) of the first excited states. At the IGISOL laser ion source in Jyväskylä, schemes using Ti:sapphire lasers have been developed for use with a gas jet [38]. Since the ionization at IGISOL does not take place inside a hot cavity, the ground and first excited state were used for finding suitable first steps. In the RILIS case, with the ion source expected to be operated at $>1500°$C, first step transitions starting from the $4f^6 6s^2$ ^{7}F with $J =1$ at $292.58 \, \text{cm}^{-1}$ or $J =2$ at $811.92 \, \text{cm}^{-1}$ state were chosen. Their population is similar and in both cases $\sim 2\times$ higher than the ground state population.

Different dyes were used for scanning over possible second step transitions, but no conclusive results were achieved: several transitions were observed, but were found to be alternative first steps. Finally, a first step transition leading from the $J =1$ first excited state to $4f^5 5d6s^2$ ^{7}G$_1^o$ at $23243.84 \, \text{cm}^{-1}$ was chosen. It had been used in [79] and showed a behavior hinting at a 2-step 1-color resonance ionization scheme (shown in Figure 4.4), in which the first step energy leads to an AIS in a second resonant transition. For the purpose of testing the hypothesis, a second Ti:sapphire laser at the same wavelength was set up. One of the Ti:sapphire lasers was kept at the fixed wavelength, providing the first step transition. In order to reduce the effective power in the ion source, the beam was defocussed to about $2\times$ the diameter of the ion source. The wavelength of the

Table 4.3: *Thermal population of the first excited states of samarium, calculated according to Equation 4.1 - 4.3 for a temperature of 1500° C. The low temperature was assumed due to the use of GdB$_6$ as ion source material.*

Energy [cm^{-1}]	Population [%]
0	9.2
292.58	21.8
811.92	23.9
1489.55	19.3
2273.09	13.1
3125.46	8.0
4020.66	4.6

second Ti:sapphire laser was then scanned and the ion current recorded. The maximum ion current was observed at the same wavelength as the first step, confirming that the AIS is reached resonantly with the same energy.
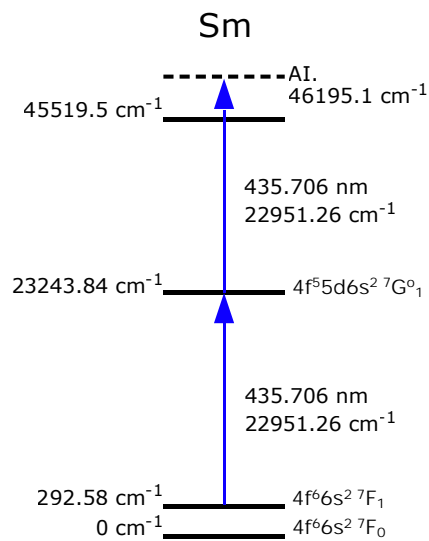

Figure 4.4: *Samarium 2-step 1-color laser ionization scheme, used at RILIS.*

The resulting scheme, comprised of only a single laser, was used during on-line operation, providing an enhancement of a factor 10 over surface ionization. Full saturation of the transition is reached with a total power of 1.2 W before the launch into the ion source. Due to time restrictions, a planned efficiency measurement could not take place. Nevertheless, the yield measurements done during the initial target/ion source and mass separator set up are comparable to the yields achieved with the pure dye laser scheme in the past.

In-Source Laser Spectroscopy

5.1 Method - Nuclear Properties Derived from Optical Spectra

As was briefly described before in subsection 2.3.3 and also in **Publication 1** ([90]), in-source laser spectroscopy is a tool which can be used to determine nuclear properties like the nuclear spin, changes in mean-squared charge radii and electromagnetic moments. This is possible because these nuclear properties often have a detectable influence on the spacing and structure of the atomic energy levels. In the case of in-source laser spectroscopy, the atomic transitions are resonantly probed with a laser tuned to the energy of the transition. The resulting optical spectra can then subsequently be used for extracting the desired nuclear properties. This section is mainly based on the textbook of W.H. King [91] and the reviews by E.W. Otten [92] and B. Cheal, T.E. Cocolios, S. Fritzsche [93].

Isotope Shift

The shift in energy of the individual atomic levels between two isotopes of the same element is called the isotope or isotopic shift (IS). The difference in transition frequency ν between isotopes A and A' can be written as

$$\delta\nu^{A,A'} = \nu^A - \nu^{A'}. \tag{5.1}$$

The IS $\delta\nu^{A,A'}$ is a result of the change in mass of the nuclei, the so called mass shift (MS) $\delta\nu_{MS}^{A,A'}$, and the change in the nuclear charge distribution, the so called field shift (FS) $\delta\nu_{FS}^{A,A'}$, between the nuclei. The total IS can therefore be considered to arise from two separate components, such that

$$\delta\nu^{A,A'} = \delta\nu_{MS}^{A,A'} + \delta\nu_{FS}^{A,A'}. \tag{5.2}$$

Even though the field shift contains the desired information about the nuclear charge distribution, both components need to be carefully evaluated in order to extract the nuclear charge distribution information. As was shown e.g. in [94], the contribution of the mass shift to the overall shift weakens with growing atomic number Z, while the field shift influence increases. This makes it easier to determine the field shift contribution for heavier nuclei.

Mass Shift

Since the angular momentum of an atomic level is fixed, a variation in mass of the nucleus results in a change of energy of the corresponding atomic energy level. This translates into a variation in transition frequency ν from the atomic ground state. There are two components to the mass shift, the normal mass shift (NMS) and the specific

mass shift (SMS). The NMS accounts for a change in the reduced mass correction, due to the finite mass of the nucleus. The SMS on the other hand accounts for changes in electron-electron correlations. The total MS can be written as

$$\delta\nu_{MS}^{A,A'} = (N + S)\frac{m^{A'} - m^A}{m^{A'}m^A} \tag{5.3}$$

where $m^{A'}$ and m^A correspond to the mass of isotopes A' and A, respectively and N and S are constants related to the NMS and SMS. Whilst N can be calculated trivially, S requires a theoretical model or calibration via non-optical experimental data.

Field Shift

The field shift is the result of the electron wave function $\psi_e(r)$ overlapping with the nucleus. If an atomic transition is chosen, in which the overlap of the electron orbital with the nucleus is large (e.g. an s-electrons), the shift tends to be larger, facilitating the experimental study of this effect. The FS $\delta\nu_{FS}^{A,A'}$ can be expressed as

$$\delta\nu_{FS}^{A,A'} = \frac{Ze^2}{6h\epsilon_0}\Delta|\psi_e(0)|^2\delta\langle r^2\rangle^{A,A'}, \tag{5.4}$$

where Z is the number of protons, e is the charge of the electron, h is the Planck constant, ϵ_0 is the free space permittivity, $\Delta|\psi_e(0)|^2$ is the change in electron density at the nucleus ($r = 0$) between the two atomic energy levels and $\delta\langle r^2\rangle^{A,A'}$ is the change in mean-squared charge radii between isotopes A and A'. The heavier the nuclei become, the less reliable the approximation of a constant $\Delta|\psi_e(0)|^2$ across the nuclear volume becomes. Typically, Equation 5.4 is replaced by

$$\delta\nu_{FS}^{A,A'} = F\lambda^{A,A'}, \tag{5.5}$$

where F is the electronic factor, which is proportional to the electronic density at the nucleus between atomic energy levels. $\lambda^{A,A'}$ is the so-called Seltzer moment [95]. It can

be approximated as

$$\lambda^{A,A'} = k\langle r^2 \rangle^{A,A'}, \tag{5.6}$$

where k is a calculable constant. $\langle r^2 \rangle^{A,A'}$ is the variation in charge radii between two isotopes A and A'. It can be compared to the expected variation from a spherical nucleus with equal volume and to a second order approximation written as

$$\langle r^2 \rangle^{A,A'} = \langle r^2 \rangle_0^{A,A'} + \langle r^2 \rangle_0 \frac{5}{4\pi} \delta \langle \beta_2^2 \rangle^{A,A'}. \tag{5.7}$$

$\langle r^2 \rangle_0$ is the mean-squared charge radius of the spherical nucleus. It can be calculated using

$$R = R_0 A^{1/3} (1 + \bar{\epsilon}) \tag{5.8}$$

where R_0 is a constant ≈ 1.2 fm, A is the number of nucleons and $\bar{\epsilon}$ is an empirically determined coefficient, last updated in 1985 by D. Berdichevsky and F. Tondeur [96]. $\delta \langle \beta_2^2 \rangle^{A,A'}$ is the change in the mean-squared quadrupole deformation parameter between two states and offers the possibility of model-independent determinations of shape changes of the nucleus.

Isomer Shift

The isomer shift is similar to the isotope shift, described above. It denotes the shift in the atomic fine structure energy level between the nuclear ground state g and the isomeric (excited) state m of one isotope. Just like for the isotope shift described before, the study of $\delta \nu^{A g,m}$ enables the comparison of $\delta \langle \beta_2^2 \rangle$. This way, nuclear shape changes, resulting from the differing proton/neutron configurations, between ground and isomer state can be determined. Since the mass of the ground and isomer state is virtually the same, there is no mass shift component included in the isomer shift.

Hyperfine Structure

The hyperfine structure coupling of the nuclear and electronic angular momenta I and J to the total angular momentum F of the atom leads to the energy splitting ΔE_F

$$\Delta E_F = AK/2 + B\frac{\frac{3}{4}K(K+1) - I(I+1)J(J+1)}{2(2I-1)(2J-1)IJ} \tag{5.9}$$

with $K = F(F+1) - I(I+1) - J(J+1)$ and the HFS-coupling coefficients A and B. A is related to the nuclear magnetic dipole moment μ by

$$A = \frac{\mu B}{IJ} \tag{5.10}$$

while B is related to the nuclear electric quadrupole moment Q_s:

$$B = eQ_s\overline{V_{JJ}(0)} \tag{5.11}$$

Theoretical calculations of B and $\overline{V_{JJ}(0)}$ are difficult. If they are known for one isotope though, they can be determined using scaling relations.

5.2 Applications

There have been extensive experimental campaigns utilizing the method of in-source spectroscopy. Since the Doppler-broadening of the lines inside the hot-cavity environment is the main limitation, the achievable resolution for heavier elements, which are less affected by Doppler effects, is better. Figure 5.1 shows the dependence of the Doppler-broadening $\Delta\omega_D$ on the (ion source) temperature T, the atomic mass M and the transition wavelength ω_0, calculated according to

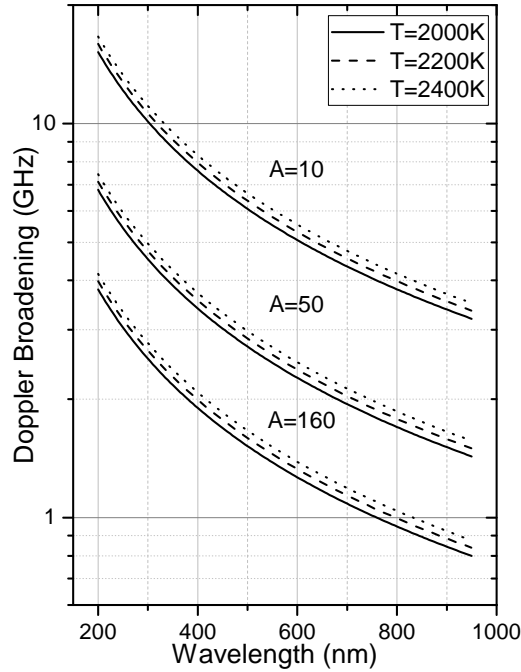$$\Delta\omega_D = 7.16 \times 10^{-7}\omega_0(T/M)^{1/2}. \tag{5.12}$$

Figure 5.1: *Dependence of the Doppler-broadening on the ion source temperature, the atomic mass and the transition wavelength, calculated using Equation 5.12, derived in [34].*

At ISOLDE, laser spectroscopy is a long-standing and well-established technique. Originally, the proposal for in-source resonance laser ionization had the aim to perform spectroscopy on rare isotopes [97], specifically those, that could not be produced with high enough yields to be measurable in any of the collinear laser spectroscopy experiments. At the ISOLDE RILIS, the first in-source spectroscopy studies were performed on Cu [98, 99, 100, 101], and after that the lead region became the scope of the in-source experiments. The lead region, as is evident from Figure 5.1 shows a comparably small Doppler-broadening, making it possible to study the fine and even hyperfine structure with a sub 100 MHz accuracy. The isotopic chains for Au up to At have been investigated thoroughly. Most recently, the Bi isotopic chain (187, 188, 191, 194-203, 214-218) has been studied extensively at ISOLDE under experiment numbers IS650 and IS608. The sensitivity of the technique stems from the fact that it is the initial ion beam production process that is being probed, and not relying on a secondary measurement of the ion

beam. Coupled to the experimental installations for mass spectrometry (ISOLTRAP Penningtrap/MR-ToF MS) and decay spectroscopy (Windmill, IDS), for efficient and selective ion registration, yields as low as a few ions/min suffice [15].

5.3 Experimental Requirements

In order to successfully perform in-source laser spectroscopy, there are three main criteria that need to be fulfilled:

- Spectroscopic laser step with subsequent (efficient) ionizing steps

- Ion detection

- Fixed measurement cycle (triggered and matched to proton-on-target-conditions)

All of the above points have been described in detail in [50] and are only briefly summarized here.

5.3.1 Laser System

The laser system needs to include lasers which are suitable for scanning a spectroscopic transition with maximum achievable resolution and also lasers which are optimized in terms of linewidth, repetition rate and pulse energy to ensure that each atom has a chance of being efficiently ionized. The linewidth of the laser used for excitation after the spectroscopic transition has to be broader than the HFS of the lower level of the transition for which it is used. If it is not broad enough for this purpose, the wavelength has to be tuned synchronously to the spectroscopic step. If this is not done, it will lead to an incorrect intensity distribution of the HFS structure, so that A and B factors, needed for extraction of magnetic quadrupole and electric dipole moments, cannot be correctly determined. In addition this leads to a shift of the centroids of the structure, which in turn leads to wrong determinations of the isotope (and isomer) shifts.

Before or at the beginning of each experiment, the laser providing the spectroscopic step is decreased in power to below 80 % of the saturation value. This way, any broadening

effect resulting from saturation can be avoided. The power is kept constant over the complete scanning range by means of a software controlled motorized $\lambda/2$-plate, coupled to a stabilization software. Polarization dependent optics are used behind the plate, so that a change in polarization leads to a loss or increase in power according to the set value. At RILIS, the laser used to provide the spectroscopic step is either a dual-etalon Ti:sapphire Z-cavity, the grating Ti:sapphire with an additional thick etalon (see subsection 3.3.3) or a dye laser with a grating and thick etalon. Usually the fundamental linewidths lie at about 800 MHz [76].

5.3.2 Ion Detection

Detection of the ions, produced with the resonance laser ionization technique, can be achieved at ISOLDE in different ways. For stable or abundantly produced species with little isobaric contamination, the simplest method of detection are Faraday cups installed in the beam line following the mass separator magnet(s).

The easiest way of detecting and identifying radioactive isotopes is from their decay characteristics. At ISOLDE the tapestation, also used for yield measurements, can be used for this purpose. The ion beam is implanted into a tape, which can then be moved in between the detectors. For the in-source spectroscopy of dysprosium (see section 5.5), the two γ-detectors were used for the studies. A more elaborate and much more sensitive set up is the ISOLDE Decay Station (IDS) [17], which became part of the in-source collaboration in 2017. It consists of at least four High Purity Germanium (HPGe) clovers (total of 16 crystals) but can house several more HPGe detectors if required for the experiment. A tape is used for implantation and can be moved in and out of the detection area. Prior to the availability of IDS, the WINDMILL detector was used for the decay studies (see e.g. [102, 103, 13]).

Another method of detection is the multi-reflection time-of-flight mass spectrometer (MR-ToF MS) set up of the ISOLDE Penningtrap (ISOLTRAP) experiment [104]. Single ions can be detected and their masses measured with high precision.

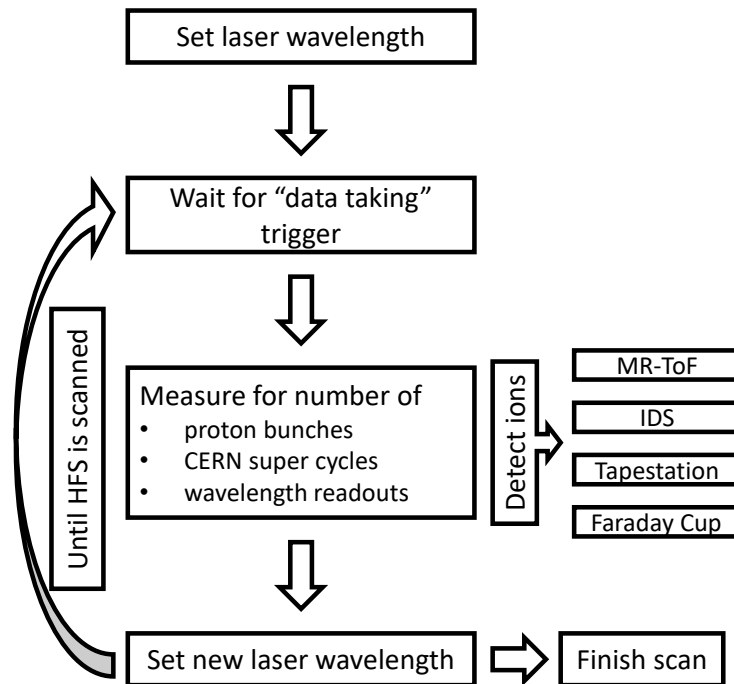### 5.3.3 Measurement Procedure

Figure 5.2: *The flowchart summarizes the laser scan procedure for in-source spectroscopy. The complete description can be found in the text.*

The overview of the procedure is summarized in Figure 5.2. During the data taking, the wavelength of the laser is changed in steps. Depending on the width of the HFS, the steps between the main parts of the structure can be increased in order to save time. Usually, a certain number of measurement are recorded within a time interval, set by a trigger. In most cases, the CERN super cycles are used: within one super cycle some of the proton bunches go to the ISOLDE target, producing the isotopes. In general a stable number and order of proton bunches upon the target is required, so that a steady production rate can be established. If the release from the target is fast, this is especially important, since the number of atoms available in the ion source is directly proportional to the number of ions created. Strong fluctuations can e.g. lead to a distortion of the recorded spectrum and therefore to extraction of incorrect results from the data.

For all measurements, a so-called "reference isotope" is chosen. If possible, it is supplied

from an external reservoir attached to the target unit. On a regular basis, the mass is changed to the reference isotope, measuring its HFS. This way, possible drift of the wavelength readout over time can be detected, and corrected in the spectra of the radioactive isotopes during data analysis.

5.4 Analysis and Extraction of Nuclear Properties

The spectra consist of signal intensity over wavenumber, obtained by scanning the spectroscopic step and recording the transition dependent ion signal. Usually, the data for the wavenumber measurements is already averaged over a certain number of data points and the standard deviation resulting from this can be directly included in the fitting procedure. In addition, depending on the method of ion detection binning and/or averaging along with gating for decay specific energies is required. The analysis (fitting) is done by taking into account the known transition/HFS properties. Provided that the atomic and nuclear spins are known, the total number of peaks is known, even if the HFS cannot be fully resolved. In most cases, the A- and B-values are not known, but the ratio between them is. Additionally, the Racah intensities, derived from the angular momentum and nuclear spin, can be used for determining the relative strength of the HFS peaks. This is of importance for determining if the centroid in an unresolved transition is reasonable in accordance with the expected intensity distribution. If the spectrum is well enough resolved, the A- and B-factors can be evaluated and hence the magnetic dipole and electric quadrupole moments can be calculated.

Unless the electronic factor F and the mass-shift constant M have been theoretically calculated, at least two different atomic transitions have to be used in order to determine the changes mean-squared charge radii. This method was first proposed by W.H. King in 1963 [105] for the case of samarium. He later described it in more detail in [91]. The procedure puts the isotope shifts measured in two different transitions into a linear relationship, as shown in Figure 5.3. Assuming

$$IS_1 = \frac{A - A'}{AA'}M_1 + F_1\lambda^{AA'} \quad \text{and} \quad IS_2 = \frac{A - A'}{AA'}M_2 + F_2\lambda^{AA'} \qquad (5.13)$$

with $(N + S) = M$ (see Equation 5.3) and multiplying both IS with $AA/(A - A')$, the renormalized IS can be plotted. The data points of the two sets lie on a straight line with slope F_2/F_1 and intersection of the y-axis at $M_2 - M_1F_2/F_1$. For calculating absolute values of mean-squared charge-radii, at least one mean-squared charge-radius needs to be measured directly experimentally, either from muonic x-ray or from electron scattering experiments.
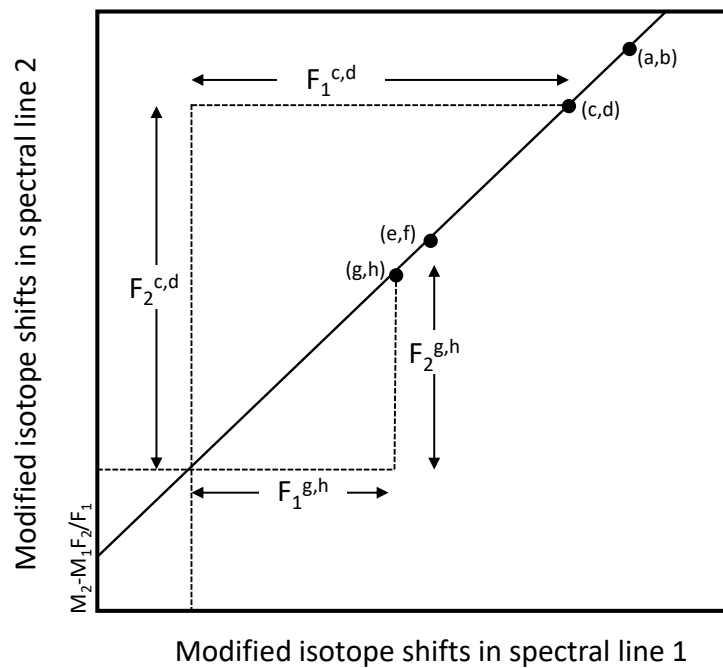

Figure 5.3: *An exemplary King plot. The data points are isotope pairs, measured for two different spectral lines 1 and 2. All data points should lie on the straight line.*

5.5 <u>Publication 4</u> - In-source laser spectroscopy of dysprosium isotopes at the ISOLDE-RILIS

The in-source laser spectroscopy experiment on dysprosium took place in parallel to collections of Dy for medical applications. In order to be able to quickly and efficiently change the laser from ionization of Dy for the collections (highest possible ion rates

required) to in-source spectroscopy (narrow linewidth and reduced power), the grating Ti:sapphire laser was modified so that it could accommodate a thick etalon (described in more detail in subsection 3.3.3).

The Dy transition in the mass range of $A = 139-169$ shows Doppler-broadening which is just below 1 GHz, making it possible to obtain sufficiently high resolution HFS scans for the extraction of useful nuclear-structure information. In general, the lanthanides are some of the lightest well accessible elements with in-source laser spectroscopy, as can be deduced e.g. from Figure 5.1. Not only is the Doppler-broadening low enough to allow resolution of the HFS but the field shift is the dominant contribution to the overall IS (see Fig. 7(b) in **Publication 1** or [94]) by orders-of-magnitude compared to the mass shift. Since the field shift is the result of the electron wave function overlapping with the nucleus, it is the part of the IS which is truly sensitive the nuclear structure, as is evident from Equation 5.4.

Most lanthanides have been extensively studied with laser spectroscopy since the 80s. The experimental interest in this region is related to the effect of a proton subshell closure at $Z = 64$ on the nuclear structure systematics either side of the $N = 82$ shell closure, which is crossed by all of the lanthanide isotope chains. In the region of $N > 82$ to about $N = 90$ for elements with ± 5 in proton number, at $N = 88$ a distinct transition happens: since the influence of the subshell closure diminishes for $N > 88$ a distinct "kink" or change can be observed in the trend of deformation [106]. This is especially evident in the two stable isotopes of Eu ($Z = 63$, stable isotopes at $N = 88$ and $N = 90$), which show a strong difference in trend of deformation (see Fig. 40 in [92]). For Tm with $Z = 69$ this kink vanishes and a smooth trend is observed for increasing neutron numbers [107]. Isotopes with $N < 82$ exhibit odd-even staggering. The closer they are to $Z = 64$, the bigger the additional underlying deformation of the nucleus becomes. Even though it was predicted that reaching the subshell closure, which is the case with Gd, would stabilize the nucleus and therefore smooth out deformation, no such behavior has been observed [108]. In order to better understand the behavior of the deformation of nuclei, it is important to continue the studies of nuclei around $Z = 64$ with $N < 88$.

As is evident from Figure 5.4, extracted from the latest review on nuclear ground state charge radii by I. Angeli and K.P. Marinova [109], such data does not exist for elements with $Z > 64$. Therefore, the experiment described in the following publication aimed at filling the gaps in this region. Due to experimental limitations, especially concerning the ground state production rate and the detection systems, only the isomers ^{145m,147m}Dy were measured. As will be discussed, odd-even staggering seems to vanish for those high-spin isomers. Further experiments are therefore required for measuring the ground state properties and continuing the investigations in the region.
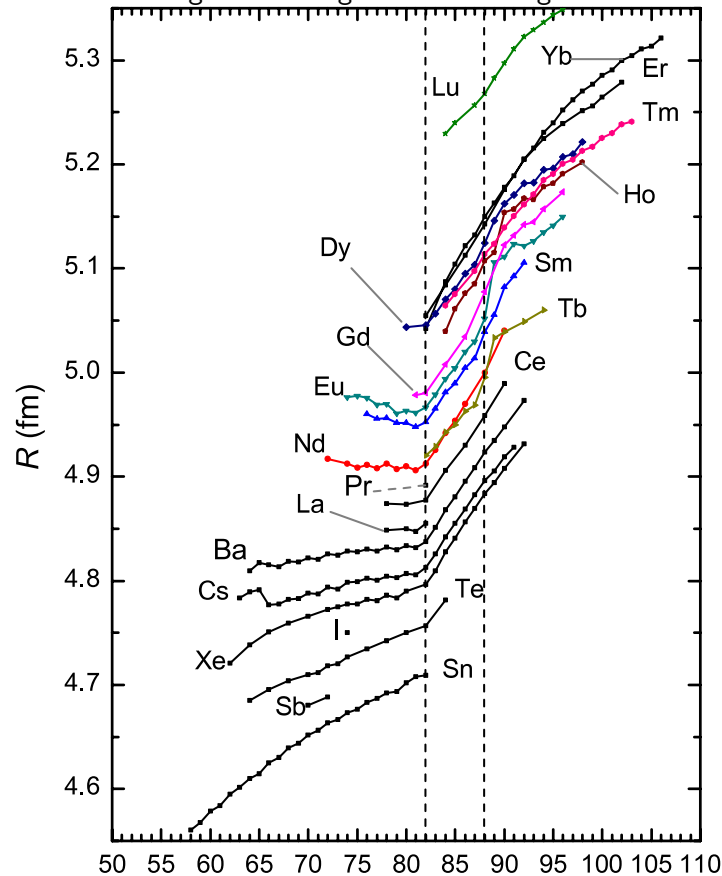

Figure 5.4: *Charge radii in the lanthanide region, extracted from [109]. A second line has been added at $N = 88$ to guide the eye to the region at which the influence of the $Z = 64$ subshell closure starts to vanish. This is especially evident in Ho, Eu and Tb, but clearly visible still in all other elements with Z close to 64. Below the neutron shell closure, odd-even-staggering is obvious, along with a trend towards strong deformation of the ground state, increasing towards the $Z = 64$ subshell closure.*
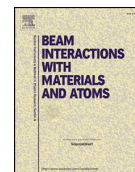
Contribution: I helped to plan and perform the experiment, described in the publications. I prepared the laser set up and did the developments necessary for achieving the required laser linewidth (see subsection 3.3.3). I was present for all measurements, performed the data analysis in parallel to A. Barzakh and finally prepared the manuscript.

In-source laser spectroscopy of dysprosium isotopes at the ISOLDE-RILIS

K. Chrysalidis[a,b,*], A.E. Barzakh[c], R. Ahmed[d], A.N. Andreyev[e], J. Ballof[a,f], J.G. Cubiss[e], D.V. Fedorov[c], V.N. Fedosseev[a], L.M. Fraile[a,g], R.D. Harding[e], U. Köster[h], B.A. Marsh[a], C. Raison[e], J.P. Ramos[a], R.E. Rossel[a], S. Rothe[a], K. Wendt[b], S.G. Wilkins[a]

[a] CERN, CH-1211 Geneva, Switzerland
[b] Institut für Physik, Johannes Gutenberg-Universität, D-55099 Mainz, Germany
[c] Petersburg Nuclear Physics Institute (NRC Kurchatov Institute), RU-188300 Gatchina, Russia
[d] National Center for Physics, PAK-2141 Islamabad, Pakistan
[e] Department of Physics, University of York, UK-YO10 5DD York, United Kingdom
[f] Institut für Kernchemie, Johannes Gutenberg-Universität, D-55099 Mainz, Germany
[g] Grupo de Física Nuclear & IPARCOS, Universidad Complutense de Madrid, E-28040 Madrid, Spain
[h] Institut Laue-Langevin, F-38042 Grenoble, France

ARTICLE INFO

ABSTRACT

A number of radiogenically produced dysprosium isotopes have been studied by in-source laser spectroscopy at ISOLDE using the Resonance Ionization Laser Ion Source (RILIS). Isotope shifts were measured relative to ^{152}Dy in the $4f^{10}6s^2\,^5I_8$ (gs) $\rightarrow 4f^{10}6s6p\,(8,\,1)^o_8$ (418.8 nm$_{\text{vac}}$) resonance transition. The electronic factor, F, and mass shift factor, M, were extracted and used for determining the changes in mean-squared charge radii for ^{145m}Dy and ^{147m}Dy for the first time.

1. Introduction

The Resonance Ionization Laser Ion Source (RILIS) is the most selective of all ion sources available at the ISOLDE radioactive beam facility [1]. The selectivity is an intrinsic property of the ionization mechanism, based on stepwise resonance excitation and ionization via element-specific atomic levels. The isotope production takes place inside a thick target, on which protons, provided by CERN's Proton Synchrotron Booster (PSB), impinge with an energy of 1.4 GeV. The reaction products are released from the target material and effuse via a transfer line into a resistively heated tubular cavity, where the atom-laser interaction takes place. The resulting ions are then extracted, accelerated up to 60 keV and mass separated by a dipole magnet according to their mass-to-charge ratio.

During so-called 'in-source laser spectroscopy', the RILIS lasers are used a to probe a specific spectroscopic transition of the ionization scheme of different isotopes of one element. By determining the isotope shift (IS) of a chosen transition, changes in the nuclear mean-squared charge radii can be deduced. For states with nonzero nuclear spin I which exhibit a sufficiently large hyperfine structure (HFS), the nuclear moments (spin, magnetic dipole and electric quadrupole moments) can be extracted. Additionally, if the HFS of different isomers can be resolved (due to different spins and magnetic moments), isomer-selective

ionization is possible. The spectral resolution of in-source measurements is limited by Doppler-broadening of the spectral lines inside the ion source (which is typically heated to $\approx$ 2100 °C). There have been several experimental campaigns, in which this in-source spectroscopy has been successfully applied (e.g. [2]) or where isomer separation was provided for higher selectivity during nuclear spectroscopy experiments (e.g. [3]).

Here, we report on the first in-source spectroscopy study of dysprosium radioisotopes, demonstrating the suitability of this method for a future extended study of IS in the dysprosium isotopic chain.

2. Experimental setup

The experiment was performed using beam provided by target #655 (target with tantalum rolls from mixed 25 and 6 μm foils at 1950 °C with a tungsten surface ion source at 1985 °C). No stable supply of dysprosium was available initially, so that the optimization was performed on radiogenically produced ^{159}Dy. During the experiment, a proton current of 0.2 μA was used on target, providing a continuous supply of dysprosium.

The transition chosen for the spectroscopy leads from the $[\text{Xe}]4f^{10}6s^2\,^5I_8$ ground state to the $4f^{10}6s6p\,(8,\,1)^o_8$ excited state at 23877.74 cm^{-1} ($\approx$ 418.8 nm) [4] (note: wavelengths given for vacuum).

---

* Corresponding author at: CERN, CH-1211 Geneva, Switzerland.
E-mail address: kchrysal@cern.ch (K. Chrysalidis).

A second laser, a non-tunable Nd:YVO$_4$ laser (2nd harmonic, 532 nm), results in efficient ionization of Dy from the $4f^{10}6s6p$, $J = 8$ excited level, despite the photon energy at 532 nm being below that required to reach the ionization continuum. The ionization efficiency saturates with an estimated 7 W of laser power in the ionization region (≈ 3 mm laser beam diameter). From this we conclude that the 532 nm light is coincidentally resonant with a second step transition to a high-lying level, from which a second 532 nm photon induces ionization via an auto-ionizing state. In the transition metals, the atomic level density, and the richness of the autoionizing spectrum, greatly increase the likelihood of such a coincidence in required transition wavelengths.

A newly developed narrow-linewidth intra-cavity frequency-doubled mode for the Ti:sapphire grating laser was applied for the first time, scanning across the 418.8 nm transition. It will be described in more detail in [5]. The wavelength was recorded with two High-Finesse/Angstrom WS7 wavelength meters installed in the RILIS laboratory. The wavemeters were calibrated before the measurements with a CW diode laser locked to the rubidium hyperfine structure. As the transition probability lies at $A = 1.26 \times 10^8$ s^{-1} [6], the power of the first-step laser beam had to be reduced significantly, to < 1 mW in order to avoid saturation.

For the cases of ^{148,149,165,158,159}Dy, the ISOLDE Faraday cups were used for ion beam detection, as the resonant ion rates were sufficiently high (> 1 pA). For ^{145,149,147}Dy the ISOLDE tape station gamma detector was utilized (for more details see [7]). An overview over the yields measured with the tape station β-counting is given in Table 1.

3. Results

In the case of ^{147}Dy, a long-lived isomeric state ($I_m = 11/2^-$ with $T_{1/2} = 55$ s) exists in addition to the ground state ($I_g = 1/2^+$ with $T_{1/2} = 67$ s). When monitoring the number of photoions in dependence of the first-step laser frequency by the intensity of the internal nuclear transition (678 keV, [12]) one obtains the optical spectrum of the pure high-spin isomer. Several γ-lines following the β-decay of ^{147g}Dy and ^{147m}Dy (101, 253, 365 keV [12]) were also present in the collected γ-spectra. Corresponding optical spectra are the mixture of that for metastable and ground state. The yield of ^{147m}Dy is estimated to be ~ 5 times larger than the yield of ^{147g}Dy, following analysis of the γ-line intensities. As a result, it is impossible to estimate the IS of the ground state with reasonable accuracy.

For the case of ^{145}Dy ($I_m = 11/2^-$ with $T_{1/2} = 14$ s and $I_g = 1/2^+$ with $T_{1/2} = 6/$,s), only the γ-line resulting from the ^{145m}Dy β-decay at 639 keV was observed. The missing observation of other lines is attributed to the high background from the β-decay of the surface ionized isobars. Correspondingly, only results for the isomeric state were obtained.

The optical spectra are summarized in Fig. 1 and the IS are

Table 1
Extracted yields for different dysprosium isotopes with target #655. For ^{145,147}Dy it is not possible to give separate yields, as the ratio of the isomer production is not known. For ^{149}Dy the isomer contribution is assumed to be negligible due to the much shorter $T_{1/2}$. The accuracy of the measured yields can be estimated as a factor of two, taking into account the daughter activity contribution, isomer mixture and the possible contributions from the adjacent masses.

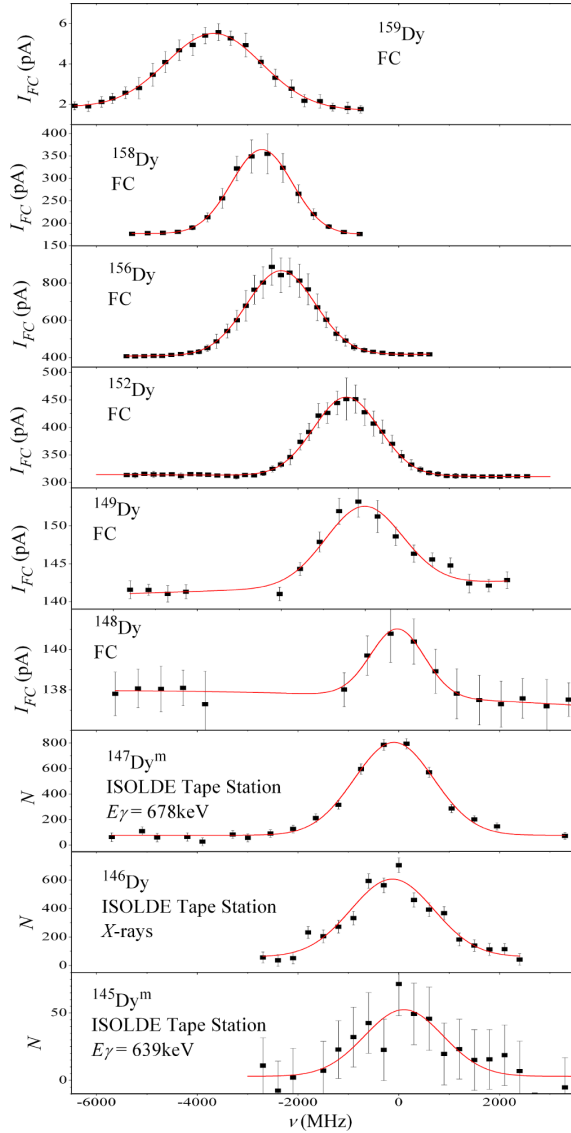| Dy mass	$T_{1/2}$	Yield [1/µC]	ABRABLA [8] in-target production
145(g/m)	14.5/6 s	1.3×10^5	1.9×10^9
146	29 s	2.1×10^6	3.5×10^9
147(g/m)	55/40 s	5.5×10^6	9.1×10^9
148	3.1 m	2.4×10^7	2.6×10^{10}
149	4.2 m	2.0×10^7	1.9×10^{10}
152	2.4 h	3.1×10^8	2.6×10^{10}
155	10.0 h	2.6×10^8	7.6×10^9

Fig. 1. Spectra for ^{159,158,156,152,149,148,147m,146,145m}Dy isotopes. For the odd-A dysprosium isotopes, the resolution was not high enough to resolve the HFS and therefore only the isotope shifts were extracted. The shift in center of gravity (CoG), introduced by the underlying HFS for these cases, was taken into account by estimating it with reasonable A and B HFS-constants: A- and B-constants ratios for the excited and ground states were taken from [9], for ^{159,148,147m}Dy the known Q and μ values [10] were used to calculate A and B constants by the standard scaling relation [11], μ (^{145m}Dy) and Q (^{145m}Dy) were set to be equal to the corresponding values for ^{147m}Dy with the same shell-model configuration ($\nu h_{11/2}$). The shift proved to be less than ~ 40 MHz and was added to the uncertainties of the IS for the odd Dy isotopes.

summarized in Table 2. Due to high background levels, stemming from the surface ionization of dysprosium and other isobaric (lanthanide) contaminants, the uncertainties of the IS are rather large (200–400 MHz). The signal-to-background ratio in case of e.g. ^{148}Dy is only 0.014. The same is true for the γ-spectra, where close lying, more intense γ-lines from isobaric contaminants dominate.

For extracting variations of the mean-squared charge radii $\delta\langle r^2\rangle$, results of the IS measurements with the 421.3 nm transitions from [13]

K. Chrysalidis, et al.

Table 2
Isotope shifts and changes in the mean-square charge radii for Dy isotopes. The errors result from the fitting procedure, described in Fig. 1.

A	$\delta\nu_{A,152}$ (MHz)	$\delta\langle r^2\rangle_{A,152}$ (fm^2)[a]	$\delta\langle r^2\rangle_{A,152}$ (fm^2)[b]
145 m	2270(430)	−0.63(12)	
146	1980(210)	−0.55(6)	−0.55(5)
147 m	1970(230)	−0.55(7)	
148	1970(120)	−0.55(3)	−0.53(5)
149	1560(280)	−0.43(8)	−0.41(4)
156	−2580(120)	0.72(3)	0.73(7)
158	−3380(100)	0.94(3)	0.94(9)
159	−3390(300)	0.94(8)	0.95(9)

[a] Present work.
[b] Reference [13].

were used for comparison. A 'standard' King-plot procedure (see e.g. [11]) is not possible, due to missing IS data for the light dysprosium isotopes (only $\delta\langle r^2\rangle$ are cited in [13,11]). A modified approach was used. Starting with the well-known relation that

$$\delta\nu_{A,A_0} = F\cdot\delta\langle r^2\rangle_{A,A_0} + M\cdot\frac{A-A_0}{A\cdot A_0}, \tag{1}$$

it follows that the modified IS

$$\sigma_\nu = \delta\nu_{A,A_0}\cdot\frac{A\cdot A_0}{A-A_0} \tag{2}$$

is linearly dependent on the modified $\delta\langle r^2\rangle$

$$\sigma_r = \delta\langle r^2\rangle_{A,A_0}\cdot\frac{A\cdot A_0}{A-A_0} \tag{3}$$

with the slope equal to the electronic factor *F* and the intercept equal to the mass-shift constant *M*:

$$\sigma_\nu = F\cdot\sigma_r + M \tag{4}$$

The nuclear masses *A* and A_0 used in the calculations by Eqs. (1)–(3) were taken from [14].

As shown in Fig. 2, all newly measured modified IS for the 418.8 nm transition, as well as the previously measured $\sigma_{418.8\,nm}$ for $A, A_0 = 164, 160$ [15] over modified $\delta\langle r^2\rangle$ lie on a straight line, testifying to the consistency of the newly obtained data. From this plot, the electronic factor *F* and mass-shift factor *M* were determined to be $F_{418.8\,nm} = -3580(110)$ MHz fm^{-2} and $M_{418.8\,nm} = -60(360)$ GHz amu (note, that the uncertainty of the *F* and *M* factors for the previously
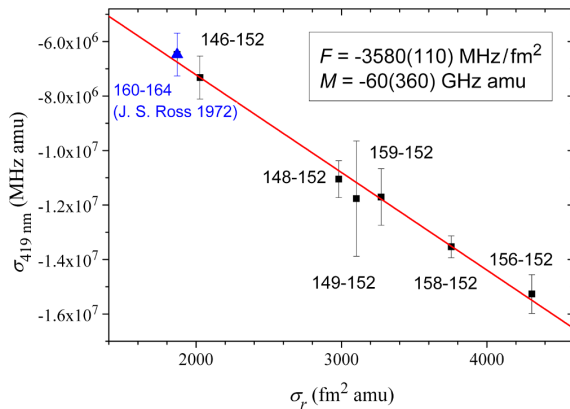

Fig. 2. Modified King-plot for extraction of the *F* and *M* factors for the 418.8 nm transition. IS data for this transition are from the present work (black squares) and from Ref. [15] (blue triangle). (For interpretation of the references to colour in this figure legend, the reader is referred to the web version of this article.)
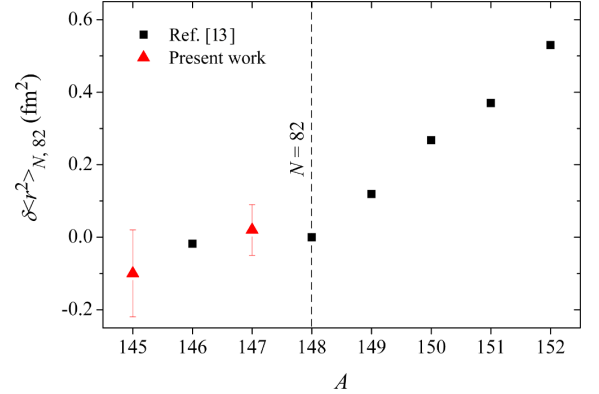

Fig. 3. Changes in $\delta\langle r^2\rangle$ in the vicinity of the $N = 82$ shell closure with the newly obtained values for the high-spin isomers of ^{145m,147m}Dy and data taken from [13].

studied 421-nm transition are not taken into account. These values were cited in [11] without uncertainties). With the derived *F* and *M* factors, changes in $\delta\langle r^2\rangle$ for the high-spin isomers in ^{147,145}Dy were derived for the first time (see Table 2).

Fig. 3 shows the newly obtained values for $\delta\langle r^2\rangle^{145m,148}$ and $\delta\langle r^2\rangle^{147m,148}$ together with the data taken from [13] for $N = 78, 83 - 86$ relative to ^{148}Dy (kink at $N = 82$) is evident for odd- and even-*N* isotopes. It was found previously that there is a marked isomer shift between $1/2^+$ ground states and $11/2^-$ isomers in $_{62}$Sm and $_{64}$Gd nuclei at $N < 82$ [16,17]. This isomer shift leads to the disappearance of the odd-even staggering (OES) in $\delta\langle r^2\rangle$ of the $11/2^-$ isomers. The results obtained in the present work for $11/2^-$ dysprosium isomers do not contradict this observation, although no definite conclusion can be inferred due to the large experimental uncertainties.

4. Outlook

In order to better investigate the disappearance of normal OES in the vicinity of $N = 82$ for the high-spin isomers in dysprosium, expected to be influenced by the $\nu h_{11/2}$-state, further studies with dedicated beam time are necessary. A better resolution of the γ-spectra and detection efficiency, using the ISOLDE Decay Station (IDS), would help to separate the ground from isomeric state. The relative uncertainties could be additionally reduced by using the transition to the $4f^{10}6s6p$, $J = 9$ state at 23736.61 cm^{-1} ($\approx$ 421.3 nm). This transition has been shown to have an isotope-shift sensitivity twice the size of the 418.8 nm transition [11]. As seen in Table 2 and Fig. 1, at the signal to background ratio larger than ~ 1 and sufficient statistics the uncertainty of the IS determination can be reduced to 100 MHz (^{158}Dy) and lower (taking into account reduction of the uncertainty also for CoG measurement for the reference isotope). This accuracy is expected to be sufficient to investigate the evolution of OES (see results for similar $11/2$-state in Sm [16]). However, more accurate results may be achieved with better resolution which would enable reliable analysis of the odd Dy isotope HFS.

It is estimated that dysprosium isotopes down to around $A = 141$ are accessible for IS measurements by the in-source spectroscopy method, provided sufficient suppression of isobaric background is achieved (e.g. with the Laser Ion Source and Trap (LIST) [18]). It is worth to note that dysprosium isotopes with $A < 146$ have noticeable delayed proton branching and photo-ion current monitoring by delayed protons detection might give more favorable background conditions. Near this point, a strong onset of deformation is expected which would be reflected in the IS values.

Acknowledgments

References

[1] V. Fedosseev, et al., J. Phys. G 44 (2017) 084006 .
[2] B.A. Marsh, et al., Nat. Phys. 14 (2018) 1163–1167.
[3] M. Piersa, et al., Phys. Rev. C 99 (2019) 024303 .
[4] NIST Atomic Level Database (last extracted 01.12.2018).
[5] K. Chrysalidis, et al., Technical review of Ti:sapphire laser development within the scope of JRA RESIST, In preparation (2019).
[6] NIST Atomic Lines Database (last extracted 01.12.2018).
[7] R. Catherall, et al., J. Phys. G 44 (2017) 094002 .
[8] A. Kelic, et al., 2009. arXiv:0906.4193.
[9] N. Leefer, et al., Opt. Lett. 34 (2009) 2548.
[10] N. Stone, At. Data Nucl. Data Tables 90 (2005) 75–176.
[11] E.W. Otten, Treatise on heavy ion science, Nuclei Far From Stab. 8 (1989) 517–638.
[12] Brookhaven National Nuclear Data Center (extracted 26.10.2018).
[13] I. Angeli, K. Marinova, At. Data Nuclear Data Tables 99 (2013) 69–95.
[14] M. Wang, et al., Chin. Phys. C 41 (2017) 030003 .
[15] J.S. Ross, J. Opt. Soc. Am. 62 (1972) 548–554.
[16] V.S. Letokhov, et al., J. Phys. G 18 (1992) 1177.
[17] A.E. Barzakh, et al., Phys. Rev. C 72 (2005) 017301 .
[18] D. Fink, et al., NIMB 344 (2015) 83–95.

Doppler-Free In-Source 2-Photon Spectroscopy

As the previous chapters of this thesis have shown, the RILIS is not only a selective and efficient ion source, but also a powerful spectroscopy tool. So far "standard" RILIS operational and experimental requirements have been described along with the developments leading towards new wavelength ranges, resonance ionization schemes and specifically the spectroscopy of Dy isomers using the established in-source RIS method. In this chapter, one of the main limitations of the RILIS method for laser spectroscopy, namely Doppler-broadening of atomic lines due to the laser-atom interaction region within a hot cavity, is addressed. In the application of RILIS for in-source spectroscopy [15] or isomer selectivity [75], once the laser linewidth is reduced significantly below 1 GHz, Doppler-broadening dominates the experimentally observed spectral lines. For this reason in-source spectroscopy at a RILIS has typically been applied to the heavier

isotope (near $Z =$82), where Doppler broadening is smaller and where, nevertheless, useful charge radii information can be extracted, even with poor spectral resolution.Since the temperature and the resulting electrostatic potentials inside the hot cavity are crucial for atom diffusion, ion creation, confinement and extraction, simply reducing the temperature is not the solution and would, in fact, only insufficiently reduce Doppler-broadening. A method is required which can be used at high temperatures whilst not suffering from the corresponding Doppler effects. The ansatz under investigation, which will be discussed in the following chapter in detail is therefore **2-photon excitation with counter-propagating laser beams, eliminating the Doppler-effect.**

If the method proves to be successfully applicable at on-line facilities such as ISOLDE, a new realm of sensitivity for laser spectroscopy can be reached. Not only will light nuclei become accessible to in-source laser spectroscopy, but also the intermediate mass ranges, which have so far suffered from low production yields for isotopes far away from stability, could be addressed due to the high sensitivity of the in-source spectroscopy method. The work presented in this thesis aims at investigating the feasibility of Doppler-free in-source spectroscopy inside a hot cavity, such as the ISOLDE-RILIS. The ion source design is closely matched in design at the RISIKO mass separator at the University of Mainz. At both facilities studies have been performed as a proof of principle. The promising results from these experiments have been published and form part of this thesis as **Publication 5** in section 6.3.

6.1 Theoretical Background

The method of Doppler-free in-source 2-photon laser spectroscopy is based on 2-photon absorption processes, first described theoretically by M. Göppert-Meyer in her PhD thesis in 1931 [110]. The theory is very similar to the Raman effect, which had been described just a few years prior (see [56]). M. Göppert-Meyer showed for the first time, that there is a possibility for an excited atom of emitting two photons, where the sum equals the excitation energy, but is distributed arbitrarily between the two photons. In analogy to this emission process, she also described the absorption of two photons via a so-called

"virtual state".

Even though the Raman effect was demonstrated many years before the invention of the laser, this was not the case for 2-photon absorption (first demonstrated in 1961 [111]). Since the transition probabilities can be very low, high photon densities are required, making lasers a necessity for successful excitation of the transitions. Taking into account that two photons are absorbed, the selection rules for the transition differ in some aspects from the ones for single photon absorption (introduced in Equation 2.18).

6.1.1 Selection Rules

For developing a resonance laser ionization scheme with a 2-photon transition, the modified selection rules have to be taken into account. Derivations for the selection rules can be found in a multitude of texts such as [110, 112, 113, 114]. Here, only an overview is given for convenience.

The most easily derived selection rule is the one for the parity: since two photons are absorbed, for each of the photons the parity of the atom has to change once, in order to conserve it. Overall, the parity of the ground and the excited state therefore need to be the same (in contrast to the single photon transition). The selection rules for the orbital angular momentum L are also easily derived: each time a photon is absorbed, the orbital angular momentum must change by ± 1, so that

$$\Delta L = 0, \pm 2. \tag{6.1}$$

The total angular momentum J changes with

$$|\Delta J| \leq 2 \tag{6.2}$$

from which it follows that

$$|\Delta F| \leq 2. \tag{6.3}$$

There are a number of special cases, mainly depending on the polarization operator q of the light. For circularly polarized light σ^+ and σ^-, $q_{\sigma^+} = +1$ and $q_{\sigma^-} = -1$, respectively. Linearly polarized light π (or σ polarization orthogonal to π) has $q_\pi = 0$. For the magnetic quantum number m

$$\Delta m = q_1 + q_2 \tag{6.4}$$

holds true. In the case of e.g. an $S \to S$-transition, $\Delta m = 0$, it follows that, in case of the light being circularly polarized, this can only be true if the two absorbed photons have opposite polarization. This is very useful in the case of Doppler-free 2-photon excitation, which will be discussed later: if the incoming and reflected laser beams have opposite polarization, only counter propagating photons will be absorbed, leading to the total loss of Doppler-broadened background. Table 6.1 and Table 6.2 give a more complete overview of the selection rules including the additional polarization dependent forbidden transitions (main reference [114]).

Table 6.1: *Summary of general selection rules for 2-photon transitions*

$\Delta L = 0, \pm 2$	
$\lvert \Delta J \rvert \leq 2$	
$\lvert \Delta F \rvert \leq 2$	
same parity	
$\Delta F : 0 \to 0$	for $\omega_1 = \omega_2$
$\Delta F : 0 \leftrightarrow 1$	Forbidden for all polarizations
if $\Delta F = 1 \to \Delta M : 0 \to 0$	Forbidden for all polarizations

Table 6.2: *Summary of polarization dependent selection rules for 2-photon transitions*

Polarization ω_1	Polarization ω_2	Forbidden transitions
σ^+	σ^-	$\Delta M \neq 0$
σ^+	π	$\Delta F : 0 \to 0; \Delta M \neq -1$
σ^-	π	$\Delta F : 0 \to 0; \Delta M \neq 1$
π	σ	$\Delta F : 0 \to 0; \Delta M \neq \pm 1$
π	π	$\Delta F : 0 \leftrightarrow 1; \Delta M \neq 0$
σ^+	σ^+	$\Delta F : 0 \leftrightarrow 1, 0 \to 0, 1/2 \to 1/2; \Delta M \neq -2$
σ^-	σ^-	$\Delta F : 0 \leftrightarrow 1, 0 \to 0, 1/2 \to 1/2; \Delta M \neq 2$

6.1.2 Transition Probability and Cancellation of Doppler-Effect

The general transition probability P_{gf} for a 2-photon transition, assuming for the moment photons which simply fulfill the requirement of $\omega_1 + \omega_2 = \omega_{gf}$ at resonance, depends on the Hamiltonians $\mathcal{H}_1$ and $\mathcal{H}_2$ of the electric dipole interaction of the laser light and the atom. It also depends on the natural linewidth Γ_f of the excited state and of course the wave vectors $\boldsymbol{k}_1$ and $\boldsymbol{k}_2$ of the two incident lightwaves with intensity I_1 and I_2. Assuming the velocity v component to be directed along the x-axis, the frequency experienced by the atom is $\omega_1 - k_1 v_x$ and $\omega_2 + k_2 v_x$, respectively. A summation over all possible intermediate states i has to be done, in order to take into account the contribution of real intermediate states to the transition. The difference of the ground to the intermediate state is $\Delta \omega_i$. Overall, the transition probability can be written as:

$$
\begin{aligned}
P_{gf} \propto & \frac{I_1 I_2 \Gamma_f}{(\Gamma_f/2)^2 + [\omega_{gf} - (\omega_1 + \omega_2) + (k_1 - k_2)v_x]^2} \\
& \times \left| \sum_i \frac{\langle f|\mathcal{H}_1|i\rangle \langle i|\mathcal{H}_2|g\rangle + \langle f|\mathcal{H}_2|i\rangle \langle i|\mathcal{H}_1|g\rangle}{\Delta \omega_i} \right|^2
\end{aligned}
\tag{6.5}
$$

For the case of resonance, $\omega_{gf} - (\omega_1 + \omega_2) = 0$ is required, so that the first factor reduces to:

$$
\frac{I_1 I_2 \Gamma_f}{(\Gamma_f/2)^2 + (k_1 - k_2)v_x}
\tag{6.6}
$$

Additionally, the case of $\omega_1 = \omega_2 = 1/2\omega_{gf}$, $k_1 = k_2 = k$ and $\mathcal{H}_1 = \mathcal{H}_2 = \mathcal{H}$ shows

some interesting effects. A careful consideration of the sign of the wave vector k has to be taken into account, since there is a possibility of absorbing two photons from the lightwave traveling in either the same or opposite direction. Therefore, the transition probability becomes:

$$P_{gf} \propto \left(\underbrace{\frac{4I_1 I_2}{\Gamma_f}}_{\text{(Factor 1)}} + \underbrace{\frac{I_1^2 \Gamma_f}{(\Gamma_f/2)^2 + [2kv_x]^2}}_{\text{(Factor 2)}} + \underbrace{\frac{I_2^2 \Gamma_f}{(\Gamma_f/2)^2 + [2kv_x]^2}}_{\text{(Factor 3)}} \right) \times \left| \sum_i \frac{2 \langle f|\mathcal{H}|i \rangle \langle i|\mathcal{H}|g \rangle}{\Delta \omega_i} \right|^2 \tag{6.7}$$

A multitude of important results can be obtained from Equation 6.7: It becomes obvious that in the case of two photons being absorbed from counter propagating laser beams (factor 1), the Doppler-broadening completely vanishes and the final linewidth can be approximated by the Lorentzian lineshape of the excited state. This was first discussed by Vasilenko et al. in 1970 [115]. The Lorentzian shaped Doppler-free peak stands on a pedestal, represented by factors 2 and 3 of Equation 6.7, which is Doppler-broadened (see Figure 6.1). It is immediately obvious that if the intensities I of the incoming and the reflected light are not equal, the underlying Doppler-profile becomes shifted towards the side of the stronger field. Another effect of unequal intensities is that the Doppler-free interaction is reduced significantly in comparison to the Doppler-broadened component arising from the more intense laser beam. Therefore, if the counter propagation is achieved by reflecting the laser beam with a mirror back into the interaction volume, low reflectivity will lead to a shift of the Doppler-background towards the frequency component of the high intensity beam, whilst the ratio of Doppler-free to Doppler-broadened signal will drastically reduce. The lineshapes for equal light intensities (so 100 % reflectivity) and also for non-equal light intensities are shown in Figure 6.1.
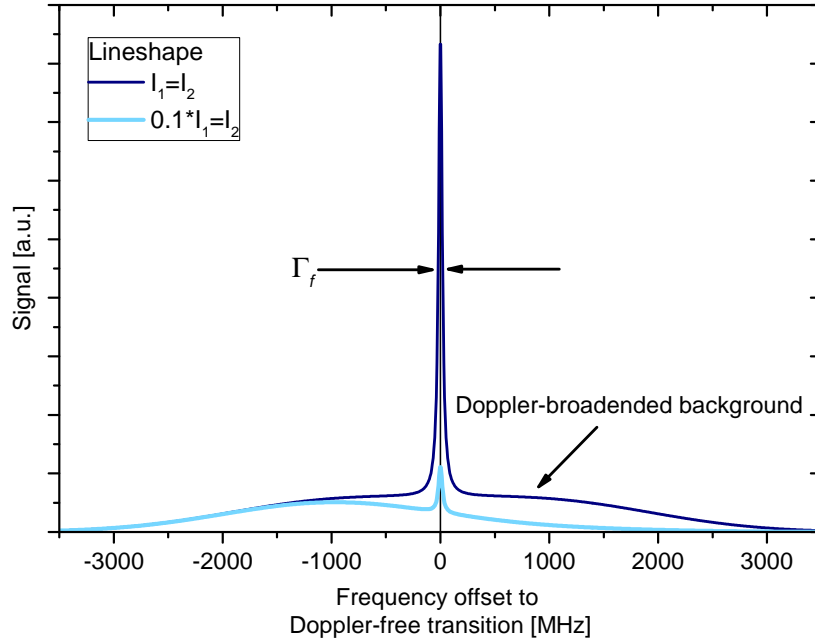
Figure 6.1: *Two-photon transition lineshapes for equal and non-equal intensities of the incoming and reflected light. In the first case, the Doppler-background is centered around the Lorentzian, Doppler-free peak. In the second case, the height of the Doppler-free peak is dramatically reduced and in addition the background is also blue-shifted (assuming a reflectivity of $\sim 10\,\%$).*

In addition to these observations concerning the lineshape, Equation 6.7 shows that the transition probability can be enhanced: If there is a real intermediate state i close to the virtual state v, which lies at $\omega_v = \omega_{gf}/2$ in case of $\omega_1 = \omega_2$, $\Delta\omega_i$ becomes small. For the case of $\omega_i = \omega_v$, the one-photon transition relations should uphold[1]. It is possible to shift the virtual state closer to an intermediate one, by detuning the frequencies so that $\omega_1 \neq \omega_2$. Whilst this enhances the transition probability, it also leads to the loss of the Doppler-free component of the spectrum.

The possible cancellation of the Doppler-effect and reduction of the linewidth to basically the natural linewidth of the excited state is what makes the 2-photon spectroscopy such a powerful tool. Instead of having to accelerate the ion beam, as is the case for the

---

[1]Note: The enhancement can only occur, if the real intermediate state is one which could be excited by a one-photon transition!

high resolution laser spectroscopy experiments like COLLAPS and CRIS at ISOLDE, the atoms can be probed inside the hot cavity, without suffering from thermal Doppler-broadening. The main difficulties arise from the need of reflecting the laser beam back onto itself and the choice of a laser excitation scheme which has high enough transition probability for a signal to be significantly above possible isobaric contamination in the extracted ion beam.

6.2 Experimental Approach

For realizing an in-source laser spectroscopy experiment with the Doppler-free 2-photon approach, two main requirements have to be fulfilled: The first is an efficient way of reflecting the incoming laser beam back onto itself. The second one is realizing a high intensity, in a combination of high laser power and spectral brightness. Both of those requirements and approaches taken to fulfill them will be explained below.

6.2.1 Reflection of Laser Beams in a High Temperature Environment

The temperatures at which the target and ion source assembly at ISOLDE is usually operated lies in the range of 1800-2200°C. Standard mirror coatings and even most substrates cannot withstand these temperatures. For this reason, materials with high melting points, such as some metals, have been considered as mirror materials. Whilst gold shows good reflectivity, especially in the mid IR to deep IR region, its melting point lies at only $\sim$1100°C. The same holds true for silver, which is reflecting well already in the UV range but has an even lower melting point. For this reason, other metals had to be considered. One of the main problems when working with metals with high melting points is that they are often brittle and can be difficult to machine, meaning that polishing their surfaces can be difficult. Figure 6.2 shows a summary of the reflectivity for various metals, compiled from [116].
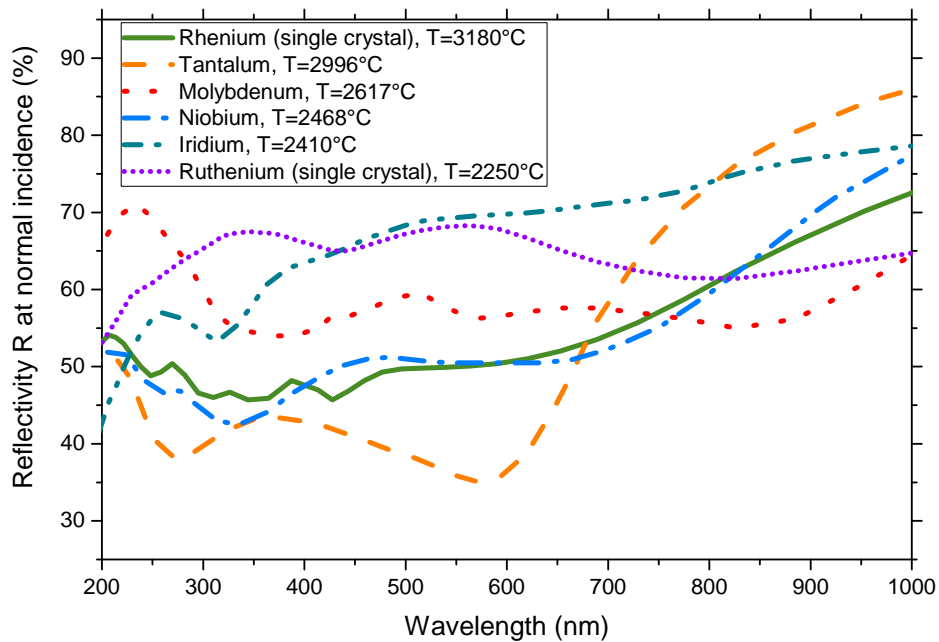
Figure 6.2: *Reflectivity for a selection of metals, data extracted from [116]. T gives the melting point temperature. Only metals with melting points $>2200°\,°C$ and a reflectivity which is $>50\,\%$ for at least part of the spectral range covered by the RILIS laser system are shown.*

All the values for the reflectivity have been measured at room temperature. No information on changes in the values for high temperatures can be found. In 2013 a test was performed at CERN for determining the possible changes in reflectivity of molybdenum, using an OPO system for covering a wide wavelength range. At about $1500°C$ the values measured were in the range of $50\,\%$, which is close to the literature value at room temperature. No other materials were tested during that time, even though iridium and ruthenium both show better reflectivity across the entire spectral range. Tantalum shows poor values for wavelengths $<700\,$nm but could be considered for cases with higher wavelengths. Since, at the time of the experiments described in **Publication 5**, no set up existed in which the temperature dependency of the reflectivity could be measured, Mo was chosen as material for the mirrors.

The approaches taken for the experiments performed at the RISIKO mass separator in
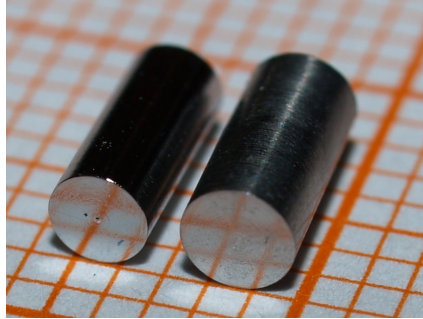
Figure 6.3: *Mo insert used at the RISIKO mass separator in Mainz. The rod on the left was used for the experiment presented in* **Publication 5**. *After the heating cycles, the surface quality looks improved.*
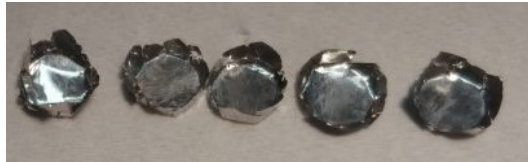

Figure 6.4: *Mo inserts as used at ISOLDE. The foil was roughly cut to have a diameter close to the transfer line. Incisions were made around the piece. This way, it was possible to bend them upwards, leading to a cup-like shape which could be inserted into the transfer line. The upwards bent sides help to keep the piece in place during handling of the target unit. An attempt was made to use iridium foils, but the foil was too brittle to be bent into a mirror insert as shown here.*

Mainz and at CERN-ISOLDE differ. In Mainz, a cylinder of Mo was machined and polished in the local workshop. The result is shown in Figure 6.3. The two depicted rods are before and after heating. It appears as if the surface smoothness and reflectivity increased with the heating cycles. Figure 6.4 shows the Mo foils which were inserted into the back of the ISOLDE transfer line. The lower reflectivity of these unpolished surfaces is clearly visible. Overall, the experimental results, specifically the ratio of the Doppler-free peaks to the Doppler-background, show that the polished rod had better reflectivity.

The proposed solutions for mirror installation in the target and ion source assembly are summarized here. At ISOLDE, modifications of the target and ion source assembly should be carefully assessed and validated before implemented for scheduled on-line

operation in routine experiments. For this reason, the scope for significant modifications of the setup for the purposes of this work, which took place somewhat parasitically, was limited. Further development of a target unit, optimally designed for Doppler-free 2-photon spectroscopy is required, but requires a dedicated study.

- **Replacing the transfer line plug:** The simplest solution would be to replace the plug with which the transfer line is closed with a polished piece. If possible, the side pointing towards the laser should be machined with a curvature. This would decrease the sensitivity to the angle of the mirror and help with overlapping the reflected with the incoming laser beam.

- **Use of the VADIS:** The VADIS has an accelerating grid situated at the end of the ion source volume, made of Mo. By closing the central hole and polishing the grid, it becomes a mirror, on which the laser beam could be reflected. Grids with this configuration have been acquired, but were difficult to polish.

- **Mirror positioned in between transfer line and ion source:** Inserting a mirror, made either of Mo, Ir or Ru, between the transfer line and the hot cavity surface ion source is also considered. This would require only slight changes to the assembly, seeing the ion source is usually inserted into the transfer line. By simply shortening the ion source or transfer line by the thickness of the mirror, it could be installed in between those two components. The mirror would completely not fill the aperture completely, but would be designed in form of a cross, maintaining stability, whilst leaving space for atoms to effuse into the ion source.

- **Mirror behind the transfer line:** For this approach, the plug of the transfer line would need to be removed. The yields should not be impacted, since in the case of short lived isotopes, the ones which condense at the back of the line are lost for the experiment in any case. A mirror could then be e.g. attached to the target container and reflect the laser light back into the ion source. The advantage of this approach would be the mirror would sit in the shadow of the target and ion source with direct contact to the cooled target container and would therefore not

need to withstand temperatures $>1000°$C. A standard mirror or retro-reflector could therefore be used. The disadvantage is that in standard assemblies the plug in the transfer line is used for holding the mass markers. Since the distance of the mirror to the ion source volume increases drastically, the alignment of the mirror becomes crucial for reflecting the beams back into the ion source.

For future developments, which will require a design change of the target and ion source assembly to encompass a thick, polished metallic mirror, investigations into iridium and ruthenium should be made. Both metals look promising and might yield better reflectivity results than molybdenum.

6.2.2 Laser (Linewidth) Requirements

As has been shown in Equation 6.7, the lineshape of the Doppler-free component in the 2-photon absorption converges to the natural linewidth of the excited state (10 MHz for 100 ns lifetime). Consequently, if the laser linewidth is bigger than the natural linewidth, the transition probability is decreased, since not all photons contribute to the transition. Decreasing the laser linewidth therefore leads to a direct increase in signal strength. At RILIS, standard "narrow band" operation before this work referred to laser linewidths of 0.8-1.0 GHz. Since the transition probability is proportional to I^2, it is also directly proportional to the power P. It follows that $P_{gf} \propto P^2$. It is therefore crucial not only to ensure a linewidth matched well to the natural one of the state, but also to achieve high power. For this application, pulsed Fourier-limited linewidth lasers with powers in the W range at 10 kHz repetition rate are required. The following options are feasible:

- **Seeded Ti:sapphire ring cavity:** A CW seeded Ti:sapphire ring cavity can cover a broad spectral range. The length of the resonator dictates the pulse length and therefore the linewidth. One such ring cavity, built for narrow linewidth applications in RILIS, has been extensively discussed in subsection 3.3.4 and was used for the results discussed in **Publication 5**. Seeded Ti:sapphire ring cavities have been

used in many (collinear) high resolution laser spectroscopy experiments, some of the most recent at ISOLDE having been performed by CRIS (see e.g. [9]).

- **Pulsed dye amplifier (PDA):** In order to cover the spectral range not reached with the Ti:sapphire laser, a PDA can be used. It requires a narrow linewidth light source in the dye range, e.g. from a CW dye or a diode laser. This light can be amplified in multiple stages, as is the case in a standard dye laser. The more stages are being used, the higher the possible power output becomes. Due to the requirements of repetition rates $\geq$10 kHz, available OPO systems are not an option. So far, no alternative to a PDA system, especially concerning possible power output, exists.

6.3 <u>Publication 5</u> - First demonstration of Doppler-free 2-photon in-source laser spectroscopy at the ISOLDE-RILIS

The final publication presented in this thesis combines many developments, some of which were already mentioned in earlier chapters of this thesis. The experiments presented here aimed at showing that, in principle, Doppler-free 2-photon laser ionization can be applied inside a hot cavity ion source, such as the ISOLDE one. Even with the low reflectivity achieved so far, Doppler-free 2-photon spectroscopy was achieved. This work demonstrates that, once the optimal mirror for retroflection of the laser beams is determined, the technique should become a new, powerful spectroscopy tool, capable of achieving sub-Doppler resolution, combined with the inherent sensitivity of in-source resonance ionization spectroscopy.

Contribution: I planned and performed all the experiments presented in the manuscript. I built and commissioned the Ti:sapphire laser (see subsection 3.3.4) used in the measurements at ISOLDE. I analyzed the data and finally prepared the manuscript.
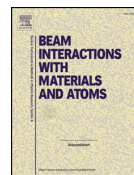
First demonstration of Doppler-free 2-photon in-source laser spectroscopy at the ISOLDE-RILIS

K. Chrysalidis[a,b,*], S.G. Wilkins[a], R. Heinke[b], A. Koszorus[c], R. De Groote[d], V.N. Fedosseev[a], B. Marsh[a], S. Rothe[a], R. Garcia Ruiz[a], D. Studer[b], A. Vernon[e], K. Wendt[b]

[a] CERN, CH-1211 Geneva, Switzerland
[b] Institut für Physik, Johannes Gutenberg-Universität, D-55099 Mainz, Germany
[c] KU Leuven, Instituut voor Kern- en Stralingsfysica, 3001 Leuven, Belgium
[d] Department of Physics, University of Jyväskylä, P. O. Box 35(YFL), FI-40014 Jyväskylä, Finland
[e] School of Physics and Astronomy, The University of Manchester, Manchester M13 9PL, United Kingdom

ARTICLE INFO

ABSTRACT

Collinear Doppler-free 2-photon resonance ionization has been applied inside a hot cavity laser ion source environment at CERN-ISOLDE. An injection-seeded Ti:sapphire ring laser was used to generate light pulses with a Fourier-limited linewidth for high-resolution spectroscopy. Using a molybdenum foil as a reflective surface positioned at the end of the target transfer line, rubidium was successfully ionized inside the hot cavity. The results are presented alongside previously obtained data from measurements performed at the RISIKO mass separator at Mainz University, where collinear and perpendicular ionization geometries were tested inside an RFQ ion guide. This work is a pre-cursor to the application of the Doppler-free 2-photon in-source spectroscopy method at ISOLDE. This approach aims to take advantage of the unmatched sensitivity of in-source spectroscopy, without the disadvantage of Doppler broadening.

1. Introduction

The Resonance Ionization Laser Ion Source (RILIS) is by far the most commonly used ion source at the CERN-ISOLDE facility [1]. As it is based on the principle of stepwise resonant ionization, atomic properties of an element can be directly extracted from the energy information measured by the corresponding resonant transition, making it a valuable spectroscopic tool.

This so-called 'in-source resonance ionization spectroscopy' has been applied in numerous experimental campaigns, measuring the isotope shifts (IS) and hyperfine structure (HFS) of atomic transitions. Some of the most recent examples include investigations into the odd-even staggering effects in mercury [2], which was the first nuclear structure study using the newly-established RILIS-mode of the ISOLDE Versatile Arc Discharge (Laser) Ion Source (VAD(L) IS) [3].

The achievable resolution of the technique is limited by the Doppler broadening of the atomic spectral lines at the operating temperature of the ion source cavity ($\sim 2000\,°C$). For this reason, its application has been limited to the heavier elements (for which the Doppler broadening is reduced) and to atomic transitions that show high sensitivity to changes in the nuclear charge radius or nuclear moments (respectively, the IS or the HFS should be greater than the Doppler broadening).

Here we report on an approach to largely eliminate the Doppler broadening of the spectroscopic transition through the use of 2-photon transitions induced by co- and counter-propagating laser beams from the same laser source. The general theory of a 2-photon quantum transition was first described in the thesis of M. Göppert-Mayer in 1930 [4], whilst the method for Doppler-free spectroscopy was first suggested by Vasilenko et al. in [5]: two photons with opposite momentum get resonantly absorbed via a virtual state inside the atom, eliminating any contribution from its relative movement. Applying Doppler-free 2-photon ionization in-source in combination with the array of ion or radioisotope identification methods available at the ISOLDE facility, will enable high-resolution (<100 MHz) and high sensitivity (<1 ion/s) studies, without limitation to the heavy mass range.

Under these conditions, the spectral resolution becomes limited by the laser linewidth. For a given laser power, the relatively low cross section of the 2-photon transition is mitigated by the gain in spectral brightness achieved by the desired reduction of the experimental laser linewidth.

Nevertheless, it is expected that achieving a high efficiency will require a transition for which the intermediate virtual state lies close in
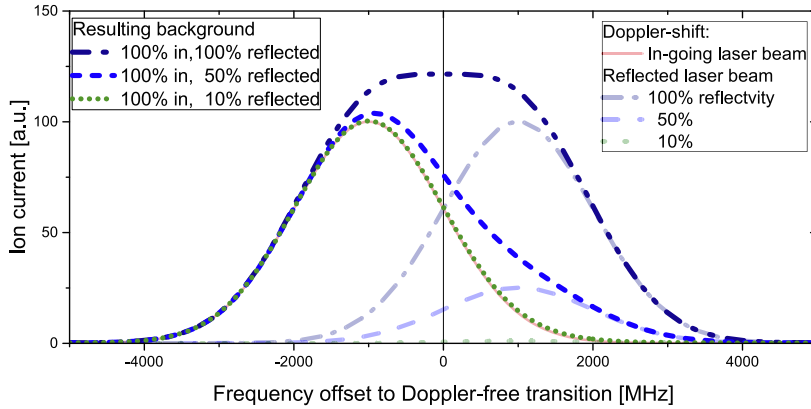
Fig. 1. Simulated Doppler broadened and -shifted background. In case of equal light intensities, the center of gravity (CoG) is not shifted. The lower the reflectivity and therefore the intensity of the out-going light, the more the CoG is shifted towards lower frequencies. Additionally, the overall broadening is reduced and the asymmetry increased as the impact of the high frequency shift component reduces.
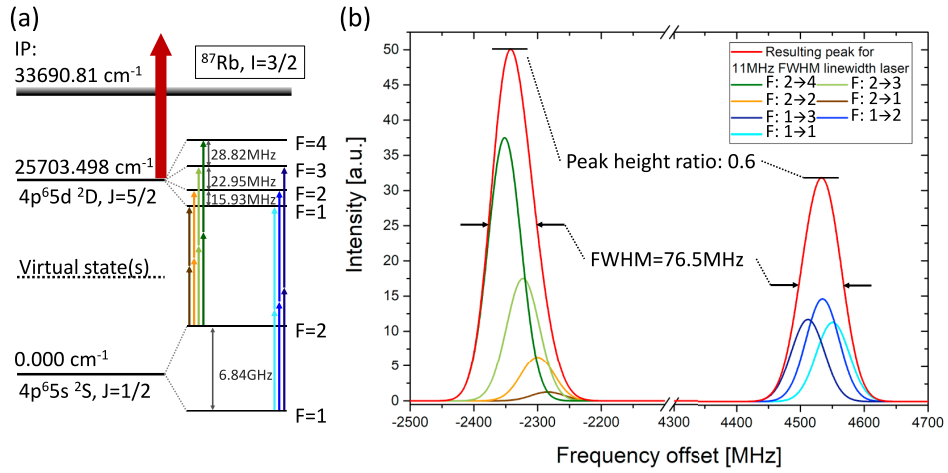

Fig. 2. (a) Laser ionization scheme for rubidium. The hyperfine structure is depicted along with the corresponding shifts (not to scale) and the possible 2-photon transitions. (b) Simulated spectrum of the 2-photon HFS transitions with an assumed laser linewidth of 11 MHz (corresponding to 20 MHz minimal achievable transition linewidth). The individual transitions are included, but can not be resolved under the experimental conditions. All data used for the simulated spectrum has been taken from [8].

energy to a real state. This can be seen from the simplified form of the equation for the transition probability P_{gf} for a transition $g \rightarrow f$ in the case of two photons of equal energy:

$$P_{gf} \propto \left(\sum_n \frac{\langle f|H|n \rangle \langle n|H|g \rangle}{\Delta \omega_n} \right)^2 \times \frac{1}{\Gamma_f}, \tag{1}$$

where H is the Hamiltonian of the electric dipole interaction between the photon and the atom, $\Delta \omega_n$ is the wavelength difference from the virtual to a real single photon transition and Γ_f is the natural linewidth of the excited state f. In a more detailed description, given in [6], the complete formula for the transition probability is given, alongside the added components for the case of absorption of two photons with the same propagation vector. As will be seen in the spectra in section 2, this gives rise to a Doppler broadened background, upon which the Doppler-free peak is superimposed. Additionally, in the experiments presented here, this background is shifted: the atom source, transfer line and ion source geometry results in an atomic sample with predominantly forward-directed velocity components (towards the extraction electrode). In the rest-frame of an atom traveling towards the exit of the ion source, the light entering the source is blue-shifted, whereas the reflected light, from the rear of the ion source is red-shifted. The shift is in the order of the temperature induced Doppler broadening and overall, in case of

equal intensities of the in- and out-going light, there will be no shift evident in the overall Doppler-broadened laser spectrum obtained. If, however, the reflectivity is less than 100%, the Doppler-broadened spectrum will be dominated by the signal associated with the incoming (blue-shifted) light. As a result, the center of gravity (CoG) of the spectrum will be shifted to the lower frequency side (see Fig. 1) of the Doppler-free center of the transition. Due to the nature and size of the Doppler broadening, it is impossible to disentangle the two different shifts from one another.

The feasibility of Doppler-free 2-photon resonance ionization spectroscopy inside a hot cavity environment has been demonstrated at Mainz University, where stable silicon isotopes were studied inside an atomic beam unit [7]. For this experiment, an open tube was used as the hot cavity, with a mirror placed outside of the vacuum chamber for reflecting the light for collinear laser beam propagation. This method is not suited for foreseen applications at ISOLDE, as the ion source and target areas are not accessible during on-line operation. Additionally, glass windows or mirrors would not survive the high radiation level. In this work we present results of experimental development performed both at Mainz University and CERN, which enabled Doppler-free measurements of rubidium 2-photon resonances inside a real ion source/target configuration of the CERN-ISOLDE facility.
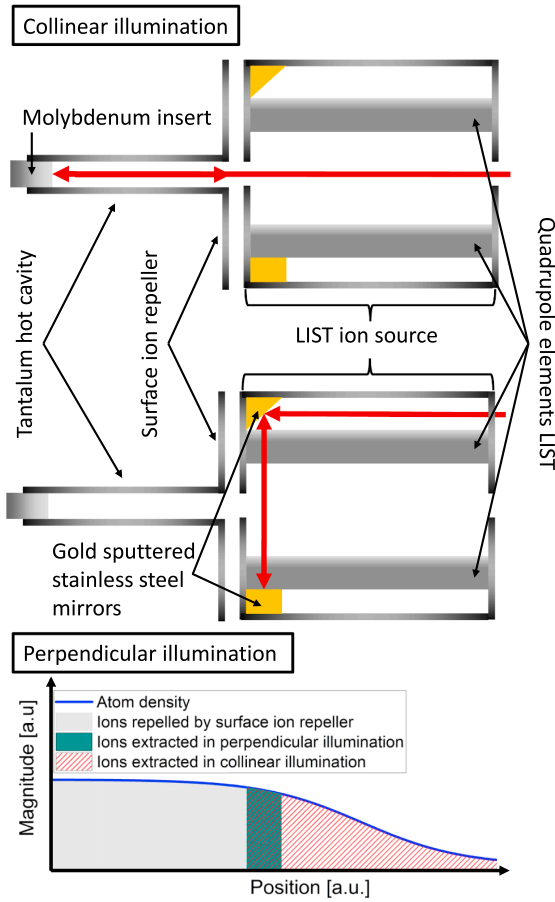
Fig. 3. Schematic depiction of the two possible operating modes of laser ionization with the LIST. In collinear mode the laser beam is reflected by the polished surface of the molybdenum insert placed at the end of the ion source. In perpendicular mode the laser beam is entering the LIST off-axis and reflected on gold plated stainless steel mirrors. For both modes suppression of ions originating inside the hot cavity is achieved by applying a positive voltage to a repeller electrode located behind the hot cavity. The ionization probability (lower plot) is the same for collinear and perpendicular illumination, but the number of atoms with which the photons interact is higher for collinear illumination (see [14] for more details).

2. Experimental setup and results

Spectroscopy was performed on ^{87}Rb. The 2-photon transition excites atoms from the $5S_{1/2}$ ground state to the $5D_{1/2}$ state. The transition, along with the HFS splitting is depicted in Fig. 2. Rubidium has been extensively studied and therefore comprehensive data is available for comparison of the spectra. However, the goal of this work was not an absolute measurement of the transition energies, but rather a measurement of the Doppler-free linewidth, in order to determine the feasibility of laser linewidth limited high-resolution in-source spectroscopy. In this work, HFS parameter as given in [8] were used for deriving the expected spectra for comparison with the data. Nevertheless, they were not used for fitting the measured spectra, since this went beyond the scope of the work presented here. At 2000 K the Doppler broadening is ~ 2.2 GHz for stable rubidium isotopes. The frequency of the spectra is given relative to the transition centroid at 25703.498 cm^{-1}.

2.1. Experiments performed at the RISIKO mass separator in Mainz

The Laser Ion Source and Trap (LIST) was used for this test since it offers the ability to suppress surface-ionized contaminants, as has been shown previously in [9]. A molybdenum cylinder (2.8 mm diameter, 6 mm length) with polished top surface was inserted into the end of the hot cavity and used for reflecting the laser beam back into the ion source, as shown in Fig. 3. In a separate test, the reflectivity of Mo was measured to be close to 50% from 250 to 800 nm at up to 1600 °C. The newest LIST design [10] also includes the possibility of perpendicular illumination of the atomic beam by displacing the laser beam and directing it towards stainless steel substrates covered with a gold layer by pulsed laser deposition. The two different geometries for the laser ionization are depicted schematically in Fig. 3. As rubidium is easily surface ionized (IP = 4.18 eV [11]) it was necessary to operate the LIST in surface-ion-suppression mode by applying a positive voltage to a repeller electrode located behind the hot cavity (offering 4–5 orders of magnitude suppression).

The laser system used for the tests comprises wavelength stabilized continuous wave (CW) diodes, fiber coupled to a seeded Ti:sapphire ring laser cavity, which was pumped by a 10 kHz Nd:YAG laser operating at 532 nm (see [7]). The Ti:sapphire cavity is based on the design by T. Kessler [12] and has been further developed by V. Sonnenschein [13]. An output power of up to 1.4 W was generated at a wavelength of 778.1 nm.

2.1.1. Collinear illumination

In order to minimize saturation broadening of the spectral lines, the power was gradually reduced until the measured linewidth did not reduce further. The corresponding power was measured to be 1.3 μW. In accordance with Eq. 1, the saturation power required for the Rb 2-photon transition is lower than that required in a transition with a bigger separation of real and virtual state(s). Although saturation was reached with powers in the μW-range, this is not expected to be the case for most applications of this technique. As will be shown later on (see subsection 2.2), higher powers are required e.g. if the mirror reflectivity is low.

The full spectral range spanning the splitting of the ground-state was scanned but is not shown in the spectrum, as no additional structures were observed. As was explained in section 1, the asymmetry of the Doppler-background stems from the non-equal intensities for photons absorbed from the co- and counter-propagating laser beams. Since the laser beams are focused to the ion-source diameter over a distance of >3 m, it can be assumed that the in-going and reflected laser beam have similar size. Therefore, no contribution to the asymmetry from the laser beam size is expected. The relatively large shift shows that the reflectivity of the molybdenum is low (estimated to be ≪ 50%).

The extracted FWHM for the quadruplet and the triplet were determined to be 85.7 ± 0.4 MHz and 81.2 ± 1.0 MHz, respectively. Taking into account the distance of the outer peaks of the multiplets and the additional linewidth broadening effects due to the absorption of two photons, the upper linewidth limit for the laser was determined to be ⩽ 12.5 MHz (compared to the Fourier-limited linewidth of ∼ 10 MHz). It was extracted by varying the assumed laser linewidth (see Fig. 2). The ratio of the peak heights was determined to be 0.84. This deviates from the expected ratio of 0.6 determined through angular-momentum coupling considerations (see [8]), but could be attributed to either saturation effects or ion source temperature fluctuations and resulting fluctuations in atom density at the ionization region. The ratio of Doppler-free signal to Doppler broadened background is 2.6 for the quadruplet and 2.7 for the triplet.

2.1.2. Perpendicular illumination

For perpendicular illumination the laser beam was directed through an off-center hole inside the extraction electrode. In this case the laser is incident upon a 45° tilted gold plated stainless steel mirror surface,
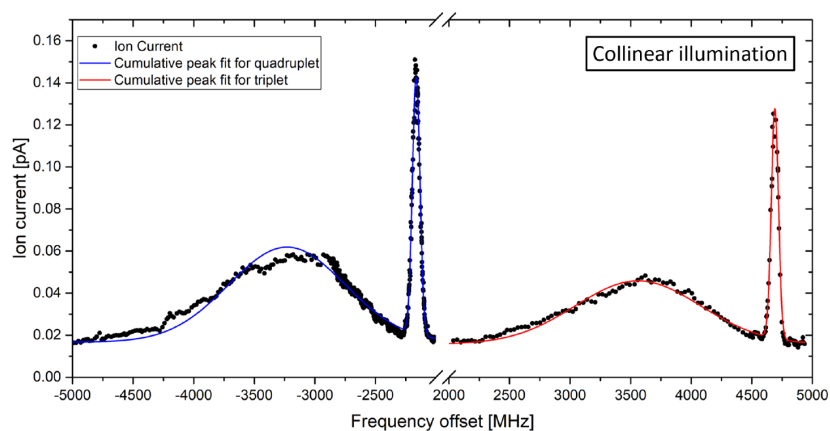
Fig. 4. Spectrum for collinear illumination of the atomic beam. The Doppler-free 2-photon excitation peaks dominate the spectrum and are flanked by a Doppler broadened and shifted background.
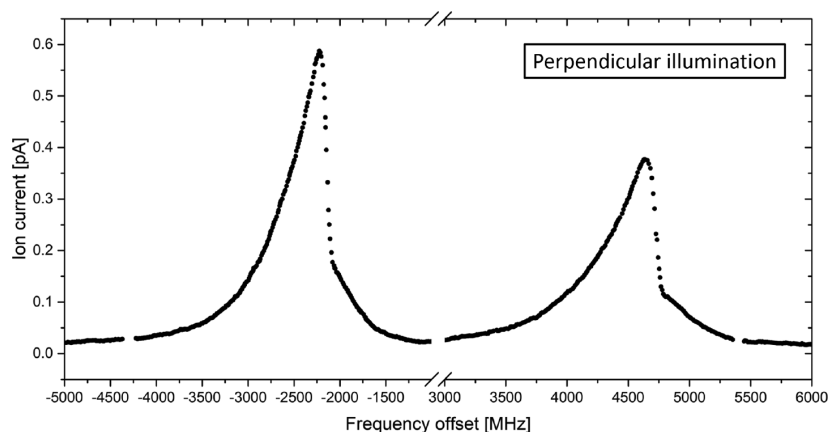

Fig. 5. Spectrum for perpendicular illumination of the atom beam. The Doppler-free 2-photon absorption peaks are completely entangled with the Doppler broadened and -shifted background. Overall the achievable resolution is reduced due to the background becoming inseparable from the signal.
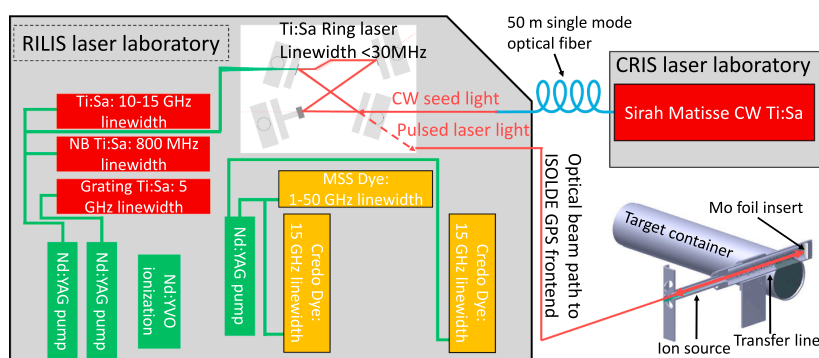

Fig. 6. Schematic layout of laser setup used for 2-photon spectroscopy at ISOLDE. The RILIS lasers along with their linewidth capabilities are shown. The newly installed seeded Ti:sapphire ring cavity is pumped by a 10 kHz repetition rate Nd:YAG pump laser at 532 nm. The seed light is provided via a 50 m long single mode optical fiber. It transports laser light at ∼ 778 nm from the CRIS to the RILIS laser laboratory. The resulting pulsed light was transported via the optical beam path leading through the GPS mass separator, into the ISOLDE target/ion source assembly. It was reflected on a molybdenum foil at the end of the transfer line, for bi-directional illumination of the atomic vapor.

positioned near the hot cavity exit, adjacent to the LIST RFQ rods (see Fig. 3). The mirrors used for perpendicular illumination of the atom cloud emerging from the hot cavity are located in the shadow of the LIST repeller, shielded from radiative heating by the hot cavity.

The obtained spectrum, shown in Fig. 5, was taken with a laser power of 240 mW after the launch mirror and not optimized for saturation broadening suppression. Perpendicular illumination results in

a reduced Doppler-broadening of the atomic line [15]. With perfect perpendicular alignment of the laser in respect to an ideal collimated atom beam, no asymmetry would be seen. Indeed this explains the lower separation distance of the Doppler broadened components of the spectrum to the Doppler-free components. The observed asymmetry in the presented spectrum is a result of the atom beam divergence and the angle of incidence of the laser beam.
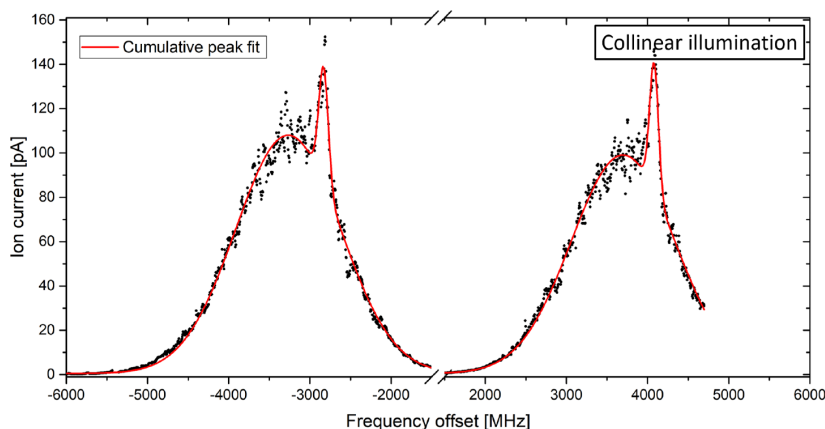
Fig. 7. Measured spectral profiles of the 2-photon resonance excitation of rubidium atoms inside the ISOLDE RILIS hot cavity. The Doppler-free 2-photon absorption peaks have linewidths of 126.7 ± 2.2 MHz for the triplet and 138.0 ± 2.4 MHz for the quadruplet.

2.2. Experiments performed at the CERN-ISOLDE facility

A schematic overview over the pump and tunable lasers in RILIS, together with their according linewidth capabilities, is depicted in Fig. 6. The ISOLDE RILIS is optimized for efficient ion beam production. The optimal laser linewidth is one which enables excitation of all atoms of interest in the interaction volume. Therefore, the lasers of the RILIS installation possess linewidths exceeding 800 MHz. For this work, to satisfy the laser linewidth requirements (<100 MHz) a new seeded Ti:-sapphire ring laser, pumped by a 10 kHz doubled Nd:YAG at 532 nm, was constructed on a breadboard. It is a miniaturized cavity based on the design from [12] and the layout of this bow-tie cavity is shown in Fig. 6. More details on this laser will be published in [16].

The CW light at 778 nm for seeding the Ti:sapphire cavity was generated by a commercial CW ring Ti:sapphire laser (Matisse 2 TS, Sirah-Lasertechnik GmbH) installed in the CRIS laser laboratory [17]. The seed light was transported via a 50 m long single-mode (SM) optical fiber, connecting the RILIS with the main laser laboratory of the CRIS collaboration. The total output power of the Matisse was 2 W, of which 100 mW were used for coupling into the fiber. After a first short (1 m) SM fiber, 70 mW were measured. With a commercial mating sleeve for SM fibers, this was then attached to the 50 m long fiber, where 25 mW emerged in RILIS. Measures, taken to avoid burning of the fiber by reverse direction light from the ring cavity (optical Faraday insulator), further attenuated the CW light transmission to the laser to ~ 10 mW. A second fiber connecting the two laser laboratories was used to measure the wavelength of the seeding CW laser simultaneously with that of the pulsed light emitted by the ring cavity using a HighFinesse/Angstrom WS7 wavelength meter installed in the RILIS laboratory. The wave-meter was calibrated before the measurements with a CW diode laser locked to the rubidium hyperfine structure (1-photon transition).

This experiment was performed in March 2018 using a dedicated ISOLDE target and ion source development assembly (#594, Ta ion source) with a flat molybdenum foil inserted into the back of the transfer line. This unit had been used in the year 2017 for laser ionization scheme development of selenium [18]. A Rb dispenser was connected to the target/ion source assembly. These dispensers can be individually resistively heated to release an atomic vapor of the element of interest. The GPS front end and mass separator (General Purpose Separator with one 60° bending magnet) were used for the tests, and the ion beam current was recorded using a Faraday cup (GPS.FC490), situated behind the mass separation magnet. A sufficient suppression of rubidium surface ionization was achieved by reducing the heating

currents of target and ion source cavity to 200 A and 50 A, respectively, corresponding to temperatures of <850 °C and <400 °C. The values cannot be given more precisely as the temperature calibration for target and ion source were performed under different conditions.

The laser beam positions were optimized to maximize the Doppler-free signal. This corresponds to the best possible overlap of the counter-propagating laser beams, so that finally the height ratio between narrow Doppler-free signal and Doppler broadened and -shifted back-ground of 1.3 for the quadruplet and 1.4 for the triplet were reached, as can be seen in Fig. 7. The FWHM of the Doppler-free resonance, measured at a laser power of 2 W before the laser beam delivery system to the ion source, was extracted to be 126.7 ± 2.2 MHz for the triplet and 138.0 ± 2.4 MHz for the quadruplet. Taking into account the high laser power compared to the below-saturation measurements in Mainz, power broadening is assumed to be the main reason for the higher experimental linewidth. Additionally, the shorter resonator length leads to a shorter pulse length, increasing the Fourier-limited linewidth of the ring laser to ~ 21 MHz.

Judging by the reduced Doppler-free to Doppler broadened signal height ratio, we conclude that the mirror reflectivity in this case was lower than was the case for the RISIKO measurements (see Fig. 4). As the target had been used prior to the experiment in 2018, a number of explanations for poor reflectivity of the foil are plausible:

- Depositions on the foil.
- Ablation of the molybdenum foil: a high power laser, which has been shown to cause ablation of the molybdenum foil during on-line experiments in 2018, had been used extensively with target #594. It is therefore assumed that the central part of the foil was damaged.
- Deformation or repositioning of the foil after repeated heating and cooling cycles of the target, or during target handling.

3. Outlook

In this first demonstration of in-source Doppler-free 2-photon spectroscopy at ISOLDE, the new seeded Ti:sapphire ring cavity has been shown to perform as required. A Doppler-free signal was successfully recorded. However, the signal height ratios indicate that there is room for significant improvement through an increase in mirror reflectivity. To this end, an alternative approach will be attempted. The mirror will be combined with the anode grid of the VADIS. An optimized environment for resonance laser ionization can be provided in the new VAD(L) IS design, suppressing surface ionization and

K. Chrysalidis, et al.

enhancing extraction of laser-ionized species [19]. The possibility to install a perforated molybdenum mirror at the junction of the transfer line with the hot cavity is an alternative to this which is also being explored.

Systematic investigations into laser linewidth dependency of efficiency and saturation effects will be performed alongside studies of the impact of close-lying real intermediate steps to the signal-to-background ratio. This method opens perspectives to development of resonance ionization schemes for elements with first step transitions requiring laser light at extremely short wavelengths, not easily achievable at RILIS. Schemes based on 2-photon transitions can be developed to overcome this limitation, enabling resonance laser ionization for elements that have so far been inaccessible. There are several examples, e.g. P, Kr, C and many more. Some feasible 2-photon transitions from the ground state can be found in the reviews '*A resonance ionization spectroscopy/resonance ionization mass spectrometry data service. I-V*' by E. Saloman [20–24], giving a starting point for such developments.

Acknowledgments

References

[1] V. Fedosseev, et al., J. Phys. G 44 (2017) 084006.
[2] B.A. Marsh, et al., Nat. Phys. 14 (2018) 1745–2473.
[3] T.D. Goodacre, et al., NIM B 376 (2016) 39–45.
[4] M. Göppert-Mayer, Ann. Phys. 401 (1931) 273–294.
[5] L. Vasilenko, et al., JETP Lett. 12 (1970) 113.
[6] N. Bloembergen, M.D. Levenson, 1976, pp. 315–369.
[7] K. Wendt, et al., Phys. Rev. A 88 (2013) 1–8.
[8] F. Nez, et al., Opt. Commun. 102 (1993) 432–438.
[9] D. Fink, et al., NIM B 344 (2015) 83–95.
[10] R. Heinke, et al., Hyperfine Interact. 238 (2016) 6.
[11] NIST Atomic Spectra Database (extracted 08.10.2018).
[12] T. Kessler, et al., Laser Phys. 18 (2008) 842.
[13] V. Sonnenschein, et al., Characterization of a pulsed injection-locked Ti:sapphire laser and its application to high resolution resonance ionization spectroscopy of copper, Laser Phys. (2017).
[14] R. Heinke, et al., NIM B, 2019. In this issue.
[15] D.N. Stacey, K. Burnett, Sci. Prog. (1933-) 73 (1989) 351–387.
[16] K. Chrysalidis, M. Reponen, et al., Technical review of Ti:sapphire laser development within the scope of JRA RESIST, 2019. (In preparation).
[17] A. Koszorus, et al., NIM B, 2019. In this issue.
[18] K. Chrysalidis, et al., Developments towards the delivery of selenium ion beams at ISOLDE, 2019. In preparation.
[19] Y.M. Palenzuela, et al., NIM B 431 (2018) 59–66.
[20] E. Saloman, Spectrochim. Act. B (1990).
[21] E. Saloman, Spectrochim. Act. B (1991).
[22] E. Saloman, Spectrochim. Act. B (1992).
[23] E. Saloman, Spectrochim. Act. B (1993).
[24] E. Saloman, Spectrochim. Act. B (1994).

Conclusion and Outlook

The main goals of the RILIS are ion beam production and laser spectroscopy. This thesis has addressed these applications and the related laser development requirements for improving the RILIS capabilities in both areas.

The laser ionization scheme development presented here serves the purpose of further extending the number of available elements, namely for selenium, molybdenum and titanium. Additionally, an alternative ionization scheme for samarium was established, this time, with the attained goal of greatly simplifying the laser setup without sacrificing ionization efficiency. On the other hand, the goal was to identify and simplify ionization schemes utilizing e.g. three steps generated by dye lasers. One of the shortcomings of the RILIS installation, which becomes particularly apparent during ionization scheme development, is the inconvenience of accessing the spectral range between 470-540 nm. In order to address this, an efficient and robust solid-state Raman laser has been developed. It can be be pumped by the tunable Ti:sapphire lasers, effectively extending

their spectral range into the UV-pumped dye laser range, extending the spectral range covered by solid-state lasers significantly. This will help to further decrease the use of dye lasers, in this way reducing maintenance and increasing the operational capacity of RILIS. The Raman laser developments are still on-going, but an improved cavity design will help to make the laser simpler and more efficient. Its first applications at RILIS are foreseen in mid 2020.

The in-source laser spectroscopy of dysprosium has pushed the RILIS resolution to its limits. Most applications of in-source RIS for nuclear structure studies have been devoted to the heavier ($Z = 82$) region, where the field shift dominates the overall isotope shift. This work on Dy ($Z = 66$) approaches the resolution limitations of this technique for nuclear charge radii measurements. Nevertheless, the changes in mean-squared charge radii for ^{145m,147m}Dy were extracted and add to the understanding of the $Z = 64$ proton subshell closure. The newly developed intra-cavity frequency doubled grating Ti:sapphire with the integrated thick etalon for linewidth reduction was used, offering the required flexibility to rapidly switch between "ion production" and "spectroscopy" modes. The unsurpassed sensitivity and combination of laser spectroscopy with high precision mass and decay measurements is unique at ISOLDE. Improving the resolution and going towards the Doppler-free method of 2-photon spectroscopy will expand the useful reach of the in-source spectroscopy method to other areas of the nuclear chart. The first demonstration of feasibility at ISOLDE required the construction and characterization of a seeded ring Ti:sapphire laser cavity, adding the first pulsed sub 100 MHz linewidth laser to the RILIS installation. The first results have shown that the reflectivity of the mirror needs to be improved in order to increase the overall Doppler-free signal and decrease the background asymmetry. Rb has proven to be an ideal element for probing and characterizing the mirror properties. Nevertheless, once optimal conditions for reflecting the laser beams have been found, existing 2-photon excitation schemes should be tested and applied e.g. to increase the resolution on elements already studied with the in-source technique. Investigations into the application of 2-photon excitation for increased isomer selectivity and accessibility of elements with high lying first steps, like

Se, are envisaged. The main aim is of course to study lighter isotopes, especially far from stability, making use of the high sensitivity and therefore low yield requirements of in-source laser spectroscopy.

Bibliography

[1] P. P. Sorokin and J. R. Lankard.

Stimulated Emission Observed from an Organic Dye, Chloro-aluminum Phthalo-
cyanine.

IBM J. Res. Dev., 10(2):162–163, mar 1966.

[2] Fritz P. Schäfer, Werner Schmidt, and Jürgen Volze.

ORGANIC DYE SOLUTION LASER.

Appl. Phys. Lett., 9(8):306–309, oct 1966.

[3] O. G. Peterson, S. A. Tuccio, and B. B. Snavely.

cw OPERATION OF AN ORGANIC DYE SOLUTION LASER.

Appl. Phys. Lett., 17(6):245–247, sep 1970.

[4] T. W. Hänsch.

Repetitively Pulsed Tunable Dye Laser for High Resolution Spectroscopy.

Appl. Opt., 11(4):895, apr 1972.

[5] V.S. Letokhov R.V. Ambartsumian, V.P. Kalinin.

Selective two-step photoionization of rubidium atoms with laser radiation.

JETP Lett., 13(6):217–219, 1971.

[6] R. V. Ambartzymian and V. S. Letokhov.

Selective Two-Step (STS) Photoionization of Atoms and Photodissociation of Molecules by Laser Radiation.

Appl. Opt., 11(2):354, feb 1972.

[7] P. Campbell, I.D. Moore, and M.R. Pearson.

Laser spectroscopy for nuclear structure physics.

Prog. Part. Nucl. Phys., 86:127–180, jan 2016.

[8] R. Neugart, S. L. Kaufman, W. Klempt, G. Moruzzi, E.-W. Otten, and B. Schinzler.

High-Resolution Spectroscopy in Fast Atomic Beams.

pages 446–447. 1977.

[9] Á. Koszorús, J. Billowes, C.L. Binnersley, M.L. Bissell, T.E. Cocolios, B.S. Cooper, R.P. de Groote, G.J. Farooq-Smith, V.N. Fedosseev, K.T. Flanagan, S. Franchoo, R.F. Garcia Ruiz, W. Gins, K.M. Lynch, G. Neyens, F.P. Gustafsson, C.M. Ricketts, H.H. Stroke, A. Vernon, S.G. Wilkins, and X.F. Yang.

Resonance ionization schemes for high resolution and high efficiency studies of exotic nuclei at the CRIS experiment.

Nucl. Instruments Methods Phys. Res. Sect. B Beam Interact. with Mater. Atoms, apr 2019.

[10] R.F. Garcia Ruiz, M.L. Bissell, A. Gottberg, M. Stachura, L. Hemmingsen, G. Neyens, and N. Severijns.

Perspectives for the VITO beam line at ISOLDE, CERN.

EPJ Web Conf., 93:07004, may 2015.

[11] S. Sels, P. Fischer, H. Heylen, V. Lagaki, S. Lechner, F.M. Maier, P. Plattner, M. Rosenbusch, F. Wienholtz, R.N. Wolf, W. Nörtershäuser, L. Schweikhard, and S. Malbrunot-Ettenauer.

First steps in the development of the Multi Ion Reflection Apparatus for Collinear Laser Spectroscopy.

NIM B, 10.1016/j., may 2019.

[12] G.D. Alkhazov, A.E. Barzakh, V.P. Denisov, K.A. Mezilev, Yu.N. Novikov, V.N. Panteleyev, A.V. Popov, E.P. Sudentas, V.S. Letokhov, V.I. Mishin, V.N. Fedosseev, S.V. Andreyev, D.S. Vedeneyev, and A.D. Zyuzikov.

A new highly efficient method of atomic spectroscopy for nuclides far from stability.

Nucl. Instruments Methods Phys. Res. Sect. B Beam Interact. with Mater. Atoms, 69(4):517–520, jul 1992.

[13] S. Sels, T. Day Goodacre, B.A. Marsh, A. Pastore, W. Ryssens, Y. Tsunoda, N. Althubiti, B. Andel, A.N. Andreyev, D. Atanasov, A.E. Barzakh, M. Bender, J. Billowes, K. Blaum, T.E. Cocolios, J.G. Cubiss, J. Dobaczewski, G.J. Farooq-Smith, D.V. Fedorov, V.N. Fedosseev, K. T. Flanagan, L. P. Gaffney, L. Ghys, P.-H. Heenen, M. Huyse, S. Kreim, D. Lunney, K. M. Lynch, V. Manea, Y. Martinez Palenzuela, T. M. Medonca, P. L. Molkanov, T. Otsuka, J. P. Ramos, R.E. Rossel, S. Rothe, L. Schweikhard, M.D. Seliverstov, P. Spagnoletti, C. Van Beveren, P. Van Duppen, M. Veinhard, E. Verstraelen, A. Welker, K.D.A. Wendt, F. Wienholtz, R. N. Wolf, and A. Zadvornaya.

Shape staggering of midshell mercury isotopes from in-source laser spectroscopy compared with density-functional-theory and Monte Carlo shell-model calculations.

Phys. Rev. C, 99(4):044306, apr 2019.

[14] J.G. Cubiss, A.E. Barzakh, M.D. Seliverstov, A.N. Andreyev, B. Andel, S. Antalic, P. Ascher, D. Atanasov, D. Beck, J. Bieroń, K. Blaum, Ch. Borgmann, M. Breitenfeldt, L. Capponi, T.E. Cocolios, T. Day Goodacre, X. Derkx, H. De Witte, J. Elseviers, D.V. Fedorov, V.N. Fedosseev, S. Fritzsche, L. P. Gaffney, S. George, L. Ghys, F. P. Heßberger, M. Huyse, N. Imai, Z. Kalaninová, D. Kisler, U. Köster, M. Kowalska, S. Kreim, J. F. W. Lane, V. Liberati, D. Lunney, K. M. Lynch, V. Manea, B.A. Marsh, S. Mitsuoka, P. L. Molka-

nov, Y. Nagame, D. Neidherr, K. Nishio, S. Ota, D. Pauwels, L. Popescu, D. Radulov, E. Rapisarda, J. P. Revill, M. Rosenbusch, R.E. Rossel, S. Rothe, K. Sandhu, L. Schweikhard, S. Sels, V. L. Truesdale, C. Van Beveren, P. Van den Bergh, Y. Wakabayashi, P. Van Duppen, K.D.A. Wendt, F. Wienholtz, B. W. Whitmore, G. L. Wilson, R. N. Wolf, and K. Zuber.

Charge radii and electromagnetic moments of $^{195-211}$At.

Phys. Rev. C, 97(5):054327, may 2018.

[15] B.A. Marsh, T. Day Goodacre, S. Sels, Y. Tsunoda, B. Andel, A.N. Andreyev, N. A. Althubiti, D. Atanasov, A.E. Barzakh, J. Billowes, K. Blaum, T.E. Cocolios, J.G. Cubiss, J. Dobaczewski, G.J. Farooq-Smith, D.V. Fedorov, V.N. Fedosseev, K.T. Flanagan, L. P. Gaffney, L. Ghys, M. H. Huyse, S. Kreim, D. Lunney, K.M. Lynch, V. Manea, Y. Martinez Palenzuela, P.L. Molkanov, T. Otsuka, A. Pastore, M. Rosenbusch, R.E. Rossel, S. Rothe, L. Schweikhard, M.D. Seliverstov, P. Spagnoletti, C. Van Beveren, P. Van Duppen, M. Veinhard, E. Verstraelen, A. Welker, K.D.A. Wendt, F. Wienholtz, R.N. Wolf, A. Zadvornaya, and K. Zuber.

Characterization of the shape-staggering effect in mercury nuclei.

Nat. Phys., 2018.

[16] J.G. Cubiss, A.E. Barzakh, A.N. Andreyev, M. Al Monthery, N. Althubiti, B. Andel, S. Antalic, D. Atanasov, K. Blaum, T.E. Cocolios, T. Day Goodacre, R.P. de Groote, A. de Roubin, G.J. Farooq-Smith, D.V. Fedorov, V.N. Fedosseev, R. Ferrer, D.A. Fink, L.P. Gaffney, L. Ghys, A. Gredley, R.D. Harding, F. Herfurth, M. Huyse, N. Imai, D.T. Joss, U. Köster, S. Kreim, V. Liberati, D. Lunney, K.M. Lynch, V. Manea, B.A. Marsh, Y. Martinez Palenzuela, P.L. Molkanov, P. Mosat, D. Neidherr, G.G. O'Neill, R.D. Page, T.J. Procter, E. Rapisarda, M. Rosenbusch, S. Rothe, K. Sandhu, L. Schweikhard, M.D. Seliverstov, S. Sels, P. Spagnoletti, V.L. Truesdale, C. Van Beveren, P. Van Duppen, M. Veinhard, M. Venhart, M. Veselský, F. Wearing, A. Welker, F. Wienholtz, R.N. Wolf, S.G. Zemlyanoy, and K. Zuber.

Change in structure between the I = 1/2 states in ^{181}Tl and ^{177,179}Au.

Phys. Lett. B, 786:355–363, nov 2018.

[17] R. Lică, H. Mach, L. M. Fraile, A. Gargano, M.J.G. Borge, N. Mărginean, C. O. Sotty, V. Vedia, A.N. Andreyev, G. Benzoni, P. Bomans, R. Borcea, L. Coraggio, C. Costache, H. De Witte, F. Flavigny, H. Fynbo, L. P. Gaffney, P. T. Greenlees, L. J. Harkness-Brennan, M. Huyse, P. Ibáñez, D. S. Judson, J. Konki, A. Korgul, T. Kröll, J. Kurcewicz, S. Lalkovski, I. Lazarus, M. V. Lund, M. Madurga, R. Mărginean, I. Marroquín, C. Mihai, R. E. Mihai, A. I. Morales, E. Nácher, A. Negret, R. D. Page, J. Pakarinen, S. Pascu, V. Paziy, A. Perea, M. Pérez-Liva, E. Picado, V. Pucknell, E. Rapisarda, P. Rahkila, F. Rotaru, J. A. Swartz, O. Tengblad, P. Van Duppen, M. Vidal, R. Wadsworth, W. B. Walters, and N. Warr.

Fast-timing study of the l-forbidden $1/2^+ \rightarrow 3/2^+$ M1 transition in ^{129}Sn.

Phys. Rev. C, 93(4):044303, apr 2016.

[18] R.N. Wolf, D. Beck, K. Blaum, Ch. Böhm, Ch. Borgmann, M. Breitenfeldt, F. Herfurth, A. Herlert, M. Kowalska, S. Kreim, D. Lunney, S. Naimi, D. Neidherr, M. Rosenbusch, L. Schweikhard, J. Stanja, F. Wienholtz, and K. Zuber.

On-line separation of short-lived nuclei by a multi-reflection time-of-flight device.

Nucl. Instruments Methods Phys. Res. Sect. A Accel. Spectrometers, Detect. Assoc. Equip., 686:82–90, sep 2012.

[19] B.A. Marsh, L.-E. Berg, D.V. Fedorov, V.N. Fedosseev, O. J. Launila, M. Lindroos, R. Losito, F. K. Österdahl, T. Pauchard, I. T. Pohjalainen, U. Sassenberg, M.D. Seliverstov, A.M. Sjödin, and G. Tranströmer.

The ISOLDE RILIS pump laser upgrade and the LARIS Laboratory.

Hyperfine Interact., 196(1-3):129–141, feb 2010.

[20] S. Rothe.

An all-solid state laser system for the laser ion source RILIS and in-source laser spectroscopy of astatine at ISOLDE, CERN.

(September), 2012.

[21] R.E. Rossel.

Network Distributed Data Acquisition, Storage, and Graphical Live Display Software for a Laser Ion Source at CERN.

PhD thesis, Fachhochschule Wiesbaden, 2014.

[22] R.E. Rossel.

A Distributed Monitoring and Control System for the Laser Ion Source RILIS at CERN-ISOLDE.

PhD thesis, Fachhochschule Wiesbaden, 2015.

[23] T.E. Cocolios, B.A. Marsh, V.N. Fedosseev, S. Franchoo, G. Huber, Mark Huyse, A.M. Ionan, K. Johnston, U. Köster, Y. Kudryavtsev, M.D. Seliverstov, E. Noah, T. Stora, and P. Van Duppen.

Resonant laser ionization of polonium at rilis-isolde for the study of ground- and isomer-state properties.

Nucl. Instruments Methods Phys. Res. Sect. B Beam Interact. with Mater. Atoms, 266(19-20):4403–4406, oct 2008.

[24] D.A. Fink, S. Richter, K. Blaum, R. Catherall, B. Crepieux, V.N. Fedosseev, A. Gottberg, T. Kron, B.A. Marsh, C. Mattolat, S. Raeder, R.E. Rossel, S. Rothe, F. Schwellnus, M.D. Seliverstov, A.M. Sjödin, T. Stora, P. Suominen, and K.D.A. Wendt.

On-line implementation and first operation of the Laser Ion Source and Trap at ISOLDE/CERN.

Nucl. Instruments Methods Phys. Res. Sect. B Beam Interact. with Mater. Atoms, 344:83–95, feb 2015.

[25] D.A. Fink, R. Ferrer, K. Sandhu, M. Veselský, S. Rothe, L. Ghys, R.P. de Groote, K.M. Lynch, C. Van Beveren, P. Van Duppen, A.N. Andreyev, M. Venhart, U. Köster, J. Lane, B.A. Marsh, V. Liberati, T.E. Cocolios, P.L. Molkanov,

E. Rapisarda, M.D. Seliverstov, M. H. Huyse, D.V. Fedorov, V.N. Fedosseev, A.E. Barzakh, T. J. Procter, and A.M. Sjödin.

Changes in mean-squared charge radii and magnetic moments of Tl179–184 measured by in-source laser spectroscopy .

Phys. Rev. C, 95(1):1–12, 2017.

[26] D.A. Fink.

Improving the Selectivity of the ISOLDE Resonance Ionization Laser Ion Source and In-Source Laser Spectroscopy of Polonium.

Phd thesis, Universität Heidelberg, 2014.

[27] S. Richter.

Implementierung der Laserionenquellenfalle LIST bei ISOLDE und Validierung der Spezifikationen, Effizienz und Selektivität.

Phd thesis, Johannes Gutenberg-Universität Mainz, 2015.

[28] F. Schwellnus, R. Catherall, B. Crepieux, V.N. Fedosseev, B.A. Marsh, Ch. Mattolat, M. Menna, F.K. Österdahl, S. Raeder, T. Stora, and K.D.A. Wendt.

Study of low work function materials for hot cavity resonance ionization laser ion sources.

Nucl. Instruments Methods Phys. Res. Sect. B Beam Interact. with Mater. Atoms, 267(10):1856–1861, may 2009.

[29] S. Rothe, R. Catherall, B. Crepieux, T. Day Goodacre, V.N. Fedosseev, T. Giles, B.A. Marsh, J.P. Ramos, and R.E. Rossel.

Advances in surface ion suppression from RILIS: Towards the Time-of-Flight Laser Ion Source (ToF-LIS).

Nucl. Instruments Methods Phys. Res. Sect. B Beam Interact. with Mater. Atoms, 376:86–90, jun 2016.

[30] T. Day Goodacre.

Developments of the ISOLDE RILIS for radioactive ion beam production and the results of their application in the study of exotic mercury isotopes.

Phd thesis, University of Manchester, 2016.

[31] T. Day Goodacre, J. Billowes, R. Catherall, T.E. Cocolios, B. Crepieux, D.V. Fedorov, V.N. Fedosseev, L. P. Gaffney, T. Giles, A. Gottberg, K.M. Lynch, B.A. Marsh, T. M. Mendonça, J. P. Ramos, R.E. Rossel, S. Rothe, S. Sels, C. O. Sotty, T. Stora, C. Van Beveren, and M. Veinhard.

Blurring the boundaries between ion sources: The application of the RILIS inside a FEBIAD type ion source at ISOLDE.

Nucl. Instruments Methods Phys. Res. Sect. B Beam Interact. with Mater. Atoms, 376:39–45, 2016.

[32] Y. Martinez Palenzuela, B.A. Marsh, J. Ballof, R. Catherall, K. Chrysalidis, T.E. Cocolios, B. Crepieux, T. Day Goodacre, V.N. Fedosseev, M. H. Huyse, P. B. Larmonier, J. P. Ramos, S. Rothe, J. D.A. Smith, T. Stora, P. Van Duppen, and S.G. Wilkins.

Enhancing the extraction of laser-ionized beams from an arc discharge ion source volume.

Nucl. Instruments Methods Phys. Res. Sect. B Beam Interact. with Mater. Atoms, 431(June):59–66, 2018.

[33] Y. Martinez Palenzuela.

Characterization and optimization of a versatile laser and electron-impact ion source for radioactive ion beam production at ISOLDE and MEDICIS.

Phd thesis, KU Leuven, 2019.

[34] W. Demtröder.

Experimentalphysik 3.

Springer-Lehrbuch. Springer Berlin Heidelberg, Berlin, Heidelberg, 2016.

[35] V.S. Letokhov.

Laser Photoionization Spectroscopy.

Acadamic Press, Inc., 1 edition, 1987.

[36] Malvin Carl Teich Bahaa E. A. Saleh.

Fundamentals of Photonics.

Wiley, 2 edition, 2013.

[37] W. Demtröder.

Laserspektroskopie.

Springer Berlin Heidelberg, Berlin, Heidelberg, 2000.

[38] M. Reponen, I.D. Moore, T. Kessler, I. Pohjalainen, S. Rothe, and V. Sonnen-
schein.

Laser developments and resonance ionization spectroscopy at IGISOL.

EPJ A, 48(4):1–15, 2012.

[39] Robert Karplus and Julian Schwinger.

A Note on Saturation in Microwave Spectroscopy.

Phys. Rev., 73(9):1020–1026, may 1948.

[40] S. Raeder.

*Spurenanalyse von Aktiniden in der Umwelt mittels Resonanzionisations-
Massenspektrometrie*.

PhD thesis, Johannes Gutenberg-Universität Mainz, 2011.

[41] J. Eggert.

Über den Dissoziationszustand der Fixsterngase.

Phys. Zeitschriften, 20:570, 1919.

[42] Megh Nad Saha.

LIII. Ionization in the solar chromosphere.

London, Edinburgh, Dublin Philos. Mag. J. Sci., 40(238):472–488, oct 1920.

[43] M. J. Dresser.

The Saha-Langmuir Equation and its Application.

J. Appl. Phys., 39(1):338–339, jan 1968.

[44] K. H. Kingdon and Irving Langmuir.

The Removal of Thorium from the Surface of a Thoriated Tungsten Filament by
Positive Ion Bombardment.

Phys. Rev., 22(2):148–160, aug 1923.

[45] U. Fano.

Effects of configuration interaction on intensities and phase shifts - Fano - Phys Rev 124 1866.pdf.

Phys. Rev., 124(6):1866–1878, 1961.

[46] B.A. Marsh.

Resonance Ionization Laser Ion Sources.

61 pages,:61, 2013.

[47] S. Rothe, T. Day Goodacre, D.V. Fedorov, V.N. Fedosseev, B.A. Marsh, P.L. Molkanov, R.E. Rossel, M.D. Seliverstov, M. Veinhard, and K.D.A. Wendt.

Laser ion beam production at CERN-ISOLDE: New features – More possibilities.

Nucl. Instruments Methods Phys. Res. Sect. B Beam Interact. with Mater. Atoms, 376:91–96, jun 2016.

[48] L. Gastaldo, K. Blaum, K. Chrysalidis, T. Day Goodacre, A. Domula, M. Door, H. Dorrer, Ch. E. Düllmann, K. Eberhardt, S. Eliseev, C. Enss, A. Faessler, P. Filianin, A. Fleischmann, D. Fonnesu, L. Gamer, R. Haas, C. Hassel, D. Hengstler, J. Jochum, K. Johnston, U. Kebschull, S. Kempf, T. Kieck, U. Köster, S. Lahiri, M. Maiti, F. Mantegazzini, B.A. Marsh, P. Neroutsos, Yu. N. Novikov, P. C. O. Ranitzsch, S. Rothe, A. Rischka, A. Saenz, O. Sander, F. Schneider, S. Scholl, R. X. Schüssler, Ch. Schweiger, F. Simkovic, T. Stora, Z. Szücs, A. Türler, M. Veinhard, M. Weber, M. Wegner, K.D.A. Wendt, and K. Zuber.

The electron capture in 163Ho experiment – ECHo.

Eur. Phys. J. Spec. Top., 226(8):1623–1694, jun 2017.

[49] R. Catherall, W Andreazza, M Breitenfeldt, A Dorsival, G.J. Focker, T P Gharsa, Giles T J, J-L Grenard, F Locci, P Martins, S Marzari, J Schipper, A Shornikov, and T. Stora.

The ISOLDE facility.

J. Phys. G Nucl. Part. Phys., 44(9):094002, sep 2017.

[50] B.A. Marsh, B. Andel, A.N. Andreyev, S. Antalic, D. Atanasov, A.E. Barzakh, B. Bastin, Ch. Borgmann, L. Capponi, T.E. Cocolios, T. Day Goodacre, M. Dehairs, X. Derkx, H. De Witte, D.V. Fedorov, V.N. Fedosseev, G.J. Focker, D.A. Fink, K.T. Flanagan, S. Franchoo, L. Ghys, M. H. Huyse, N. Imai, Z. Kalaninova, U. Köster, S. Kreim, N. Kesteloot, Yu. Kudryavtsev, J. Lane, N. Lecesne, V. Liberati, D. Lunney, K.M. Lynch, V. Manea, P.L. Molkanov, T. Nicol, D. Pauwels, L. Popescu, D. Radulov, E. Rapisarda, M. Rosenbusch, R.E. Rossel, S. Rothe, L. Schweikhard, M.D. Seliverstov, S. Sels, A.M. Sjödin, V. Truesdale, C. Van Beveren, P. Van Duppen, K.D.A. Wendt, F. Wienholtz, R.N. Wolf, and S.G. Zemlyanoy.
New developments of the in-source spectroscopy method at RILIS/ISOLDE.
Nucl. Instruments Methods Phys. Res. Sect. B Beam Interact. with Mater. Atoms, 317:550–556, dec 2013.

[51] K. Chrysalidis, A.E. Barzakh, R. Ahmed, A.N. Andreyev, J. Ballof, J.G. Cubiss, D.V. Fedorov, V.N. Fedosseev, L.M. Fraile, R.D. Harding, U. Köster, B.A. Marsh, C. Raison, J.P. Ramos, R.E. Rossel, S. Rothe, K.D.A. Wendt, and S.G. Wilkins.
In-source laser spectroscopy of dysprosium isotopes at the ISOLDE-RILIS.
Nucl. Instruments Methods Phys. Res. Sect. B Beam Interact. with Mater. Atoms, apr 2019.

[52] B. Lyot.
Un monochromateur à champ utilsant les interference en lumiere polarisee.
C. R. Acad. Sci., 197:1593–1595, 1933.

[53] D. R. Preuss and J. L. Gole.
Three-stage birefringent filter tuning smoothly over the visible region: theoretical treatment and experimental design.
Appl. Opt., 19(5):702, mar 1980.

Bibliography

[54] Shidong Zhu.

Birefringent filter with tilted optic axis for tuning dye lasers: theory and design.

Appl. Opt., 29(3):410, jan 1990.

[55] Adolf Smekal.

Zur Quantentheorie der Dispersion.

Naturwissenschaften, 11(43):873–875, oct 1923.

[56] C. V. RAMAN and K. S. KRISHNAN.

A New Type of Secondary Radiation.

Nature, 121(3048):501–502, mar 1928.

[57] Gr. Landsberg.

Molekulare Lichtzerstreuung in festen Körpern. I.

Zeitschrift für Phys., 43(9-10):773–778, sep 1927.

[58] G. Eckhardt, R. W. Hellwarth, F. J. McClung, S. E. Schwarz, D. Weiner, and E. J. Woodbury.

Stimulated Raman Scattering From Organic Liquids.

Phys. Rev. Lett., 9(11):455–457, dec 1962.

[59] R. H. Stolen, E. P. Ippen, and A. R. Tynes.

Raman Oscillation in Glass Optical Waveguide.

Appl. Phys. Lett., 20(2):62–64, jan 1972.

[60] S. Brueck and H. Kildal.

Efficient Raman frequency conversion in liquid nitrogen.

IEEE J. Quantum Electron., 18(3):310–312, mar 1982.

[61] H.M. Pask.

The design and operation of solid-state Raman lasers.

Prog. Quantum Electron., 27(1):3–56, jan 2003.

[62] E. Granados.

Mode locked lasers in the deep ultraviolet and the visible.

PhD thesis, Macquarie University, 2010.

[63] Tasoltan T. Basiev, Alexander A. Sobol, Petr G. Zverev, Vyacheslav V. Osiko, and
　　　Richard C. Powell.
　　Comparative spontaneous Raman spectroscopy of crystals for Raman lasers.
　　Appl. Opt., 38(3):594, jan 1999.

[64] H.M. Pask, P. Dekker, Richard P. Mildren, David J. Spence, and J.A. Piper.
　　Wavelength-versatile visible and UV sources based on crystalline Raman lasers.
　　Prog. Quantum Electron., 32(3-4):121–158, jan 2008.

[65] F. Scheerer, V.N. Fedosseev, H.-J. Kluge, V.I. Mishin, V.S. Letokhov, H.L. Ravn,
　　　Y. Shirakabe, S. Sundell, and O. Tengblad.
　　A chemically selective laser ion source for on-line mass separation.
　　Rev. Sci. Instrum., 63(4):2831–2833, apr 1992.

[66] Esma Mobs.
　　The CERN accelerator complex - August 2018. Complexe des accélérateurs du
　　　CERN - Août 2018.
　　OPEN-PHO-ACCEL-2016-009, OPEN-PHO-A, 2018.

[67] M.J.G. Borge and Björn Jonson.
　　ISOLDE past, present and future.
　　J. Phys. G Nucl. Part. Phys., 44(4):044011, apr 2017.

[68] K. Chrysalidis, T. Day Goodacre, V.N. Fedosseev, B.A. Marsh, P. Naubereit,
　　　S. Rothe, C. Seiffert, T. Kron, and K.D.A. Wendt.
　　Resonance ionization scheme development for europium.
　　Hyperfine Interact., 238(1):34, nov 2017.

[69] T. Day Goodacre, K. Chrysalidis, D.V. Fedorov, V.N. Fedosseev, B.A. Marsh, P.L.
　　　Molkanov, R.E. Rossel, S. Rothe, and C. Seiffert.
　　The identification of autoionizing states of atomic chromium for the resonance
　　　ionization laser ion source of the ISOLDE radioactive ion beam facility.
　　Spectrochim. Acta Part B At. Spectrosc., 129:58–63, mar 2017.

[70] T. Day Goodacre, J. Billowes, K. Chrysalidis, D.V. Fedorov, V.N. Fedosseev, B.A. Marsh, P.L. Molkanov, R.E. Rossel, S. Rothe, C. Seiffert, and K.D.A. Wendt.
RILIS-ionized mercury and tellurium beams at ISOLDE CERN.
Hyperfine Interact., 238(1):41, nov 2017.

[71] T. Day Goodacre, J. Billowes, C.L. Binnersley, M.L. Bissell, K. Chrysalidis, T.E. Cocolios, R.P. de Groote, G.J. Farooq-Smith, D.V. Fedorov, V.N. Fedosseev, K.T. Flanagan, S. Franchoo, R.F. Garcia Ruiz, W. Gins, R. Heinke, Á. Koszorús, K.M. Lynch, B.A. Marsh, P.L. Molkanov, P. Naubereit, G. Neyens, C.M. Ricketts, S. Rothe, C. Seiffert, M.D. Seliverstov, H.H. Stroke, D. Studer, A.R. Vernon, S.G. Wilkins, K.D.A. Wendt, and X.F. Yang.
Radium ionization scheme development: The first observed autoionizing states and optical pumping effects in the hot cavity environment.
Spectrochim. Acta Part B At. Spectrosc., 150:99–104, dec 2018.

[72] S. Rothe, J. Sundberg, J. Welander, K. Chrysalidis, T. Day Goodacre, V.N. Fedosseev, S. Fiotakis, O. Forstner, R. Heinke, K. Johnston, T. Kron, U. Köster, Yuan Liu, B.A. Marsh, A. Ringvall-Moberg, R.E. Rossel, C. Seiffert, D. Studer, K.D.A. Wendt, and D. Hanstorp.
Laser photodetachment of radioactive ^{128}I$^-$.
J. Phys. G Nucl. Part. Phys., 44(10):104003, oct 2017.

[73] P. Naubereit, J. Marín-Sáez, F. Schneider, A. Hakimi, M. Franzmann, T. Kron, S. Richter, and K.D.A. Wendt.
Resonance ionization spectroscopy of sodium Rydberg levels using difference frequency generation of high-repetition-rate pulsed Ti:sapphire lasers.
Phys. Rev. A, 93(5):052518, may 2016.

[74] R. Riedel, J. Rothhardt, K. Beil, B. Gronloh, A. Klenke, H. Höppner, M. Schulz, U. Teubner, C. Kränkel, J. Limpert, A. Tünnermann, M.J. Prandolini, and F. Tavella.
Thermal properties of borate crystals for high power optical parametric chirped-

pulse amplification.

Opt. Express, 22(15):17607, jul 2014.

[75] M. Piersa, A. Korgul, L.M. Fraile, J. Benito, E. Adamska, A.N. Andreyev, R. Álvarez-Rodríguez, A.E. Barzakh, G. Benzoni, T. Berry, M.J.G. Borge, M. Carmona, K. Chrysalidis, J. G. Correia, C. Costache, J.G. Cubiss, T. Day Goodacre, H. De Witte, D.V. Fedorov, V.N. Fedosseev, G. Fernández-Martínez, A. Fijałkowska, M. Fila, H. Fynbo, D. Galaviz, P. T. Greenlees, R. Grzywacz, L. J. Harkness-Brennan, C. Henrich, M. H. Huyse, A. Illana, Z. Janas, K. Johnston, D. S. Judson, V. Karanyonchev, M. Kicińska-Habior, J. Konki, J. Kurcewicz, I. Lazarus, R. Lică, H. Mach, M. Madurga, I. Marroquín, B.A. Marsh, M. C. Martínez, C. Mazzocchi, N. Mărginean, R. Mărginean, K. Miernik, C. Mihai, E. Nácher, A. Negret, B. Olaizola, R. D. Page, S. Paulaskalas, S. Pascu, A. Perea, V. Pucknell, P. Rahkila, E. Rapisarda, J.-M. Régis, F. Rotaru, S. Rothe, V. Sánchez-Tembleque, G. Simpson, C. O. Sotty, L. Stan, M. Stănoiu, M. Stryjczyk, O. Tengblad, A. Turturica, J.M. Udías, P. Van Duppen, V. Vedia, A. Villa, S. Viñals, R. Wadsworth, W.B. Walters, and N. Warr.

β decay of ^{133}In: γ emission from neutron-unbound states in ^{133}Sn.

Phys. Rev. C, 99(2):024304, feb 2019.

[76] S. Rothe, V.N. Fedosseev, T. Kron, B.A. Marsh, R.E. Rossel, and K.D.A. Wendt. Narrow linewidth operation of the RILIS titanium: Sapphire laser at ISOLDE/CERN.

Nucl. Instruments Methods Phys. Res. Sect. B Beam Interact. with Mater. Atoms, 317(PART B):561–564, 2013.

[77] T. Kessler, H. Tomita, C. Mattolat, S. Raeder, and K.D.A. Wendt.

An injection-seeded high-repetition rate Ti:Sapphire laser for high-resolution spectroscopy and trace analysis of rare isotopes.

Laser Phys., 18(7):842–849, jul 2008.

Bibliography

[78] V. Sonnenschein, I.D. Moore, S Raeder, M. Reponen, H. Tomita, and K.D.A. Wendt.

Characterization of a pulsed injection-locked Ti:sapphire laser and its application to high resolution resonance ionization spectroscopy of copper.

Laser Phys., 27(8):085701, aug 2017.

[79] V. Sonnenschein.

Laser developments and high resolution resonance ionization spectroscopy of actinide elements.

PhD thesis, 2015.

[80] National Institute of Standards and Technology.

NIST Atomic Spectra Database.

link.

[81] Peter L. Smith, Claas Heise, Jim R. Esmond, and Robert L. Kurucz.

Kurucz Database.

link.

[82] V V Kazakov Yatsenko, V G Kazakov, V S Kovalev, O I Meshkov, and A S.

Electronic structure of atoms: atomic spectroscopy information system.

Phys. Scr., 92(10).

[83] E. Leistenschneider, M. P. Reiter, S. Ayet San Andrés, B. Kootte, J. D. Holt, P. Navrátil, C. Babcock, C. Barbieri, B. R. Barquest, J. Bergmann, J. Bollig, T. Brunner, E. Dunling, A. Finlay, H. Geissel, L. Graham, F. Greiner, H. Hergert, C. Hornung, C. Jesch, R. Klawitter, Y. Lan, D. Lascar, K. G. Leach, W. Lippert, J. E. McKay, S. F. Paul, A. Schwenk, D. Short, J. Simonis, V. Somà, R. Steinbrügge, S. R. Stroberg, R. Thompson, M. E. Wieser, C. Will, M. Yavor, C. Andreoiu, T. Dickel, I. Dillmann, G. Gwinner, W. R. Plaß, C. Scheidenberger, A. A. Kwiatkowski, and J. Dilling.

Dawning of the N=32 Shell Closure Seen through Precision Mass Measurements of Neutron-Rich Titanium Isotopes.

158

Phys. Rev. Lett., 120(6):62503, 2018.

[84] S. Rothe.

Aufbau eines Chrom:Forsterit-Lasers und Resonanzionisationsspektroskopie an Strontium, Titan, Nickel, Scandium und Silicium.

Diploma thesis, Johannes Gutenberg-Universität Mainz, 2009.

[85] V.N. Fedosseev and A.K. Yusupov.

Effect of polarization of laser emission on the multistage photoionization yieldof ytterbium isotopes.

Opt. Spectrosc., 57(5):552, 1984.

[86] C. Seiffert.

Production of radioactive molecular beams for CERN-ISOLDE.

Phd thesis, TU Darmstadt, 2014.

[87] F Wenander.

Charge breeding of radioactive ions with EBIS and EBIT.

J. Instrum., 5(10):C10004–C10004, oct 2010.

[88] L. Penescu, R. Catherall, J. Lettry, and T. Stora.

Development of high efficiency Versatile Arc Discharge Ion Source at CERN ISOLDE.

Rev. Sci. Instrum., 81(2):02A906, feb 2010.

[89] V.I. Mishin, S.K. Sekatsky, V.N. Fedosseev, N.B. Buyanov, V.S. Letokhov, A.E. Barzakh, V.I. Denisov, A.G. Dernyatin, V.S. Ivanov, I.Ya. Chubukov, and G.D. Alkhazov.

Resonance photoionization spectroscopy and laser separation of ^{141}Sm and ^{164}Tm nuclear isomers.

Opt. Commun., 61(6):383–386, mar 1987.

[90] V.N. Fedosseev, K. Chrysalidis, T. Day Goodacre, B.A. Marsh, S. Rothe, C. Seiffert, and K.D.A. Wendt.

Ion beam production and study of radioactive isotopes with the laser ion source at ISOLDE.

J. Phys. G Nucl. Part. Phys., 44(8):084006, aug 2017.

[91] W. H. King.

Isotope Shifts in Atomic Spectra.

Springer US, Boston, MA, 1984.

[92] Ernst W. Otten.

Nuclear Radii and Moments of Unstable Isotopes.

In *Treatise Heavy Ion Sci.*, pages 517–638. Springer US, Boston, MA, 1989.

[93] B. Cheal, T.E. Cocolios, and S. Fritzsche.

Laser spectroscopy of radioactive isotopes: Role and limitations of accurate isotope-shift calculations.

Phys. Rev. A, 86(4):042501, oct 2012.

[94] K. Blaum, J. Dilling, and W. Nörtershäuser.

Precision atomic physics techniques for nuclear physics with radioactive beams.

Phys. Scr., T152(T152):014017, jan 2013.

[95] E. C. SELTZER.

K X-Ray Isotope Shifts.

Phys. Rev., 188(4):1916–1919, dec 1969.

[96] D. Berdichevsky and F. Tondeur.

Nuclear core densities, isotope shifts, and the parametrization of the droplet model.

Zeitschrift für Phys. A Atoms Nucl., 322(1):141–147, mar 1985.

[97] G.D. Alkhazov, E.Ye. Berlovich, and V.N. Panteleyev.

A new highly efficient selective laser ion source.

Nucl. Instruments Methods Phys. Res. Sect. A Accel. Spectrometers, Detect. Assoc. Equip., 280(1):141–143, aug 1989.

[98] U Köster, V.N. Fedosseev, V.I Mishin, L. Weissman, M Huyse, K Kruglov, W.F Mueller, P Van Duppen, J Van Roosbroeck, P Thirolf, H.G Thomas, D Weis-

shaar, W Schulze, R. Borcea, M La Commara, H Schatz, K Schmidt, S Röttger, G Huber, V. Sebastian, K.L Kratz, R. Catherall, U. Georg, J Lettry, M Oinonen, H.L. Ravn, H Simon, and ISOLDE collaboration.
Isomer separation of ^{70g}Cu and ^{70m}Cu with a resonance ionization laser ion source.
Nucl. Instruments Methods Phys. Res. Sect. B Beam Interact. with Mater. Atoms, 160(4):528–535, apr 2000.

[99] L. Weissman, U. Köster, R. Catherall, S. Franchoo, U. Georg, O. Jonsson, V.N. Fedosseev, V. I. Mishin, M.D. Seliverstov, J. Van Roosbroeck, S. Gheysen, M. Huyse, K. Kruglov, G. Neyens, and P. Van Duppen.
Magnetic moments of ^{68}Cu^{g,m} and ^{70}Cu^{g,m_1,m_2} nuclei measured by in-source laser spectroscopy.
Phys. Rev. C, 65(2):024315, jan 2002.

[100] N.J. Stone, U. Köster, J. Rikovska Stone, D.V. Fedorov, V.N. Fedosseev, K. T. Flanagan, M. Hass, and S. Lakshmi.
Magnetic dipole moments of ^{58}Cu and ^{59}Cu by in-source laser spectroscopy.
Phys. Rev. C, 77(6):067302, jun 2008.

[101] K. T. Flanagan, P. Vingerhoets, M. Avgoulea, J. Billowes, M.L. Bissell, K. Blaum, B. Cheal, M. De Rydt, V.N. Fedosseev, D. H. Forest, Ch. Geppert, U. Köster, M. Kowalska, J. Krämer, K. L. Kratz, A. Krieger, E. Mané, B.A. Marsh, T. Materna, L. Mathieu, P. L. Molkanov, R. Neugart, G. Neyens, W. Nörtershäuser, M.D. Seliverstov, O. Serot, M. Schug, M. A. Sjoedin, J. Rikovska Stone, N.J. Stone, H.H. Stroke, G. Tungate, D. T. Yordanov, and Yu. M. Volkov.
Nuclear Spins and Magnetic Moments of ^{71,73,75}Cu: Inversion of $\pi 2p_{3/2}$ and $\pi 1f_{5/2}$ Levels in ^{75}Cu.
Phys. Rev. Lett., 103(14):142501, oct 2009.

[102] A.N. Andreyev, J. Elseviers, M. Huyse, P. Van Duppen, S. Antalic, A. Barzakh, N. Bree, T.E. Cocolios, V. F. Comas, J. Diriken, D.V. Fedorov, V.N. Fedosseev, S. Franchoo, J. A. Heredia, O. Ivanov, U. Köster, B.A. Marsh, K. Nishio, R. D.

Page, N. Patronis, M.D. Seliverstov, I. Tsekhanovich, P. Van den Bergh, J. Van De Walle, M. Venhart, S. Vermote, M. Veselsky, C. Wagemans, T. Ichikawa, A. Iwamoto, P. Möller, and A. J. Sierk.

New Type of Asymmetric Fission in Proton-Rich Nuclei.

Phys. Rev. Lett., 105(25):252502, dec 2010.

[103] M.D. Seliverstov, T.E. Cocolios, W. Dexters, A.N. Andreyev, S. Antalic, A. E. Barzakh, B. Bastin, J. Büscher, I. G. Darby, D.V. Fedorov, V.N. Fedosseev, K. T. Flanagan, S. Franchoo, G. Huber, M. Huyse, M. Keupers, U. Köster, Yu. Kudryavtsev, B.A. Marsh, P. L. Molkanov, R. D. Page, A. M. Sjödin, I. Stefan, P. Van Duppen, M. Venhart, and S. G. Zemlyanoy.

Electromagnetic moments of odd-A $^{193--203,211}$Po isotopes.

Phys. Rev. C, 89(3):034323, mar 2014.

[104] R.N. Wolf, F. Wienholtz, D. Atanasov, D. Beck, K. Blaum, Ch. Borgmann, F. Herfurth, M. Kowalska, S. Kreim, Yu. A. Litvinov, D. Lunney, V. Manea, D. Neidherr, M. Rosenbusch, L. Schweikhard, J. Stanja, and K. Zuber.

ISOLTRAP's multi-reflection time-of-flight mass separator/spectrometer.

Int. J. Mass Spectrom., 349-350:123–133, sep 2013.

[105] W. H. King.

Comments on the Article "Peculiarities of the Isotope Shift in the Samarium Spectrum".

J. Opt. Soc. Am., 53(5):638, may 1963.

[106] R. F. Casten, D. D. Warner, D. S. Brenner, and R. L. Gill.

Relation between the Z=64 Shell Closure and the Onset of Deformation at N=88-90.

Phys. Rev. Lett., 47(20):1433–1436, nov 1981.

[107] G.D. Alkhazov, A.E. Barzakh, I.Ya. Chubukov, V.P. Denisov, V.S. Ivanov, V.N. Panteleev, V.E. Starodubsky, N.B. Buyanov, M.N. Fedoseyev, V.S. Letokhov, V.I. Mishin, and S.K. Sekatsky.

Nuclear electromagnetic moments and charge radii of deformed thulium isotopes with the mass numbers A $= 157 - 172$.

Nucl. Phys. A, 477(1):37–54, feb 1988.

[108] A.E. Barzakh, D.V. Fedorov, A. M. Ionan, V. S. Ivanov, F. V. Moroz, K. A. Mezilev, S. Yu. Orlov, V. N. Panteleev, and Yu. M. Volkov.

Laser spectroscopic studies of ^{145}Gd,^{145}Gd^m, and ^{143}Gd^m.

Phys. Rev. C, 72(1):017301, jul 2005.

[109] I. Angeli and K.P. Marinova.

Table of experimental nuclear ground state charge radii: An update.

At. Data Nucl. Data Tables, 99(1):69–95, jan 2013.

[110] Maria Göppert-Mayer.

Über Elementarakte mit zwei Quantensprüngen.

Ann. Phys., 401(3):273–294, 1931.

[111] W. Kaiser and C. G. B. Garrett.

Two-Photon Excitation in CaF$_2$: Eu^{2+}.

Phys. Rev. Lett., 7(6):229–231, sep 1961.

[112] B. Cagnac, G. Grynberg, and F. Biraben.

Spectroscopie d'absorption multiphotonique sans effet Doppler.

J. Phys., 34(10):845–858, 1973.

[113] N. Bloembergen and M D Levenson.

Doppler-free two-photon absorption spectroscopy.

volume 13 of *Topics in Applied Physics*, chapter 8, pages 315–369. Springer Berlin Heidelberg, Berlin, Heidelberg, 1976.

[114] Keith D Bonin and Thomas J. McIlrath.

Two-photon electric-dipole selection rules.

J. Opt. Soc. Am. B, 1(1):52, mar 1984.

[115] Shishaev A.V . Vasilenko L.S., Chebotaev V.P.

Line Shape of Two-Photon Absorption in a Standing-Wave Field in a Gas.

JETP Lett., 12(3):113, 1970.

[116] David R. Lide, editor.
CRC Handbook of Chemistry and Physics.
American Chemical Society, CRC Press/Taylor & Francis Group: Boca Raton, 88
edition, jan 2008.

Corrigendum

This addendum addresses parts of the thesis which, after thorough review, need to be corrected.

Corrections to chapter 2

- section 2.1 has been based on the following references, as described in the original publication (cds record no. 2227955):

  (1) W. Demtröder, *Experimentalphysik 3: Atome, Moleküle und Festkörper*, Springer-Verlag, 3. edition, 2005

  (2) W. Demtröder, *Laserspektroskopie: Grundlagen und Techniken*, Springer-Verlag, 5. edition, 2007

  (3) V.S. Letokhov, *Laser Photionization Spectroscopy*, Academic Press, Inc., 1. edition, 1987

  (4) Jean-Patrick Connerade, *Highly Excited Atoms*, Cambridge University Press,

1998, Cambridge Books Online, URL

(5) D. Meschede, *Gerthsen Physik*, Springer-Verlag, 24. edition, 2010

- Equation 2.2 should read:

$$-\frac{\hbar^2}{2m_e}\Delta_e\psi - \frac{\hbar^2}{2m_p}\Delta_p\psi - \frac{e^2}{4\pi\epsilon_0 r}\psi = E\psi(\boldsymbol{r}_e, \boldsymbol{r}_p)$$

- p. 8, last paragraph should read as follows:

  [...] $n \in \mathbb{N}, 0$ is the principal quantum number, l is the orbital angular momentum ($0 \leq l \leq n-1$) and m is the magnetic quantum number (-l$\leq m \leq$l). l and m can take on a number of different values for a definite n but still lead to the same energy (see Equation 2.7), corresponding to a n^2 degeneracy of the energy levels. [...]

- Equation 2.8 should read

$$E_{IP} = -E_n$$

  with E_n defined as in Equation 2.7.

- Equation 2.10 should read

$$\Delta E \approx \frac{\mu_0 e^2}{4\pi m_e^2 r^3}(\boldsymbol{l} \cdot \boldsymbol{s}) \propto \frac{\hbar^2}{2}\left[j(j+1) - l(l+1) - s(s+1)\right]$$

  and Equation 2.11 should read

$$E_{nj} = E_n\left[1 + \frac{\alpha^2}{n}\left(\frac{1}{j+1/2} - \frac{3}{4n}\right)\right]$$

  where both are defined for the hydrogen atom.

- p. 10, 6$^{\text{th}}$ line should be:

  [...] The selection rule is $|I - J| \leq F \leq I + J$ where a transition is only possible if ΔF is ± 1 or 0.[...]

- p.15, below Equation 2.16, the sentence is missing a more exact definition of the wave functions and should therefore read:

  [...] For a transition $E_2 \rightarrow E_1$ the radial wave functions $\psi_{1,2}$ of both states have to be taken into account. [...]

Corrections to the bibliography

The following references were not correctly given and are presented here either in a corrected form or through addition of their DOI:

- [8] Neugart R., Kaufman S.L., Klempt W., Moruzzi G., Otten EW., Schinzler B. (1977) High-Resolution Spectroscopy in Fast Atomic Beams. In: Hall J.L., Carlsten J.L. (eds) Laser Spectroscopy III. Springer Series in Optical Sciences, vol 7. Springer, Berlin, Heidelberg

- [9] DOI: 10.1016/j.nimb.2019.04.043

- [11] DOI: 10.1016/j.nimb.2019.04.076

- [15] Marsh, B.A., Day Goodacre, T., Sels, S. *et al.* Characterization of the shape-staggering effect in mercury nuclei. *Nature Phys* **14**, 1163–1167 (2018) doi:10.1038/s41567-018-0292-8

- [46] DOI: 10.5170/CERN-2013-007.203

- [79] V. Sonnenschein, Laser developments and high resolution resonance ionization spectroscopy of actinide elements, PhD Thesis, Department of Physics Jyväskylä, 2015, ISBN 978-951-39-6050-6 (electronic version)